



Wave propagation under influence of currents



Wave propagation under influence of currents

Caroline Gautier
Andre van der Westhuysen

Title

Wave propagation under influence of currents

Client
Waterdienst

Project
1202119-003

Reference
1202119-003-HYE-0002

Keywords

SBW-Waddenze, SWAN, radar, wave-current interaction

Summary

The present study aims to assess the prediction of wave penetration into tidal inlets under ambient current in SWAN. The performance of SWAN in the modelling of wave-current interaction was studied for two field cases, namely Port Phillip Bay Heads, Australia, and the Amelander Zeegat in the Dutch Wadden Sea. In-situ wave observations were available for both field situations. In addition, the Amelander Zeegat field case includes recently obtained marine (X-band) radar fields of a number of variables over the tidal inlet.

The ambient current was shown to have a significant effect on the wave parameters. The addition of enhanced current-induced whitecapping using the expression of Deltares (2010b) has an important, but comparatively smaller impact, which is mainly seen in the significant wave height and mean period. In the Port Phillip Bay field case, which features near-idealised swell and wind sea conditions, the enhanced dissipation term clearly reduces H_{m0} during ebb, for which negative current gradients are found, improving the agreement with observations. For slack and flood, which feature positive or small negative current gradients, generally small impacts on wave height were found. By contrast, in the Amelander Zeegat, reductions in H_{m0} were found during ebb, but also for slack and flood, since negative gradients in the current field were found during all tidal phases. Although the results for H_{m0} improved with the application of the enhanced current-induced dissipation, $T_{m-1,0}$ remains underestimated in the Amelander Zeegat field case. The optimal value for the proportionality coefficient C_{ds3} in the enhanced current-induced dissipation term has not been found yet. For some situations $C_{ds3} = 0.8$ is better, for others $C_{ds3} = 1.6$, suggesting that the parameterisation of Deltares (2010b) should be further refined. Therefore, calibration for specific situations is recommended at present.

Comparison of SWAN results with the spatial fields processed from the radar observations has given valuable insight into the spatial performance of SWAN. Furthermore, qualitative agreement has been found between the observed wave lengths and computed values.

References

Projectplan SBW-Waddenze 2010

Version	Date	Author	Initials	Review	Initials	Approval	Initials
	13/09/2010	André van der Westhuysen, Caroline Gautier		Jacco Groeneweg			
	22/09/2010	AW, CG		Jacco Groeneweg			
	25/10/2010	AW, CG		James Kaihatu		Marcel van Gent	
	19/11/2010	AW, CG	J	James Kaihatu	JMK	Marcel van Gent	C

Title
Wave propagation under influence of currents

Client Waterdienst	Project 1202119-003	Reference 1202119-003-HYE-0002
------------------------------	-------------------------------	--

Executive Summary

General

In compliance with the Dutch Water Act ('Waterwet, 2009'), the safety of the Dutch primary sea and flood defences must be assessed every six years (2011, 2017, etc.) for the required level of protection. This assessment is based on the Hydraulic Boundary Conditions (HBC) and the Safety Assessment Regulation (VTV: *Voorschrift op Toetsen op Veiligheid*). These HBC are derived every six years in the project WTI ('Wettelijk Toets Instrumentarium') and are approved by the Minister of Transport, Public Works and Water Management. The spectral wind wave model SWAN (Booij et al.1999) plays a key role in the estimation of these HBC. Since there was some uncertainty about the reliability of SWAN for application to the geographically complex area of the the Wadden Sea, a number of activities has been initiated under the project 'SBW-Waddenzee' to improve the model.

Problem Statement

Further assessment of wave propagation in SWAN under extreme conditions in the Wadden Sea is hampered by a scarcity of data. Although the Wadden Sea observational campaign of Zijderveld and Peters (2008) features a large number of wave buoys, the coverage remains too sparse, and observations of current in the tidal channels have been infrequent. In situ wave and current observations under near-idealized conditions in the tidal inlet of Port Phillip Bay Heads, Australia, provides a valuable data set in this regard. In addition, recently, analysis software was installed on the X-band ship's radar deployed on the island of Ameland in the Wadden Sea, overlooking the Amelander Zeegat. This provides the opportunity to assess the spatial propagation patterns produced by SWAN under field conditions, including the influence of current and to elucidate the discrepancies in low-frequency results observed in earlier hindcast studies.

Study Aim

The aim of the present study is to assess the prediction of wave penetration into tidal inlets under ambient current in SWAN, using in situ and remote sensing observations of waves and current.

Approach

This study is comprised of two parts: Port Phillip Bay Heads and the Amelander Zeegat.

- Port Phillip Bay Heads

Port Phillip Bay Heads, Australia, is characterised by dominant SW swell that is strongly influenced by the tidal current through the heads, with episodes of local storms generating wind sea. Simulations are carried out with both the default version of SWAN and with the enhanced dissipation of Deltires (2010b). The enhanced dissipation is likely to improve the SWAN results. The performance of these two versions of SWAN in the prediction of wave propagation in ambient current will be evaluated in terms of integral parameters and

Title
Wave propagation under influence of currents

Client	Project	Reference
Waterdienst	1202119-003	1202119-003-HYE-0002

frequency spectra, using the observations at the AWAC instruments between the heads of Port Phillip Bay.

- Amelander Zeegat

The Amelander Zeegat field case is characterized by actively growing (yet mature) wind sea originating from the North Sea. Since the beginning of 2010, X-band radar images have been recorded here. From these data, current, water depth, wave length and wave direction fields can be obtained, spanning the entire Amelander Zeegat tidal inlet (up to the ebb tidal delta). This data, together with in situ (point) data from the AZG wave buoys, forms a rich data set for hindcasting. Stationary SWAN simulations are performed for eight storm instants. To check the sensitivity, several variations with different settings of the enhanced dissipation term (C_{ds3}) and of the current fields were applied. The SWAN results – both spectra and parameters will be compared with buoy observations. From the radar data, mainly the wave direction and wave length is to be used to compare with the SWAN observations. Also the spectra from the radar data will be compared with the SWAN results and buoy spectra but rather in a qualitative than in a quantitative way.

Conclusions and Recommendations

Based on the findings of this study, the following main conclusions are drawn:

- The ambient current was shown to have a significant effect on the wave parameters (wave height, mean period and direction) in the Port Phillip Bay Heads and Amelander Zeegat cases. The addition of enhanced current-induced whitecapping has an important, but comparatively smaller impact, which is mainly seen in the significant wave height and mean period.
- In the Port Phillip Bay field case, which features near-idealised swell and wind sea conditions, the enhanced dissipation term clearly reduces H_{m0} during ebb, for which negative current gradients are found, improving the agreement with observations. For slack and flood, which feature positive or small negative current gradients, generally small impacts on wave height were found. By contrast, in the Amelander Zeegat, reductions in H_{m0} were found during ebb, but also for slack and flood. This is because negative gradients in the current field were found during all tidal phases, i.e. both increasing opposing current and decreasing following current along the wave path. Although the results for H_{m0} improved with the application of the enhanced current-induced dissipation, $T_{m-1,0}$ remains underestimated in the Amelander Zeegat field case.
- The results of this study show that no definitive value for the proportionality coefficient C_{ds3} has been found yet. From the values considered here, $C_{ds3} = 1.6$ appears to be a suitable value in the Port Phillip Bay Heads case. By contrast, in the Amelander Zeegat case, either the value $C_{ds3} = 0.8$ or 1.6 was found to be optimal, depending on whether a selection or all of the buoys are considered. The SWAN calibration for WTI (Deltaires (2010a)) resulted in $C_{ds3} = 0.8$, based on Amelander Zeegat cases of January, March and November 2007. Deltaires (2010b) found an optimal value of 0.7

Title
Wave propagation under influence of currents

Client	Project	Reference
Waterdienst	1202119-003	1202119-003-HYE-0002

on the basis of laboratory flume cases and Amelander Zeegat field cases recorded in 2004 and 2005.

- Comparison of SWAN results with the spatial fields processed from the radar observations has given valuable insight into the spatial performance of SWAN. Wave directions are predicted well in general, capturing refraction over the main tidal channel banks and, elsewhere, components that cross over the tidal channel. However, differences are found moving deeper into the tidal inlet. Since both sources have their uncertainties, it is unknown whether SWAN or the radar performs better here. Qualitative agreement has been found between the observed wave lengths and computed values (based on the computed peak period and dispersion relation without currents).
- The study has given valuable insight into the quality and usefulness of the radar data. The quality appears to vary with tidal phase, with larger scatter in results during ebb. Caution needs to be applied over regions with large bottom gradients and small wave heights. In addition, the frequency range of the observations is limited to values below 0.34 Hz, making it more suitable for studying lower-frequency components. However, until a verified Modulation Transfer function (MTF) is found, neither the wave spectra nor wave heights are useful for model validation.

The following main recommendations are formulated:

- The optimal value for C_{ds3} has not been found yet. For some situations $C_{ds3} = 0.8$ is better, for others $C_{ds3} = 1.6$, suggesting that the parameterisation of Deltares (2010b) should be further refined. Therefore, calibration for specific situations is recommended at present.
- The radar observations provide valuable measurements. However, more experience must be gained in order to benefit from all its possibilities.
- It is strongly recommended to keep in close contact with Seadarq, who develops the radar processing software, and to make joint improvements. The development of a reliable MTF would be of great interest. Furthermore, it is suggested to check the influence of the postprocessing settings (for instance cube size and number of images to base spectra on) on the wave data and optimise them.
- During the last months, the processing of radar data has been further improved. A better filter technique is available to remove the low frequency energy peak. Also, improvements to suppress the mirror frequency are made. It is recommended to produce updated radar observations and make another comparison between radar data, buoy data and SWAN results.

Contents

List of Tables	iii
List of Figures	iv
List of Symbols	vii
1 Introduction	1
1.1 General problem statement of SBW project	1
1.2 Problem statement of present project	2
1.3 Study aim	3
1.4 Approach	3
1.5 Project team	4
1.6 Report structure	4
1.7 Acknowledgement	4
2 Approach	5
2.1 Introduction	5
2.2 Enhanced dissipation on current gradients	5
2.3 Model settings	6
3 Port Phillip Bay Heads	7
3.1 Introduction	7
3.2 Description of field case	7
3.3 Validation cases	8
3.4 Model setup	8
3.5 Model results	10
3.5.1 Storm 1: SW Swell	10
3.5.2 Storm 3: SW swell with wind sea	11
3.6 Conclusions	12
4 Tidal Inlet Ameland	14
4.1 Approach	14
4.2 Available data	14
4.3 Storm selection	15
4.4 SWAN simulations	16
4.4.1 General setup, input and output	16
4.4.2 Input: grids and bathymetry	17
4.4.3 General, physical and numerical settings	18
4.4.4 Input: Wind and wave boundary conditions	18
4.4.5 Input: water level and currents	19
4.4.6 SWAN results	20
4.5 Comparison SWAN simulations with buoy observations	21
4.5.1 Transects	21
4.5.2 Spectra at buoy locations	22
4.5.3 Scatterplots	24
4.5.4 Tables	24
4.5.5 Statistical Tables	24

4.6	Comparison SWAN simulations with radar observations	25
4.6.1	Introduction	25
4.6.2	Wave parameters	26
4.6.3	Wave spectra	28
4.7	Conclusions hindcast Ameland	29
4.7.1	Hindcast and buoy observations	29
4.7.2	Hindcast and radar observations	30
5	Conclusions and recommendations	31
6	References	33

Appendices

A	Brief description of radar processing	A-1
B	SWAN input file Amelander Zeegat G1	B-1
C	SWAN input file Amelander Zeegat, grid G2	C-1
D	Tables	D-1
E	Figures	E-1

List of Tables

- 3.1 Stationary hindcast cases for Port Phillip Bay Heads
- 4.1 Observation locations for waves, wind and water levels
- 4.2 Selected time instants for the Amelander Zeegat simulations
- 4.3 Characteristics of frequency, directional and geographical grids for the Amelander Zeegat simulations
- 4.4.a Results SWAN simulations (series A,B,C,D,E,F) and observations Amelander Zeegat; Hm0 [m] for times t1, t2, t3, t4
- 4.4.b Results SWAN simulations (series A,B,C,D,E,F) and observations Amelander Zeegat; Hm0 [m] for times t5, t6, t7, t8
- 4.4.c Results SWAN simulations (series A,B,C,D,E,F) and observations Amelander Zeegat; Tm-1,0 [s] for times t1, t2, t3, t4
- 4.4.d Results SWAN simulations (series A,B,C,D,E,F) and observations Amelander Zeegat; Tm-1,0 [s] for times t5, t6, t7, t8
- 4.5 Statistical parameters SWAN (series A,B,C,D,E,F) and observations Amelander Zeegat Hm0 and Tm-1,0; times 1-8
- 4.6 Statistical Parameters

List of Figures

- 3.1 Location map of Port Phillip Bay Heads, Australia (top) with positions of observation stations (bottom) (WL & Lesser 2007).
- 3.2 Bathymetry of Port Phillip Bay Heads, with observation stations and output curve, and curvilinear output curve (after WL & Lesser 2007).
- 3.3 Comparison of observed and reproduced frequency spectra at the Triaxis buoy WAVE_A, for Storm 1 (ebb, slack and flood).
- 3.4 Comparison of observed and reproduced frequency spectra at the Triaxis buoy WAVE_A, for Storm 3 (ebb, slack and flood).
- 3.5 Model results for the Port Phillip Bay Heads field case for Storm 1: 28-Jun-2006 06:30 (ebb). Enhanced whitecapping $C_{ds3} = 0.00$.
- 3.6 Model results for the Port Phillip Bay Heads field case for Storm 1: 28-Jun-2006 06:30 (ebb). Enhanced whitecapping $C_{ds3} = 0.80$.
- 3.7 Model results for the Port Phillip Bay Heads field case for Storm 1: 28-Jun-2006 10:30 (slack). Enhanced whitecapping $C_{ds3} = 0.00$.
- 3.8 Model results for the Port Phillip Bay Heads field case for Storm 1: 28-Jun-2006 10:30 (slack). Enhanced whitecapping $C_{ds3} = 0.80$.
- 3.9 Model results for the Port Phillip Bay Heads field case for Storm 1: 28-Jun-2006 14:00 (flood). Enhanced whitecapping $C_{ds3} = 0.00$.
- 3.10 Model results for the Port Phillip Bay Heads field case for Storm 1: 28-Jun-2006 14:00 (flood). Enhanced whitecapping $C_{ds3} = 0.80$.
- 3.11 Model results of H_{m0} for the Port Phillip Bay field case for Storm 1 (ebb, slack and flood).
- 3.12 Model results of T_{m01} for the Port Phillip Bay field case for Storm 1 (ebb, slack and flood).
- 3.13 Model results for the Port Phillip Bay field case spectra for Storm 1 (ebb, slack and flood).
- 3.14 Model results for the Port Phillip Bay Heads field case for Storm 3: 27-Oct-2006 20:30 (ebb). Enhanced whitecapping $C_{ds3} = 0.00$.
- 3.15 Model results for the Port Phillip Bay Heads field case for Storm 3: 27-Oct-2006 20:30 (ebb). Enhanced whitecapping $C_{ds3} = 0.80$.
- 3.16 Model results for the Port Phillip Bay Heads field case for Storm 3: 27-Oct-2006 23:30 (slack). Enhanced whitecapping $C_{ds3} = 0.00$.
- 3.17 Model results for the Port Phillip Bay Heads field case for Storm 3: 27-Oct-2006 23:30 (slack). Enhanced whitecapping $C_{ds3} = 0.80$.
- 3.18 Model results for the Port Phillip Bay Heads field case for Storm 3: 27-Oct-2006 03:30 (flood). Enhanced whitecapping $C_{ds3} = 0.00$.
- 3.19 Model results for the Port Phillip Bay Heads field case for Storm 3: 27-Oct-2006 03:30 (flood). Enhanced whitecapping $C_{ds3} = 0.80$.

- 3.20 Model results of H_{m0} for the Port Phillip Bay field case for Storm 3 (ebb, slack and flood).
- 3.21 Model results of T_{m01} for the Port Phillip Bay field case for Storm 3 (ebb, slack and flood).
- 3.22 Model results for the Port Phillip Bay field case spectra for Storm 3 (ebb, slack and flood).
- 4.1 Bathymetry and measurement locations Amelander Zeegat
- 4.2 Data coverage SBW multibeam 2009
- 4.3 Timeseries waves, wind, current, water level
 - 4.4.a Grids G1 and G2 and locations for wave boundary conditions
 - 4.4.b SWAN results H_{m0} [m] and wave direction on grid G1
- 4.5 Timeseries wind velocity and direction
 - 4.6.a SWAN Input water level [m + NAP] standard
 - 4.6.b SWAN Input water level [m + NAP] optimised D3D
- 4.7.a SWAN Input current velocity [m/s] standard
- 4.7.b SWAN Input current velocity [m/s] optimised D3D
- 4.7.c SWAN Input current velocity [m/s] radar + D3D
- 4.8.a SWAN Results H_{m0} [m], series A, B, C, D; instants 1-4
- 4.8.b SWAN Results H_{m0} [m], series A, B, C, D; instants 5-8
- 4.8.c Overview SWAN results H_{m0} [m] and position transect
- 4.9.a SWAN Results $T_{m-1,0}$ [s], series A, B, C, D; instants 1-4
- 4.9.b SWAN Results $T_{m-1,0}$ [s], series A, B, C, D; instants 5-8
- 4.10.a Model Results of H_{m0} for series A, B, C, D, E, F on transect; instants 1-4
- 4.10.b Model Results of H_{m0} for series A, B, C, D, E, F on transect; instants 5-8
- 4.11.a Model Results of $T_{m-1,0}$ for series A, B, C, D, E, F on transect; instants 1-4
- 4.11.b Model Results of $T_{m-1,0}$ for series A, B, C, D, E, F on transect; instants 5-8
- 4.12.a Model Results of wave direction for series A, B, C, D on transect; instants 1-4
- 4.12.b Model Results of wave direction for series A, B, C, D on transect; instants 5-8
- 4.13 Wave spectra of variance density, wave direction and wave spreading, series A B C D

- 4.14 Scatter diagram Amelander Zeegat series A, B, C, D, E, F; H_{m0}
- 4.15 Scatter diagram Amelander Zeegat series A, B, C, D, E, F; $T_{m-1,0}$
- 4.16 Scatter diagram Amelander Zeegat series A, B, C, D, E, F; mean wave direction
- 4.17.a Comparison dominant wave direction SWAN and radar, instants 1-3
- 4.17.b Comparison dominant wave direction SWAN and radar, instantss 4-6
- 4.17.c Comparison wave direction SWAN and radar, instants 7-8
- 4.18.a Model, buoy and radar results of Wave Peak Direction for series C, times 1-4
- 4.18.b Model, buoy and radar results of Wave Peak Direction for series C, times 5-8
- 4.19 Comparison wave length SWAN and radar, instants 1, 3, 5, 7
- 4.20 Comparison wave spectra RADAR, BUOY, SWAN; instant1, AZB21/22/31/32
- 4.21 2d Radar intensity spectrum location AZB31
- 4.22 Comparison wave height [m] SWAN and radar

List of Symbols

Symbol	Unit	Description
AHD	m	Australian Height Datum (approximately equivalent to mean sea level)
$B(k)$	-	Saturation spectrum
B_r	-	Threshold saturation level
c_g	m.s^{-1}	Group velocity
c_σ	rad.s^{-2}	Propagation velocity in frequency space
C_{ds3}	-	Proportionality coefficient in enhanced whitecapping expressions
Dir	${}^\circ\text{N}$	Mean wave direction (Nautical Convention)
E	$\text{m}^2/\text{Hz}/\text{deg}$	Variance density
g	m.s^{-2}	Gravitational acceleration
H_{m0}	m	Significant wave height
\vec{k}	rad.m^{-1}	Wave number vector; $\vec{k} = (k_x, k_y)$
\overline{L}	m	Wave length ($L=2\pi/ \vec{k} $)
m_n	m^2Hz^n	n^{th} moment
NAP	m	Dutch national levelling datum
RD	km	Dutch Rijksdriehoek coordinate system
σ	rad.s^{-1}	Radian frequency
θ_w	${}^\circ$	Mean wave direction (Cartesian Convention)
$T_{m-1,0}$	s	Spectral mean wave period ($= (m_1/m_0)$)
T_{m01}	s	Spectral mean wave period ($= (m_0/m_1)$)
U_{10}	m.s^{-1}	Wind speed (at 10 m elevation)
U_{dir}	${}^\circ\text{N}$	Wind direction
\vec{U}	m.s^{-1}	Current velocity

1 Introduction

1.1 General problem statement of SBW project

In compliance with the Dutch Water Act ('Waterwet, 2009'), the safety of the Dutch primary sea and flood defences must be assessed every six years (2011, 2017, etc.) for the required level of protection. This assessment is based on the Hydraulic Boundary Conditions (HBC) and the Safety Assessment Regulation (VTV: *Voorschrift op Toetsen op Veiligheid*). These HBC are derived every six years in the project WTI ('*Wettelijk Toets Instrumentarium*') and are approved by the Minister of Transport, Public Works and Water Management.

The HBC are used to subject the sea and flood defences to a stepwise assessment ranging from 'simple' to 'advanced' tests, resulting in a statement of whether a section of the sea or flood defence is safe or unsafe. During these assessments, so-called 'knowledge vacuums' (*kennisleemtes*) may be identified. The result may be that the assessment cannot be completed and sections of the sea or flood defence are labelled 'geen oordeel' (no judgement; safety level unknown), which is an undesirable situation. Another possibility may be that sea or flood defences would erroneously pass or fail the assessment.

Because of this problem of a 'knowledge vacuum' with respect to the assessment of the safety of sea and flood defences, the overall SBW ('Strength and Loading of Water Defenses' (SBW: *Sterkte en Belasting Waterkeringen*)) project, in which the present project forms one step, has the following general objective:

'To fill the most important knowledge vacuums in order to achieve a better estimate of the safety against failing of the primary sea and flood defences.'

As part of this larger project, the subproject SBW-Waddenzee was started in 2006. By that time, the starting point was the observation that there was uncertainty concerning the quality of the HBC, which are an important input into the assessment, in particular those for the Wadden Sea sea defences. The uncertainty in the quality of the HBC was due to the fact that they were obtained from an inconsistent set of measurements and design values (WL (2002)), while for the rest of the Dutch coast (the closed Holland Coast and the Zeeland Delta) they have been determined with a probabilistic method, in which offshore wave statistics are transformed to nearshore locations. For the latter the wave model SWAN (Booij et al. (1999)) has been applied. Due to lack of verification data, there was insufficient confidence in the wave model SWAN (initially mainly regarding the penetration of low-frequency storm waves) to use it to obtain reliable boundary conditions in the Wadden Sea for HBC2006. In addition to initially recognized problems with respect to low-frequency wave penetration, the subproject SBW-Waddenzee sets out to determine the general suitability of SWAN in the Wadden Sea and to specify the improvements required to produce reliable HBC in this region.

The objective of the SBW-Waddenzee project is therefore to:

'Verify, and where possible improve, the quality of the models and methods for the Wadden Sea so that in 2011 and beyond better HBC can be calculated.'

The path towards meeting this objective is laid out in a Plan of Action (WL,2006) which describes a step by step approach of performing hindcasts of storm events in the Wadden Sea and other relevant areas, analysis of the results, and sensitivity and uncertainty analyses. Despite recent and ongoing measurement campaigns in the Dutch part of the Wadden Sea, the storm events required for such an approach are scarce, and information about the performance of the wave model in other relevant (i.e. similar) areas is highly valued.

1.2 Problem statement of present project

Hindcast studies in the Wadden Sea and the inlet of the Eastern Scheldt (Svašek, 2007; WL, 2007; WL & Alkyon, 2007; Alkyon, 2008; Royal Haskoning, 2008; Witteveen+Bos, 2008) have identified the following three main areas of unsatisfactory performance of the wind wave model SWAN in these regions: (i) an insufficient amount of low-frequency (swell range) energy of offshore North Sea waves penetrates into the Wadden Sea interior and the Eastern Scheldt Inlet, (ii) wave heights are overestimated in opposing current (ebb) in the tidal channels and (iii) wave heights are underestimated under finite depth wave growth conditions on the shallow flats in the Wadden Sea interior. The latter model inaccuracy has been addressed by a new expression for depth-induced breaking (Van der Westhuysen, 2009, 2010), whereas the overprediction of wave heights on negative gradients in opposing current has been corrected by a formulation for enhanced whitecapping dissipation (Deltares, 2010b). Regarding the penetration of low-frequency energy into the Wadden Sea and Eastern Scheldt Inlet, sensitivity analyses (Svašek, 2007, Alkyon, 2008; Alkyon, 2009; Deltares and Alkyon, 2009a, Zijlema, 2009) have identified model sensitivities that could account for the underprediction of energy found in the interior, namely the settings for bottom friction and an alteration to the calculation of wave refraction over swell-range frequencies.

Alkyon (2009) and Zijlema (2009) show that a reduction of the Hasselmann et al. (1973) bottom friction coefficient from 0.067 to 0.038 m²/s³ could explain part, but not all of the observed discrepancies. Van Vledder et al. (2010) motivated the use of this lower value on the basis of a reanalysis of the study by Bouws and Komen (1983). Alkyon (2009) shows that a reduction in the amount of linear refraction on low-frequency components (0.05-0.2 Hz) could explain the remainder of the discrepancy with the nearshore observations. Therefore, these two remedies have been taken up as so-called fall back options for computing HBCs in the Wadden Sea (Deltares and Alkyon 2009a). However, apart from accounting for some smoothing of energy over the domain, there is no clear reason as to why altering refraction should improve model predictions nearshore. Alkyon (2009) and Deltares and Alkyon (2009b) studied propagation patterns in the Wadden Sea by means of an inter-comparison between the spectral wind wave model SWAN, a MSE diffraction model and a ray-tracing linear refraction model. This study identified refraction as the dominant propagation process over diffraction. However, due to unavailability, these studies did not include a comparison with observed data, and also did not include the influence of currents in the tidal inlets on the wave propagation. As a result, it is still not clear whether SWAN produces accurate propagation patterns over the complex topography of the Wadden Sea.

Further assessment of wave propagation in SWAN under extreme conditions in the Wadden Sea is hampered by a scarcity of data. Although the Wadden Sea observational campaign of Zijderveld and Peters (2008) features a large number of wave buoys, the coverage remains too sparse, and observations of current in the tidal channels have been infrequent. In situ wave and current observations under near-idealized conditions in the tidal inlet of Port Phillip

Bay Heads, Australia, provides a valuable data set in this regard. In addition, recently, analysis software was installed on the X-band ship's radar deployed on the island of Ameland in the Wadden Sea, overlooking the Amelander Zeegat. This provides the opportunity to assess the spatial propagation patterns produced by SWAN under field conditions, including the influence of current and to elucidate the discrepancies in low-frequency results observed in earlier hindcast studies.

1.3 Study aim

The aim of the present study is to assess the prediction of wave penetration into tidal inlets under ambient current in SWAN, using in situ and remote sensing observations of waves and current.

1.4 Approach

This study is comprised of two parts. In the first, the performance of SWAN in the prediction of wave propagation in ambient current is investigated for the near-idealised, deep water situation of Port Phillip Bay Heads, using in situ point measurements. In the second part, the modelling of wave propagation in SWAN is assessed for the Amelander Zeegat field case in the Wadden Sea, using – besides the in situ point measurements - spatial data derived from X-band radar.

Port Phillip Bay Heads

Port Phillip Bay Heads, Australia, is characterised by dominant SW swell that is strongly influenced by the tidal current through the heads, with episodes of local storms generating wind sea. A number of in situ and remote sensing observations are available in this region, operational at various times since 2006: two bottom-mounted AWACs have been deployed between the heads and a Triaxys buoy further offshore. Waves and current fields in the entrance are observed by land-based X-band radar. There is however, no overlapping time interval for the AWAC and X-band radar deployment. As a result, SWAN is evaluated for two storm events in 2006, previously considered by WL and Lesser (2007), hereafter WL07, during which the two AWAC sensors were deployed in the heads. This data set features one case with pure swell, and one with combined wind sea and swell. Using a model setup based on that of WL07, simulations are carried out with both the default version of SWAN and with the enhanced dissipation of Deltires (2010b). The enhanced dissipation term has been developed after the study of WL07 and is likely to improve the SWAN results. The performance of these two versions of SWAN in the prediction of wave propagation in ambient current will be evaluated in terms of integral parameters and frequency spectra, using the observations at the AWAC instruments between the heads.

Amelander Zeegat

The Amelander Zeegat field case is characterized by actively growing (yet mature) wind sea originating from the North Sea. In this respect, the conditions are expected to be distinct from those of Port Phillip Bay Heads, and more complex. Since the beginning of 2010, X-band radar images have been recorded from the lighthouse on the western end of Ameland. Using their specialized software, Seadarq – the company that develops the radar observations – derives from these data, current, water depth, wave length and wave direction fields spanning the entire Amelander Zeegat tidal inlet (up to the ebb tidal delta) .This data has been

recorded for a moderate NW storm during 27-28 January 2010. Together with in situ (point) data from the AZG wave buoys, this forms a rich data set for hindcasting. This data set is used here for the detailed analysis of wave-current interaction. The activities are as follows: (a) A selection of eight stationary cases in one tidal cycle (e.g. ebb, slack, flood) has been made during 27-28 Jan 2010 to hindcast with SWAN. (b) A coupled Delft3D-SWAN model has been set up and run for the storm period to provide current and water level fields. (c) Stationary SWAN simulations have been performed for each of the eight storm instants. The following variations to the model input are applied: (i) Default run, with pre-WTI settings, (ii) a sensitivity test without current (to check influence of current), (iii) a sensitivity test with the enhanced dissipation term of Deltires (2010b), (iv) a sensitivity test with enhanced strength of the Deltires (2010b) term ($C_{ds3} = 1.6$), (v) as iii but with optimised current fields, (vi) as iv but with observed current fields.

1.5 Project team

This project was carried out by Andre van der Westhuysen and Caroline Gautier, with the assistance of Jan Kleijweg and Jos van Heesen of Seadarq and Herman Peters of Rijkswaterstaat DID. The internal quality assurance was carried out by Jacco Groeneweg, and the external review was performed by James Kaihatu of Texas A&M University, USA.

1.6 Report structure

This report is structured as follows: Chapter 2 presents the approach followed in the study. The hindcast of Port Phillip Bay Heads is presented in Chapter 3. The hindcast of the Amelander Zeegat can be found in Chapter 4. Chapter 5 closes the report with general conclusions and recommendations.

1.7 Acknowledgement

The data of the Port Phillip Bay Heads are used by kind permission of the Port of Melbourne Company.

The radar data of the Amelander Zeegat is helpfully provided by Seadarq.

2 Approach

2.1 Introduction

This section presents the modeling approach followed in the present study. First, for reference, the source term for enhanced breaking dissipation of Deltaires (2010b) is summarized (Section 2.2). Because of its impact in the modeling of wave evolution in the presence of current, it will receive special attention in the evaluation of wave propagation in the following sections. Section 2.3 describes the remaining settings for model physics and numerics applied in this study.

2.2 Enhanced dissipation on current gradients

Following Ris and Holthuijsen (1996), Deltaires (2010b) shows that the overprediction of wave heights in a negative gradient in counter current by SWAN can be corrected by applying enhanced whitecapping dissipation in such situations. Deltaires (2010b) proposes to use the basic form of the saturation-based expression of Van der Westhuysen et al. (2007) for this purpose. In order to isolate the contribution of currents in the wave height overestimation, the degree of enhanced dissipation is scaled with the increase in steepness due to negative gradients in the current, which is linked to the degree of current-induced Doppler shifting per spectral component. Note that this can occur for negative gradients in both opposing and following currents. This yields an additional dissipation term $S_{wc,cur}$ in the total source term in the action balance equation of SWAN (refer Booij et al. 1999):

$$S_{tot} = S_{in} + S_{wc} + S_{nl4} + S_{bot} + S_{brk} + S_{nl3} (+ S_{wc,cur}) \quad (2.1)$$

given by:

$$S_{wc,cur} = -C_{ds3} \max\left[\frac{c_\sigma(\sigma, \theta)}{\sigma}, 0\right] \left[\frac{B(k)}{B_r}\right]^{p/2} E(\sigma, \theta) . \quad (2.2)$$

Here $B(k) = c_g k^3 E(\sigma)$ is the saturation spectrum and B_r a threshold saturation level. The parameterizations of B_r and p are taken similar to those of Van der Westhuysen et al. (2007). The term (2.2) increases whitecapping dissipation in regions with negative current gradients, characterized by positive values of the propagation speed in relative frequency space c_σ :

$$c_\sigma = \frac{d\sigma}{dt} = \frac{\partial\sigma}{\partial d} \left[\frac{\partial d}{\partial t} + \vec{U} \cdot \nabla d \right] - c_g \vec{k} \cdot \frac{\partial \vec{U}}{\partial s} , \quad (2.3)$$

in which d is the depth, \vec{U} the current velocity and s the space coordinate in the propagation direction θ . Expression (2.2) contains one additional calibration parameter relative to the latter expression, namely the proportionality coefficient C_{ds3} . In Deltaires (2010b) this coefficient was calibrated to a value of $C_{ds3} = 0.7$, based on an extensive data set of laboratory and field cases. This was subsequently adjusted to $C_{ds3} = 0.8$ in a calibration study by Deltaires (2010a) for use in the determination of the HBC within the project WTI. This latter setting is

applied in the present study, while a higher value of 1.60 is also considered in sensitivity tests.

2.3 Model settings

The computations presented in this study were performed using the SWAN model version 40.72ABCDE, in stationary third-generation mode. The following formulations for model physics are applied: For the deep water physics, the combination of wind input S_{in} and saturation-based whitecapping S_{wc} proposed by Van der Westhuysen (2007) was used. Quadruplet nonlinear interaction S_{nl4} was modelled using the Discrete Interaction Approximation (DIA) of Hasselmann et al. (1985). The shallow water source terms include triad nonlinear interaction S_{nl3} according to Eldeberky (1996) and bottom friction S_{bot} according to Hasselmann et al. (1973), the latter with $cfjon=0.038 \text{ m}^2/\text{s}^3$. For depth-induced breaking S_{brk} , the biphasic breaker model of Van der Westhuysen (2010) was used, with the extension proposed by Van der Westhuysen (2009). The model setup with these source term expressions will be referred to hereafter as the default model and serves as reference.

In addition, the formulation for enhanced whitecapping dissipation on negative current gradients $S_{wc,cur}$ of Deltires (2010b), presented above, was applied. The use of this term is mentioned explicitly in the following.

The parameter settings applied in the default model setup are the following:

```

GEN3 WESTH
WCAP WESTH cds2=5.0E-5 br=1.75E-3 p0=4. cds3=0.000
QUAD iquad=2 lambda=0.25 Cnl4=3.00e+07
BREA WESTH alpha=0.96 pown=2.5 bref=-1.39630 shfac=500.
TRIAD trfac=0.100 cutfr=2.500
FRIC JONSWAP cfjon=0.038

```

In order to ensure sufficiently converged results, the so-called curvature convergence criteria of Zijlema and Van der Westhuysen (2005) were applied, using strict tolerances. A small degree of underrelaxation was applied to improve the convergence behaviour. The primary settings applied are:

```
NUM STOPC 0 0.01 0.001 99.5 STAT mxitst=120 alfa=0.002
```

3 Port Phillip Bay Heads

3.1 Introduction

In this first part of the study, wave propagation under the influence of current is investigated for the field case of Port Phillip Bay Heads, previously studied by WL07. Here near-idealised conditions of swell waves interacting approximately co-linearly with tidal currents are found. For these conditions, the performance of SWAN is assessed on the basis of in-situ observations located between the heads. Sections 3.2 and 3.3 present a general description of the field case and of the data used for model validation respectively. Section 3.4 gives a description of the model setup applied. These three sections are based on descriptions in WL (2007). Section 3.5 presents the model results for this field case, followed by the conclusions of this part of the study in Section 3.6.

3.2 Description of field case

The Heads of Port Phillip Bay, Melbourne, Australia (PP Heads) (Figures 3.1 and 3.2) are subject to an energetic wave climate, and strong tidal currents due to the filling and emptying of the Port Phillip Bay tidal prism. The domain features a deep canyon cutting through the Heads, and a submerged ebb tidal delta offshore with a crest elevation of about -18 m AHD (Figure 3.2, top panel). The tidal flows at PP Heads are predictable and are approximately aligned with the approach direction of the incoming swell waves. Typical depth-averaged ebb and flood current velocities reach 2 to 3 m/s and offshore significant wave height is typically in the range 1 to 4 m with a peak swell period in the range of 10 to 20 s. Shorter period wind-sea components may also be present.

The Port of Melbourne Corporation has collected wave data offshore of PP Heads for many years using Triaxys wave buoys. Two wave buoys are permanently deployed, in close proximity to each other, approximately 10 km southeast of PP Heads (Figure 3.1, bottom panel, blue dots). These buoys measure waves that are unaffected by the tidal flows in and out of Port Phillip Bay and produce directional wave spectra based on 20 minute data bursts every half hour. Wave parameters and directional spectra are analysed on the buoy and are transmitted ashore as 'MeanDir' or '1.5D' spectrum consisting of the energy, mean direction and directional spreading width for each frequency band. These 'offshore' buoy data are available since July 2004.

Waves and currents in between the Heads are measured using Nortek AWAC instruments bolted to the rocky channel floor on the centreline of the shipping channel in approximately 18 m of water (Figure 3.1, bottom, red dots). The AWACs record velocity profiles in 1 m vertical bins every 10 minutes and perform a 17 minute wave burst every hour. A unique feature of the AWAC instrument is that it incorporates a vertical acoustic surface-tracking beam sampled at 2 Hz which allows accurate measurement of the water surface elevation even under the challenging conditions experienced in PP Heads. Pairs of AWAC instruments have been placed in PP Heads for a series of 6-week deployments more or less continuously from June 2005 to July 2007. After this period, the instruments were removed for a channel deepening project, and only replaced in January 2010.

Additional data required by this study include hourly records of wind speed and direction recorded at the Point Lonsdale lighthouse, and tidal water levels recorded at Point Lonsdale and Lorne (Figure 3.1, bottom). A high-resolution (2 m) digital bathymetry obtained by multi-beam hydrographical survey in the heads was also provided by the Port of Melbourne.

3.3 Validation cases

From the data described above, two spring tide events ('storms') were selected by WL07, labelled 'Storm 1' and 'Storm 3'. An additional event, 'Storm 2', was initially identified, but not further considered in their study.

Storm 1 (28/06/2006 06:10-14:00 AEST) occurred during a time of relatively clean high swell from a distant source. The wave height at the Triaxys buoys (Figure 3.2, top, labelled 'WAVE_A'), outside of the strong tidal current between the heads, was $H_{m0} = 2.7$ m with a peak spectral period of approximately $T_p = 16$ s. The wind at Point Lonsdale was low and consistent at $U_{10} = 4$ m/s from 30°N. These conditions were reasonably constant during this swell event. During this swell event, flood and ebb currents of up to 2.5 m/s were observed in the tidal inlet. The second event, Storm 3 (27/10/2006 20:10 to 28/10/2006 03:30 AEST), occurred during a time of high distant swell coinciding with a strong local wind. The wave height at the Triaxis buoys was approximately $H_{m0} = 4.4$ m with a peak period of about $T_p = 12$ s. The wind at Point Lonsdale was strong at $U_{10} = 17$ m/s, with the direction gradually veering from 270 to 220°N during the course of the storm. Although the wind direction varied slowly, the measured offshore wave conditions were reasonably constant. During this storm period, flood currents of up to 1.8 m/s and ebb currents of up to 2.4 m/s were observed in the tidal inlet.

During each storm, the time of peak ebb and flood tides were identified, along with the time of near-slack. These six times, listed in Table 3.1, were selected as stationary cases for model-measurement comparison. The locations of the AWAC deployment during these events are known as Rip Bank Outer (RBO) and Rip Bank (RB), shown in Figure 3.2, top panel.

Case	Date and time	H_{m0} (m)	T_{m01} (s)	U_{10} (m/s)	U_{dir} (°N)	U_c (m/s)
Storm 1, ebb	28/06/2006 06:30	3.1	14.0	2.6	21	2.5
Storm 1, slack	28/06/2006 10:30	2.1	11.6	3.0	4	0.2
Storm 1, flood	28/06/2006 14:00	2.4	12.0	5.7	44	1.8
Storm 3, ebb	27/10/2006 20:30	4.0	8.0	14.9	257	2.4
Storm 3, slack	27/10/2006 23:30	4.7	8.6	12.3	280	0.2
Storm 3, flood	28/10/2006 03:30	4.2	8.0	15.4	216	1.8

Table 3.1 Stationary hindcast cases for Port Phillip Bay Heads

3.4 Model setup

The model setup for this field case features a single curvilinear grid, dimensioned such that possible inaccuracies in the lateral boundary conditions do not affect either the region of the tidal inlet or the location of the offshore wave buoys, and so that it extends far enough offshore so that offshore conditions can be assumed to be spatially constant along the offshore boundary (Figure 3.2, bottom panel). As the wave conditions were reasonably

constant during the storm of 28 June 2006, the offshore boundary conditions are held constant for all three stormtimes, using the mean of all half-hourly wave observations during the event. This had the benefit of removing the noise in the offshore observed signal. For the storm of 27-28 October 2006, the measured offshore wave conditions are again reasonably constant, even though the wind direction varies slowly. Therefore, despite the gradual increase in wave energy observed during the storm, the wave boundary conditions are again assumed constant for the duration of the event.

For the offshore (southwest), and lateral (northwest and southeast) wave model boundaries, 1.5D spectra measured at the Triaxis buoy location WAVE_A, outside of the tidal channel, were applied. To compensate for the offshore displacement of the observed data, the measured spectra applied at these boundaries were modified by trial and error until the observed spectra at the buoy location WAVE_A were recovered. Unlike in WL07, in the present study wind forcing was deactivated for both 'Storm 1' (swell) and 'Storm 3' (swell plus wind sea). This was done because (a) there is negligible fetch for SW winds between the buoy location WAVE_A and the stations RBO and RB (b) it was not attempted to trace back the complex effects of wind growth to the boundary (including an increase in variance, a frequency downshift and changes in direction). As a result, the back transformation of the spectra to the boundary compensates mainly for the effects of propagation (refraction) and bottom friction.

Current fields were modelled using a three-dimensional Delft3D hydrodynamic model of Port Phillip Bay, driven using measured tidal water levels from the Lorne tide gauge. Since the flow is tidally dominated, wind forcing was excluded. The results compare well with the point measurements in the tidal inlet (see WL 2007). The depth-averaged fields from these hydrodynamic model results were used as input to the wave model simulations.

Figures 3.3 and 3.4 compare the results of the wave boundary back-tracing procedure for Storm 1 and Storm 3 respectively, including the effect of current. These figures show the results of both the present study and those of a simulation with the settings of WL07, in which wind was included in the simulation. Figure 3.3 shows that with the present model setup the swell spectra at WAVE_A are recovered well in terms of both variance density and mean direction for all three tidal stages. This is not the case for the boundary setup followed in WL07, which under ebb conditions develops a significant wind sea peak (including a change in direction) that is not seen in the observations. This wind sea peak, which grows slowly under the light wind, was not detected in the study WL07, which used less strict convergence criteria than in the present study.

Figure 3.4 shows the corresponding results for Storm 3. The dashed line presents the spectrum at WAVE_A according to the simulations with physical settings and boundary conditions as applied in WL 2007, so with wind forcing. It can be seen that this model setup results in some overestimation of the variance in the wind sea range on the high-frequency flank of the spectrum. Also, the energy levels at the spectral peak were slightly underestimated. In the present study, the derived spectra at the model boundary were increased by 10% relative to those of WL07, and the simulation was conducted without wind. Figure 3.4 shows that this results in a better reproduction of the observations in the high-frequency flank and at the spectral peak, validating the applied wave boundary values.

3.5 Model results

The sections below present the model results for the Port Phillip Bay field case for respectively the pure swell condition (Storm 1) and the combined swell and wind sea condition (Storm 3). The results are presented in terms of spatial plots of integral parameters, parameter results along an output transect and frequency spectra at the observations stations.

3.5.1 Storm 1: SW Swell

Figures 3.5 to 3.10 present spatial plots of the current fields and wave parameters in the PPH for the SW swell dominated case of Storm 1. Figure 3.5(c) shows the strong ebb tides through the PPH. These oppose the swell waves arriving from SW, resulting in a significant local increase in H_{m0} (panel (a)) and some decrease in T_{m01} (panel (b)) in the results of the default model ($C_{ds3} = 0.0$) between the Heads. As a consequence, the mean wave steepness increases, with a focal point at the RBO and RB stations (panel (d)). Also shown on these plots is an output curve running approximately along the wave path, through RBO and RB and into the Heads, used to compare model results and observations (see below). Figure 3.6 shows the corresponding ebb tide results for the model variant including enhanced whitecapping dissipation, with $C_{ds3} = 0.80$. With this model setting the H_{m0} values at RBO and RB between the Heads are somewhat lower, and so are the levels of mean steepness. The region of reduced H_{m0} (greater dissipation) corresponds to the area of largest opposing current gradients (panel (c)), as expected. The enhanced whitecapping dissipation with $C_{ds3}=0.8$ results in a somewhat higher wave period T_{m01} inside the inlet (Fig 3.6.b vs 3.5.b)

Figures 3.7 and 3.8 present the default model results for the slack case in Storm 1. For this case, with weak tidal currents and gradients, no increase of H_{m0} , or changes in mean period or mean steepness is found. Furthermore, due to the low current speeds, the source term for enhanced dissipation has little effect on the model results, as expected. Figures 3.9 and 3.10 show the model results for the Storm 1 flood case. Figure 3.9(c) shows the strong following current of up to 2.5 m/s. The significant wave height is somewhat reduced towards the Heads under the accelerating following current. A slight reduction in the mean steepness can be seen within the Heads. Figure 3.10 presents the results for the model variant with $C_{ds3} = 0.80$. Since waves are elongated by the accelerating following current (positive gradient) in the region of RBO and RB, no enhanced breaking is expected. This is confirmed by the results of H_{m0} , T_{m01} and mean steepness, which are similar to those of the default model in Figure 3.9.

Figures 3.11 and 3.12 present the variation of H_{m0} and T_{m01} , respectively, along the output curve through the PPH (see Figures 3.5-3.10) for the ebb, slack and flood cases of Storm 1. The ebb current through the Heads yields a strong increase in the default model results of H_{m0} , leading to overestimations at the stations RB and RBO (Figure 3.11, panel (a)). Application of the enhanced whitecapping dissipation with $C_{ds3} = 0.80$ results in some reduction of H_{m0} values, but not enough to bridge the difference with the observations. Also shown in Figure 3.11(a) are the results of a sensitivity run with $C_{ds3} = 1.60$, which yields further reduced H_{m0} results. However, this is still not sufficient to reproduce the observed H_{m0} , in particular that at station RB. During slack tide, wave heights are fairly constant between the offshore and the Heads (Figure 3.11(b)). However, for this condition, H_{m0} values are overestimated at the stations RB and RBO. This may suggest inaccuracies in the boundary values directly upwave, or dissipation processes along the propagation path (e.g. bottom friction), even though the spectra to the SE at station WAVE_A are recovered well (Figure

3.3). Since the current is weak, the variants with $C_{ds3} = 0.80$ and 1.60 yield similar results to the default. During flood, a small reduction in H_{m0} relative to the offshore values is found at RB and RBO. However, a degree of overestimation of the H_{m0} values at RB and RBO is again found. The results for $C_{ds3} = 0.80$ and 1.60 again yield similar values to the default model for this case with accelerating following current, as expected. Figure 3.12 shows that the default model reproduces the mean period T_{m01} well at RB and RBO during the flood condition (as do $C_{ds3} = 0.80$ and 1.60). However, T_{m01} is overestimated under slack. During ebb the default model overestimates T_{m01} at RBO and underestimates at RB. The agreement with the observations deteriorates with $C_{ds3} = 0.80$ and 1.60 , overestimating the wave period at both locations.

Figure 3.13 shows the frequency spectra at stations RBO and RB for the ebb, slack and flood cases. During ebb, the default model generally overestimates the variance spectra in the opposing current, particularly at RBO. Another salient feature is the overestimation at the higher frequencies, just below the blocking frequency (at frequencies higher than this the variance drops sharply). Application of the enhanced whitecapping dissipation ($C_{ds3} = 0.80$) strongly reduces the overprediction at these near-blocking frequencies, also reducing the overall overestimation. However, to reach the observed levels of variance at RB, the setting $C_{ds3} = 1.60$ is required. This setting is higher than the values of $C_{ds3} = 0.70$ - 0.80 obtained previously in calibration studies by Deltires (2010a,b) using laboratory and field observations. However, even with this setting, variance levels at RBO are still overestimated, as seen above. Variance levels are also strongly overestimated during slack (as also seen above), with no difference between the model variants. By contrast, during flood, the variance densities at RBO are well predicted, and fairly well at RB. Again, no difference is found when applying enhanced dissipation, as expected.

3.5.2 Storm 3: SW swell with wind sea

Figures 3.14 to 3.19 present the spatial model results for the combined swell and wind sea case of Storm 3. Figure 3.14(c) presents the strong wave-opposing current model result through the Heads for the ebb tide case, which is of comparable strength to that found for Storm 1 (refer Figure 3.5). As with Storm 1, the opposing current gradient results in a strong local increase in H_{m0} of the SW wave field within the Heads in the default model results. The increase in H_{m0} is accompanied by a small reduction in T_{m01} and a large increase in the mean steepness, concentrated at the stations RBO and RB (panel d). Figure 3.15 shows the corresponding results for the variant with enhanced whitecapping ($C_{ds3} = 0.80$). With the enhanced dissipation, the increase in H_{m0} leading up to and within the Heads is strongly reduced, and so is the mean wave steepness. The mean period T_{m01} is largely unaffected. Figures 3.16 to 3.19 show the model results of the default and enhanced dissipation variants for the slack and flood cases of Storm 3. As found for Storm 1, the slack case results in little effect on the wave field within the Heads, and only relatively small differences between the default and enhanced whitecapping variants (Figures 3.16 and 3.17). The flood case yields some reduction of H_{m0} and mean steepness within the Heads relative to offshore values. However, again no significant differences are found between the default and enhanced dissipation variants at RBO and RB for this accelerating following current case, as expected (Figures 3.18 and 3.19). An exception is the removal of two small peaks in the mean steepness (compare Figures 3.18d and 3.19d), where the flood current strongly decelerates locally, causing enhanced steepness in the default model.

Figures 3.20 and 3.21 show the results of H_{m0} and the mean period T_{m01} along the transect through RBO, RB and the Heads for the three tidal stages of Storm 3. Figure 3.20(a) shows that the H_{m0} results of the default model increase strongly due to the negative gradient in the ebb current between the Heads (panel (d)), significantly overestimating the observations at RBO and RB. Application of enhanced whitecapping dissipation (with $C_{ds3} = 0.80$) leads to a significant reduction in H_{m0} in the region of the strong opposing current gradient, improving the agreement with the observations at RBO and particularly at RB. The sensitivity run with $C_{ds3} = 1.60$ reduces the wave heights further, yielding acceptable agreement with the observations. Panels (b) and (c) show the results for the slack and flood cases respectively. The default model yields quite good agreement with the observations for both of these conditions. For the slack case, the variants with $C_{ds3} = 0.80$ and 1.60 yield somewhat lower wave heights than the default model, due to some mild gradients in the current field. Smaller differences in H_{m0} are found during flood, since the current gradient is positive in the region of RBO and RB. Notice, however, some reduction in the wave height inside the Heads, beyond a deceleration region of the following current, at a chainage of approximately 6 km. Figure 3.21 presents the corresponding results for the mean period T_{m01} . In the default model, T_{m01} is not significantly affected by the current during any of the tidal phases. These tend to overestimate the observed values during flood and slack. The model variants with $C_{ds3} = 0.80$ and 1.60 produce similar results. For ebb tide, the default model fits the observed T_{m01} at RBO and slightly underestimates the wave period at RB. The simulations with $C_{ds3} = 0.80$ and 1.60 result in slightly higher results for T_{m01} , deteriorating the agreement with the observations somewhat.

Figure 3.22 shows the model results for Storm 3 in terms of frequency spectra at RBO and RB. As suggested by the above results, the variance levels at RBO and RB are strongly overestimated by the default model during ebb. Application of enhanced whitecapping with $C_{ds3} = 0.80$ improves the agreement with the observations significantly, especially at RB. As found for Storm 1, a particular feature of the enhanced dissipation is a correction of the shape of the high-frequency flank of the spectrum near the blocking frequency. The model variant with $C_{ds3} = 1.60$ improves the agreement with the observations further, reproducing the observed spectrum at RB well, but leaving some overestimation at RBO. It is interesting to note that the peak frequency reduces slightly with increasing C_{ds3} . This is due to the whitecapping expression (2.2) being weighted towards higher frequencies, because of the increase in Doppler shifting with frequency. The default model results for slack and flood agree well with the observed spectra. As seen above, the model variants with enhanced whitecapping dissipation yield similar results to the default model, again as expected.

3.6 Conclusions

In this section, the new formulation for enhanced whitecapping dissipation on negative current gradients of Deltires (2010b) was assessed for the near-idealised wave-current interaction field case of Port Phillip Bay Heads, Australia. The model was evaluated for both swell and combined swell and wind sea conditions at various tidal stages. From the results presented in this section, the following conclusions can be drawn.

- The simulation results confirm the findings of WL & Lesser (2007) that during ebb, the negative gradient in the opposing current between the Heads results in a strong increase in H_{m0} in the default model, overestimating the observations here.

- Application of the formulation for enhanced current-induced dissipation to the present field case yields significant reduction in H_{m0} during ebb only, since this is the only tidal phase that features strong negative current gradients. For slack and flood conditions, that feature positive or only small negative current gradients in the vicinity of the observation stations RBO and RB, the present results confirm that the enhanced dissipation expression does not yield any significant differences with respect to the default model.
- Regarding ebb situations, for the pure swell condition (Storm 1), the simulation with the setting $C_{ds3} = 0.80$ (calibrated value of Deltires (2010a)), and even with $C_{ds3} = 1.60$ appear to yield insufficient dissipation to reproduce the observations. For the combined swell and wind sea condition (Storm 3), a level of $C_{ds3} = 1.60$ yields satisfactory agreement with the observations. These results suggest that the model parameterisation, and the calibration based on laboratory data and predominantly wind sea conditions in the Dutch Wadden Sea, may not be sufficient to cover the present swell-dominant conditions.

4 Tidal Inlet Ameland

4.1 Approach

Besides assessing SWANs performance of predicting wave penetration into the Amelander Zeegat under ambient currents, this study must gain experience with the use of radar wave data as validation material. Therefore, available data in the Amelander Zeegat was gathered and a number of moments during different tidal stages was selected with suitable data available. The selected storm of January 28th, 2010 was not so severe, but the most energetic there is with radar data available. The eight selected times were simulated in six different ways, varying in current input and wave current formulation. The Delft3D current fields that were used as input for the SWAN computations have been thoroughly validated with the radar current observations. After the comparison between SWAN results and buoy measurements the radar wave parameters were considered in the wave analysis. Spatial patterns of the wave direction and wave length as observed by the radar were compared with the SWAN results. Later during the study spectral radar information was received for one moment in time which helped in evaluating the reliability of the radar data and gave the possibility to compute additional wave parameters. From the radar intensity spectra wave lengths and directions were computed on a specified frequency domain. Furthermore, a first attempt was made to transform the radar intensity spectra to wave energy density spectra and to assess significant wave heights, which were compared with buoy observations and SWAN results.

Section 4.2 and 4.3 present the available data and the storm selection respectively. Section 4.4 deals with the SWAN simulations, starting with a discussion of the setup, followed by details concerning the model input, and then finally the model results. In Section 4.5 the SWAN results are compared with buoy measurements. In section 4.6 the SWAN results are compared with radar observations. The conclusions for this part of the study can be found in Section 4.7.

4.2 Available data

There are various measurement data available to perform a hindcast of the January 2010 storm in the Amelander Zeegat, to be used as input for SWAN as well as to compare the SWAN results with, see Figure 4.1, Table 4.1 and also ModelIT (2010).

buoy	X [m RD]	Y [m RD]	bed level [m +NAP]	parameter	input data	validation data
AZB11	161006.	616004.	-18.1	waves+dir		v
AZB21	167307.	610978.	-9.1	waves+dir		v
AZB31	168318.	606745.	-3.5	waves+dir		v
AZB41	168792.	600501.	-0.9	waves+dir		v
AZB51	167963.	596444.	+0.8	waves		
AZB61	167500.	592500.	-0.5	waves		
AZB12	173011.	617304.	-21.0	waves+dir		v
AZB22	170688.	611040.	-3.3	waves		v
AZB32	169349.	607115.	-10.7	waves+dir		v

AZB42	171319.	604249.	-16.7	waves+dir		v
AZB52	175490.	600699.	-12.2	waves+dir		
AZB62	180506.	598604.	-2.3	waves		v
SON	206608*	623565*	-20	waves+dir	v	
ELD	106603*	588068*	-27	waves+dir	v	
Nes	179841**	605047**	-5.8	water level	v	
Terschelling NZ	151400.	606250.		water level		
Terschelling NZ	151400.	606250.		wind	v	
Wierumergronden	192882.	614562.		wind	v	
Hoorn Terschelling	143957**	597502**		wind		
Huibertgat	221990.	621330.		wind	v	
Lauwersoog	208850.	602790.		wind		

Table 4.1 Observation locations for waves, wind and water levels

*) taken from Deltires, 2010c

**) these locations have been calculated from the lat lon given in the MATROOS database

There are twelve wave buoys in the Amelander Zeegat. Offshore wave data is available at the wave buoys SON and ELD. Water levels have been measured at Terschelling Noordzee and Nes.

During the winter of 2010 new offshore wind observation stations near the Amelander Zeegat have become operational: Wierumergronden and Terschelling Noordzee. Others, like Huibertgat, Lauwersoog and West Terschelling are also still available.

Besides the in-situ measurements mentioned in Table 4.1, marine radar data from the lighthouse at Ameland have become available since January 2010. This provides spatial information on current speed and direction, wave direction and wave length, covering about half a circle with ca 15 km diameter. At present, radar data is available for two storm periods, namely January 27th/28th, 2010 and March 2010. Since the January storm was more severe than the one in March, only the January data was processed further, resulting in the following parameters: latitude, longitude, date, time, depth, current velocity, dominant wave length, dominant wave period and dominant wave direction. The dominant wave period turned out to be erroneously processed, and is not considered further. These parameters are available with a time resolution of about 13 minutes, on a grid with ca. 300 m cell size, see for instance Figure A.1 in Appendix A. More information on the radar observations can be found in Appendix A.

Within the SBW project, the bathymetry is measured regularly. For the hindcast of 2010, use is made of SBW bathymetry data measured in various months of 2009 (see Figure 4.2), completed with the bathymetry that was used in the default run of Deltires (2010c).

4.3 Storm selection

Starting point for the storm selection is the availability of radar data of the storm of January 27/28, 2010. Another consideration is the preference for a rather high (>3 m) and constant wave height at AZB11/12. Next, various tidal stages (following current, opposing current, slack tide) are chosen. Further considerations are the quality of the wave buoy observations and the stationarity, magnitude and direction of the wind. This led to the eight selected times

listed in Table 4.2. Figure 4.3 shows the time series of various parameters and the selected times.

	time on 28 Jan 2010 [GMT]		current speed [m/s]	current dir [from °N]	observed wind speed [m/s]	observed wind dir [from °N]	observed wave height H_{m0} [m]	observed wave period T_p [s]	observed water level [m+NAP]
			near AZB32	near AZB32	Huibert- gat	Huibert- gat	AZB11	AZB11	Nes
t1	2:11	flood	1.0	343	12.0	332	3.37	8.3	- 0.05
t2	3:18	flood	1.4	345	11.4	324	3.41	9.1	+ 0.50
t3	3:58	flood	1.5	345	10.5	320	2.99	9.1	+ 0.83
t4	5:19	flood	1.2	345	9.9	332	3.22	9.1	+ 1.44
t5	6:39	slack	0.1	26	8.4	315	3.35	10.0	+ 1.70
t6	7:59	ebb	1.1	162	8.2	320	3.33	9.1	+ 1.41
t7	9:09	ebb	1.4	157	7.8	311	3.26	10.0	+ 0.98
t8	9:49	ebb	1.3	156	8.9	329	3.18	10.0	+ 0.71

Table 4.2 Selected times for the Amelander Zeegat simulations

At the first four times (t1 through t4), there is a flood current with speeds over 1 m/s in the Borndiep channel between Ameland and Terschelling near AZB32. At t5 the water level at Nes has its maximum (NAP +1.7 m) and the flow is almost absent. During times t6, t7 and t8 the waves encounter ebb currents of more than 1 m/s. The wind is moderate (5-6 Beaufort, ca. 8-13 m/s), and mainly from the northwest.

Not all buoys provided reliable data at all selected times. There is no suitable data at all from buoys AZB51, AZB52 and AZB61. The waves measured by buoy AZB62 are during most moments of the storm too small to consider (The wave height reaches a maximum of 0.35 m, see Figure 4.3). Despite this, sufficient validation data is available. In the present study the focus is rather on the locations of buoys AZB21, AZB31, AZB32, AZB42 because these are located within the radar area and/or strongly influenced by current. Buoy AZB31 shows some anomalies around time t2, but the data of the other seven times can be used.

4.4 SWAN simulations

4.4.1 General setup, input and output

Stationary simulations are carried out for each of the eight storm times in Table 4.2. On a larger grid the eastern and western boundary conditions for the nested detail grid of the Amelander Zeegat are computed (see Figure 4.4.a). Besides these, the nested grid receives observed wave conditions on its northern boundary.

The model input consists of:

- Bathymetric data
- Computational grids
- Wave boundary conditions, based on observations at ELD, SON, AZB11 and AZB12
- Wind fields, based on observations at Huibertgat, Wierummergronden and Terschelling Noordzee

- Water level and current fields (non-uniform), computed using Delft3D

These are described in the following subsections.

The model output includes maps of various parameters on the entire computational grids, various wave parameters on buoy locations and on transects, and 1d and 2d wave spectra on buoy locations. For a fair comparison, the integral wave parameters of both SWAN and the buoys have been computed over the same frequency range being 0.03 Hz – 0.5 Hz.

To check the influence of the currents and the enhanced dissipation by (2.2) on the waves, six series of computations are defined. Each series contains the same eight hindcast times. In the first four series the SWAN settings concerning currents vary.

Series A: Default run (no enhanced whitecapping)	$C_{ds3}=0.0$
Series B: Deactivating the current field (to show the impact of the current)	$C_{ds3}=0.0$
Series C: Activating the enhanced whitecapping (2.2), with WTI settings	$C_{ds3}=0.8$
Series D: Enhanced whitecapping (2.2), with higher proportionality coefficient	$C_{ds3}=1.6$

The last two series have the settings of the C series, but with improved current fields.

Series E: Optimised computed flow and water level fields	$C_{ds3}=0.8$
Series F: Flow field from radar observations, completed with Delft3D results	$C_{ds3}=0.8$

The codes of the runs are as follows:

[Series] [Time][Version][Grid] where:

Series uses s one of the letters	A, B, C, D, E, F,
Time uses one of the numbers	01, 02, 03, 04, 05, 06, 07, 08
Version is always	a
Grid is	G1 G2,

For instance: C07aG2 is the run of the 7th selected moment (being January 28th, 2010 at 9:09 GMT) on the nested grid G2, with $C_{ds3}=0.8$.

4.4.2 Input: grids and bathymetry

Grids

Two curvilinear computational grids were used to carry out the simulations, see Figure 4.4.a. The larger one ‘G1’ generates wave boundary conditions for the eastern and western side of the detailed grid (‘G2’) which covers the tidal inlet with the twelve available wave buoys.

Grid G1 is identical to the grid used in previous hindcasts, for instance Deltires (2010c), which concerns the hindcast of January 31st, 2008. Its original name is “GridCL.grd”. Note that the quality of the simulations on grid G1 is not critical, especially not for the north-western winds that were selected for this hindcast. Grid G1 is merely used to apply wave conditions on the short sides of grid G2, which do not even reach the buoy locations.

The detailed grid G2 is based on the grid “azg3a” as used in previous hindcasts, for instance Deltires (2010c), but it is not identical. Grid G2 has been extended approximately 2000 m north so that the buoys AZB11 and AZB12 lie more or less on the northern model boundary. The grid characteristics can be found in Table 4.3.

The directional resolution is 36 bins of 10° covering the full circle. The range of frequencies is taken from Deltires (2010c), see Table 4.3.

Grid	min freq [Hz]	max freq [Hz]	number of freq bins	number of cells	cell size [m] in interest area	cell size [m] outside interest area
G1	0.03	1.5	42	391 x 161	ca. 400 m	ca. 1000 m
G2 (nest)	0.03	2.5	47	286 x 380	ca. 40 m	ca. 200 m

Table 4.3 Characteristics of frequency, directional and geographical grids for the Amelander Zeegat simulations

Bathymetry

Bathymetric data files are available for both computational grids. For the large area of Grid G1, the bathymetry used in the default run of Deltires (2010c) is used, which includes RWS soundings ('vaklodingen') of 2007-2008 as well as LIDAR altimetry data of 2007-2008.

For the detailed grid G2, the starting point was the bathymetry used in Deltires (2010c) (see above) but updated (where possible) by more recent SBW data of various months in 2009, see Figure 4.2. This data was provided by the Waterdienst on a regular 20 m grid.

4.4.3 General, physical and numerical settings

General settings

The simulations are carried out in stationary mode with SWAN version 40.72ABCDE.

Settings for model physics

The model settings of series A and B are those described in Section 2.3. For series C to F, enhanced whitecapping (2.2) is added, with the values for C_{ds3} given above.

Numerical settings

The numerical settings for grid G2 are slightly different from those described in Section 2.3. The 99.5% as the required percentage of wet grid points where convergence must be reached is replaced by 101% to make sure that all simulations continue until the maximum number of 120 iterations. Since Grid G1 is merely used for boundary conditions on the sides of Grid G2, a lower upper limit of iterations (80) were specified.

4.4.4 Input: Wind and wave boundary conditions

Wave boundary conditions G1

The directional wave spectra measured at ELD and SON are applied as so called “SP1-files” or “1.5D spectra” (energy, mean direction, directional spreading width for each energy band) on the boundaries of the grid G1. For the stretches west of ELD, the data of ELD is used. For the stretches east of SON, the data of SON is used. For the boundary between ELD and SON, the spectra are interpolated by SWAN, see also Figure 4.4.a. In previous hindcasts, SWAN tended to underestimate the waves at AZB11 and AZB12, see Witteveen+Bos (2010). Therefore the measured energy density of ELD and SON has been multiplied by 1.21 resulting in a 10% increase in waveheight. No time averaging and smoothing is applied on the measured data.

Wave boundary conditions G2

The directional wave spectra measured at AZB11 and AZB12 are applied as “SP1-files” on the northern boundary of grid G2. West of AZB11 the data of AZB11 are used, while east of AZB12 the data of AZB12 are used. Figure 4.4.b showing the results of the SWAN simulations on the larger G1-grid, indicates that there is not much variation in wave height along these stretches, allowing for the applied method. For the stretch in between, SWAN interpolates both spectra, see Figure 4.4.a. The wave spectra computed by the larger grid G1 are applied at five locations on the eastern and western boundary of grid G2. This method is similar to the one used in Deltires (2010c) and Witteveen + Bos (2008), but the application is slightly different. First of all, the location of E2 was moved one grid cell to the north to prevent drying of that location. It is called E22 in Fig 4.4.a. Next, the lengths of the lateral sections as mentioned in the SWAN input file (*.swn) have been adjusted. Also, the location of AZB11 and AZB12 on the northern boundary where the interpolation starts has been adjusted in the SWAN input file (*.swn) to the actual buoy locations.

Wind

In the simulations the wind is defined as a uniform wind, given by its velocity and direction. The applied wind velocity is the mean of the windspeed U_{10} at stations “Wierumergronden” and “Terschelling Noordzee”. The wind at these locations is representative for the area of interest. The observations have been corrected to 10 m height. The wind direction of these locations was not reliable since the sensors had not been tuned yet (according to correspondence with Rijkswaterstaat DID). For the wind direction, the observations at Huibertgat are used. Figure 4.5 shows as a check the wind time series at various locations. At the three offshore stations Wierumergronden, Terschelling Noordzee and Huibertgat, the time series of wind speed are in reasonable agreement. At Lauwersoog, the wind speed is in general slightly less. The wind speed at Hoorn Terschelling is generally about 25% lower than at the offshore locations. The lower panel of Figure 4.5 presents the wind direction. Wierumergronden deviates most from the three other locations.

4.4.5 Input: water level and currents

General

A Delft3D model study (Deltires (2010d)) provided time series of non-uniform water level and current fields. These are used as input for the SWAN simulations on G2 at the selected times. The interpolation technique used to produce the water level and current fields that are suitable for SWAN ensures that dry points do not erroneously influence surrounding areas.

Water levels

The simulations on grid G2 make use of non-uniform time-dependent water level fields. The eight subplots of Figure 4.6.a present a detail of the computed water level for the standard run (series A, B, C, D) for each storm time. The Delft3D sensitivity analysis indicated that the flow results improve if the option for time and space varying roughness is applied (Deltires (2009)). The accompanying water levels can be found in Figure 4.6.b. They have been used in the SWAN simulations of series E and F.

Grid G1 uses uniform water levels for each instant, based on the observations at NES (see Table 4.2, rounded to 1 decimal). This is different from Witteveen + Bos (2008) where the computed water level at AZB11 was applied on the entire grid.

Currents

The current fields used as input for the SWAN simulations on grid G2 were generated by Delft3D, see Deltires (2010d). Figure 4.7.a presents a section of the standard flow field which is used in the SWAN Series A, C and D. The flow field has been optimised by applying time and space varying bottom roughness. This optimised flow field – used in series E – is presented in Figure 4.7.b. Although this optimised flow field agrees quite well with the observed radar flow fields, a third flow field has been generated which contains the radar observations, see Figure 4.7.c. Hereto, the radar data has been filtered in time and space and anomalies have been removed. In areas where no radar current velocities were available, the flow field has been completed with data from the optimised flow field.

No currents are included on grid G1.

4.4.6 SWAN results

Maps of significant wave height H_{m0} and wave period $T_{m-1,0}$ can be found in Figure 4.8.a,b and 4.9.a,b, respectively. The plots contain only a limited area of the G2 grid. Figure 4.8.c has been included to show the significant wave height on a larger section of the G2 grid and to indicate the position of the transect which is mentioned in Paragraph 4.5.1.

The wave height plots show waves of circa 3 m at the upper boundary of the G2 grid. On the ebb tidal delta the wave height reduces strongly to roughly 1.5 m. On the Wadden Sea, wave heights are in the order of $H_{m0} = 0.5$ m. Storm times t1, t2 and t5 have the largest offshore waves. The largest wave height in the Borndiep channel occur during ebb (t6, t7, t8), but also on t1. On t4, t5 and t6, the water levels are high, flow velocities low and compared to the other instants there is more wave propagation along the western side of the inlet. On t1, t7 and t8 the low water levels explain the small wave heights in the area between the ebb tidal delta and the Amelander NW coast. On the presented scale, the differences between the series are limited.

The wave period $T_{m-1,0}$ on the upper boundary of the G2 grid increases from approximately 7 to 8 s during the eight storm moments. In the northern part of the Borndiep channel we see the wave period reduce to $T_{m-1,0} = 5-6$ s, whereas on the sides the wave period stays at 7 s. Further into the tidal inlet, south of AZB31/32 the wave period in the Borndiep channel is larger than the surrounding areas, especially during ebb. Depth patterns can be recognised in the wave period plots.

In the next paragraphs, the SWAN results are compared with observations.

4.5 Comparison SWAN simulations with buoy observations

4.5.1 Transects

In Figures 4.10 (H_{m0}), 4.11 ($T_{m-1,0}$) and 4.12 (mean wave direction) the wave parameters on a transect through buoys AZB11, AZB31, AZB42 and AZB62 (see Figure 4.8.c) are presented per storm time, to illustrate the differences between the six series. In the first five kilometres the currents are small in magnitude and the six SWAN series give more or less equal results. The reduction in wave height and period along the transect as measured by the buoys is quite well reproduced by SWAN. In general, SWAN tends to slightly underestimate the wave height at buoy AZB31 and slightly overestimate the wave height at buoy AZB42. The wave period $T_{m-1,0}$ at AZB31 and AZB42 is generally underestimated by SWAN. The wave period presented here is the absolute period, so relative to a fixed position (unlike the relative period which is considered moving with the current). In the bottom panel the flow velocity from series A is given, as well as the bottom level.

- Significant wave height H_{m0} during flood conditions

In Figure 4.10.a the flood situations are presented with following current. There is hardly any difference between series A, C and D (with respectively $C_{ds3}=0.0, 0.8, 1.6$), indicating little impact of the enhanced current-induced dissipation term. Series B – no currents present – deviates clearly from the others. In the flood cases, neglecting the currents leads to reduction in wave height north of AZB31 (km 5 – km 12), coinciding with a directional change of the waves crossing the main channel, and to higher waves south-east of AZB31 (km 13 – km 22). Especially for the smaller waves past AZB42 (km 16) the relative differences are large with typical wave heights of 0.30 m when currents are included and rather 0.60 m when the flood currents are omitted. The observations of AZB42 are clearly in favour of the simulations with currents included. On times t1 and t4 (and t5, slack tide) it can be noted that series E and F (with optimised flow field, respectively radar flow field) show more agreement with each other than with the other series on some parts of the transect. This implies that in these regions the optimised flow field agrees well with the observed radar flow field.

- Significant wave height H_{m0} during ebb conditions

During ebb (times 6, 7 and 8, Fig 4.10.b) the situation is different. First of all, series A, C and D deviate more from each other than during flood. The largest enhanced dissipation (series D: $C_{ds3}=1.6$) gives the smallest wave heights, as expected. Differences in wave height of Series D relative to series A ($C_{ds3}=0.0$) are in the order of 10-20%. Note that on the transect in the vicinity of AZB31 the flow velocity is small and hence the local differences between series A, C and D are correspondingly small as well. Series B – the simulations without currents – gives for the counter current situations (times 6, 7, 8) between km 10 and km 12 (near AZB31) on the transect higher waves than the other series. Past AZB42, neglecting the currents leads to smaller wave heights. Surprisingly, these wave heights computed without the influence of currents come slightly closer to the observations than the other series do. Series E, with the optimised flow field, does not give the best wave height results here, nor does series F with the observed radar flow field. The wave heights computed in these series often underestimate the observations.

- Mean wave period $T_{m-1,0}$

The transect results in Figures 4.11.a,b show the influence of the currents on the wave period in the SWAN simulations. For flood cases, neglecting the currents leads to larger wave periods, according to the SWAN simulations of series B compared to series A. However, wave periods are still smaller than observed. Locally the differences can be as large as 25% (km 18 – km 22) but in general the differences are small. During ebb, the simulations which omit the currents give smaller wave periods than the other series.

Figures 4.11.a,b show that the mean period $T_{m-1,0}$, is not sensitive to either the value of C_{ds3} or the flow field used. Only between km 8 and 13 some differences occur for the ebb cases. The largest dissipation (series D; $C_{ds3}=1.6$) gives about 10% larger wave periods than series A ($C_{ds3}=0.0$). The enhanced dissipation term dissipates energy mainly at higher frequencies as can be seen in the spectral plots of Fig 4.13.f/g/h, for instance at location AZB31. This explains why the D-series with a larger value of C_{ds3} – causing more dissipation and thus smaller wave heights - results in larger wave periods.

- Mean wave direction

Figures 4.12.a,b show the wave direction along the transect. The offshore mean wave direction is NNE, between 320° and 340° , at all eight times. On the transect the wave directions vary from 280° N (ebb t7 and t8, km 22) to 20° N (flood, just past AZB31 at km 12).

The SWAN wave directions generally agree well with the wave directions as observed by buoys AZB11, AZB31 and AZB42. Exception is the first hindcast moment near AZB42. At t1 SWAN is rather 15° too high (320° N instead of 305° N). The simulations without currents (Series B) clearly illustrate the influence of currents on the mean wave direction. During flood, series B gives less variation in wave direction along a transect. Also the variation in wave direction between the eight times is less in series B, see for instance at km 11-12. In the other series with currents included, the wave direction during flood is here much more from the north ($0-5^\circ$) than during ebb ($345-350^\circ$ N).

It is hard to say which of the SWAN series performs best. Per location and per moment in time there is too much variation.

4.5.2 Spectra at buoy locations

Figure 4.13 compares the wave spectra of the SWAN simulations (only series A, B, C, D) and the wave buoy observations for all eight storm moments.

- Buoys AZB21/AZB22

At AZB21 and AZB22, the measured wave spectra are reproduced quite well by SWAN. The influence of the current and also of the formulation for wave current interaction is present at these locations. The observations are reproduced quite well.

On the location of the western buoy AZB21, Series B only deviates significantly from the other series on the ebb moments t6, t7, t8. It is interesting to see that on these moments the spectra of Series B clearly have a larger energy peak at 0.1 Hz than the other series. At t6 and t8 this low-frequency peak comes closer to the observations, at t7 it overestimates the observed energy peak. It seems that the current has some effect on this low-frequency peak at AZB21 since it is not present in the spectra of series A, C and D. However, wave blocking is unlikely here since it would occur rather at higher frequencies. For AZB21 the differences between series A, C, and D (different values for C_{ds3} , in Eq. 2.2) is mainly visible at the higher

frequencies (ca 0.25 Hz), not only on t7 and t8 (ebb) but also on t1 and t2 (flood). At AZB22 the variation of A, C and D is best visible on t1 and t2. Eq. 2.2 can yield enhanced current-induced dissipation for flood cases also, if a negative gradient is found due to slowing flood currents.

- **Buoys AZB31/AZB32**

During flood and slack (t1, t2, t3, t4, t5) the observations at AZB32 in the tidal channel have a main peak at circa 0.11 Hz. During ebb, there is a second peak at 0.18 Hz. In SWAN, energy at this high-frequency peak is often overestimated (especially during flood and slack at t1-t5), while underestimated at the low-frequency peak. At AZB31 the low-frequency peak is at all times in the simulations without currents (Series B) more pronounced and closer to the observations than when currents are included.

The difference between series A, C and D is best visible at AZB32, during ebb (t6, t7, t8) but also during flood (t1, t2). Obviously, Series A with the smallest value for C_{ds3} (0.0) show most wave energy. This extra wave energy is mainly present at frequencies of 0.2 – 0.25 Hz. At these buoy locations the observations indicate also the presence of a small amount of low-frequency wave energy (< ca 0.08 Hz). In the SWAN results this is not present at all.

- **Buoys AZB41/42**

Considering the spectra at AZB41, the chosen high-frequency cut-off at 0.5 Hz for the computation of integral parameters seems to be too limiting. On the other hand, the waves at this location are so small during this storm that the observations here are not of much interest. In general, SWAN overestimates the wave energy at AZB41. At most instants (both ebb and flood) there is considerable difference between the wave energy of series A, C and D, mainly at 0.35 – 0.45 Hz. At location AZB42, the computed wave energy is generally higher than the observed values. On t6, t7, t8 (ebb), there is much difference between the series A, C and D, around 0.25 Hz. On the other times, there is hardly any difference. Series B, without current, differs considerably from the other series, mainly around 0.25 Hz. At t1, t2, t3, t4 (flood) the spectra of Series B at AZB42 contain much more energy than the other series. The following current elongates the waves, and reduces the wave height. Furthermore, the following current reduces the relative windspeed with respect to the waves, reducing the wave growth, resulting in smaller wave height and period compared to the situation without current (wave-age effect). During ebb, the spectra of Series B are much lower in energy than the spectra of the other series, as expected. It is surprising that also at slack tide (t5) the difference between series B (without currents) and the other series is large. Even the small current velocities at time t5 seem to influence the SWAN results considerably. For t1 it looks like series B matches the observed spectra at AZB42 best, while for the other flood times (t2, t3, t4) series B overestimates the wave energy. Looking at the observed time series of Figure 4.3 it strikes that the wave height at AZB42 decreases considerably from t1 to t2 whilst at the other buoys the wave height increases. This might be due to wind speed variation since the wind speed decreases slightly as well. The observed waves at AZB42 vary more in time than the SWAN results do, possibly due to local wind variations that are not caught in the uniform simulation approach.

- **Buoys AZB51/52/61/62**

Of the four buoys closest to the mainland, only AZB62 provided observations. SWAN overestimates these observations drastically. At AZB61 there is not so much difference between the SWAN results of the four series. At AZB52, the spectra of Series B (without currents) deviates strongly from the others, showing the influence of the current. As expected,

at flood and slack, Series B produces further developed, more energetic spectra than in the runs with current, and at ebb less energetic spectra.

4.5.3 Scatterplots

In Figure 4.14 the scatter plots of SWAN results and wave observations are presented for (a) H_{m0} , (b) $T_{m-1,0}$ and (c) mean wave direction. Only the buoys AZB21/31/32/42 are considered, because these experience the strongest current. Each plot refers to one of the six SWAN series. The plot titles contain a few statistical parameters, see also the paragraph on the statistical tables here below.

- H_{m0}

In general, the average model performance for H_{m0} is quite good. Series C and E make a very good fit ($y=c.x$). In particular the higher values at buoy AZB21 are much better represented in series E and F than in the other series, suggesting the positive effect of the better input current fields. It is noteworthy that the wave heights of the eastern buoys (AZB32/42; red markers in the scatter plots) are almost all overestimated by SWAN whereas the wave heights at AZB31 are structurally underestimated.

- $T_{m-1,0}$

The scatter plots clearly show that SWAN tends to underestimate wave periods here. In particular, the higher periods measured at AZB31 (8 – 9 s) are underestimated (SWAN: ca 7 s). Series D with most enhanced dissipation ($C_{ds3}=1.6$) performs best.

- Dir

The computed mean wave directions agree quite well with the observed directions. The influence of C_{ds3} (varied in series A, C, D) is negligible for this parameter. Series B shows large deviations between computations and observations, especially at buoys AZB31 and AZB32, indicating the impact of currents on the wave direction. At AZB21, the SWAN runs E and F (and surprisingly B) are clearly better than the series with the standard flow field.

4.5.4 Tables

For sake of completeness, Tables 4.4.a-d present the simulated and observed values of H_{m0} and $T_{m-1,0}$. Note that Table 4.4 includes all available values. Some are excluded from the statistical analysis because they concern very small waves ($H_{m0}<0.15$ m), or unrealistic values or the offshore waves AZB11 and AZB12.

The computed values of AZB11 and AZB12 come from the SWAN computations on the larger G1-grid. Despite the 10% increase in wave height at the upwave boundary (see § 4.4.4), the wave heights at the offshore buoys are still considerably underestimated by SWAN. The SWAN performance with respect to wave period $T_{m-1,0}$ is much better here than that for the H_{m0} .

4.5.5 Statistical Tables

An overview of statistical values can be found in Table 4.5. Per series and per wave parameter (H_{m0} , $T_{m-1,0}$), a number of statistical parameters is given, which are defined in

Table 4.6. Note that the statistical analysis concerns the seven buoys AZB 21 / 31 / 41 / 22 / 32 / 42 / 62. If for a certain location and instance the observed wave height is less than or equal to 0.15 m, that observation is excluded from the analysis. This occurred seven times (AZB62 on times t1, t2, t3, t8 and AZB41 on t2, t7, t8). Furthermore, AZB41 was not available on t11. Observations with the following thresholds are excluded too: $T_{ps} >= 33.33$ s, $T_{m-1,0} >= 20$ s, $T_{m01} > 15$ s, $H_{m0} > 4.9$ m. This resulted in the exclusion of buoy AZB31 on time t2 ($H_{m0} = 4.94$ m; $T_{m-1,0} = 24.75$ s).

It is difficult to capture the performance of SWAN for the various series in one statistical measure. For a balanced assessment, both (relative) bias and (relative) standard deviation should be considered. Additionally, the wave period should be considered as well as the wave height.

Concerning wave height, the bias of series D, both relative (-0.135%) and absolute (-0.002 m), comes closest to zero. It is the only series with a small underestimation. Furthermore, the standard deviation is good, although series C shows a smaller standard deviation, both relative (11.801%) and absolute (0.137 m). The best value of 'c' (the slope of the line $y=c.x$) comes from series F (1.000), which has a rather large standard deviation (12.801%). Series B (without currents) has the largest standard deviation, restating the impact of currents in the results. Note that for all cases the average model performance in terms of significant wave height (bias, slope 'c', relative bias), is very good.

As seen above, the statistical values of wave period $T_{m-1,0}$ are in general less good than those of the wave heights. The relative bias of series D is best with -9.1%. All series give negative biases for the $T_{m-1,0}$, implying underestimation of the wave period. However, the correlation coefficient r is slightly better for wave period than for wave height (0.986 vs 0.978). Also the relative standard deviation of the wave periods is here better than of the wave height (8.075% vs 11.801%). Overall, the Series D ($C_{ds3}=1.6$) scores best here.

4.6 Comparison SWAN simulations with radar observations

4.6.1 Introduction

Since the beginning of the SBW project (2006), many hindcasts have been conducted for the Amelander Zeegat, see Section 1.2. Experience was gained not only of the performance of the SWAN model, but also in the interpretation of the buoy measurements. The present hindcast is one of the first to make use of marine (X-band) radar data in the Amelander Zeegat, so new experience must be accumulated. The meaning, definition and reliability of the wave parameters and spectra provided by the radar is not as well-known as the buoy observations. In addition, the limited water depths and large sea bed gradients in the Amelander Zeegat domain pose difficulties to the interpretation and processing of the radar images.

Nonetheless, in this section the radar data will be compared to the SWAN results, to obtain an indication of their agreement. Note however that both the radar observations and the SWAN results have uncertainties. Where differences between the two sources occur it is unknown which of them comes closer to reality. The SWAN results from series C ($C_{ds3}=0.8$ and standard current field) gave promising results, and for sake of clarity only these series will be considered in the comparison. Where possible, the buoy data will also be included.

The marine radar data is extracted and processed by Seadarq (Appendix A). The following data was provided:

- Parameters (depth, current speed, current direction, dominant wave length, dominant wave period, dominant wave angle) at the eight storm moments on a grid with approximately 300 m resolution, covering more or less the northern half of the radar circle with 7.5 km radius. The parameters have been computed on areas with cell size of approximately 900 m x 900 m.
- Spectral data: preliminary spectral data of radar intensity as function of frequency and direction for the first storm time, on a grid with approximately 300 m cell size (but computed on areas with cell size 1900 m x 1900 m), covering the north-western quadrant of the radar circle with ca 7 km radius. Note that radar intensity is not equal to wave variance density, see Appendix A. This spectral data will be presented here briefly. Further analysis is required in order to make it reliable and useful.

The radar data contains valuable information but should be used with care. In particular for areas with large bottom gradients, the results are less reliable; this is primarily due to the spatial averaging on the relatively large resolution. Furthermore, it is important to know the exact definitions of the parameters in order to prevent inconsistent comparisons. For example, consider the difference between the dominant wave direction by the radar and the peak wave direction of SWAN. The dominant wave direction given by the radar is the direction of the energy bin with maximum energy as function of direction and frequency. The peak wave direction of SWAN is defined as the direction where the wave energy summed over all frequencies is maximum.

4.6.2 Wave parameters

- Wave direction

Figures 4.17.a-c compare the wave direction from the radar observations and from the SWAN results series C for each of the eight storm moments. In the left-hand panels, the background colors indicate the total water depth of the SWAN simulations, the black vectors the dominant wave direction by the radar and the red vectors the dominant wave direction by SWAN. The white vectors are the peak wave directions by SWAN which are often similar to SWAN's dominant direction. Also the buoys and the peak direction of the buoys are given. The contours (both in left-hand and right-hand panels) present the position of the seabed, they are equal for all moments considered. These figures show some basic features of the wave propagation into the inlet region, including waves entering over and around the ebb tidal shoal, refraction out of the tidal channel onto the shallows, and some trapping of waves on the centre shoal to the west of the main tidal channel inside the inlet. In addition, some waves arriving from the west pass over the main tidal channel and reach the head of Ameland

Overall, the radar wave directions look consistent and show mostly only gradual variations. In areas with large spatial variation in wave direction (for instance Y<607km) the data seems to be less reliable. This agrees with the requirements of small bottom gradients and sufficient wave height to keep the signal-to-noise ratio to acceptable levels.

At t1, t2, t3, t4, about 1 km south west of AZB22 there is significant difference between the peak direction of SWAN and the dominant wave direction of SWAN. The spectra show for both directions a more or less similar energy peak. SWAN's peak direction agrees here better with the wave direction from the radar than SWAN's dominant wave direction does. At t5 and t6 this phenomenon is absent, but at t7 and t8 near (X=170-171 km; Y=609 km) again large differences between SWAN's dominant and peak wave direction occur.

In the right-hand panels, the dominant direction from SWAN is subtracted from the radar wave direction, after both were interpolated onto a grid with the same resolution. Note that the dominant wave direction refers to the direction where the radar intensity as function of frequency and direction has its maximum. On some (random) locations and some times the wave direction of the radar should be rotated 180°; this is (still) a deficiency in the processing of the data. This has not been adjusted and explains some of the rather large differences in isolated areas.

Regarding the differences between the radar and SWAN directions, it is seen that the majority of the area, especially outside of the inlet, shows merely small differences. However, moving into the inlet some large differences are found. Some patterns are visible on all eight storm moments. The differences in the channel at X=169 km, Y=608-609 km (see middle circle) occur in all plots. Here the radar indicates that the dominant waves go from westnorthwest to eastsoutheast whereas SWAN computes that the waves travel rather to the east or even eastnortheast. Further south (X=169 km Y=ca. 607.5, see the lower circle), there is a region of agreement at t1, t2, t3, t4 and t5 where both SWAN and the radar indicate the waves to propagate to the east, crossing the channel. During ebb, the SWAN wave direction here is more to the south, whilst according to the radar the waves cross the channel here during ebb as well.

At X=171 km, Y=609.5 km (see the upper circle), the opposite occurs during flood (t1-t4). Here the radar vectors point to the south, whereas the SWAN vectors have an eastern direction. At the ebb times t5, t6, t7 the differences are limited. On t8 the difference is large again, but now the waves propagate to the southeast according to the radar, whereas SWAN predicts them to propagate to the south.

Note that the dominant wave direction is not a very suitable parameter to compare. Large differences may occur whilst the difference in wave spectrum could be limited. A mean direction would be more suitable. In particular, after analysing the wave spectra (see Paragraph 4.6.3), the reliability of the present dominant wave direction is questionable.

Figures 4.18.a,b present the wave directions of the SWAN results and the radar observations on the transect defined in Figure 4.8.c (repeated in Figure 4.17). Note that in this plot the wave direction of the SWAN results is the peak wave direction, whereas the radar observations present the dominant wave direction. The agreement in wave direction is limited. At t1 and t2, SWAN correctly predicts the large change in wave direction between 10 and 12 km (from ca. 320°N to 380°N), although this jump is offset by ca. 1 km relative to the results of the radar. At 12.5 km they both give more or less the same wave direction, which corresponds to wave buoy AZB31. During slack and ebb (see Figure 4.18.b) the agreement between SWAN and radar is reasonable for the stretch from km 6 to km 10. Past km 10 there are large discrepancies between the radar observations and the SWAN results. The direction of SWAN agrees with those of both the buoys AZB31 and AZB42, and the scatter in the radar results is large at the AZB31 location, suggesting lower reliability for the radar here. Unfortunately, the part of the transect with the largest differences between SWAN and radar direction (10-11 km, where waves pass over the main channel) lacks directional wave buoy information.

- Wave length

The wave length computed from the radar observations by Seadarp's software is the dominant wave length. The wave length computed by SWAN is a mean wave length derived

from the energy spectrum, including a high frequency tail. In Figure 4.19 these wave lengths are presented in the right-hand and left-hand columns respectively, for the times t1 (flood), t3 (flood), t5 (slack) and t7 (ebb) only. Note that the same colour scale is applied and that the radar dominant wave length is factors higher than SWAN's average wave length. For a better comparison, an approximate dominant wave length was computed from SWAN's peak period (middle column). For this, the dispersion relation without the influence of currents is applied to derive the field of spectral peak wave numbers. The order of magnitude of the radar dominant wave length and the "dominant" SWAN wave length is equal and some features are alike, but also large differences are visible. On t1 the agreements are best, where both SWAN and the radar show smaller wave lengths on the shallow areas (ca 60 m) and larger wave lengths in the channel (ca 90-100 m).

4.6.3 Wave spectra

Wave spectra (with a preliminary status) were only analysed for the first of the eight storm moments. The data is available on a grid with circa 300 m cell size (but each spectra is an average over an area of approximately 1900 m x 1900 m), covering the north-western quadrant of the radar circle with ca 7 km radius. The required Modulation Transfer Function (MTF) to transfer the measured spectrum to a wave energy density spectrum is not available yet. The MTF accounts for all sorts of system and environmental variables, for instance the video amplifier, the height of the antenna, the range compensation of the video signal, the angle of radiance and the sea state [Alkyon, (2006)].

Therefore, in this section a very simplified initial translation (wave variance density = radar intensity / 3000) is applied to give an indication of the radar spectra relative to the wave buoy spectra and SWAN spectra. The value of 3000 is a first guess based on the four available buoy spectra for this instant, being AZB21/22/31/32. Note that a proper MTF is frequency dependent. Figure 4.20 shows that at buoy locations AZB31 and AZB32 the agreement between radar and wave buoy is good for frequencies smaller than 0.2 Hz. The radar shows a peak at very low frequencies (<0.02 Hz) which should have been filtered out since it is probably a current component. This energy may have influenced the radar parameters like wave length and wave angle. The 2d radar spectrum at the location of AZB31 (Figure 4.21) shows that the low-frequency energy is present in most directional bins. Some improvements in the production of the spectra by Seadarq are still possible, but unfortunately not within the scope and timing of the present study. Note that the energy at the higher frequencies is underestimated by the radar. This could probably be solved with a proper MTF. However, the limited rotation speed of the radar prevents the recording of wave energy with frequencies above 0.34 Hz.

The simple translation mentioned above makes it possible to estimate the significant wave height H_{m0} , to give an indication of its spatial variation, see Figure 4.22. The radar vectors indicating mean wave direction and peak wave direction have been computed from the spectral data too. The upper panel presents the radar wave height, the lower panel the significant wave height by SWAN. Obviously, the transformation needs some improvement, but especially the eastern part of the plot shows good agreements. It is quite surprising that according to the radar data the waves in the western part ($X < 167$ km) have similar wave heights as the waves east of the channel Borndiep, whereas in SWAN the western waves are much higher.

4.7 Conclusions hindcast Ameland

The aim of this study is to assess the prediction of wave penetration into tidal inlets under ambient currents in SWAN. Eight moments during the moderate storm of 28 January 2010 have been hindcasted with six series of SWAN simulations, varying in current input and wave current formulation. During this period not only buoy observations were available, but also radar observations, covering about half a circle with 15 km diameter northwest of the Amelander lighthouse.

4.7.1 Hindcast and buoy observations

From the comparison between the SWAN hindcast results and buoy observations presented in Section 4.5, the following conclusions can be drawn:

- The agreement in wave height between SWAN and the wave buoy observations is good. The smallest bias is less than 1%, the standard deviation is 12%. The runs with enhanced dissipation for negative current gradients (series C with $C_{ds3}=0.8$ and D with $C_{ds3}=1.6$) score best. The adjusted flow fields (series E) have a limited positive effect on the bias but the standard deviation increases. The scatter plots show clearly that the wave height of the eastern buoys (AZB32/42) is mostly overestimated by SWAN, whereas the wave height at AZB31 is consistently underestimated by SWAN.
- The formulation for enhanced dissipation on negative current gradients improves the SWAN results. From the two series with $C_{ds3}=0.8$ and $C_{ds3}=1.6$, respectively, the latter seems to give the best overall results. However, when considering only buoys AZB21/42/31/32, the wave height results of series C with $C_{ds3}=0.8$ appear to be better.
- On average, the mean wave period $T_{m-1,0}$ is underestimated by SWAN for these cases. The relative bias is of the order of 10%. This is much more than the 1-2% of the significant wave height. However, the relative standard deviation of the wave period is better than of the wave height (8% vs 12%). The influence of the adjusted flow field (series E) on the wave period is very limited. The largest wave periods are observed at AZB21 and AZB31. These high periods are considerably (ca 20%) underestimated by SWAN.
- Regarding the spectra, it is striking that during flood and slack (t1, t2, t3, t4, t5) the observations at AZB32 have a main peak at circa 0.11 Hz. During ebb there is a second peak at 0.18 Hz. In SWAN, the energy at this high-frequency peak is often overestimated and levels at the low-frequency peak underestimated.
- The applied wind velocity in the SWAN simulations is the arithmetic mean of the U_{10} at "Wierummergronden" and "Terschelling Noordzee". These wind stations are new and are considered to have good positions for the area of interest. Unfortunately, the given wind directions were unreliable but this has probably been solved for more recent measurements.
- The influence of currents on the results is significant. In addition, the adjusted current fields (see Deltires (2010d)) gave slightly better results than the standard current fields.

4.7.2 Hindcast and radar observations

From the comparison between the SWAN hindcast results and the processed X-band marine radar observations presented in Section 4.6, the following conclusions can be drawn:

- On the half circle covering the area between Ameland and Terschelling radar observations are available with a spatial resolution of circa 300 m x 300 m of current speeds and direction, depth, wave angle and wave length. The data contains valuable information, but should be used with care. Especially in areas with large bottom gradients the results are less reliable for a large part due to the spatial averaging on the relatively large resolution. Also if the wave heights are too small (a few decimeter), the radar gives unreliable observed values. Furthermore it is important to know the exact definitions of the parameters in order to prevent unfair comparisons.
- The plots of wave direction presented on a transect show that the wave direction of SWAN and the buoys are more or less alike. The radar direction, on the other hand, deviates and fluctuates considerably with respect to these (especially during ebb), suggesting that the reliability should be improved. Nonetheless, the spatial patterns of the radar wave direction seem to be realistic and to agree with the SWAN results over large parts of the domain.
- During flood, both the radar observations and SWAN show that the waves cross the Borndiep channel at Y=ca. 607.5 km. Large spatial variation in wave direction occurs (especially at Y=607.5 – 608.5 km). Also during slack and ebb (t5, t6, t7, t8) the radar shows that the waves cross the channel although not as straight as during flood, rather with a southern component added. However, in the SWAN computations the waves propagate rather south east than to the east.
- The wave direction of the radar sometimes contains values that should be rotated by 180°. A better filter in the post-processing by Seadarq will solve this problem in the future.
- The rotation speed of the radar instrument determines the maximum frequency to be considered. For Ameland, where one rotation takes 2.85 seconds, this maximum frequency is 0.34 Hz.
- The dominant wave length of the radar (roughly 80 m) is much larger than the mean wave length computed by SWAN (roughly 35 m). When basing the wave length on SWAN's peak period (via dispersion relation without current) the results come much closer to the dominant wave length of the radar.

5 Conclusions and recommendations

The present study aimed to assess the prediction of wave penetration into tidal inlets under ambient current in SWAN, using in situ and remote sensing observations of waves and current. To this purpose, the performance of SWAN in the modelling of wave-current interaction was studied for two field cases, namely Port Phillip Bay Heads, Australia, and the Ameland Zeegat in the Dutch Wadden Sea. In-situ wave observations were available for both field situations. In addition, the Ameland Zeegat field case includes recently obtained marine (X-band) radar fields of a number of variables over the tidal inlet. The results of these simulations have been presented in Sections 3 and 4, and preliminary conclusions were drawn. From these results and conclusions, the following general conclusions can be drawn:

- The ambient current was shown to have a significant effect on the wave parameters (wave height, mean period and direction) in the Port Phillip Bay Heads and Ameland Zeegat cases. The addition of enhanced current-induced whitecapping of Deltaires (2010b) has an important, but comparatively smaller impact, which is mainly seen in the significant wave height and mean period.
- In the Port Phillip Bay field case, which features near-idealised swell and wind sea conditions, the enhanced dissipation of Deltaires (2010b) clearly reduces H_{m0} during ebb, for which negative current gradients are found, improving the agreement with observations. For slack and flood, which feature positive or small negative current gradients, generally small impacts on wave height were found. By contrast, in the Ameland Zeegat, reductions in H_{m0} were found during ebb, but also for slack and flood. This is because negative gradients in the current field were found during all tidal phases, i.e. both increasing opposing current and decreasing following current along the wave path. Although the results for H_{m0} improved with the application of the enhanced current-induced dissipation, $T_{m-1,0}$ remains underestimated in the Ameland Zeegat field case.
- The results of this study show that no definitive value for the proportionality coefficient C_{ds3} has been found yet. From the values considered here, $C_{ds3} = 1.6$ appears to be a suitable value in the Port Phillip Bay Heads case. By contrast, in the Ameland Zeegat case, either the value $C_{ds3} = 0.8$ or $C_{ds3} = 1.6$ was found to be optimal, depending on whether a selection or all of the buoys are considered. The SWAN calibration for WTI (Deltaires (2010a)) resulted in $C_{ds3} = 0.8$, based on Ameland Zeegat cases of January, March and November 2007. Deltaires (2010b) found an optimal value of 0.7 on the basis of laboratory flume cases and Ameland Zeegat field cases recorded in 2004 and 2005.
- Comparison of SWAN results with the spatial fields processed from the radar observations has given valuable insight into the spatial performance of SWAN. Wave directions are predicted well in general, capturing refraction over the main tidal channel banks and, elsewhere, components that cross over the tidal channel. However, differences are found moving deeper into the tidal inlet. Since both sources have their uncertainties, it is unknown whether SWAN or the radar performs better here. Qualitative agreement has been found between the observed wave lengths and computed values (based on the computed peak period and dispersion relation without currents).

- The study has given valuable insight into the quality and usefulness of the radar data. The quality appears to vary with tidal phase, with larger scatter in results during ebb. Caution needs to be applied over regions with large bottom gradients and small wave heights. In addition, the frequency range of the observations is limited to values below 0.34 Hz, making it more suitable for studying lower-frequency components. However, until a verified Modulation Transfer function (MTF) is found, neither the wave spectra nor wave heights are useful for model validation.

On the basis of these results and conclusions, the following recommendations are made:

- The optimal value for C_{ds3} has not been found yet. For some situations $C_{ds3} = 0.8$ is better, for others $C_{ds3} = 1.6$, suggesting that the parameterisation of (2.2) should be further refined. Therefore, calibration for specific situations is recommended at present.
- The radar observations provide valuable measurements. However, more experience must be gained in order to benefit from all its possibilities.
- It is strongly recommended to keep in close contact with Seadarq, who develops the radar processing software, and to make joint improvements. The development of a reliable MTF would be of great interest. Furthermore, it is suggested to check the influence of the postprocessing settings (for instance cube size and number of images to base spectra on) on the wave data and optimise them.
- In some isolated areas, the directions computed from the radar data had a 180° aliasing error. It is recommended to further improve the algorithm to remove this error.
- The wave period that came from the radar was erroneous. It is recommended to solve this, and compare the radar period with the buoy measurements.
- During the last months, the processing of radar data has been further improved. A better filter technique is available to remove the low frequency energy peak. Also, improvements to suppress the mirror frequency are made. It is recommended to produce updated radar observations and make another comparison between radar data, buoy data and SWAN results.

6 References

- Alkyon (2006). The integration of remote sensing and numerical modelling. A comparison of SHIRA and SWAN, Project GBP 2002-10, Alkyon report A1101, May 2006
- Alkyon (2008). Analysis of SWAN hindcasts Wadden Sea, Oosterschelde and Slotermeer. Alkyon Report A2085, July 2008.
- Alkyon (2009). Analysis of wave penetration into the eastern Wadden Sea. Alkyon Report 2302, June 2009.
- Booij, N., R. C. Ris and L. H. Holthuijsen (1999). A third generation wave model for coastal regions, Part I, Model description and validation, J. Geophys. Res., 104, C4, 7649-7666.
- Bouws, E. and G. J. Komen (1983). On the balance between growth and dissipation in an extreme, depth limited wind-sea in the southern North Sea, J. Phys. Oceanogr., 13, 1653-1658.
- Deltares (2009). SBW Wadden Sea, water level modelling. Deltares Report 1200114-005-HYE-0003 dd 7 December 2009
- Deltares (2010a). SWAN Calibration and Validation for HBC2011. Deltares Report 1200103-020-HYE-0002 dd May 27th, 2010.
- Deltares (2010b). Wave dissipation on counter current in SWAN, Deltares Report 1200114-003 dd March 2010.
- Deltares (2010c). SBW Wadden Sea 2009, Wave hindcast of the storm of 31 January 2008, Deltares Report 1200114-005-HYE-0004 dd 8 February 2010.
- Deltares (2010d). SBW Wadden Sea 2010, Hydrodynamic computations 28 January 2010, including radar observations. (to be completed)
- Deltares and Alkyon (2009a). Penetration of North Sea waves into the Wadden Sea. Phase 3: fallback options. Deltares Report 1200114.002, phase 3, October 14th, 2009.
- Deltares and Alkyon (2009b). Wave propagation through tidal inlet systems. Deltares report 1200114.002, phase 2 dd October 28th, 2009.
- Eldeberky, Y. (1996). Nonlinear transformations of wave spectra in the nearshore zone, Ph.D Thesis, Fac. of Civil Engineering, Delft University of Technology, 203 pp.
- Hasselmann, K., T. P. Barnett, E. Bouws, H. Carlson, D. E. Cartwright, K. Enke, J. A. Ewing, H. Gienapp, D. E. Hasselmann, P. Kruseman, A. Meerburg, O. Müller, D. J. Olbers, K. Richter, W. Sell, and H. Walden (1973). Measurement of wind-wave growth and swell decay during the Joint North Sea Wave Project (JONSWAP), Dtsch. Hydrogr. Z. Suppl., A(8), 12, 95 pp.
- Hasselmann, S., K. Hasselmann, J. A. Allender, and T. P. Barnett (1985). Computations and parameterizations of the nonlinear energy transfer in a gravity-wave spectrum. Part 2: parameterization of the nonlinear transfer for application in wave models, J. of Phys. Oceanogr. 15, 1378-1391.

- ModeliT (2010). Meetverslag Waddenzee januari 2010, dd 20 april 2010 (in Dutch)
- Svašek (2007). Hindcast tidal inlet Eastern Scheldt, Storms December 2001 and December 2003, Svašek Report CG/1461/07542/A, December 2007.
- Ris, R.C., and L.H. Holthuijsen (1996). Spectral modelling of current wave-blocking. Proc. 25th Int. Conf. on Coastal Eng., ASCE, 1247-1254.
- Royal Haskoning (2008). Hindcast tidal inlet of Ameland storms January and March 2007. Royal Haskoning Report 9T5842.A0/R0002. October 2008.
- Van der Westhuysen, A. J. (2007). Advances in the spectral modelling of wind waves in the nearshore, Ph.D Thesis, Fac. of Civil Engineering, Delft University of Technology.
- Van der Westhuysen, A. J. (2009). Modelling of depth-induced wave breaking over sloping and horizontal beds. Proc. 11th Int. Workshop on Wave Hindcasting and Forecasting.
- Van der Westhuysen, A. J. (2010). Modelling of depth-induced wave breaking under finite-depth wave growth conditions. J. Geophys. Res., 115, C01008, doi:10.1029/2009JC005433.
- Van der Westhuysen, A. J., M. Zijlema, and J. A. Battjes (2007). Nonlinear saturation-based whitecapping dissipation in SWAN for deep and shallow water, Coastal Eng., 54,151-170.
- Van Vledder, G. Ph., M. Zijlema and L. H. Holthuijsen (2010). Revisiting the Jonswap bottom friction formulation in wind-driven storm seas, Proc. 32nd Int. Conf. Coastal Eng..
- Witteveen+Bos (2008). Hindcast of the 8 and 9 November 2007 storm for the tidal inlet of Ameland, Report DT293-2/winb/011, November 2008.
- Witteveen+Bos (2010). Analysis of SWAN underpredictions of offshore wave buoys AZB11 and AZB12, Report DT328-1/rijm3/012, 14 July 2010.
- WL (2002). Kwaliteit randvoorwaardenboek en kwaliteit SWAN (in Dutch). WL | Delft Hydraulics Report H4061, January 2002.
- WL (2006). Plan van Aanpak SBW Natuurrandvoorwaarden Waddenzee (in Dutch). WL | Delft Hydraulics Rapport H4750, March 2006.
- WL (2007). Evaluation and development of wave-current interaction in SWAN. WL | Delft Hydraulics Report H4918.60, November 2007.
- WL & Alkyon (2007). Storm hindcast for Wadden Sea, Hindcasts in inlet systems of Ameland and Norderney and Lunenburg Bay. WL | Delft Hydraulics Report H4918.20, September 2007.
- WL and Lesser, G. (2007). Evaluation and development of wave-current interaction in SWAN. WL | Delft Hydraulics Report H4918.60, November 2007.
- Zijderveld, A., and H. Peters (2008). Measurement programme Dutch Wadden Sea, Proc. 31st Int. Conf. Coastal Eng., ASCE, 404–410.
- Zijlema, M. (2009). Multiscale simulations using unstructured mesh SWAN model for hindcasting in the Dutch Wadden Sea. In proc of Coastal Dynamics, Sept. 2009, Japan.

Zijlema, M., and A.J. van der Westhuysen (2005). On convergence behaviour and numerical accuracy in stationary SWAN simulations of nearshore wind wave spectra, Coastal Eng., 52, 237-256.

A Brief description of radar processing

The Ameland lighthouse (53°26.951'N, 5°37.546'E) is provided with an X-band (9.6 GHz, $\lambda=3$ cm) navigational radar.

The vertically polarized antenna rotates continuously around a vertical axis and transmits intermittently short pulses of electromagnetic energy, the reflections of which are received up to a distance of a few kilometres. After about 0.1 ms, when all the echoes of the previous pulse have died away, the next pulse is transmitted in a slightly different azimuth direction. It takes 2.85 seconds (and thus a few thousand pulses) to cover the full sector of 360°.

One requirement for X-band radars in general is that wind generated capillary waves are present. These small scale disturbances of the water surface with horizontal dimensions in the order of 1 cm are needed in order to make certain oceanographic measurements possible. Equally, strong winds, which cause whitecapping and distort the reflection from the capillary waves, will limit the capability of the X-band radar to measure properties of the large scale wave spectrum. As a guideline, wind speeds higher than 2 m/s are required for the measurement of the wave spectrum, while wind speeds above 20 m/s represent a practical upper limit for retrieving hydrographical information

The capillary waves reflect the transmitted radar signal and are considered clutter (unwanted noise) for navigational purposes. However, by virtue of a modulation mechanism they make the wave crest patterns (with their associated wave lengths and orientations) visible. There are two reasons why the wave crests are visible for the radar. First of all, the roughness on a wave crest is higher than in a wave through due to the capillary waves. Second, the wave crests cause shadow at their back slopes for low angles between the radar beam and the horizontal (< 1°).

From a series of radar images (film) the wave propagation direction and the associated phase velocity can be estimated unambiguously. Hereto, the radar images need to be transformed from (x, y, t) space via 3d FFT to (k_x, k_y, σ) space (with \vec{k} the wave number vector and σ the angular frequency).

The dispersion relation gives the relation between the wave length and the undisturbed phase velocity (no currents and in deep water). However, in practice the phase velocity estimated from the sequence of radar images will often deviate from the undisturbed phase velocity. The measured difference makes it possible to compute the current velocity as well as the average water depth. To determine the water depth, mainly the low frequency part of the dispersion relation (<0.15 Hz) is used, while the high frequency part is mainly used to estimate the surface current vector. The measured current parameters represent the depth-averaged of the vertical current profile in the upper few meters of the water column.

The radar image exists of rectangular pixels with ca. 7.5 m resolution, which form a calculation matrix of the underlying radar resolution cells. The radar range resolution dR depends on the pulse length ΔT ($dR=0.5*c*\Delta T$, with $c=3*10^8$ m/s; speed of light). The azimuthal resolution ΔL depends on the radar beam width and thus on the horizontal length D of the antenna ($\Delta L = R*\lambda / D$ with R the distance from the radar). The radius of the radar image consists of 1000 pixels.

A ‘snapshot’ presents the moving average of a number (for instance 8, 16, 32, 64) of successive images.

The radar intensity spectra as well as wave and current parameters – obtained after the adaptive filtering - are computed for areas with cell size 959 m x 959 m (but have a spatial resolution of ca 300 m). Whereas spectra from buoys are based on time series (for instance 2048 values with 0.5 sec interval) at one location, the radar spectra are based on a shorter period and more locations (for instance 128 x 128 pixels x 32 images). For less homogenous areas, it is suggested to choose a smaller grid size. Since the FFT requires rectangular pixels, the original polar pixels are linearly interpolated to rectangles.

For the measurement of certain hydrographical parameters, such as wave information and current, waves of at least 15 meters wave length and 0.5 meters wave height are necessary. It is then possible to derive from processing the radar data:

- Wave frequency/length
- Wave speed
- Wave direction
- Wave height (after calibration using a wave buoy)
- Water depth
- Current velocity

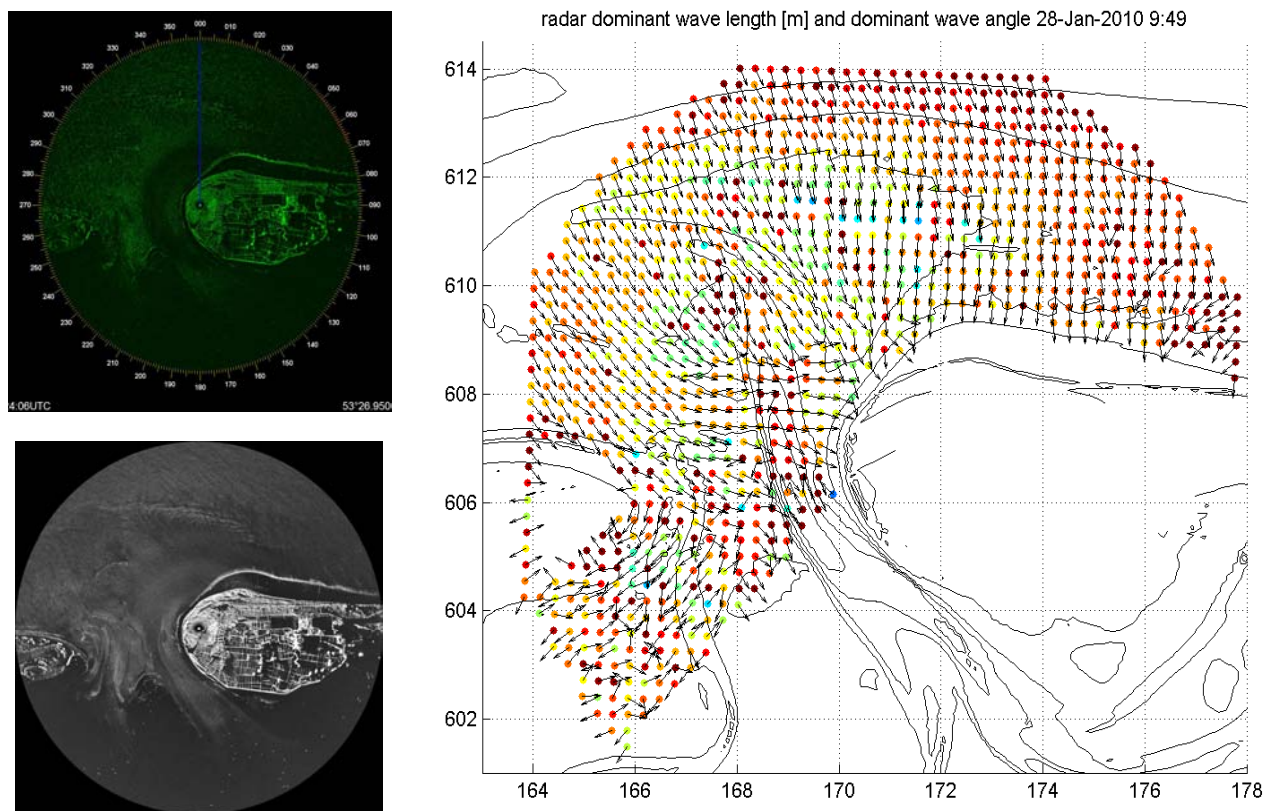


Figure A1: left panels: Radar image and snapshot Amelander Zeegat (from Seadarq); right: Scatter plot of processed dominant wave length and wave direction

The radar spectra present the radar intensity, and not the wave energy. A modulation Transfer Function (MTF) is required to assess the wave spectrum. This empirical function depends on both the measuring system (a.o. video amplifier, antenna height, range compensation of the video signal) and environmental features (a.o seastate, angle between waves and radar beam, distance to radar). In practice, it could be calibrated to buoy measurements.

B SWAN input file Amelander Zeegat G1

```

$ 1202119.003 SBW-Waddenzee2010/golndoordingradar
$ Tidal Inlet of Ameland, storm January 28th, 2010
$ Moment: 20100128 0210 GMT
$ basic swan file taken from SWIFT f102am07z015

$*****
PROJECT 'AZG2010' 'GCL'

MODE STAT
SET LEVEL = 0 MAXERR = 2 NAUT

$***** MODEL SETUP*****
CGRID CURVI 389 160 EXC -99.00 CIRCLE 36 0.03 1.50
READ COOR 1 '././INP/G1.GRD' IDLA=3 NHEDF=0 NHEDVEC=0

INP BOTTOM CURVI 0. 0. 389 160 EXC -99.0
READ BOTTOM 1 '././INP/G1.BOT' IDLA=3 NHEDF=0 FREE

$***** BOUNDARY CONDITIONS *****
WIND 12.4 330

BOU SEGMENT IJ 0 0 389 0 VAR FILE &
20766 '././BOUND/01280210bson.SP1' 1 &
152000 '././BOUND/01280210beld.SP1' 1

$ SW and NE bound
BOU SEGMENT IJ 389 0 389 160 CON FILE '././BOUND/01280210beld_2.SP1'
BOU SEGMENT IJ 0 0 160 CON FILE '././BOUND/01280210bson_2.SP1'

$***** PHYSICS *****
GEN3 WESTH
WCAP WESTH cds2=5.00e-05 br=0.00175 p0=4.00000 powst=0.00000 powk=0.00000 &
nldisp=0.00 cds3=0.8 powfsh=1.00000
QUAD iquad=2 lambda=0.25 cnl4=3.0e+07
FRIC JONSWAP cfjon=0.038
BREA WESTH alpha=0.96 pown=2.5 bref=-1.3963 shfac=500
TRIAD trfac=0.10 cutfr=2.5

```

```

$*****NUMERICAL PARAMETERS *****

NUM STOPC 0 0.01 0.001 99.5 STAT mxitst=80

$***** OUTPUT LOCATIONS/RAYS*****

$ Output locations for boundary conditions for AZG3A grid

POINTS 'E1' FILE './INP/E1.PNT'
POINTS 'E2' FILE './INP/E22.PNT'
POINTS 'E3' FILE './INP/E3.PNT'
POINTS 'E4' FILE './INP/E4.PNT'
POINTS 'E5' FILE './INP/E5.PNT'
POINTS 'W1' FILE './INP/W1.PNT'
POINTS 'W2' FILE './INP/W2.PNT'
POINTS 'W3' FILE './INP/W3.PNT'
POINTS 'W4' FILE './INP/W4.PNT'
POINTS 'W5' FILE './INP/W5.PNT'

POINTS 'P2010' FILE './INP/AZB2010.PNT'

CURVE 'TOELD' 95776 606820 60 106603 588068
CURVE 'TOSON' 194718 644160 60 206608 623565
CURVE 'TOA11' 147150 640004 60 161006 616004
CURVE 'TOA12' 160110 639650 60 173011 617304

$ *** Integrate over frequency range [FMIN,FMAX] to obtain wave parameters
QUANT HS TMM10 TM01 TM02 FMIN 0.03 FMAX 0.5

$ ***** OUTPUT *****

BLOCK 'COMPGRID' NOHEADER 'C01aG1.mat' LAYOUT 3 &
XP YP DEP BOTLEV WATLEV HS RTP TMM10 TM01 TM02 DIR DSPR &
TPS DHSIGN DRTM01 WIND VEL WLENGTH

TABLE 'P2010' HEAD 'C01aG1_P2010.TAB' &
XP YP DEP BOTLEV WATLEV HS RTP TMM10 TM01 TM02 FSPR DIR DSPR &
WLENGTH TPS DHSIGN DRTM01 WIND VEL DISSIP QB FORCE UBOT STEEP SETUP RTMM10 RTM01

```

```

TABLE 'TOELD' HEAD 'C01aG1_TOELD.LIN' &
XP YP DIST DEP WATLEV HS RTP TMM10 TM01 TM02 FSPR DIR DSPR &
WLENGTH TPS DHSIGN DRTM01 WIND DISSIP QB FORCE UBOT STEEP SETUP
TABLE 'TOSON' HEAD 'C01aG1_TOSON.LIN' &
XP YP DIST DEP WATLEV HS RTP TMM10 TM01 TM02 FSPR DIR DSPR &
WLENGTH TPS DHSIGN DRTM01 WIND DISSIP QB FORCE UBOT STEEP SETUP
TABLE 'TOA11' HEAD 'C01aG1_TOA11.LIN' &
XP YP DIST DEP WATLEV HS RTP TMM10 TM01 TM02 FSPR DIR DSPR &
WLENGTH TPS DHSIGN DRTM01 WIND DISSIP QB FORCE UBOT STEEP SETUP
TABLE 'TOA12' HEAD 'C01aG1_TOA12.LIN' &
XP YP DIST DEP WATLEV HS RTP TMM10 TM01 TM02 FSPR DIR DSPR &
WLENGTH TPS DHSIGN DRTM01 WIND DISSIP QB FORCE UBOT STEEP SETUP

SPEC 'P2010' SPEC1D 'C01aG1_P2010.SA1'
SPEC 'P2010' SPEC2D 'C01aG1_P2010.SA2'

$ output: boundary conditions for the AZG3A grid
SPECOUT 'E1' SPEC2D ABSOLUTE '../BOUND/C01aG1_E1.SA2'
SPECOUT 'E2' SPEC2D ABSOLUTE '../BOUND/C01aG1_E2.SA2'
SPECOUT 'E3' SPEC2D ABSOLUTE '../BOUND/C01aG1_E3.SA2'
SPECOUT 'E4' SPEC2D ABSOLUTE '../BOUND/C01aG1_E4.SA2'
SPECOUT 'E5' SPEC2D ABSOLUTE '../BOUND/C01aG1_E5.SA2'
SPECOUT 'W1' SPEC2D ABSOLUTE '../BOUND/C01aG1_W1.SA2'
SPECOUT 'W2' SPEC2D ABSOLUTE '../BOUND/C01aG1_W2.SA2'
SPECOUT 'W3' SPEC2D ABSOLUTE '../BOUND/C01aG1_W3.SA2'
SPECOUT 'W4' SPEC2D ABSOLUTE '../BOUND/C01aG1_W4.SA2'
SPECOUT 'W5' SPEC2D ABSOLUTE '../BOUND/C01aG1_W5.SA2'

TEST 1 0 POINTS XY & $ Observational locations
161006. 616004. & $AZB11
173011. 617304. & $AZB12
PAR 'C01aG1.PAR' &
S1D 'C01aG1.S1D' &
S2D 'C01aG1.S2D'

COMPUTE

STOP

```

C SWAN input file Amelander Zeegat, grid G2

```
$ 1202119.003 SBW-Waddenze2010/golndoordringingradar
$ Tidal Inlet of Ameland, storm January 28th, 2010
$ Moment: 20100128 0210 GMT

$ basic swan file taken from SWIFT f102am07z015

$*****
PROJECT 'AZG2010' 'AZG'

MODE STAT
SET MAXERR = 2 NAUT

$***** MODEL SETUP*****

CGRID CURVI 285 379 EXC -99.00 CIRCLE 36 0.03 2.50
READ COOR 1.'../../INP/G2.GRD' IDLA=4 NHEDF=0 NHEDVEC=1 FREE

INP BOTTOM CURVI 0.0.285 379 EXC -99.0
READ BOTTOM 1.'../../INP/G2.BOT' IDLA=4 NHEDF=0 FREE

INP WLEV CURVI 0.0.285 379 EXC -99.0
READ WLEV 1.'../../INP/WLVCUR/20100128_0210_fine.wlv' IDLA=3 NHEDF=0 FREE

INP CUR CURVI 0.0.285 379 EXC -99.0
READ CUR 1.'../../INP/WLVCUR/20100128_0210_fine.cur' IDLA=3 NHEDF=0 FREE

$***** BOUNDARY CONDITIONS *****

WIND 12.4 330

$ wave boundary conditions west
BOU SEGMENT IJ 285 0 285 379 VAR FILE &
    0  '../../BOUND/01280210A11.SP1' 1 &
    5356 '../../BOUND/C01aG1_W1.SA2' 1 &
    9617 '../../BOUND/C01aG1_W2.SA2' 1 &
    13389 '../../BOUND/C01aG1_W3.SA2' 1 &
    20368 '../../BOUND/C01aG1_W4.SA2' 1 &
    34860 '../../BOUND/C01aG1_W5.SA2' 1

$ wave boundary conditions east
BOU SEGMENT IJ 0 0 0 379 VAR FILE &
    0  '../../BOUND/01280210A12.SP1' 1 &
    4680 '../../BOUND/C01aG1_E1.SA2' 1 &
    10070 '../../BOUND/C01aG1_E2.SA2' 1 &
    13450 '../../BOUND/C01aG1_E3.SA2' 1 &
```

```

$ boundary conditon north
BOU SEGMENT IJ 0 0 47 0 CONST FILE '././BOUND/01280210A12_2.SP1' 1
BOU SEGMENT IJ 151 0 285 0 CONST FILE '././BOUND/01280210A11_2.SP1' 1
BOU SEGMENT IJ 47 0 151 0 VAR FILE &
0 '././BOUND/01280210A12_3.SP1' 1 &
12025 '././BOUND/01280210A11_3.SP1' 1

$***** PHYSICS *****
GEN3 WESTH
WCAP WESTH cds2=5.00e-05 br=0.00175 p0=4.00000 powst=0.00000 powk=0.00000 &
nldisp=0.00 cds3=0.8 powfsh=1.00000
QUAD iquad=2 lambda=0.25 cnl4=3.0e+07
FRIC JONSWAP cfjon=0.038
BREA WESTH alpha=0.96 pown=2.5 bref=-1.3963 shfac=500
TRIAD trfac=0.10 cutfr=2.5

$***** NUMERICAL PARAMETERS *****
NUM STOPC 0 0.01 0.001 101 STAT mxitst=120 alfa=0.002

$***** OUTPUT LOCATIONS/RAYS*****
$ Output locations for boundary conditions for AZG3A grid

POINTS 'P2010' FILE '././INP/AZB2010.PNT'
POINTS 'RADAR' FILE '././INP/RADAR.PNT'

CURVE 'C1' 161006 616004 50 &
165200 609100 50 &
168318 606745 50 &
171319 604249 50 &
175490 600699 50 &
180506 598604

$ *** Integrate over frequency range [FMIN,FMAX] to obtain wave parameters
QUANT HS TMM10 TM01 TM02 FMIN 0.03 FMAX 0.5

```

```

$ **** OUTPUT ****

BLOCK 'COMPGRID' NOHEADER 'C01aG2.mat' LAYOUT 3 &
XP YP DEP BOTLEV WATLEV HS RTP TMM10 TM01 TM02 DIR PDIR DSPR &
TPS DHSIGN DRTM01 WIND VEL WLLENGTH

TABLE 'P2010' HEAD 'C01aG2_P2010.TAB' &
XP YP DEP BOTLEV WATLEV HS RTP TMM10 TM01 TM02 FSPR DIR PDIR DSPR &
WLLENGTH TPS DHSIGN DRTM01 WIND VEL DISSIP QB FORCE UBOT STEEP SETUP RTMM10 RTM01

TABLE 'RADAR' HEAD 'C01aG2_RADAR.TAB' &
XP YP DEP BOTLEV WATLEV HS RTP TMM10 TM01 TM02 FSPR DIR PDIR DSPR &
WLLENGTH TPS WIND VEL DISSIP RTMM10 RTM01

TABLE 'C1' HEAD 'C01aG2_C1.TAB' &
XP YP DIST DEP BOTLEV WATLEV HS RTP TMM10 TM01 TM02 FSPR DIR PDIR DSPR &
WLLENGTH TPS WIND VEL DISSIP QB FORCE UBOT STEEP SETUP RTMM10 RTM01

SPEC 'P2010' SPEC1D ABS 'C01aG2_P2010.SA1'
SPEC 'P2010' SPEC1D REL 'C01aG2_P2010.SR1'
SPEC 'P2010' SPEC2D ABS 'C01aG2_P2010.SA2'
SPEC 'P2010' SPEC2D REL 'C01aG2_P2010.SR2'
SPEC 'RADAR' SPEC1D ABS 'C01aG2_RADAR.SA1'
SPEC 'RADAR' SPEC1D REL 'C01aG2_RADAR.SR1'
SPEC 'RADAR' SPEC2D ABS 'C01aG2_RADAR.SA2'
SPEC 'RADAR' SPEC2D REL 'C01aG2_RADAR.SR2'

TEST 1 0 POINTS XY & $ Observational locations
167307. 610978. & $AZB21
168318. 606745. & $AZB31
168792. 600501. & $AZB41
167963. 596444. & $AZB51
167500. 592500. & $AZB61
170688. 611040. & $AZB22
169349. 607115. & $AZB32
171319. 604249. & $AZB42
175490. 600699. & $AZB52
180506. 598604. & $AZB62
PAR 'C01aG2.PAR' &
S1D 'C01aG2.S1D'

COMPUTE

STOP

```

D Tables

H_{mo} [m]												
AZB	11	21	31	41	51	61	12	22	32	42	52	62
T=1												
meas	3.39	1.79	1.36	NaN	NaN	NaN	3.20	1.29	1.29	0.60	NaN	0.03
A	3.01	2.02	1.35	0.22	0.28	0.18	2.93	1.39	1.46	0.55	0.55	0.17
B	3.01	1.70	1.29	0.23	0.27	0.19	2.93	1.34	1.38	0.67	0.63	0.20
C	3.01	1.88	1.30	0.20	0.26	0.18	2.93	1.32	1.42	0.53	0.50	0.15
D	3.01	1.79	1.26	0.19	0.25	0.18	2.93	1.27	1.37	0.51	0.47	0.15
E	3.01	1.90	1.32	0.19	0.26	0.18	2.93	1.32	1.46	0.49	0.49	0.16
F	3.01	1.89	1.35	0.21	0.27	0.18	2.93	1.32	1.47	0.49	0.46	0.16
T=2												
meas	3.45	2.17	4.94	0.13	NaN	NaN	3.40	1.50	1.51	0.37	NaN	0.03
A	2.82	2.23	1.48	0.33	0.37	0.31	2.77	1.54	1.58	0.43	0.24	0.22
B	2.82	1.87	1.44	0.36	0.38	0.31	2.77	1.55	1.49	0.66	0.59	0.27
C	2.82	2.11	1.44	0.31	0.35	0.29	2.77	1.50	1.54	0.42	0.22	0.20
D	2.82	2.02	1.41	0.29	0.33	0.28	2.77	1.46	1.50	0.41	0.20	0.19
E	2.82	2.16	1.52	0.32	0.36	0.30	2.77	1.54	1.60	0.43	0.24	0.21
F	2.82	2.15	1.56	0.34	0.36	0.31	2.77	1.54	1.60	0.40	0.22	0.21
T=3												
meas	2.97	2.12	1.80	0.16	NaN	NaN	3.27	1.67	1.53	0.28	NaN	0.04
A	2.97	2.29	1.54	0.37	0.40	0.35	2.91	1.66	1.66	0.40	0.23	0.28
B	2.97	1.97	1.50	0.40	0.42	0.37	2.91	1.66	1.54	0.68	0.59	0.31
C	2.97	2.20	1.51	0.34	0.38	0.34	2.91	1.61	1.61	0.39	0.21	0.25
D	2.97	2.13	1.48	0.32	0.36	0.33	2.91	1.57	1.57	0.38	0.20	0.23
E	2.97	2.23	1.53	0.35	0.38	0.38	2.91	1.66	1.66	0.42	0.25	0.27
F	2.97	2.17	1.54	0.38	0.39	0.38	2.91	1.63	1.68	0.40	0.23	0.27
T=4												
meas	3.22	2.05	1.90	0.32	NaN	NaN	3.28	1.73	1.54	0.29	NaN	0.17
A	2.85	2.39	1.65	0.46	0.47	0.46	2.80	1.78	1.72	0.42	0.25	0.35
B	2.85	2.08	1.63	0.47	0.49	0.46	2.80	1.81	1.64	0.66	0.54	0.39
C	2.85	2.31	1.63	0.43	0.46	0.44	2.80	1.75	1.69	0.41	0.22	0.33
D	2.85	2.25	1.61	0.41	0.45	0.43	2.80	1.72	1.67	0.41	0.21	0.31
E	2.85	2.17	1.71	0.47	0.49	0.48	2.80	1.80	1.76	0.44	0.26	0.35
F	2.85	2.13	1.70	0.48	0.50	0.48	2.80	1.77	1.75	0.45	0.24	0.35

Table 4.4.a: Results SWAN simulations (series A,B,C,D,E,F) and observations Amelander Zeegat; H_{mo} [m] for times t1, t2, t3, t4

H_{mo} [m]												
AZB	11	21	31	41	51	61	12	22	32	42	52	62
T=5												
meas	3.34	1.97	1.74	0.33	NaN	NaN	3.21	1.72	1.45	0.44	NaN	0.34
A	3.11	2.20	1.64	0.57	0.53	0.47	3.11	1.71	1.61	0.43	0.40	0.40
B	3.11	2.06	1.63	0.46	0.48	0.46	3.11	1.80	1.63	0.65	0.52	0.42
C	3.11	2.15	1.60	0.54	0.51	0.46	3.11	1.69	1.58	0.41	0.39	0.39
D	3.11	2.11	1.57	0.51	0.50	0.46	3.11	1.68	1.55	0.40	0.38	0.39
E	3.11	1.86	1.67	0.59	0.54	0.47	3.11	1.71	1.71	0.42	0.39	0.40
F	3.11	1.88	1.65	0.60	0.54	0.47	3.11	1.73	1.68	0.65	0.39	0.40
T=6												
meas	3.34	1.91	1.63	0.22	NaN	NaN	3.07	1.37	1.33	0.54	NaN	0.27
A	2.89	1.75	1.43	0.36	0.56	0.43	2.85	1.50	1.57	0.72	0.61	0.43
B	2.89	1.87	1.48	0.39	0.42	0.40	2.85	1.59	1.47	0.58	0.48	0.37
C	2.89	1.70	1.40	0.33	0.49	0.42	2.85	1.48	1.49	0.66	0.57	0.41
D	2.89	1.65	1.35	0.31	0.45	0.40	2.85	1.47	1.42	0.62	0.55	0.39
E	2.89	1.62	1.35	0.31	0.46	0.43	2.85	1.47	1.47	0.66	0.56	0.38
F	2.89	1.65	1.36	0.33	0.46	0.43	2.85	1.47	1.43	0.74	0.61	0.38
T=7												
meas	3.27	1.51	1.47	0.13	NaN	NaN	3.19	1.23	1.22	0.62	NaN	0.18
A	2.86	1.61	1.25	0.26	0.41	0.36	2.84	1.27	1.39	0.83	0.75	0.31
B	2.86	1.69	1.29	0.31	0.35	0.34	2.84	1.37	1.30	0.54	0.48	0.29
C	2.86	1.55	1.22	0.24	0.36	0.35	2.84	1.26	1.31	0.73	0.65	0.29
D	2.86	1.50	1.18	0.23	0.32	0.34	2.84	1.24	1.25	0.67	0.59	0.28
E	2.86	1.47	1.21	0.22	0.33	0.32	2.84	1.25	1.11	0.70	0.64	0.25
F	2.86	1.49	1.21	0.24	0.33	0.32	2.84	1.27	1.22	0.67	0.68	0.25
T=8												
meas	3.18	1.53	1.45	0.06	NaN	NaN	3.20	1.11	1.08	0.61	NaN	0.09
A	2.84	1.55	1.24	0.29	0.39	0.35	2.79	1.18	1.30	0.92	0.79	0.28
B	2.84	1.61	1.25	0.30	0.35	0.32	2.79	1.26	1.28	0.55	0.50	0.28
C	2.84	1.50	1.20	0.27	0.35	0.33	2.79	1.16	1.24	0.81	0.68	0.27
D	2.84	1.44	1.16	0.25	0.32	0.32	2.79	1.15	1.17	0.74	0.61	0.26
E	2.84	1.43	1.18	0.24	0.32	0.30	2.79	1.19	1.03	0.77	0.62	0.23
F	2.84	1.34	1.11	0.25	0.32	0.30	2.79	1.19	1.01	0.72	0.65	0.23

Table 4.4.b: Results SWAN simulations (series A,B,C,D,E,F) and observations Amelander Zeegat; H_{mo} [m] for times t5, t6, t7, t8

Tm_10 [s]												
AZB	11	21	31	41	51	61	12	22	32	42	52	62
T=1												
meas	7.40	6.24	6.46	NaN	NaN	NaN	7.17	6.47	5.67	3.48	NaN	7.94
A	7.14	5.43	5.72	2.41	2.36	2.30	7.05	5.52	5.04	3.44	2.64	2.19
B	7.14	5.77	5.92	2.57	2.48	2.36	7.05	5.94	5.16	3.53	3.09	2.36
C	7.14	5.65	5.99	2.50	2.34	2.30	7.05	5.82	5.16	3.51	2.67	2.19
D	7.14	5.80	6.16	2.55	2.33	2.30	7.05	6.01	5.24	3.56	2.69	2.19
E	7.14	5.67	6.13	2.45	2.30	2.25	7.05	5.85	5.21	3.68	2.61	2.15
F	7.14	5.63	5.95	2.60	2.31	2.25	7.05	5.67	5.21	3.35	2.53	2.15
T=2												
meas	7.52	6.67	24.75	3.97	NaN	NaN	7.44	6.24	6.07	4.34	NaN	12.00
A	7.26	5.59	5.90	2.90	2.54	2.41	7.17	5.82	5.34	3.61	2.23	2.18
B	7.26	6.08	6.28	3.01	2.70	2.58	7.17	6.20	5.51	3.74	3.04	2.43
C	7.26	5.77	6.13	3.02	2.51	2.39	7.17	6.00	5.46	3.68	2.23	2.18
D	7.26	5.91	6.28	3.10	2.50	2.37	7.17	6.12	5.55	3.72	2.24	2.17
E	7.26	5.75	5.98	3.10	2.51	2.35	7.17	5.89	5.47	3.79	2.19	2.16
F	7.26	5.73	5.91	3.13	2.53	2.35	7.17	5.78	5.53	3.85	2.16	2.16
T=3												
meas	7.11	6.88	6.79	3.76	NaN	NaN	7.45	6.66	6.34	4.50	NaN	6.80
A	7.50	5.71	5.97	3.09	2.62	2.49	7.43	5.98	5.45	3.77	2.13	2.27
B	7.50	6.18	6.35	3.15	2.76	2.65	7.43	6.25	5.64	3.82	3.06	2.52
C	7.50	5.83	6.14	3.22	2.60	2.47	7.43	6.10	5.57	3.87	2.16	2.25
D	7.50	5.93	6.26	3.31	2.58	2.45	7.43	6.20	5.66	3.94	2.18	2.23
E	7.50	5.80	6.18	3.33	2.64	2.53	7.42	5.90	5.56	3.89	2.21	2.26
F	7.50	5.89	6.12	3.33	2.67	2.53	7.43	5.78	5.56	3.97	2.15	2.25
T=4												
meas	7.68	7.52	7.07	3.24	NaN	NaN	7.79	6.94	6.41	5.05	NaN	2.29
A	7.72	5.97	6.37	3.45	2.88	2.77	7.65	6.30	5.78	4.25	2.30	2.42
B	7.72	6.46	6.74	3.49	2.97	2.83	7.65	6.55	5.97	4.08	3.01	2.67
C	7.72	6.09	6.49	3.54	2.86	2.75	7.65	6.39	5.86	4.30	2.30	2.39
D	7.72	6.18	6.58	3.62	2.85	2.73	7.65	6.47	5.93	4.34	2.31	2.38
E	7.72	6.25	6.50	3.71	2.98	2.84	7.65	6.08	5.88	4.45	2.51	2.43
F	7.72	6.35	6.55	3.76	2.99	2.84	7.65	6.03	5.88	4.42	2.43	2.43

Table 4.4.c: Results SWAN simulations (series A,B,C,D,E,F) and observations Amelander Zeegat; $T_{m-1,0}$ [s] for times t1, t2, t3, t4

Tm_10 [s]												
AZB	11	21	31	41	51	61	12	22	32	42	52	62
T=5												
meas	8.34	7.95	8.15	3.21	NaN	NaN	8.35	7.31	6.80	4.35	NaN	2.33
A	8.30	6.24	6.95	3.34	3.04	2.86	8.28	6.29	6.08	4.30	2.59	2.61
B	8.30	6.60	6.99	3.57	2.96	2.82	8.28	6.76	6.15	4.15	3.03	2.76
C	8.30	6.32	7.05	3.37	3.01	2.84	8.28	6.37	6.15	4.37	2.58	2.60
D	8.30	6.40	7.13	3.40	2.99	2.82	8.28	6.45	6.20	4.41	2.57	2.59
E	8.30	6.79	7.03	3.46	3.02	2.86	8.28	6.82	5.97	4.23	2.65	2.59
F	8.30	6.80	6.96	3.42	3.03	2.87	8.28	6.83	6.01	3.95	2.69	2.60
T=6												
meas	8.24	7.90	8.61	2.69	NaN	NaN	8.09	7.28	6.95	5.06	NaN	2.43
A	8.22	6.48	7.04	3.26	3.00	2.79	8.17	6.86	6.11	4.48	3.41	2.63
B	8.22	6.45	6.99	3.27	2.76	2.68	8.17	6.76	6.03	3.96	2.93	2.64
C	8.22	6.63	7.34	3.27	2.87	2.73	8.17	6.91	6.28	4.47	3.39	2.60
D	8.22	6.77	7.58	3.26	2.82	2.70	8.17	6.96	6.40	4.46	3.37	2.58
E	8.22	6.55	7.33	3.10	2.82	2.65	8.17	6.95	6.35	4.64	3.45	2.60
F	8.22	6.58	7.35	3.10	2.83	2.65	8.17	6.92	6.33	4.74	3.56	2.61
T=7												
meas	8.24	7.43	9.27	2.63	NaN	NaN	8.29	7.41	7.19	5.42	NaN	2.41
A	8.23	6.16	7.05	2.77	2.77	2.58	8.17	6.79	5.98	4.73	3.82	2.53
B	8.23	6.32	6.92	2.88	2.58	2.56	8.17	6.59	5.79	3.71	2.89	2.49
C	8.23	6.35	7.37	2.73	2.66	2.54	8.17	6.86	6.14	4.73	3.78	2.49
D	8.23	6.52	7.61	2.72	2.61	2.52	8.17	6.92	6.25	4.72	3.75	2.48
E	8.23	6.24	7.29	2.62	2.61	2.51	8.17	6.82	6.38	4.77	3.78	2.50
F	8.23	6.28	7.33	2.72	2.62	2.51	8.17	6.79	6.25	4.66	3.85	2.51
T=8												
meas	8.28	7.36	8.60	3.08	NaN	NaN	8.03	7.46	6.76	5.36	NaN	2.30
A	8.10	6.04	6.77	2.80	2.77	2.60	7.96	6.64	5.86	4.70	3.86	2.47
B	8.10	6.21	6.74	2.79	2.58	2.53	7.96	6.50	5.59	3.60	2.91	2.42
C	8.10	6.25	7.13	2.76	2.69	2.56	7.96	6.70	6.00	4.69	3.80	2.44
D	8.10	6.43	7.37	2.75	2.65	2.53	7.96	6.76	6.10	4.67	3.76	2.43
E	8.10	6.18	7.12	2.68	2.65	2.53	7.96	6.53	6.19	4.71	3.74	2.44
F	8.10	6.17	7.14	2.75	2.65	2.53	7.96	6.58	6.22	4.55	3.79	2.44

Table 4.4.d: Results SWAN simulations (series A,B,C,D,E,F) and observations Amelander Zeegat; $T_{m-1,0}$ [s] for times t5, t6, t7, t8

Hm0													
	bi	as	stdev	r	c	a	b	xmean	ymean	rel bi	as	rel std	N
	[m]							[m]	[m]	[%]			
A	0.079	0.146	0.973		1.044	0.954	0.133	1.164	1.243	6.823	12.547	47	
B	0.053	0.161	0.973		1.008	0.863	0.212	1.164	1.217	4.593	13.806	47	
C	0.035	0.137	0.978		1.009	0.929	0.118	1.164	1.199	3.041	11.801	47	
D	-0.002	0.139	0.978		0.979	0.908	0.106	1.164	1.162	-0.135	11.929	47	
E	0.028	0.145	0.975		1.002	0.923	0.118	1.164	1.191	2.397	12.483	47	
F	0.030	0.149	0.975		1.000	0.903	0.142	1.164	1.194	2.576	12.801	47	
Tm_10													
	bi	as	stdev	r	c	a	b	xmean	ymean	rel bi	as	rel std	N
	[s]							[s]	[s]	[%]			
A	-0.742	0.586	0.979		0.865	0.734	0.847	5.974	5.233	-12.418	9.807	47	
B	-0.682	0.648	0.954		0.877	0.767	0.710	5.974	5.292	-11.424	10.849	47	
C	-0.628	0.524	0.983		0.885	0.767	0.766	5.974	5.347	-10.505	8.771	47	
D	-0.544	0.482	0.984		0.900	0.793	0.691	5.974	5.431	-9.100	8.075	47	
E	-0.602	0.522	0.985		0.888	0.762	0.818	5.974	5.373	-10.073	8.730	47	
F	-0.624	0.506	0.986		0.885	0.768	0.762	5.974	5.351	-10.442	8.464	47	
Hm0													
	flood	t1	t2	t3	t4								
A	0.083	0.140	0.980		1.049	0.986	0.100	1.246	1.329	6.663	11.194	22	
B	0.043	0.195	0.980		0.983	0.779	0.319	1.246	1.290	3.486	15.630	22	
C	0.038	0.133	0.982		1.012	0.950	0.100	1.246	1.284	3.010	10.639	22	
D	0.000	0.134	0.983		0.983	0.922	0.098	1.246	1.247	0.018	10.743	22	
E	0.062	0.125	0.984		1.028	0.950	0.124	1.246	1.308	4.968	10.002	22	
F	0.056	0.124	0.985		1.021	0.937	0.134	1.246	1.302	4.482	9.971	22	
Hm0													
	ebb	t6	t7	t8									
A	0.074	0.166	0.957		1.030	0.839	0.247	1.071	1.145	6.891	15.457	18	
B	0.050	0.136	0.967		1.033	0.970	0.082	1.071	1.121	4.655	12.703	18	
C	0.025	0.154	0.966		0.991	0.832	0.205	1.071	1.096	2.363	14.354	18	
D	-0.016	0.156	0.967		0.956	0.816	0.181	1.071	1.055	-1.515	14.571	18	
E	-0.023	0.159	0.966		0.950	0.810	0.181	1.071	1.048	-2.169	14.834	18	
F	-0.024	0.166	0.962		0.948	0.802	0.188	1.071	1.047	-2.256	15.498	18	

Table 4.5: Statistical parameters SWAN (series A,B,C,D,E,F) and observations Amelander Zeegat H_{m0} and Tm-1,0; times 1-8. For H_{m0} also flood and ebb separately. In bold the best series.

$\bar{x} = \frac{1}{N} \sum_{i=1}^N x_i$	Mean value of measured values
$\bar{y} = \frac{1}{N} \sum_{i=1}^N y_i$	Mean of the simulated values
$bias = \frac{1}{N} \sum_{i=1}^N (y_i - x_i) = \bar{y} - \bar{x}$	The bias is positive if the mean of the modelled results exceeds the mean of the observations
$relbias = \frac{bias}{\bar{x}}$	Relative bias
$std = \sqrt{\frac{1}{N-1} \sum_{i=1}^N (y_i - x_i - BIAS)^2}$	Standard deviation
$relstd = \frac{std}{\bar{x}}$	Relative standard deviation
$r = \frac{\sum_{i=1}^N (x_i - \bar{x})(y_i - \bar{y})}{\left\{ \sum_{i=1}^N (x_i - \bar{x})^2 \right\}^{1/2} \left\{ \sum_{i=1}^N (y_i - \bar{y})^2 \right\}^{1/2}}$	Coefficient of linear correlation

Table 4.6 Statistical Parameters

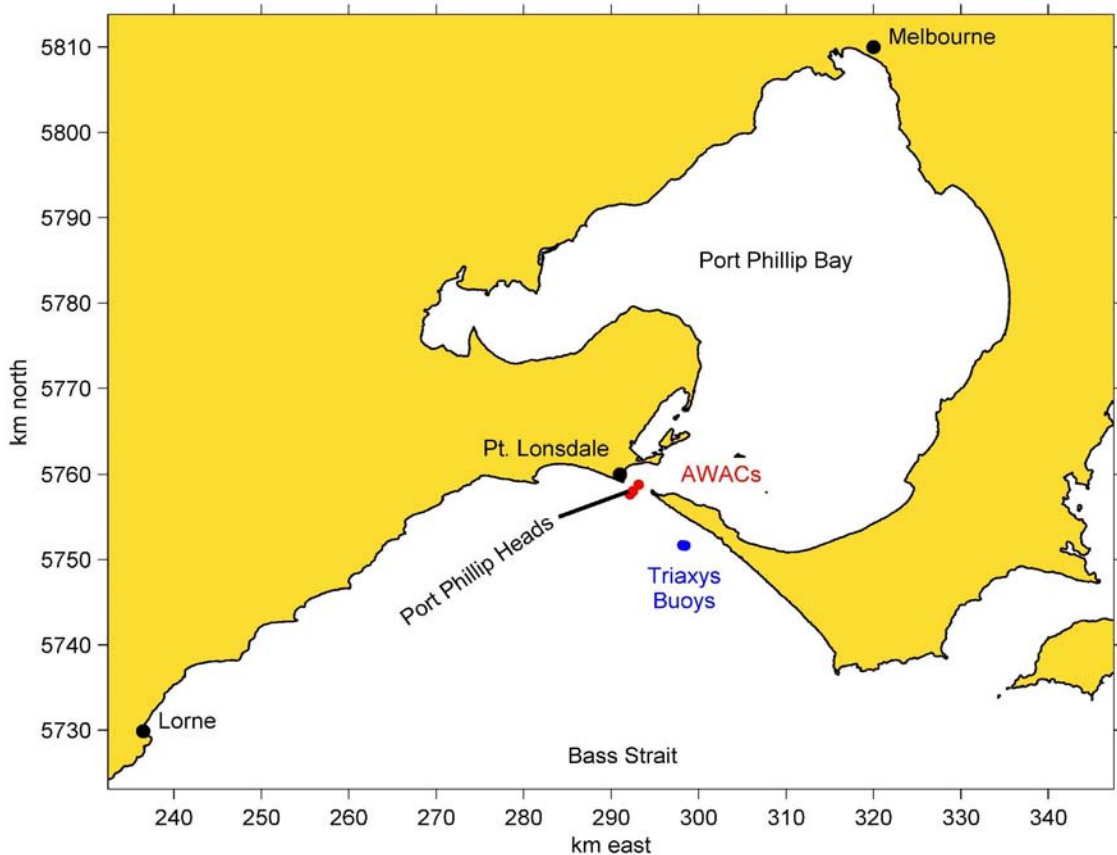
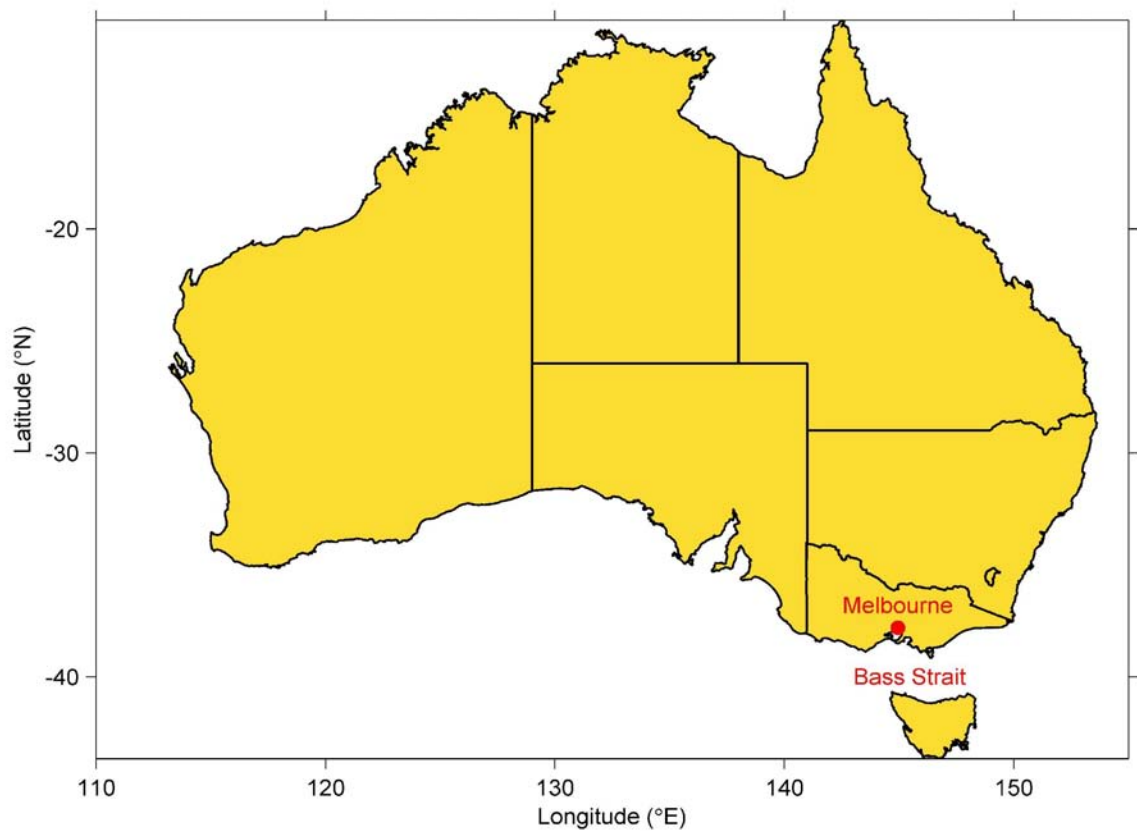
$y = ax + b$

a=slope;
b=y-intercept

$y = c.x$
 $b=0$

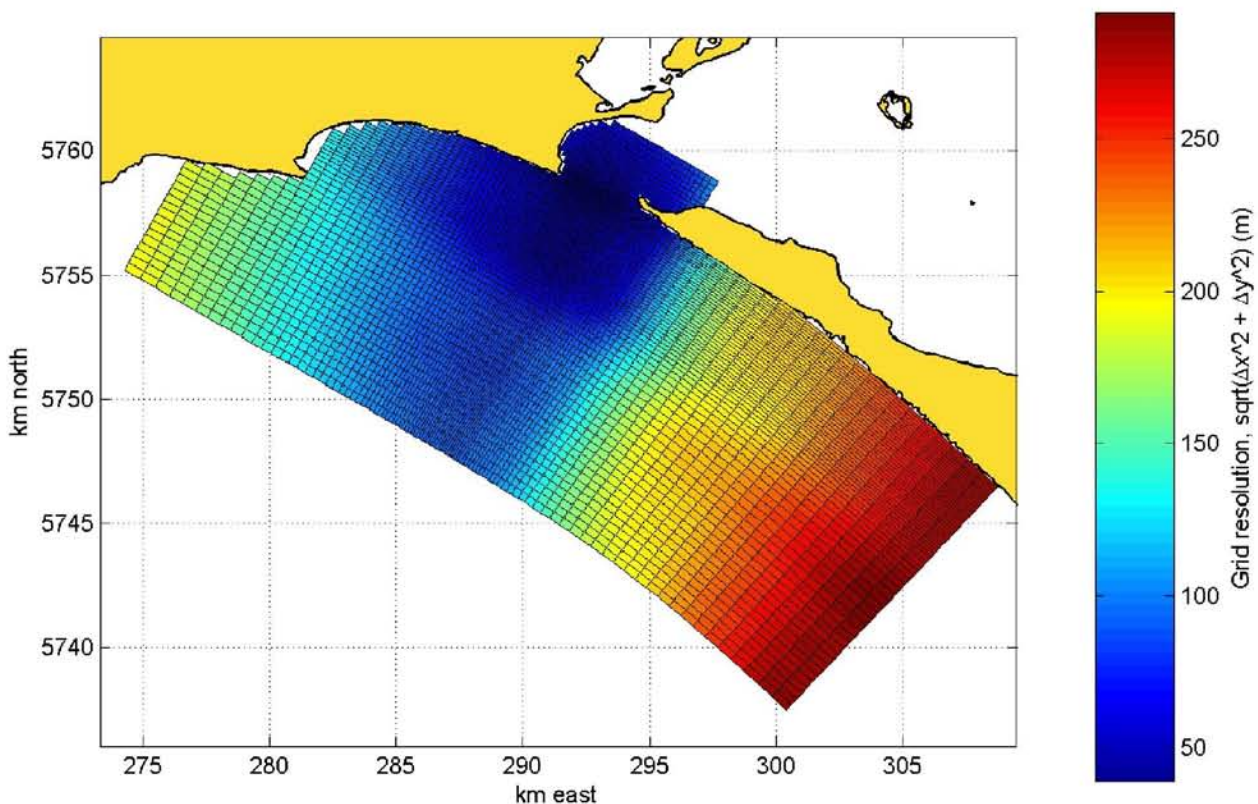
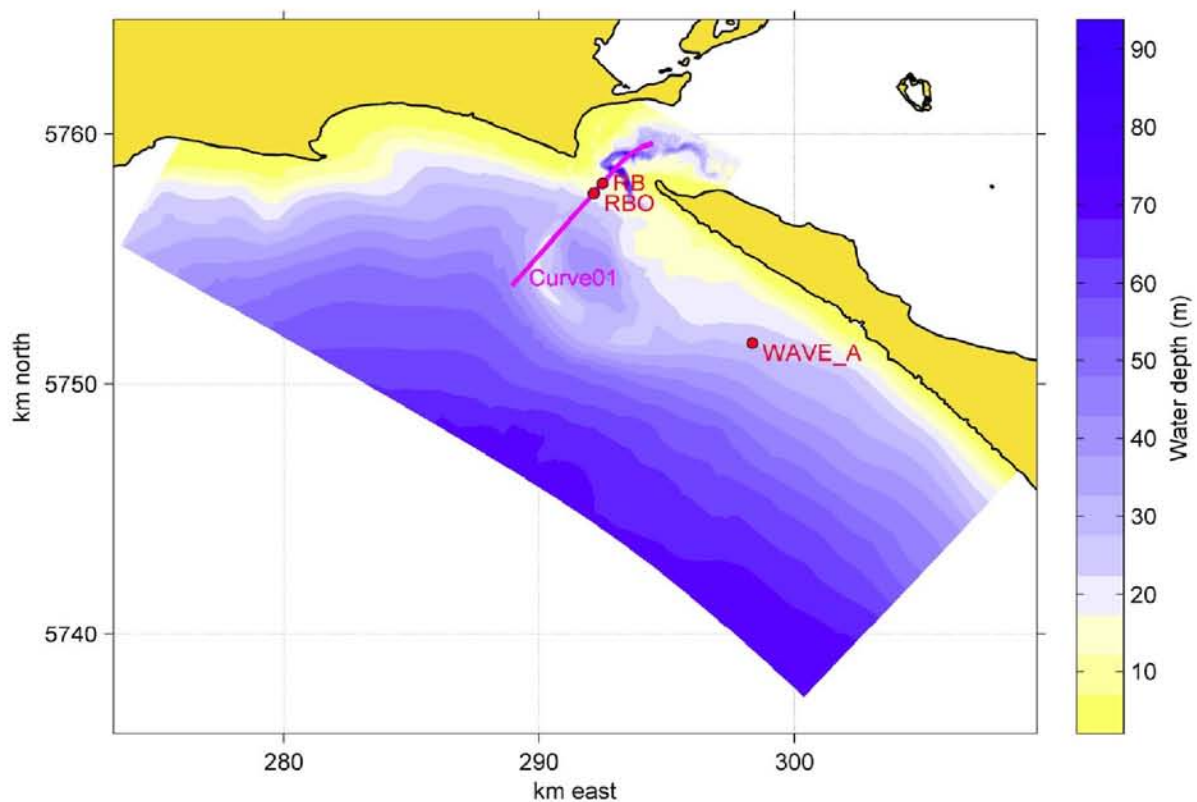
c=slope;

E Figures



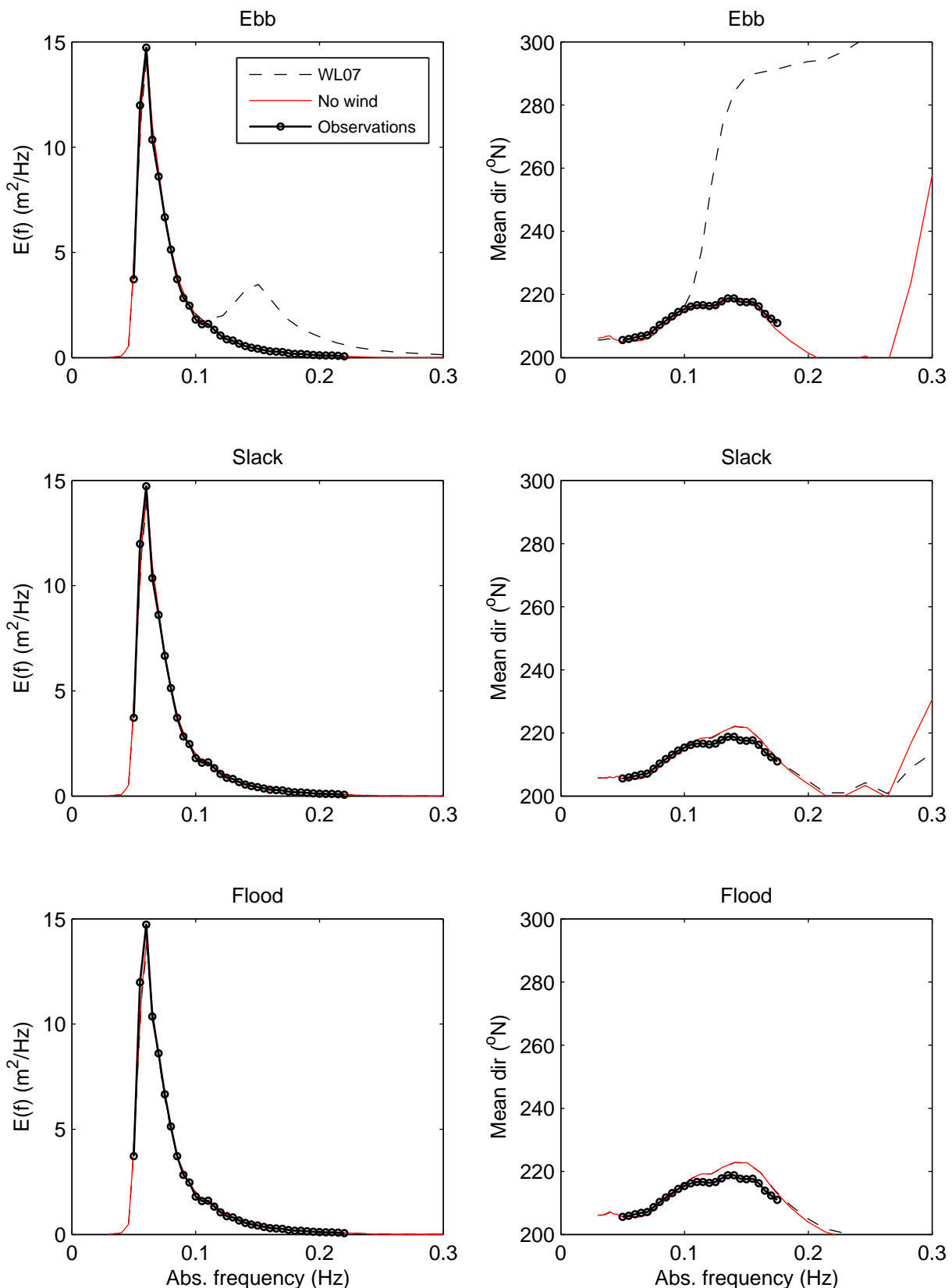
Location map of Port Phillip Bay Heads, Australia (top)
with positions of observation stations (bottom) (WL & Lesser 2007)

Wave-current interaction



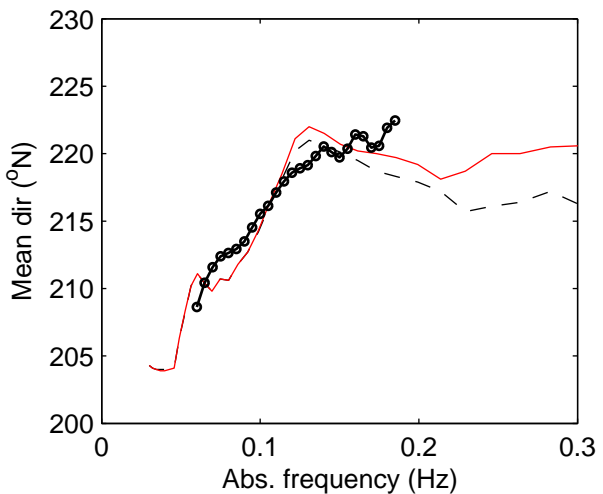
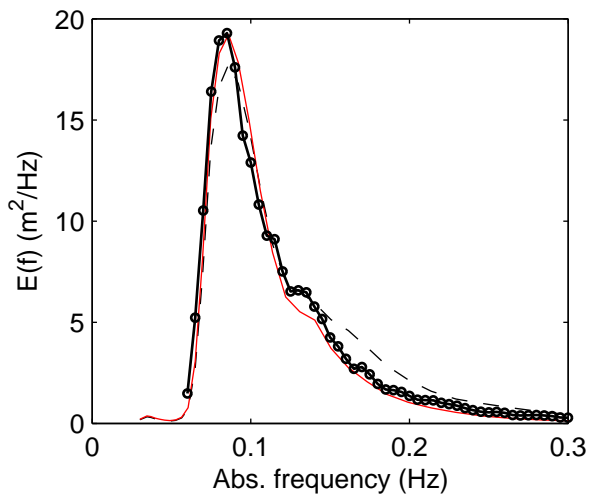
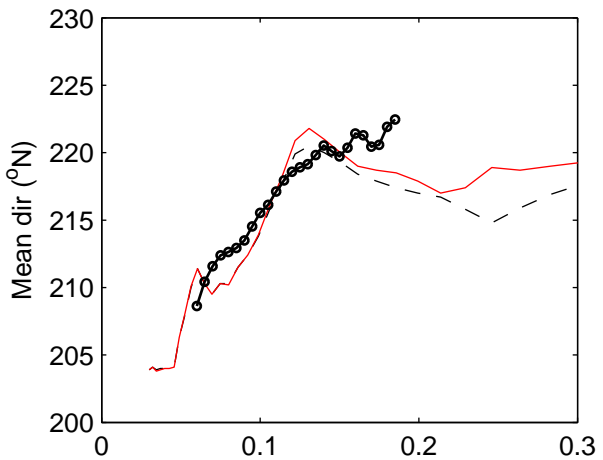
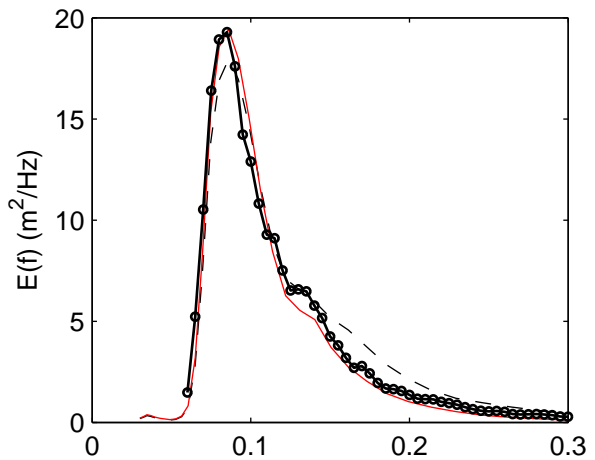
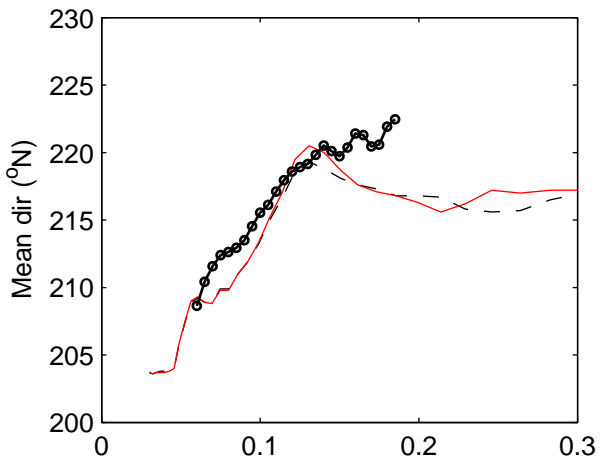
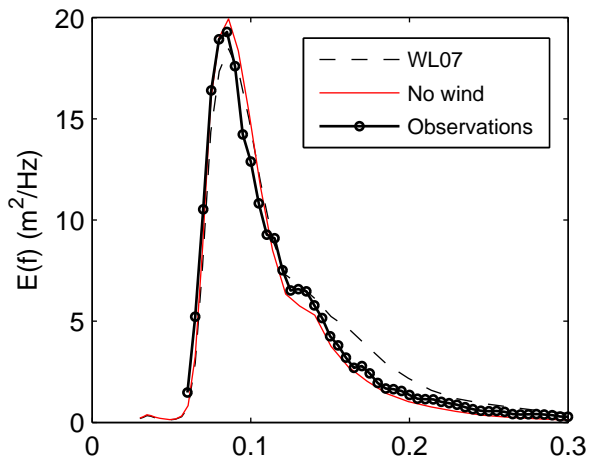
Bathymetry of Port Phillip Bay Heads, with observation stations and output curve (top), and curvilinear output curve (bottom, every 2nd line shown)
(after WL & Lesser 2007).

Wave-current interaction



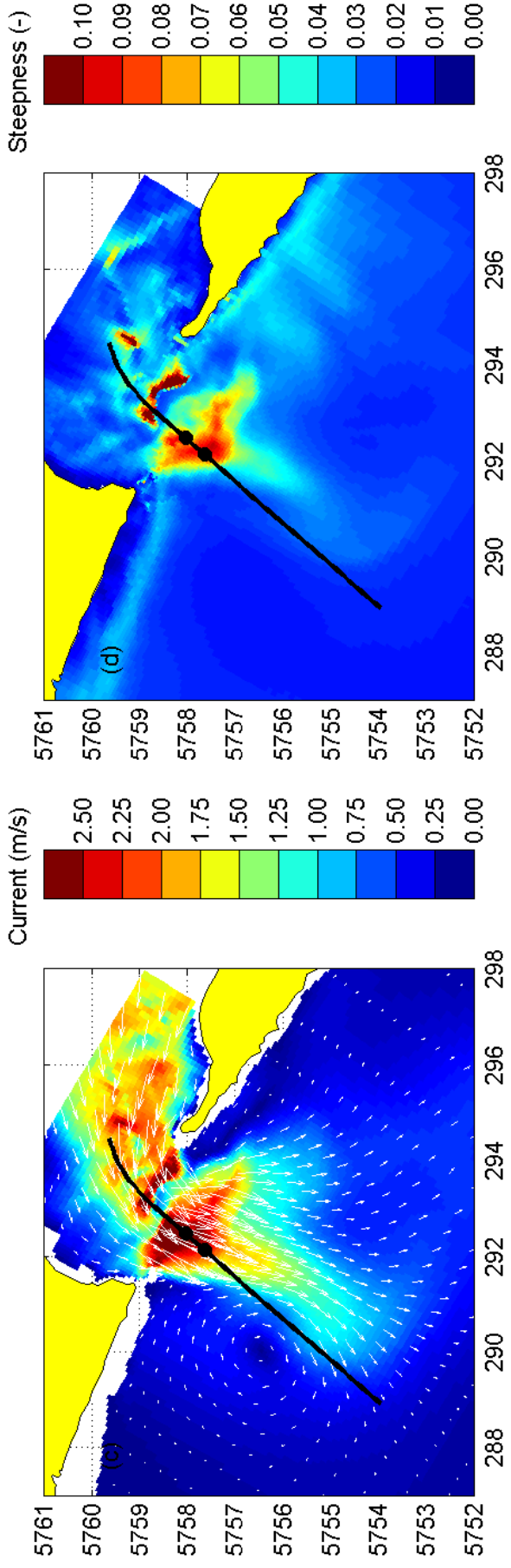
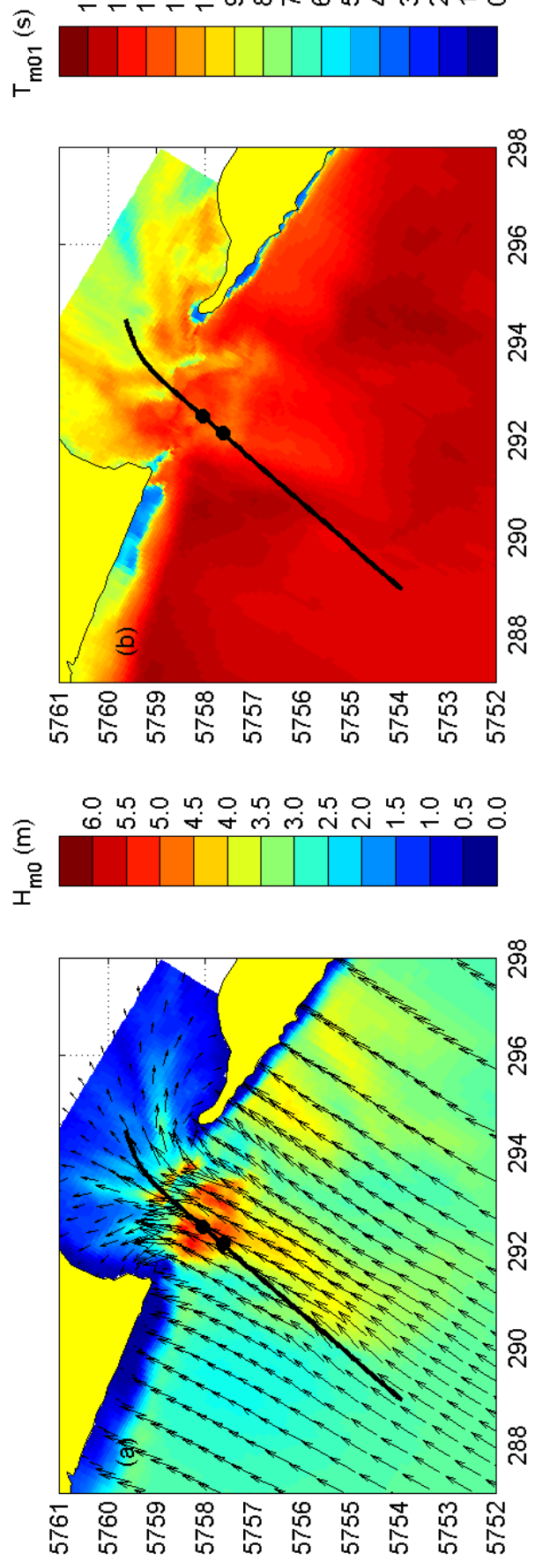
Comparison of observed and reproduced frequency spectra
at the Triaxis buoy WAVE_A, for Storm 1 (ebb, slack and flood)

Wave-current interaction



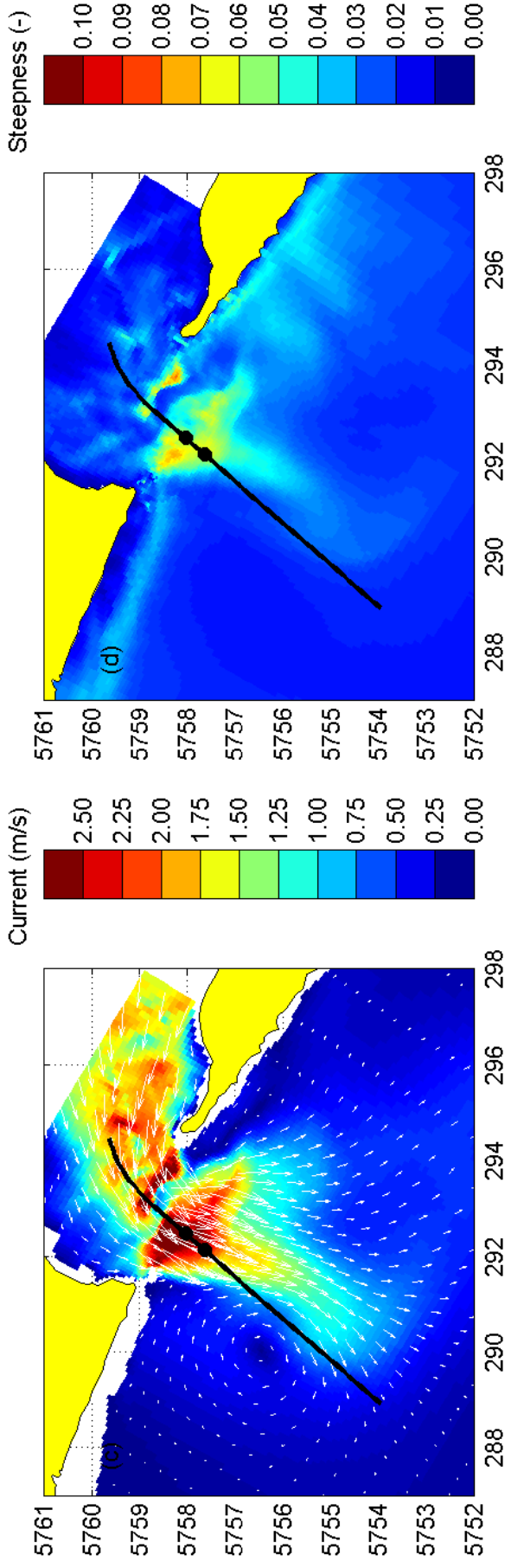
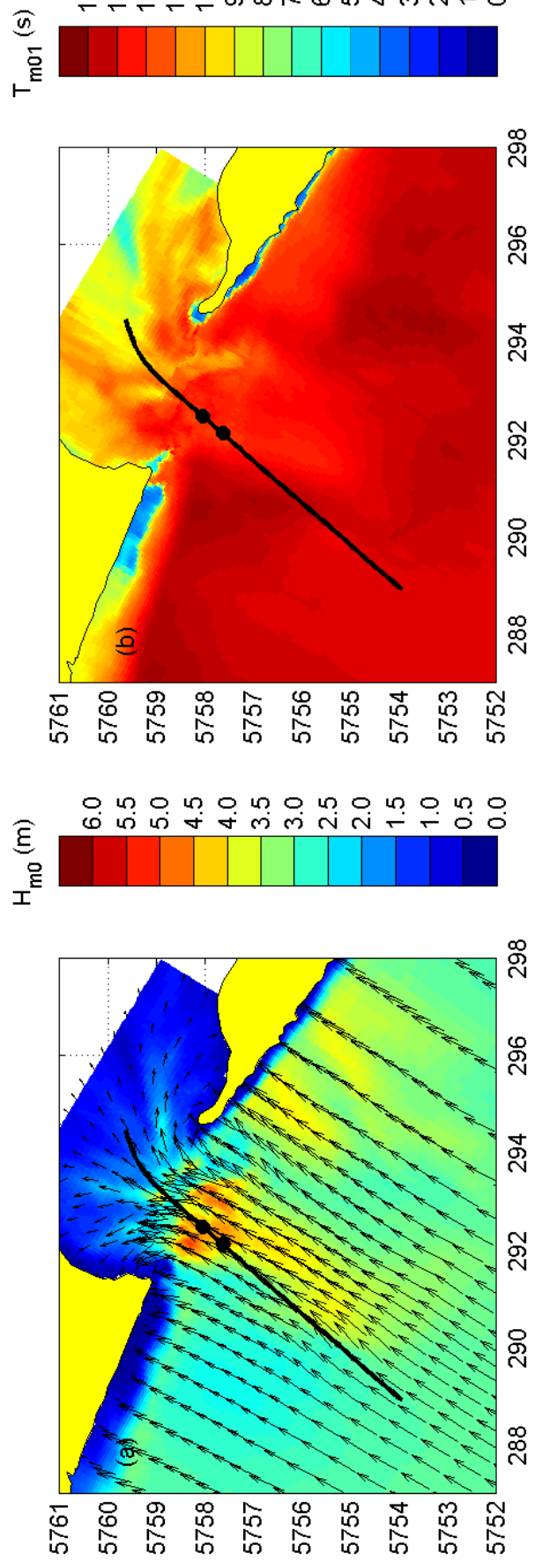
Comparison of observed and reproduced frequency spectra
at the Triaxis buoy WAVE_A, for Storm 3 (ebb, slack and flood)

Wave-current interaction



Model results for the Port Phillip Bay field case
for Storm 1: 28-Jun-2006 06:30 (ebb)
Enhanced whitecapping Cds3 = 0.00

Wave-current interaction



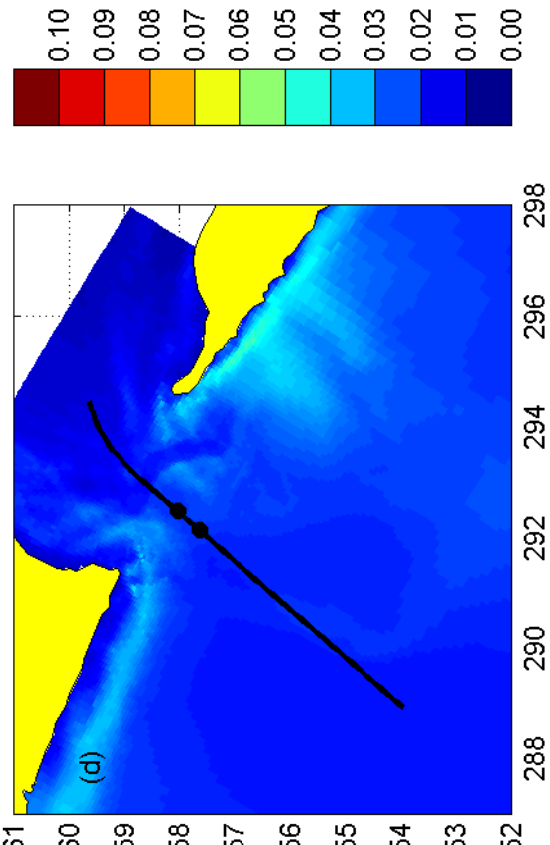
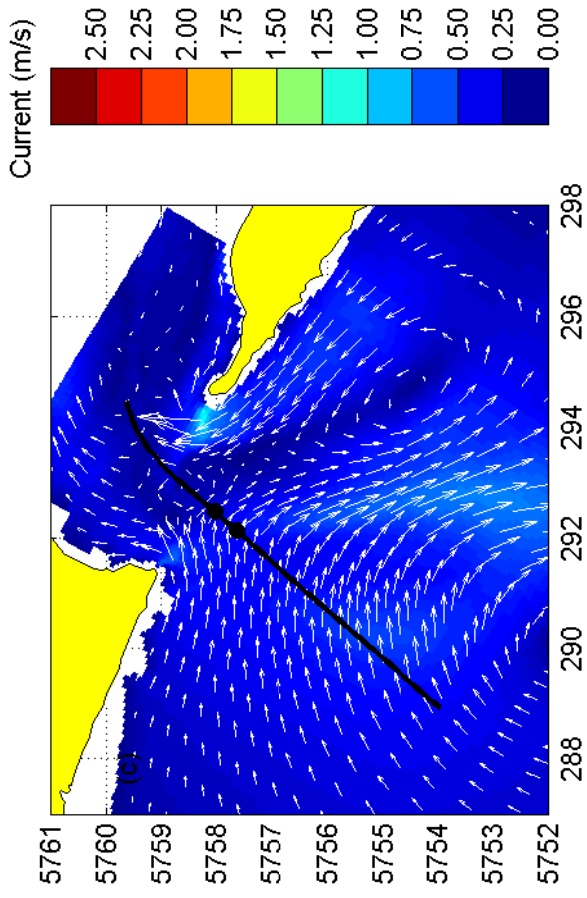
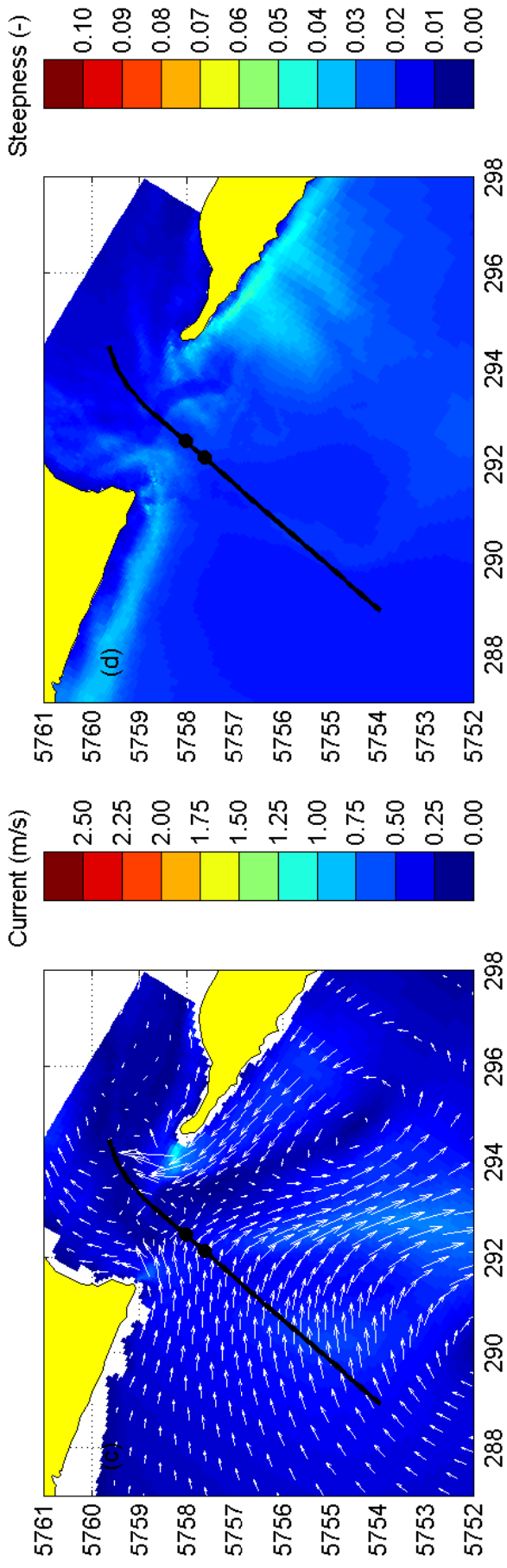
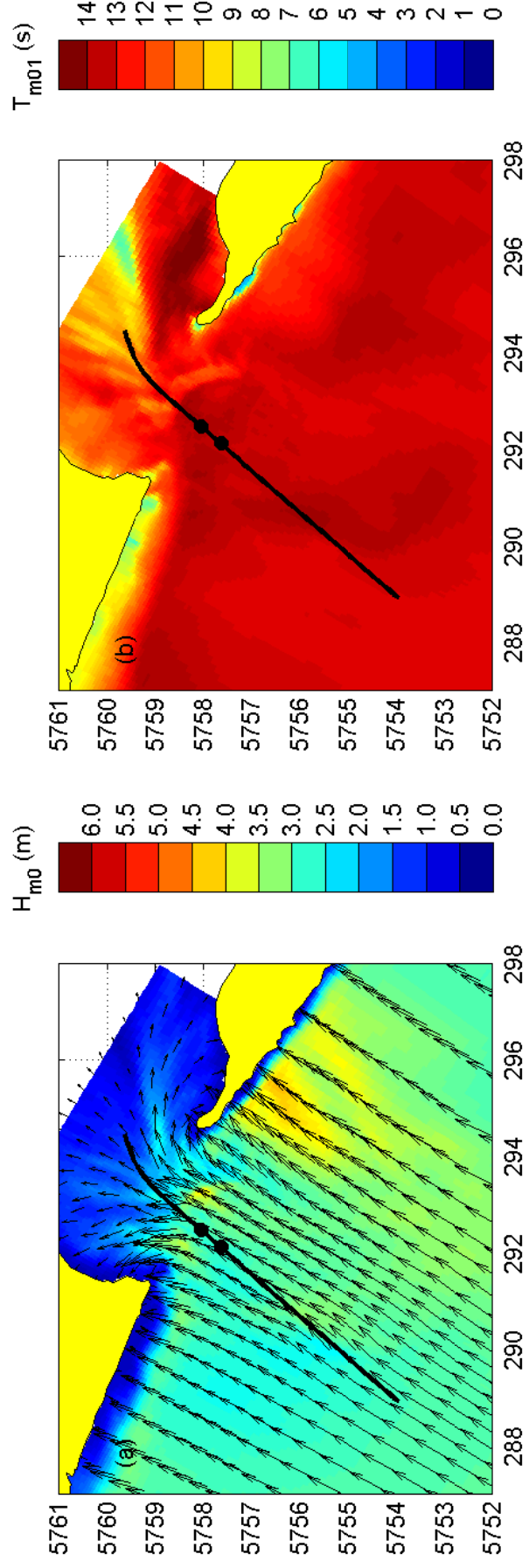
Model results for the Port Phillip Bay field case
for Storm 1: 28-Jun-2006 06:30 (ebb)
Enhanced whitecapping Cds3 = 0.80

Wave-current interaction

DELTARES

1202119.003

Fig. 3.6



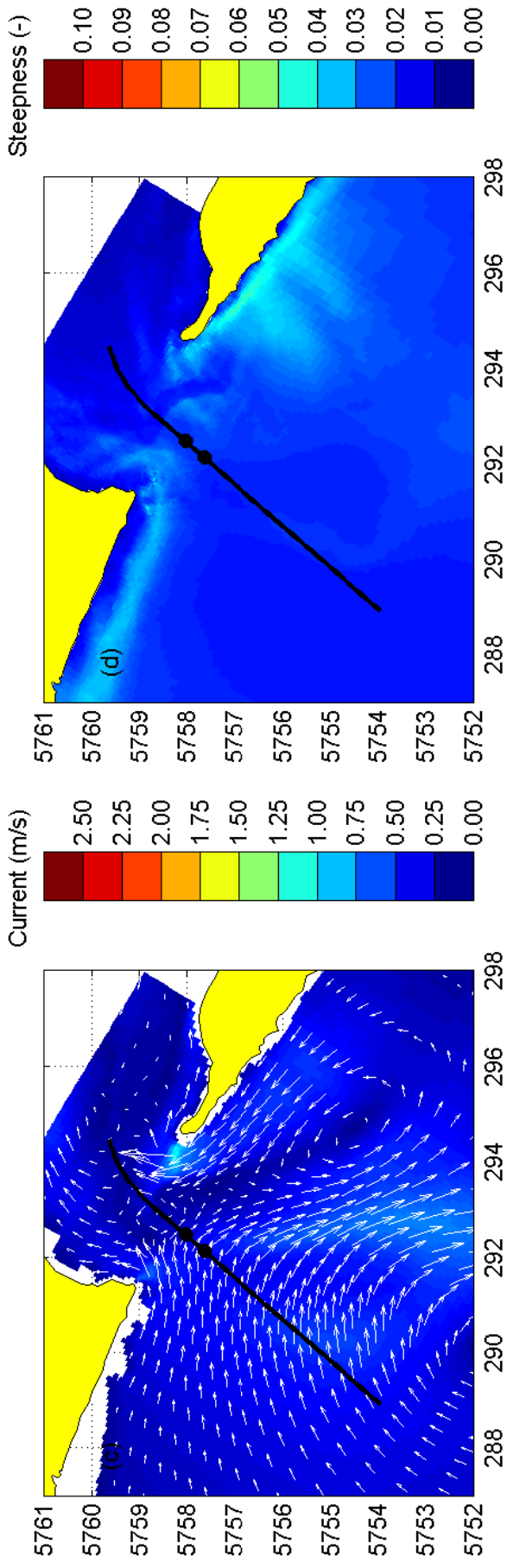
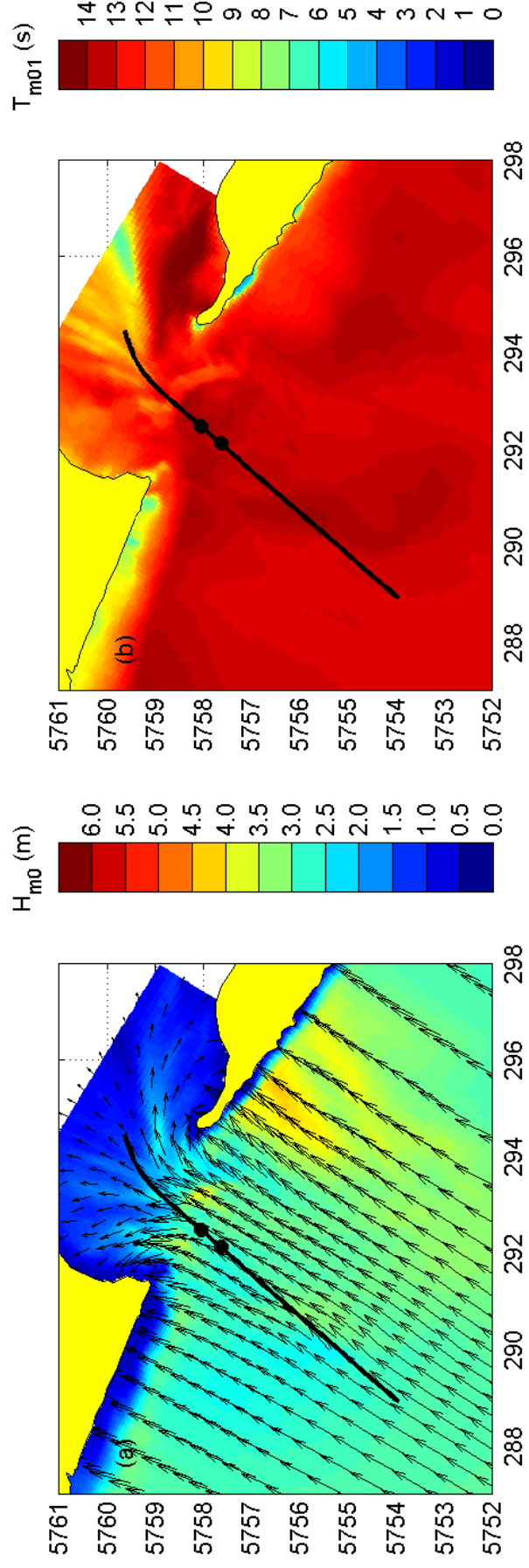
Model results for the Port Phillip Bay field case
for Storm 1: 28-Jun-2006 10:30 (slack)
Enhanced whitecapping Cds3 = 0.00

Wave-current interaction

DELTARES

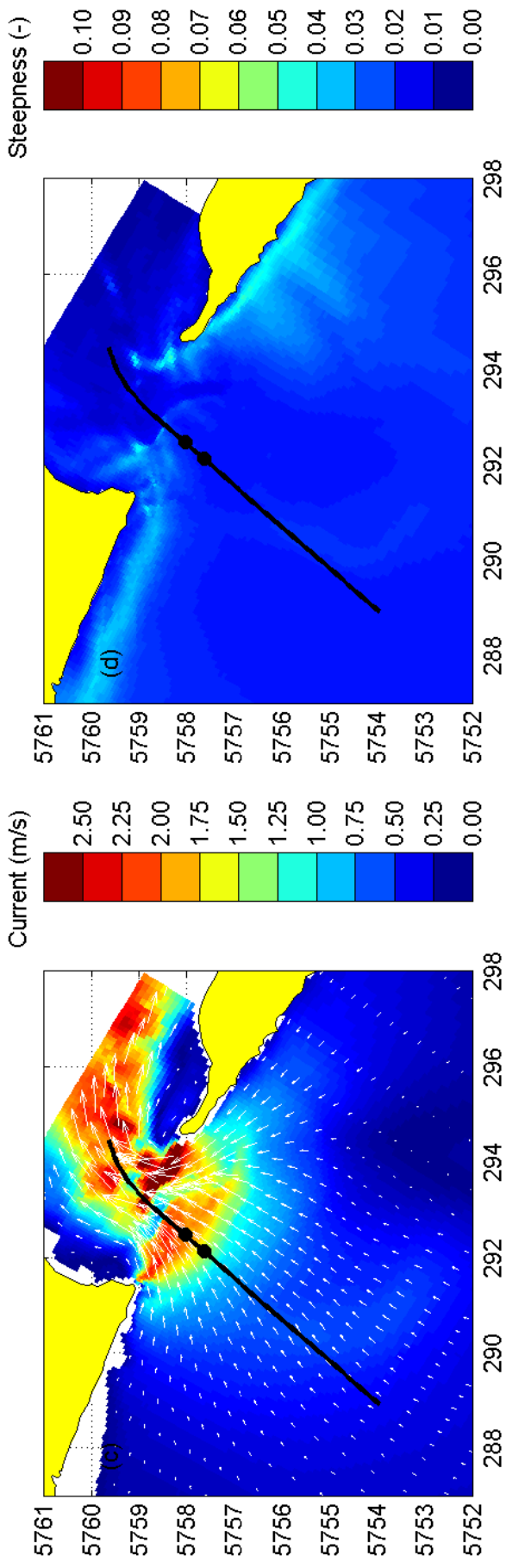
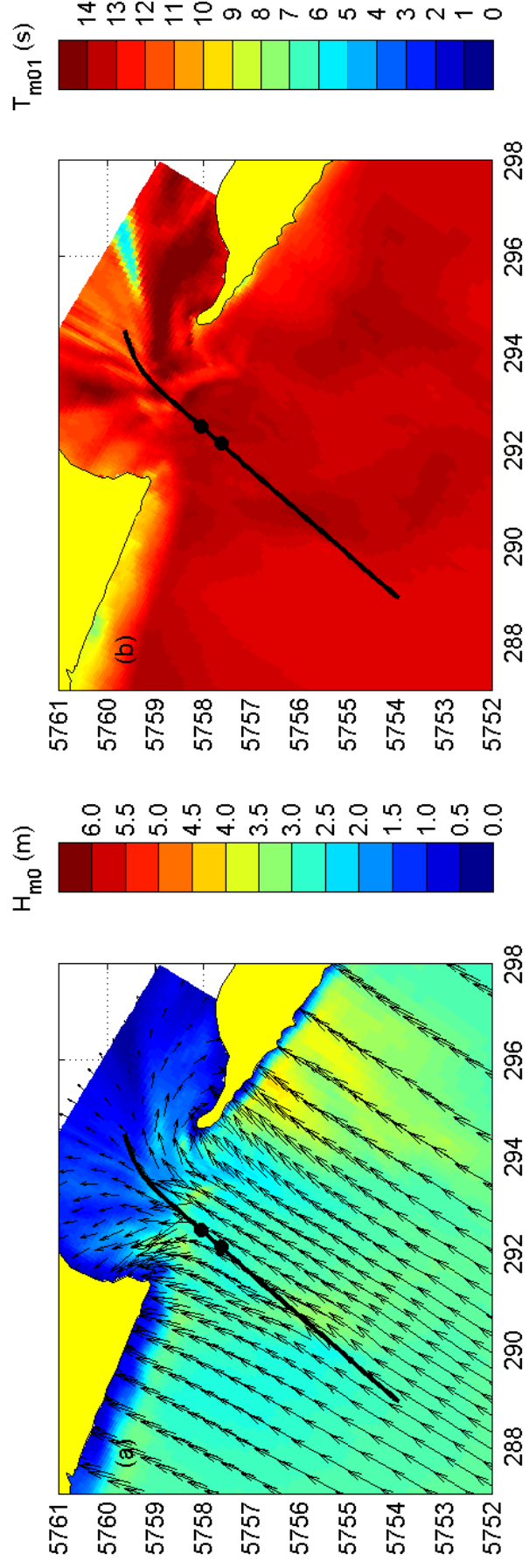
1202119.003

Fig. 3.7



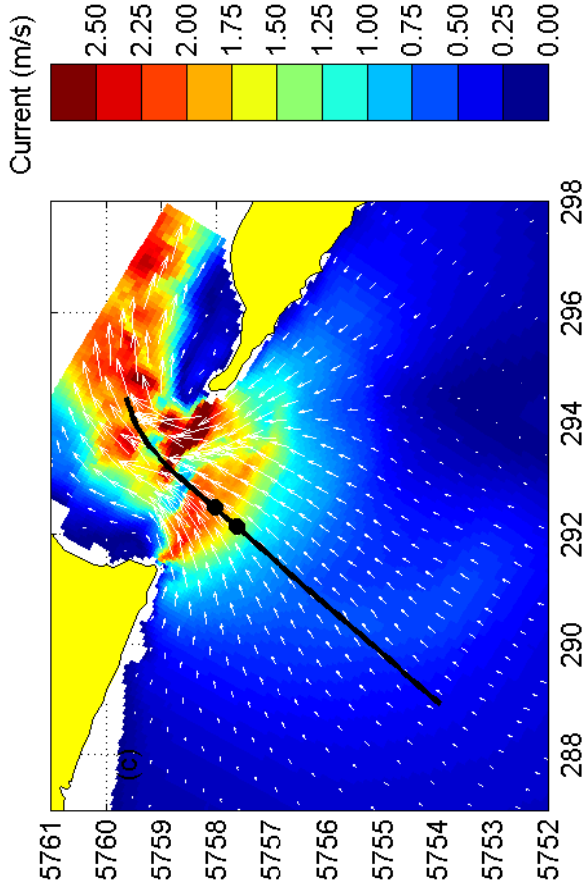
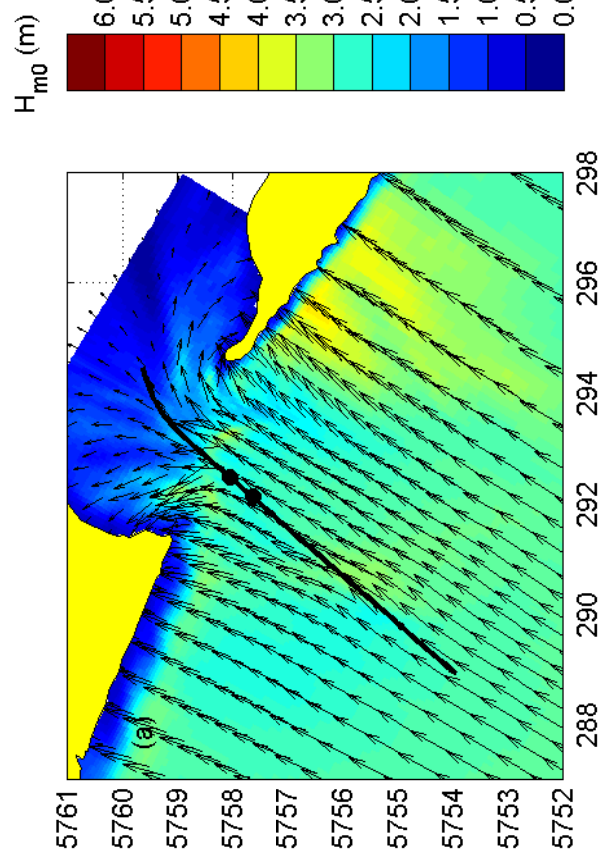
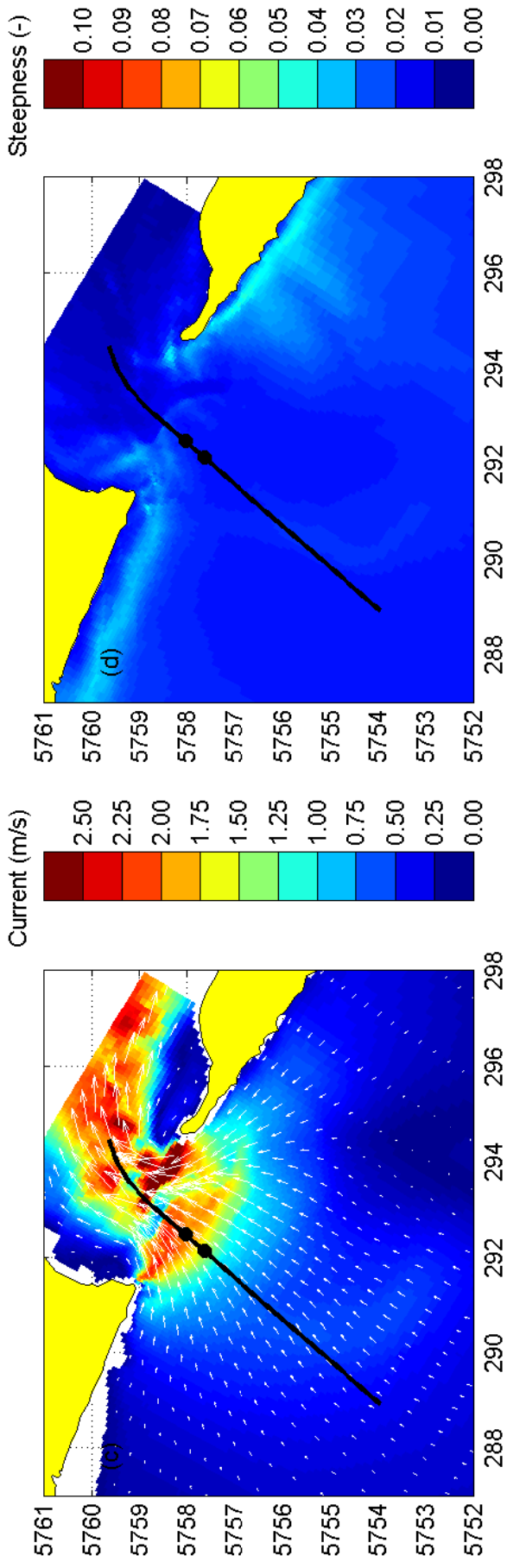
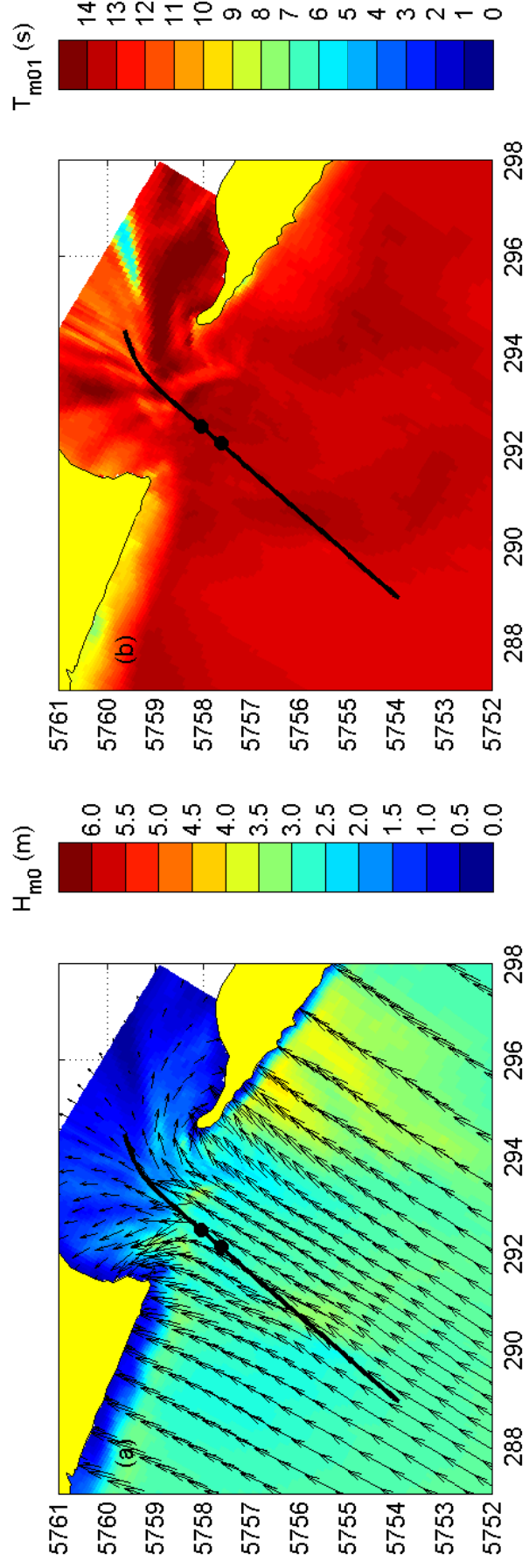
Model results for the Port Phillip Bay field case
 for Storm 1: 28-Jun-2006 10:30 (slack)
 Enhanced whitecapping Cds3 = 0.80

Wave-current interaction



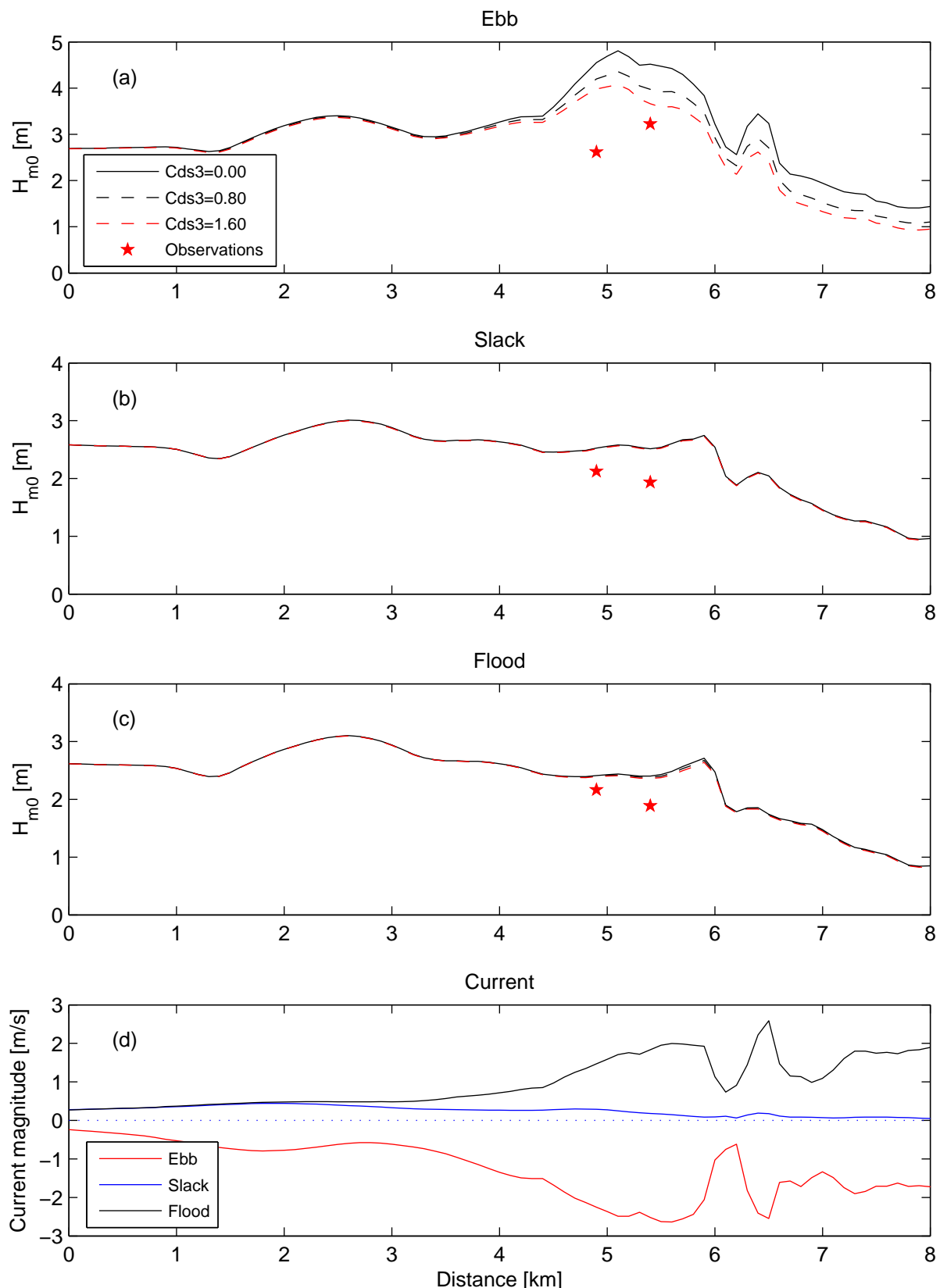
Model results for the Port Phillip Bay field case
 for Storm 1: 28-Jun-2006 14:00 (flood)
 Enhanced whitecapping Cds3 = 0.00

Wave-current interaction



Model results for the Port Phillip Bay field case
for Storm 1: 28-Jun-2006 14:00 (flood)
Enhanced whitecapping Cds3 = 0.80

Wave-current interaction



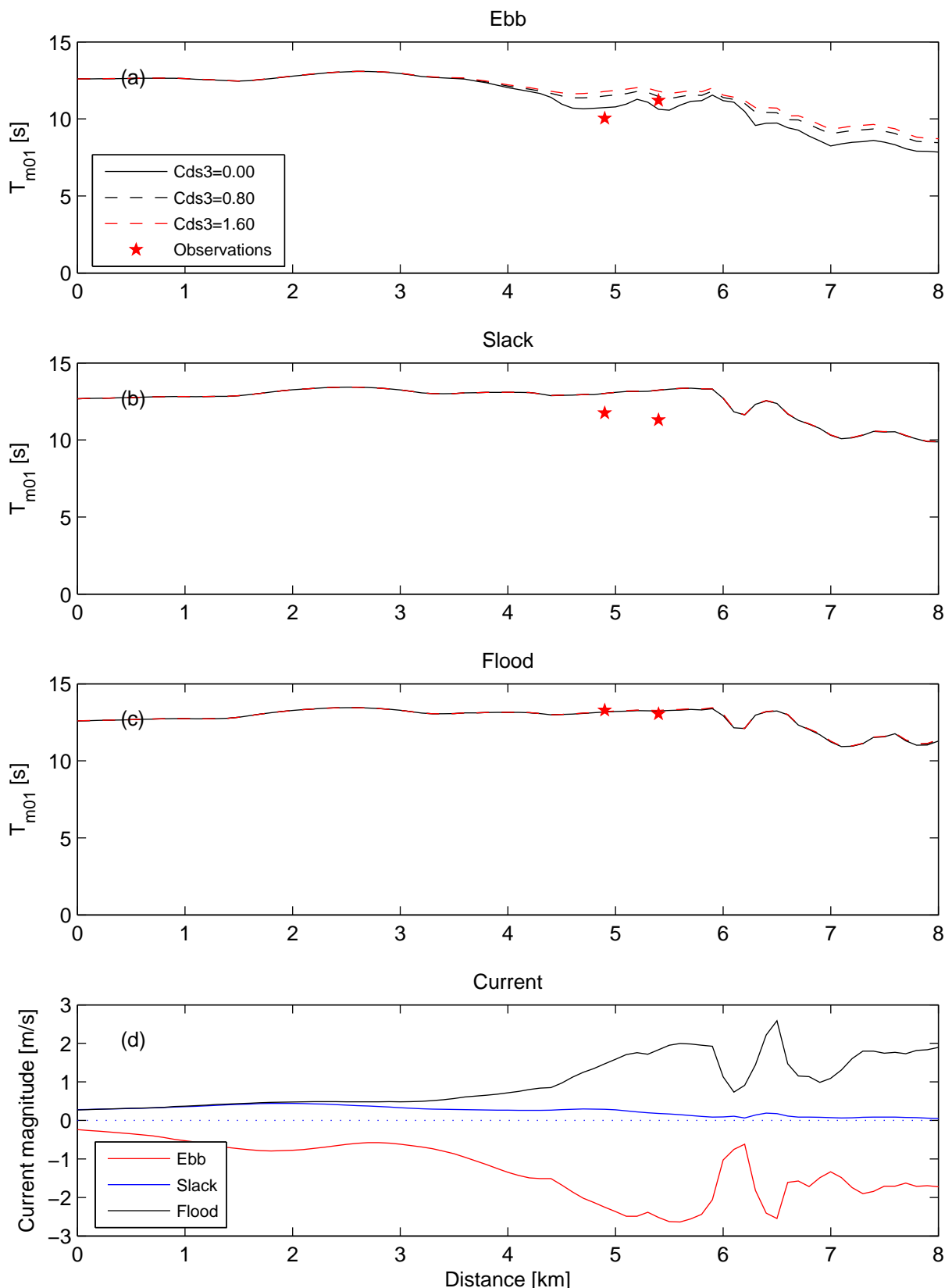
Model results of H_{m0} for the Port Phillip Bay field case
for Storm 1 (ebb, slack and flood)

Wave-current interaction

DELTARES

1202119.003

Fig. 3.11



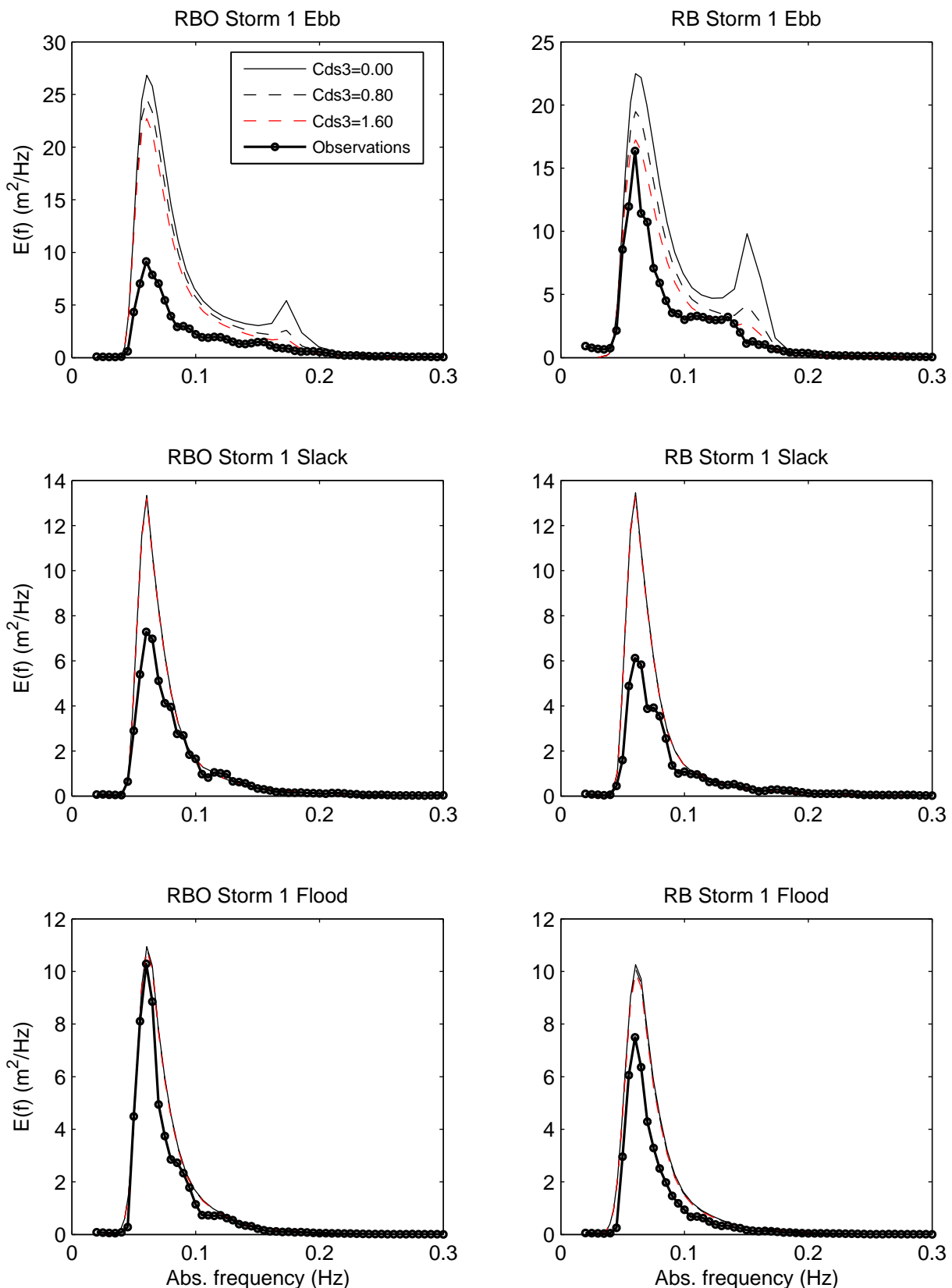
Model results of T_{m01} for the Port Phillip Bay field case
for Storm 1 (ebb, slack and flood)

Wave-current interaction

DELTARES

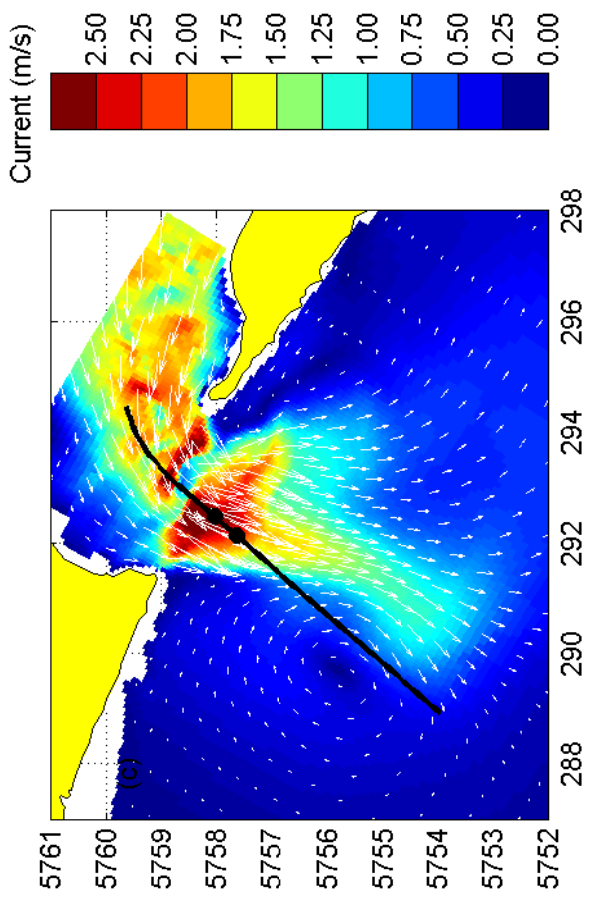
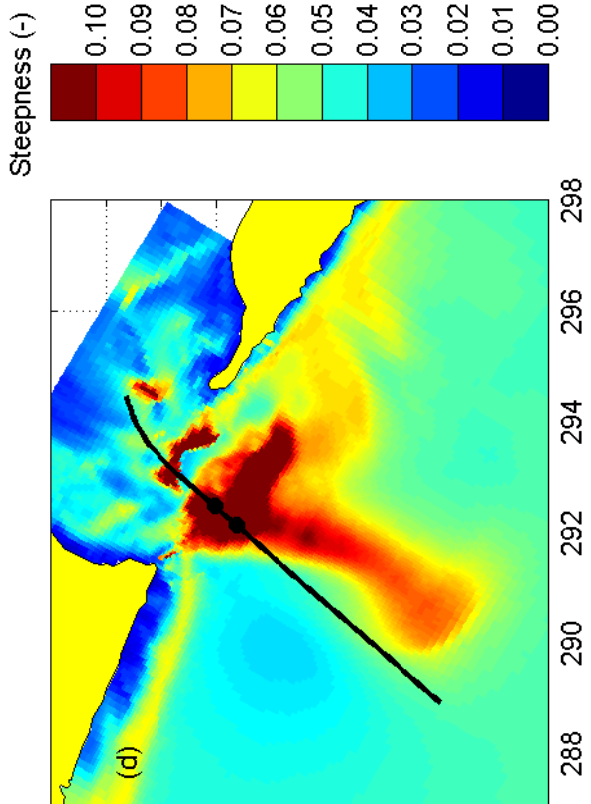
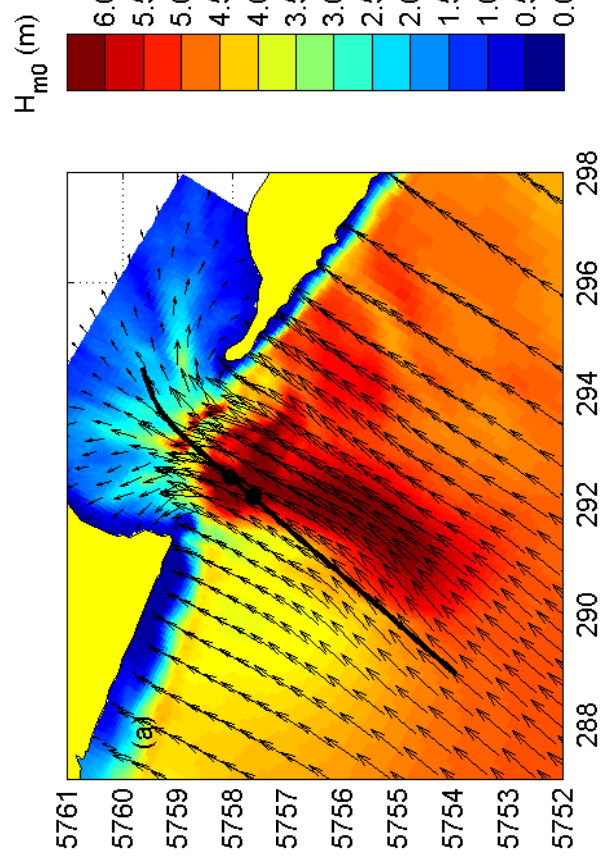
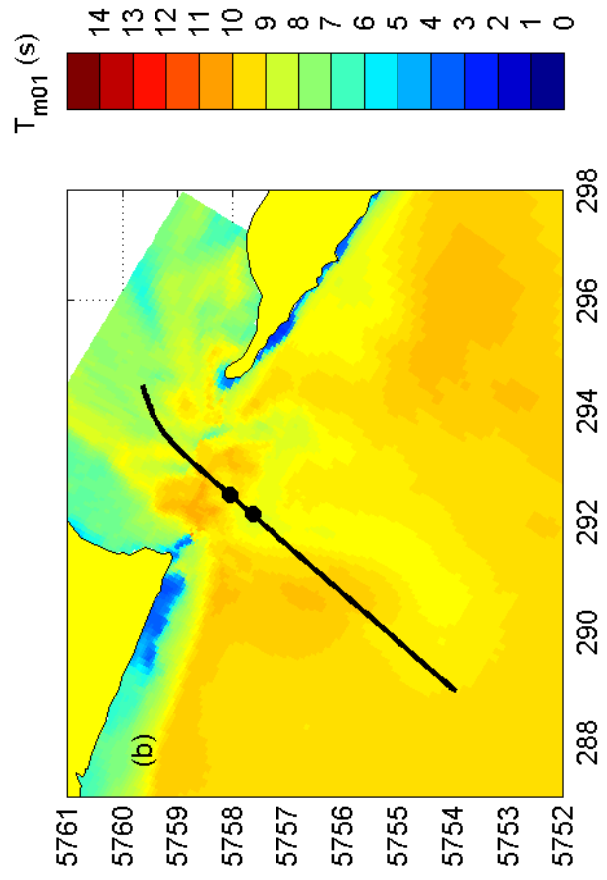
1202119.003

Fig. 3.12



Model results for the Port Phillip Bay field case spectra for Storm 1 (ebb, slack and flood)

Wave-current interaction



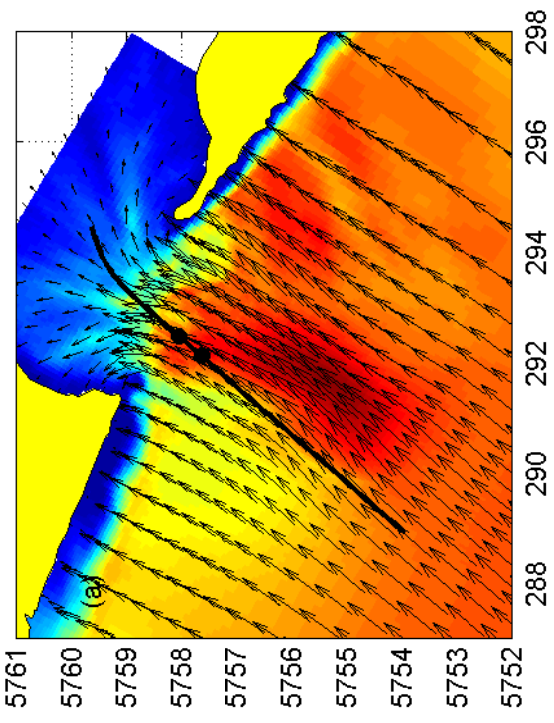
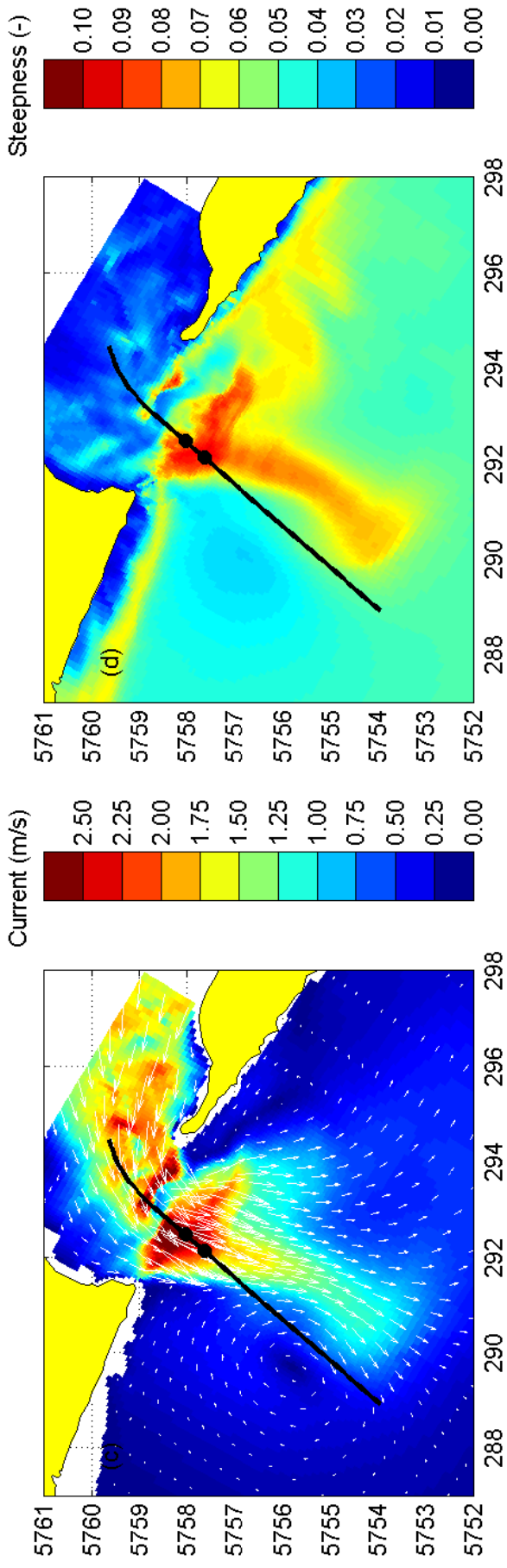
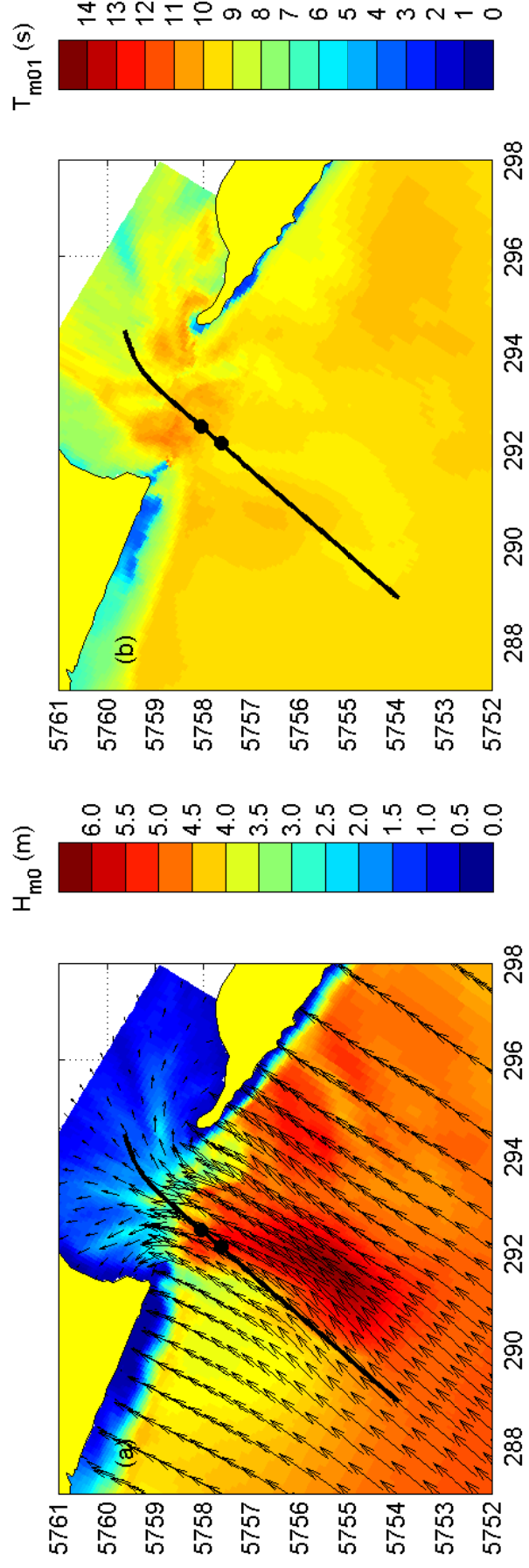
Model results for the Port Phillip Bay field case
for Storm 3: 27-Oct-2006 20:30 (ebb)
Enhanced whitecapping Cds3 = 0.00

Wave-current interaction

DELTARES

1202119.003

Fig. 3.14



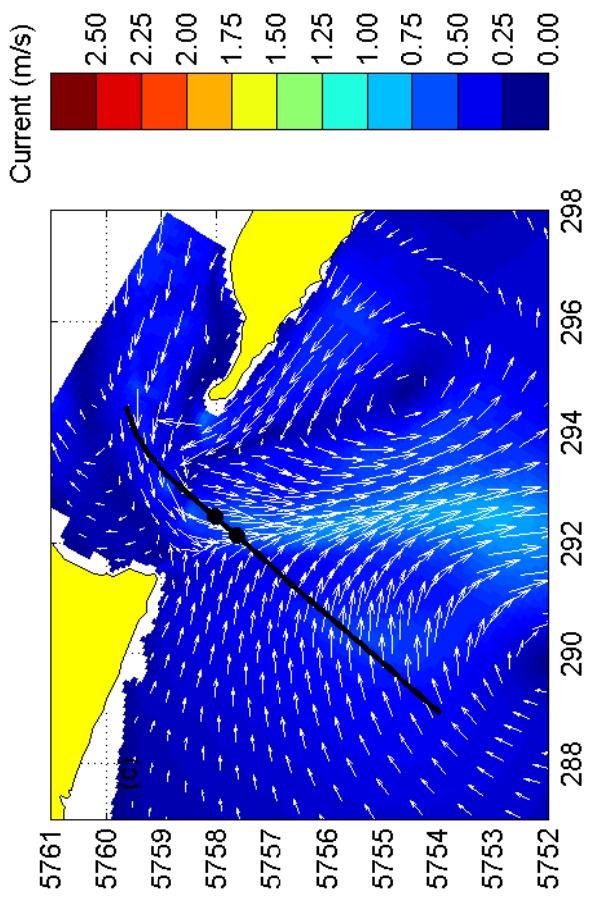
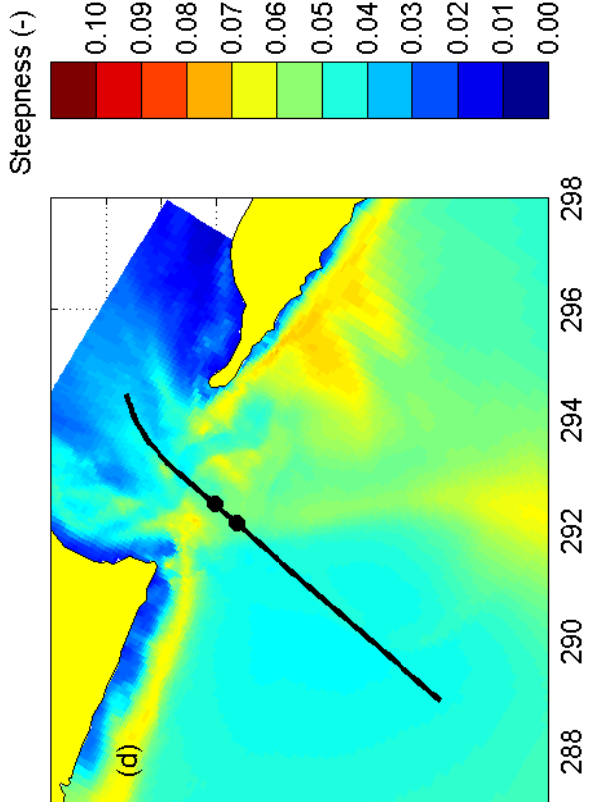
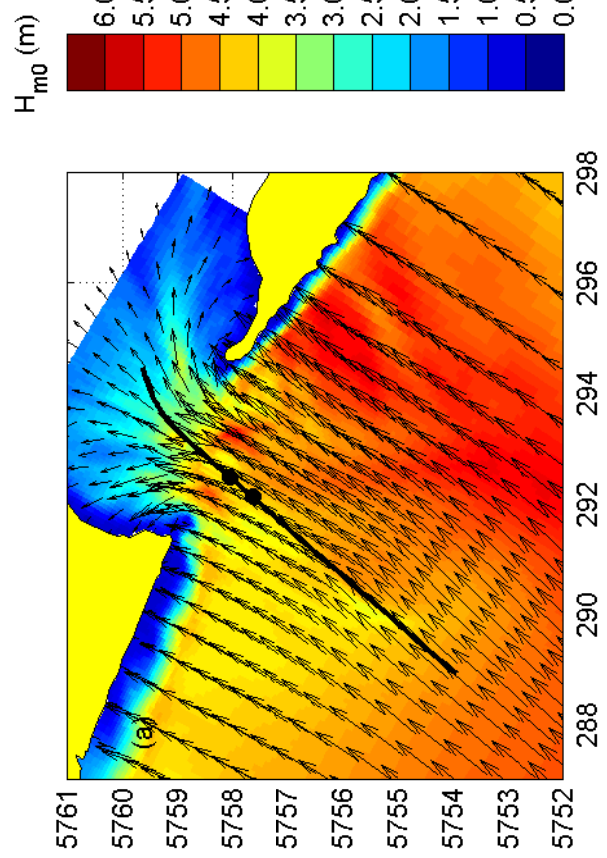
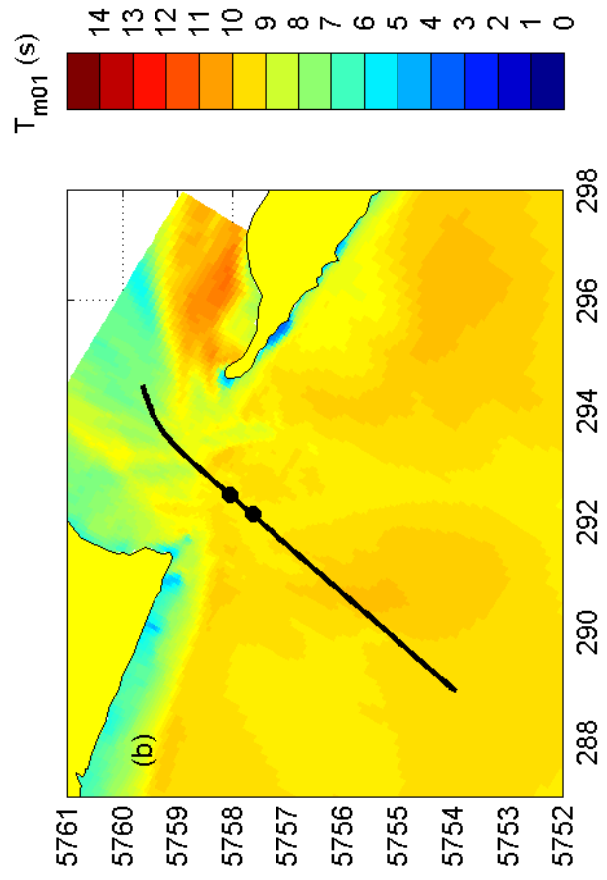
Model results for the Port Phillip Bay field case
for Storm 3: 27-Oct-2006 20:30 (ebb)
Enhanced whitecapping Cds3 = 0.80

Wave-current interaction

DELTARES

1202119.003

Fig. 3.15



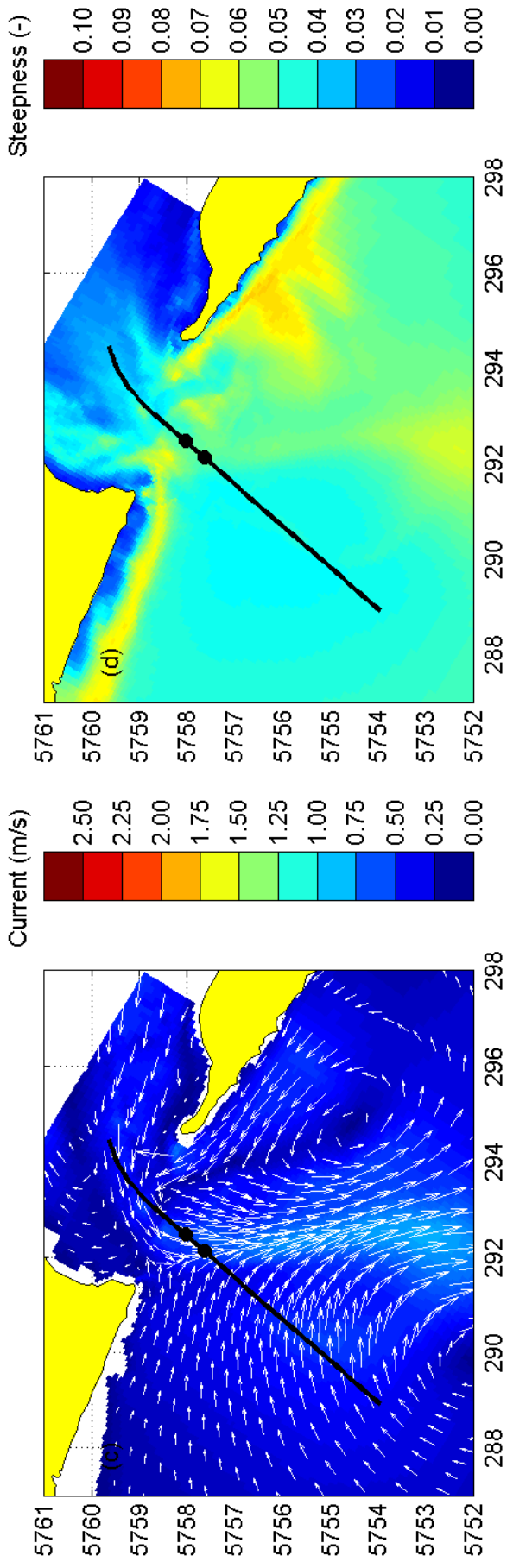
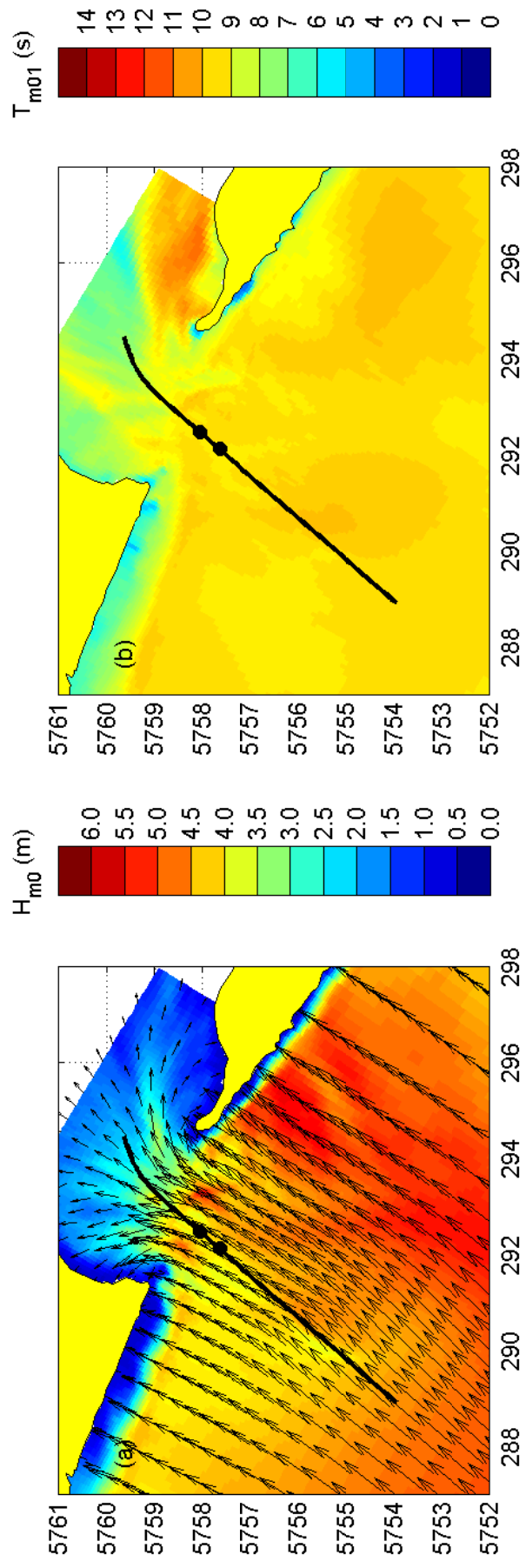
Model results for the Port Phillip Bay field case
for Storm 3: 27-Oct-2006 23:30 (slack)
Enhanced whitecapping Cds3 = 0.00

Wave-current interaction

DELTARES

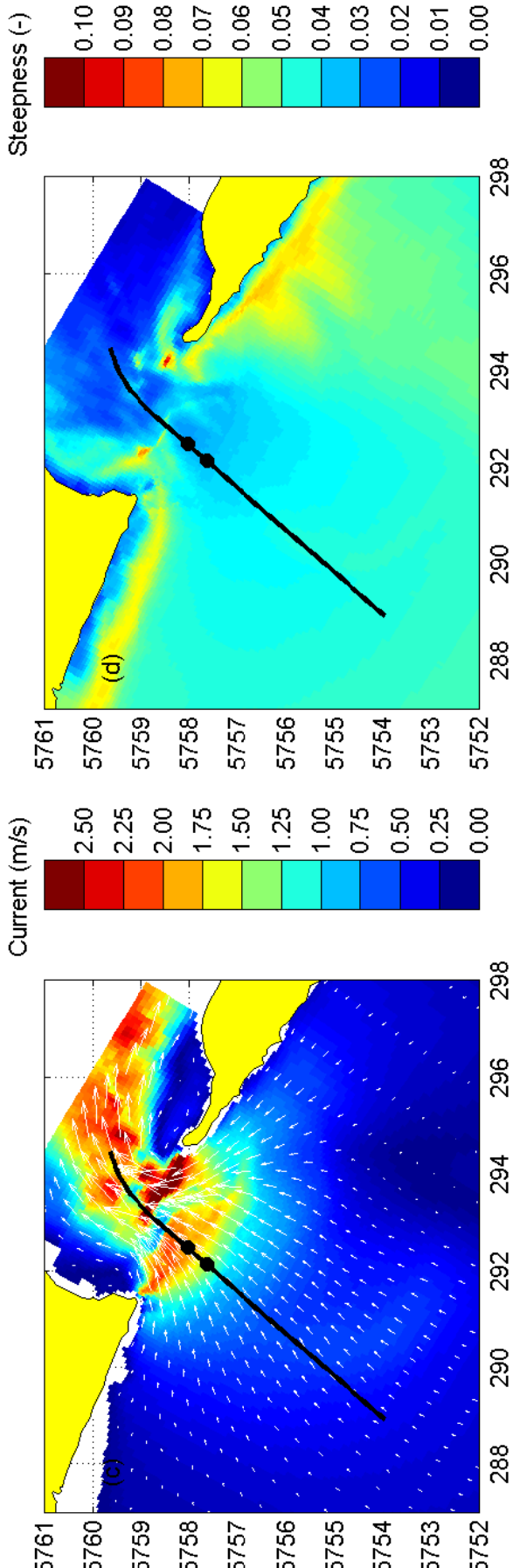
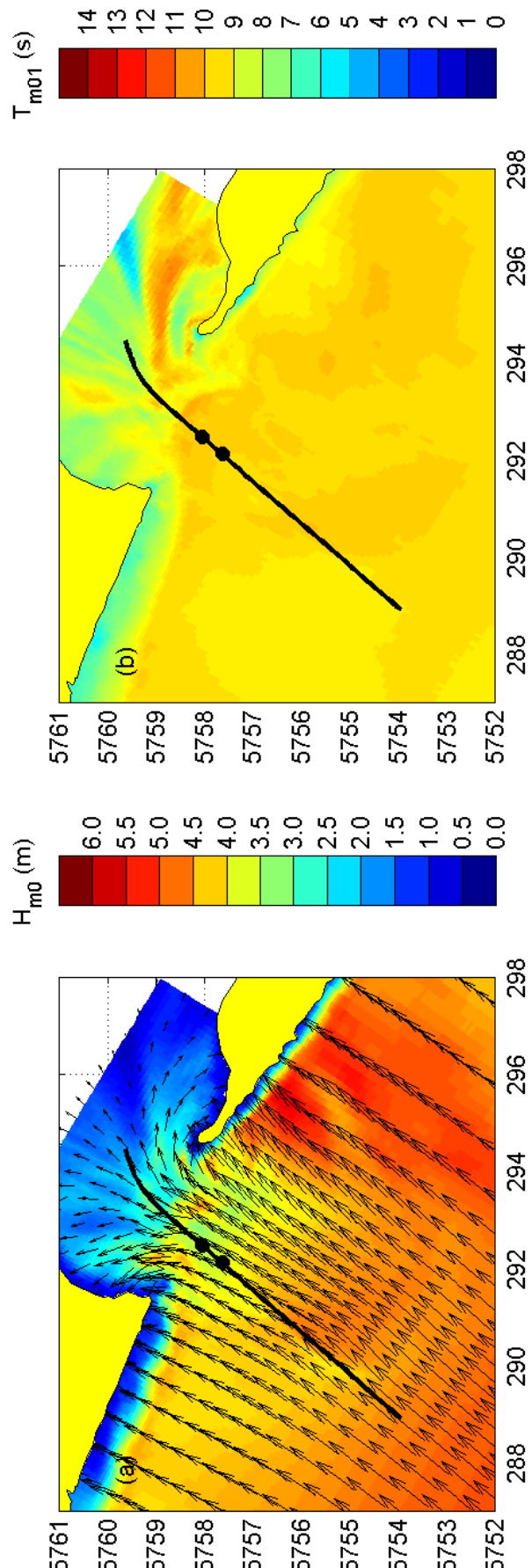
1202119.003

Fig. 3.16



Model results for the Port Phillip Bay field case
for Storm 3: 27-Oct-2006 23:30 (slack)
Enhanced whitecapping Cds3 = 0.80

Wave-current interaction



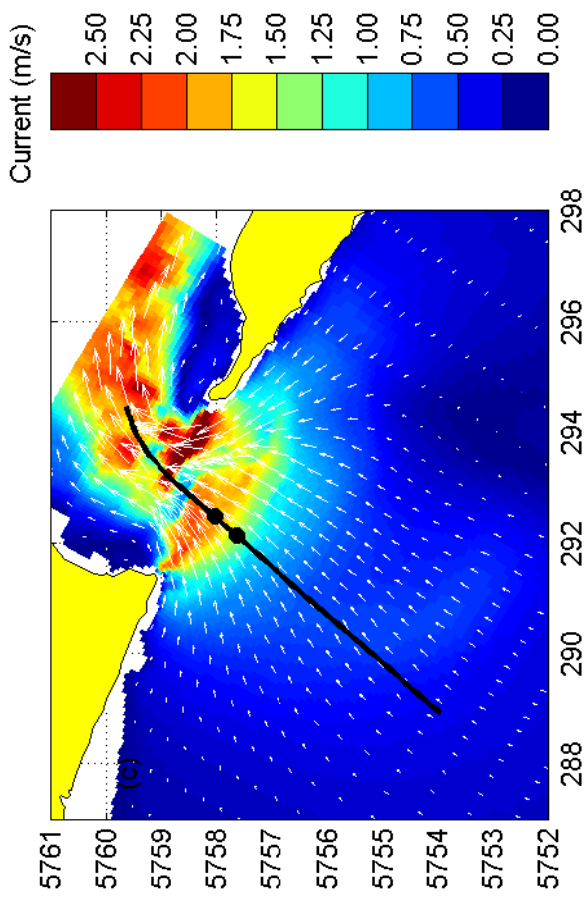
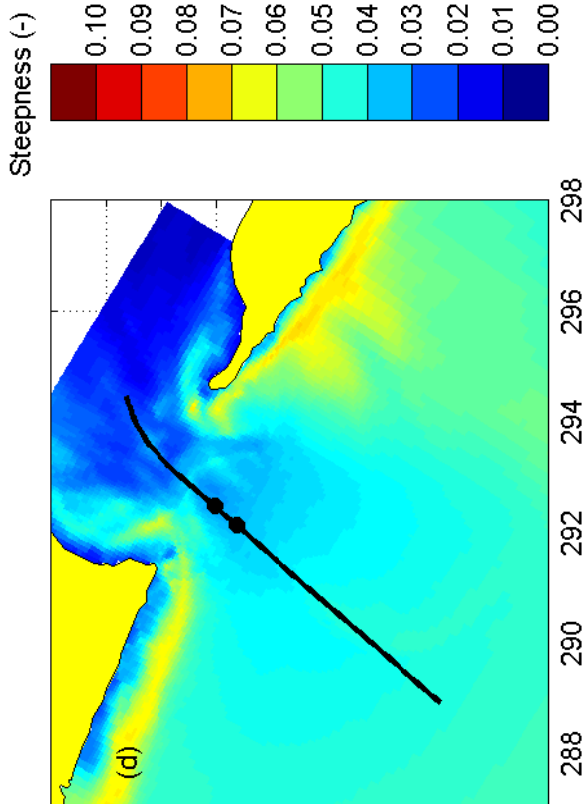
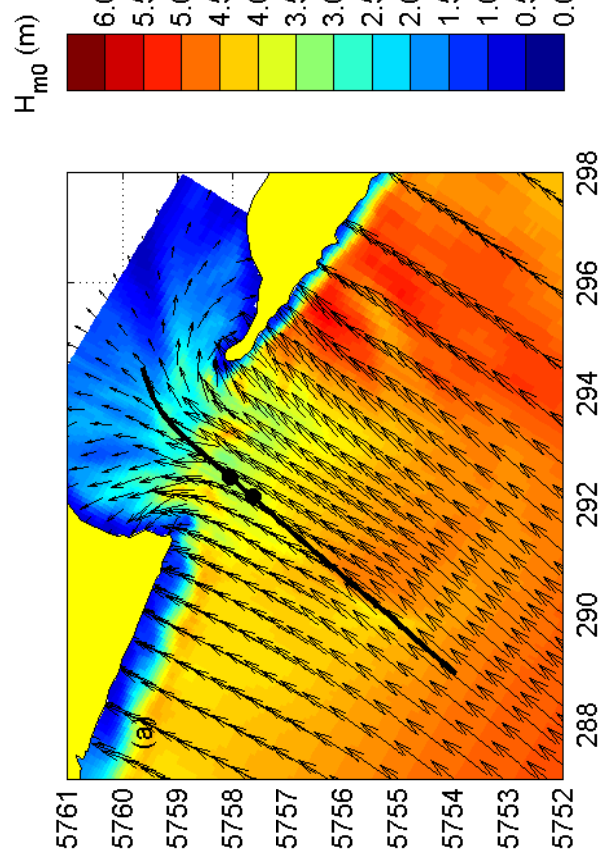
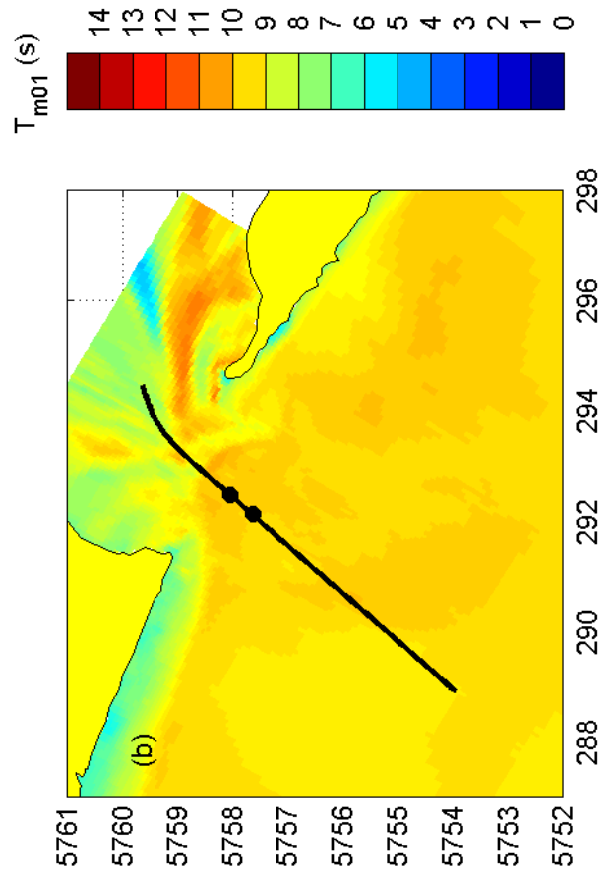
Model results for the Port Phillip Bay field case
for Storm 3: 28-Oct-2006 03:30 (flood)
Enhanced whitecapping Cds3 = 0.00

Wave-current interaction

DELTARES

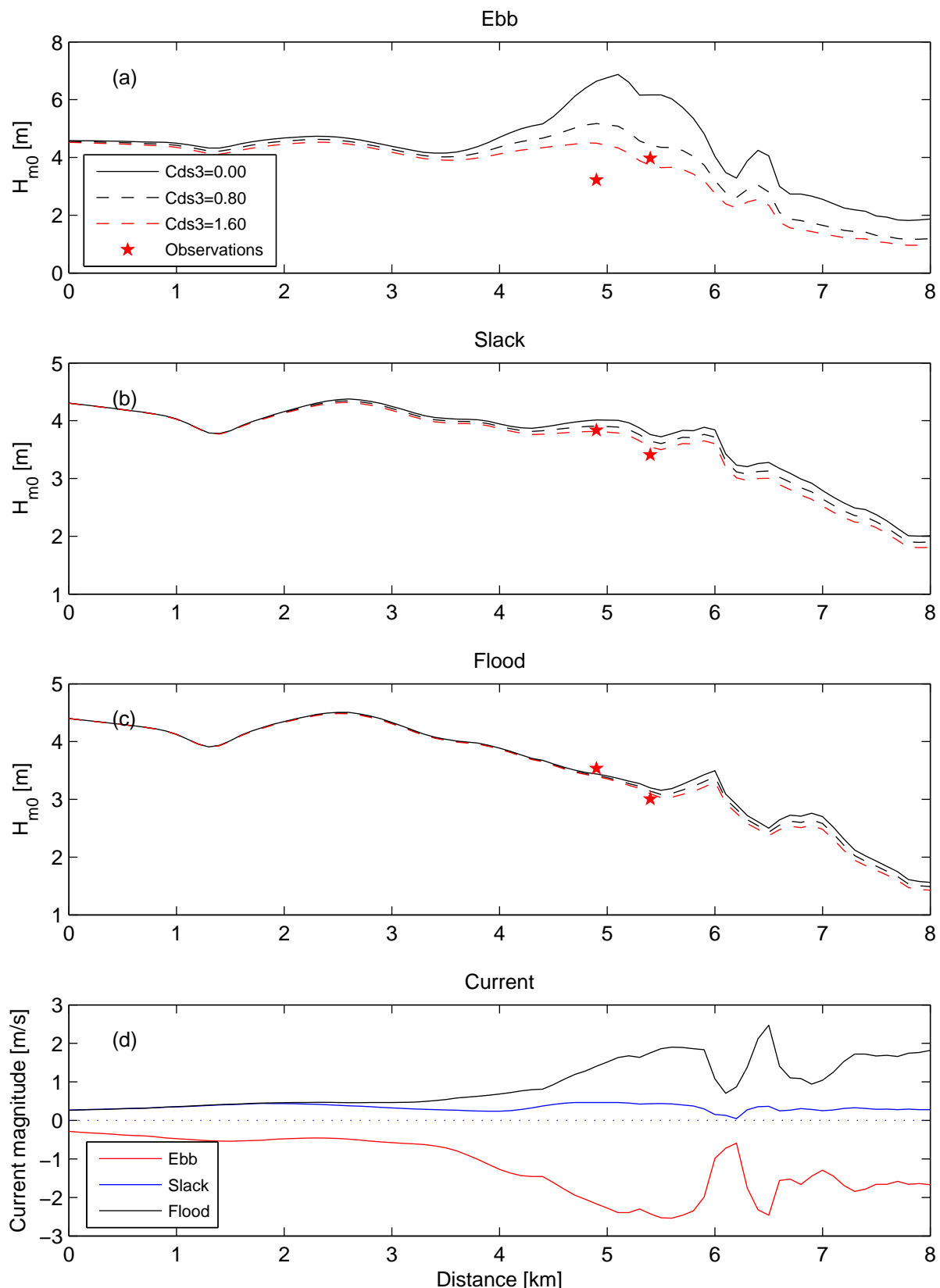
1202119.003

Fig. 3.18



Model results for the Port Phillip Bay field case
for Storm 3: 28-Oct-2006 03:30 (flood)
Enhanced whitecapping Cds3 = 0.80

Wave-current interaction



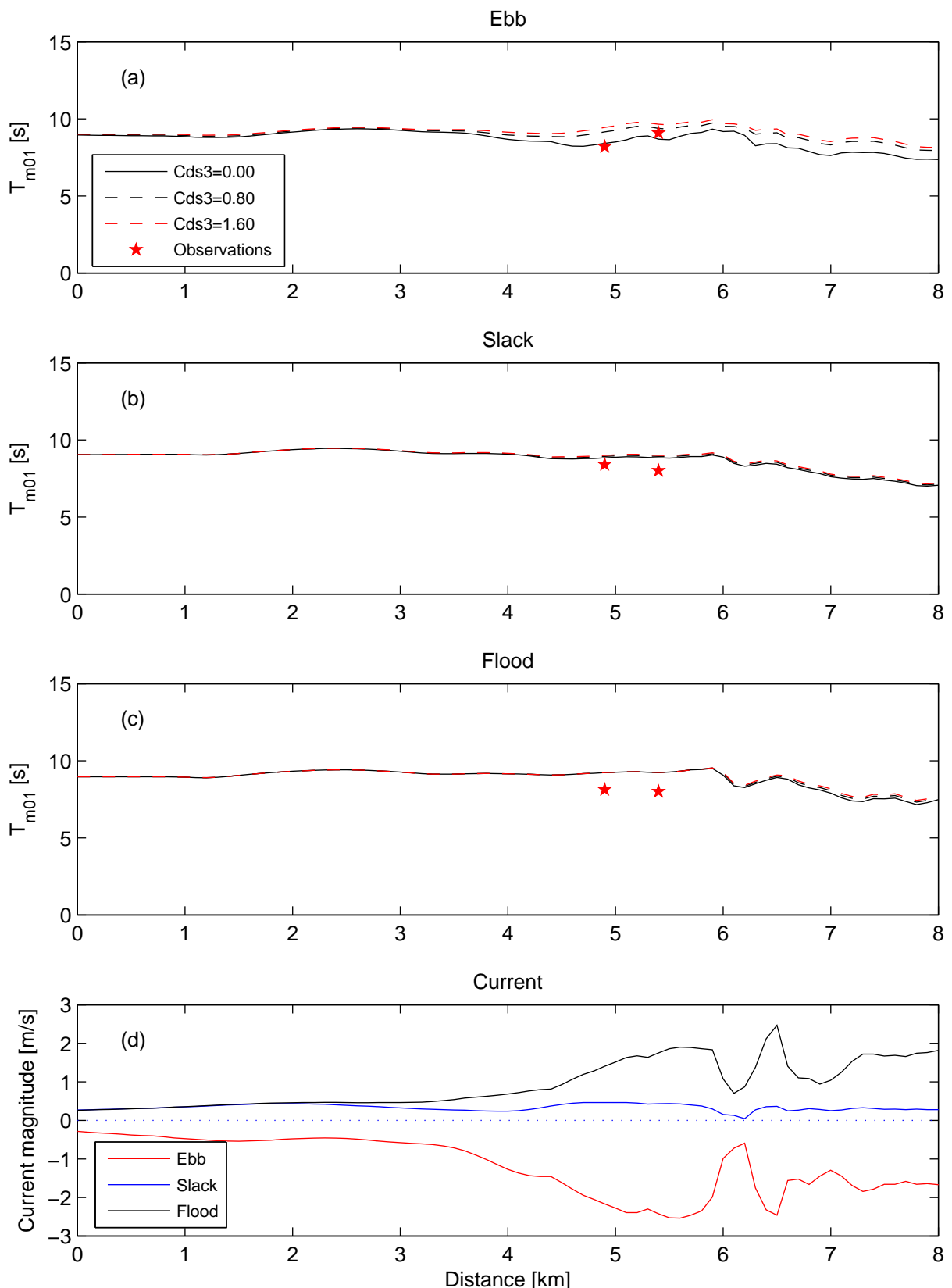
Model results of H_{m0} for the Port Phillip Bay field case
for Storm 3 (ebb, slack and flood)

Wave-current interaction

DELTARES

1202119.003

Fig. 3.20



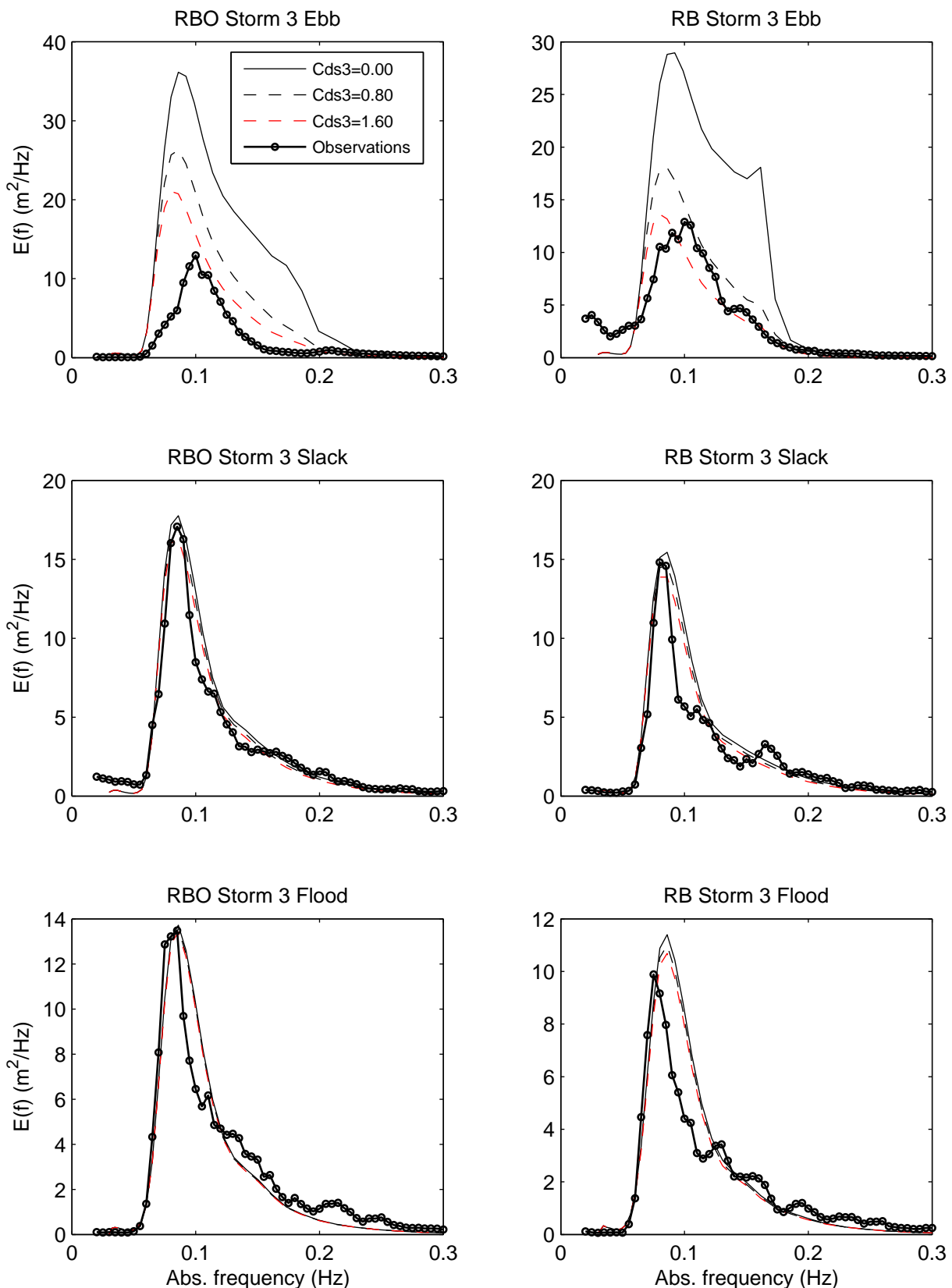
Model results of T_{m01} for the Port Phillip Bay field case
for Storm 3 (ebb, slack and flood)

Wave-current interaction

DELTARES

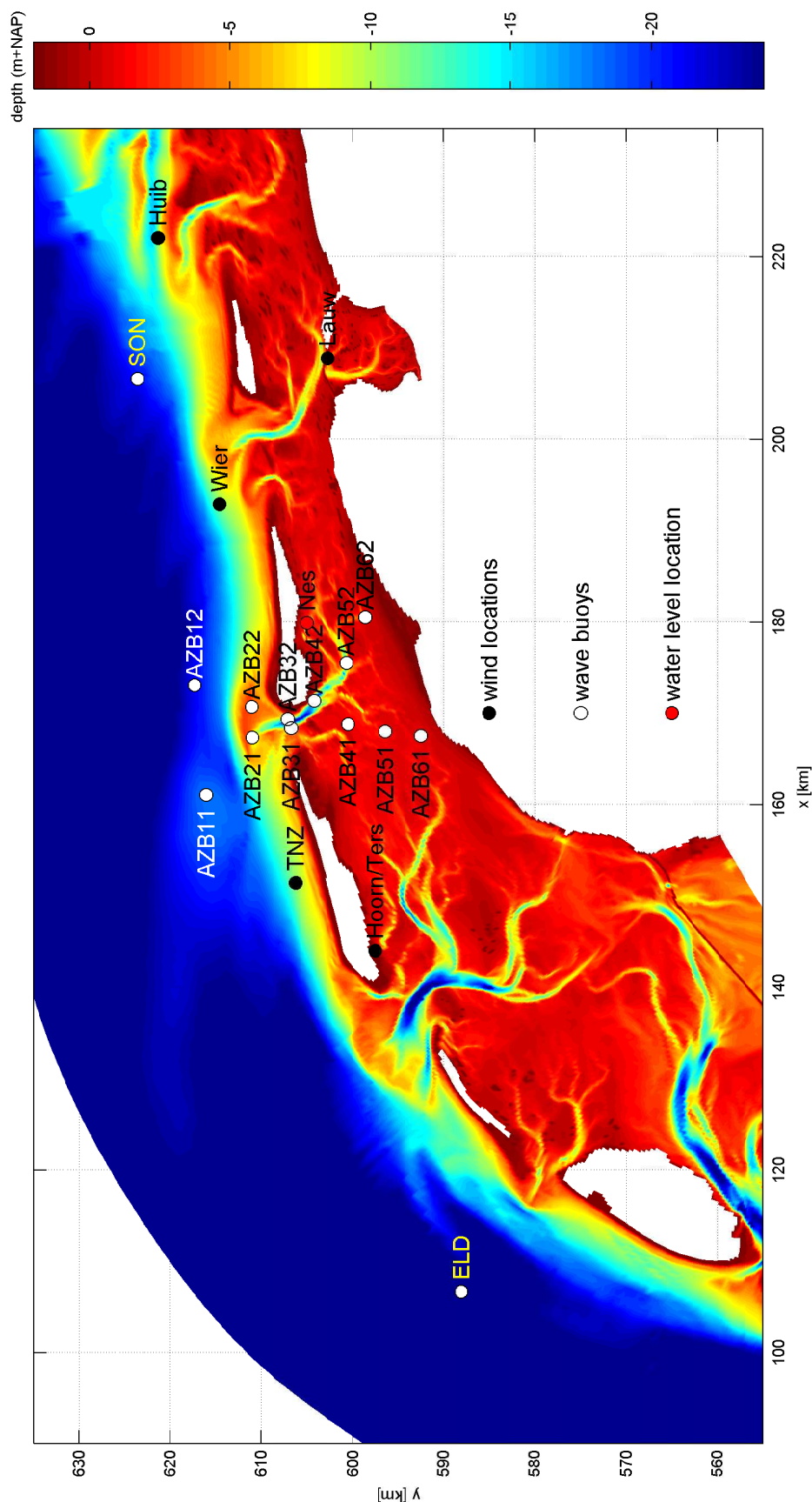
1202119.003

Fig. 3.21



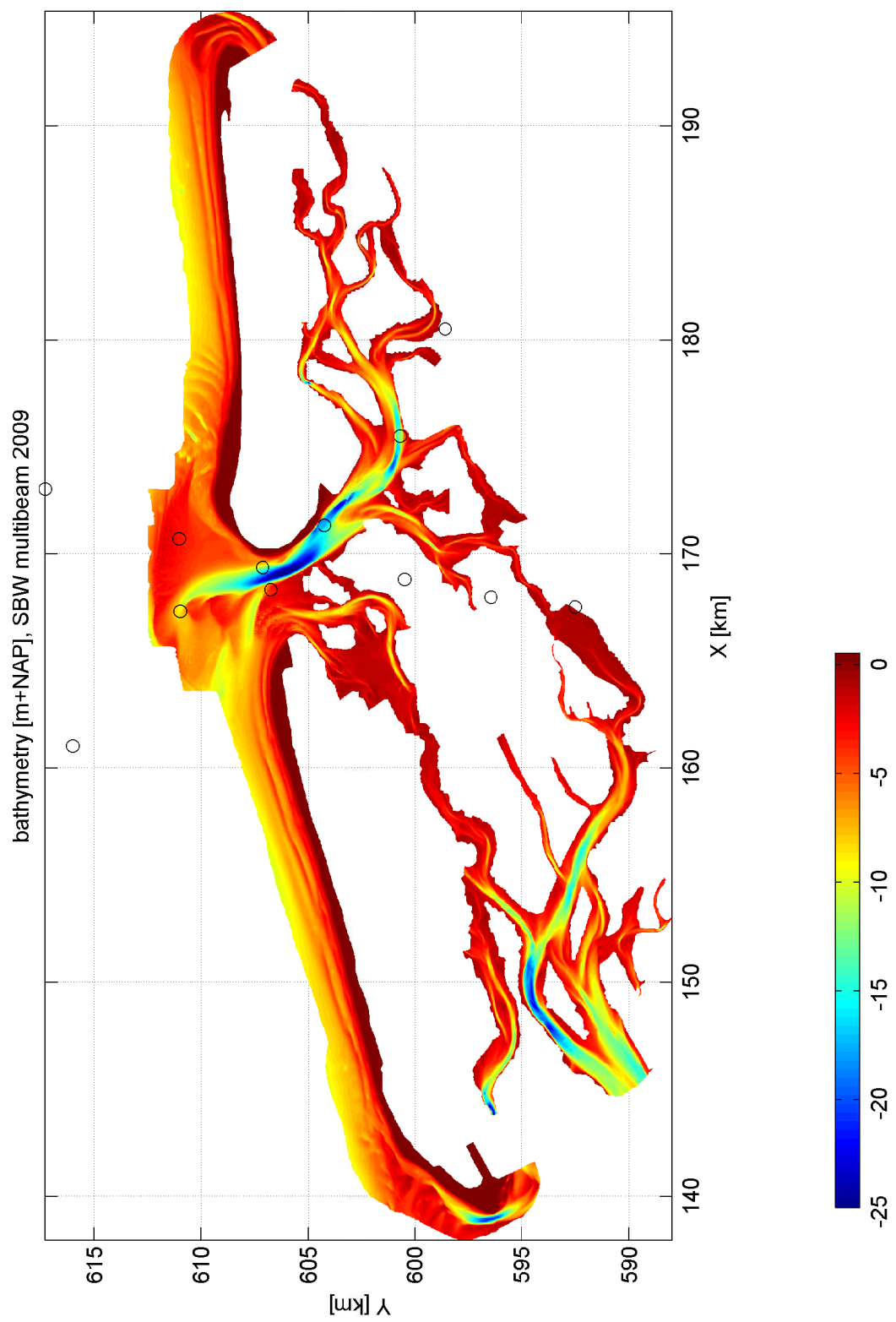
Model results for the Port Phillip Bay field case spectra for Storm 3 (ebb, slack and flood)

Wave-current interaction



Bathymetry and measurement locations Ameland-Zeegat

Wave-current interaction



Data coverage SBW multi beam 2009

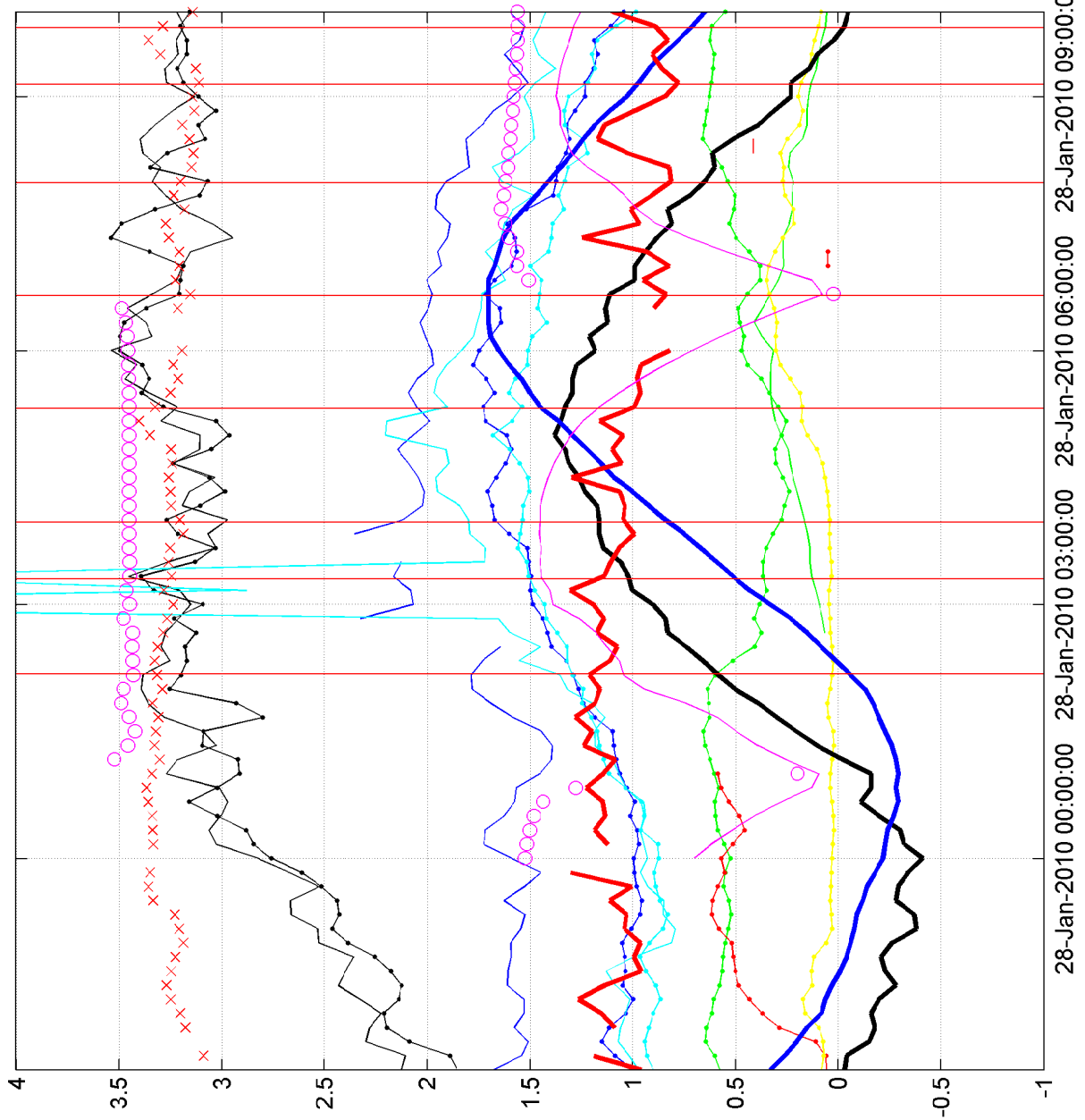
Amelander
Zeegat

Wave-current interaction

DELTAES

1202119.003

Fig 4.2



Timeseries waves, wind, current, water level
vertical red lines indicate selected simulation instants

28 jan 2010

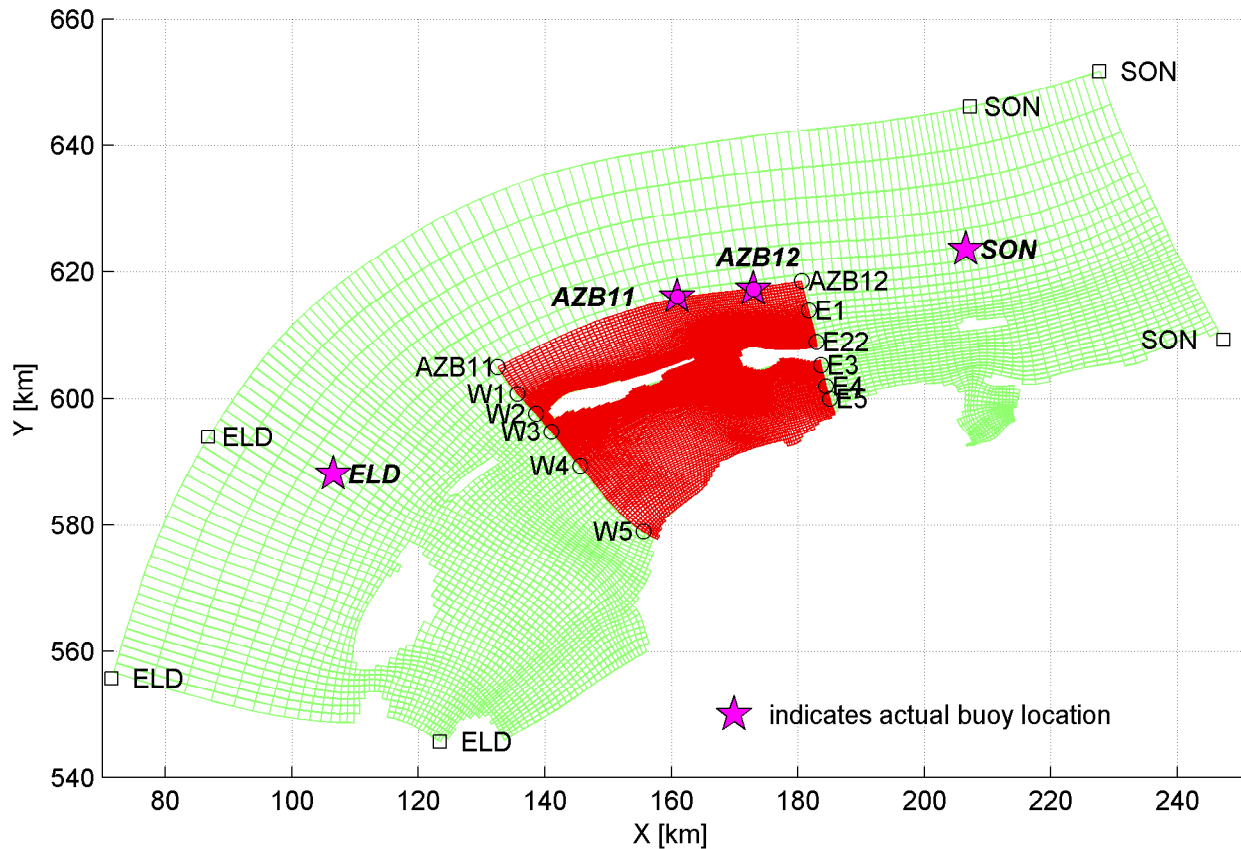
Amelander
Zeegat

Wave-current interaction

DELTARES

1202119.003

Fig 4.3



$$W_1 = (135693.334; 600756.578) \quad E_1 = (181690.734; 613917.952)$$

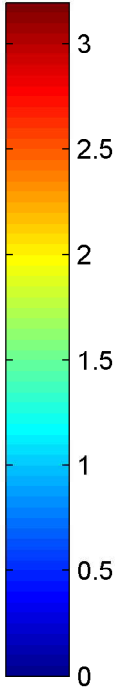
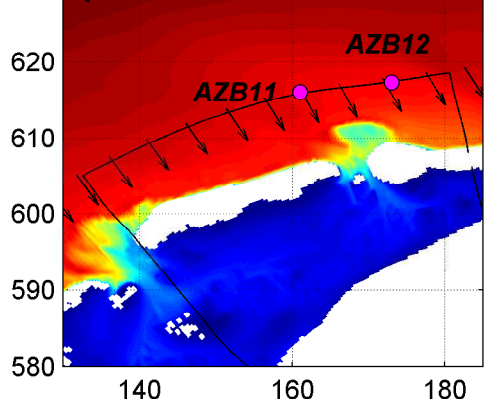
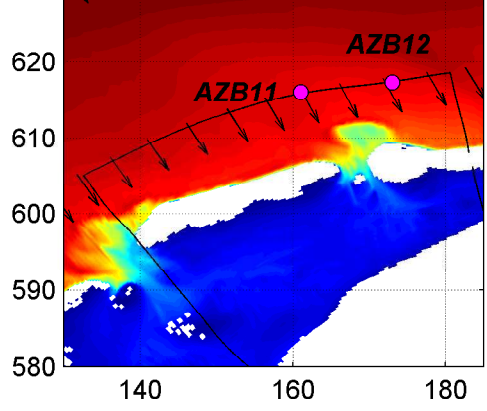
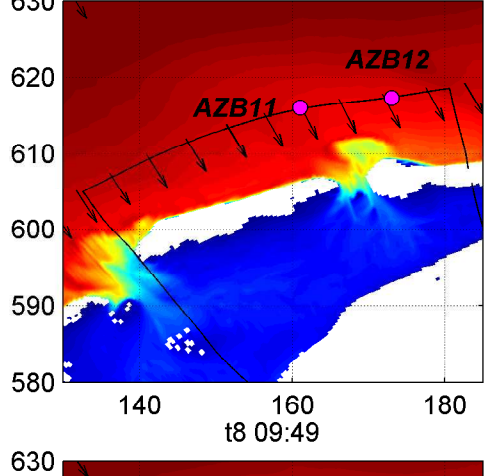
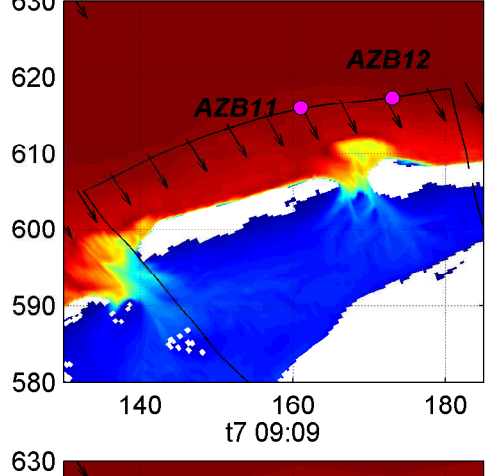
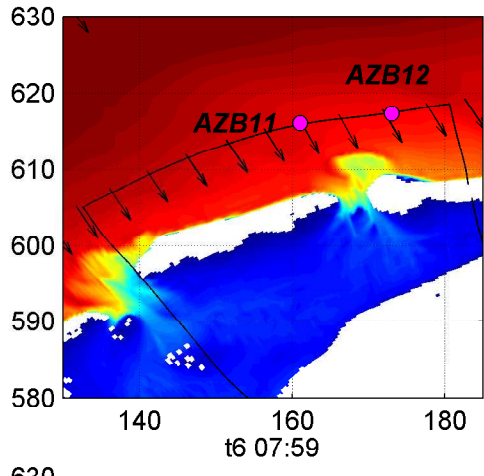
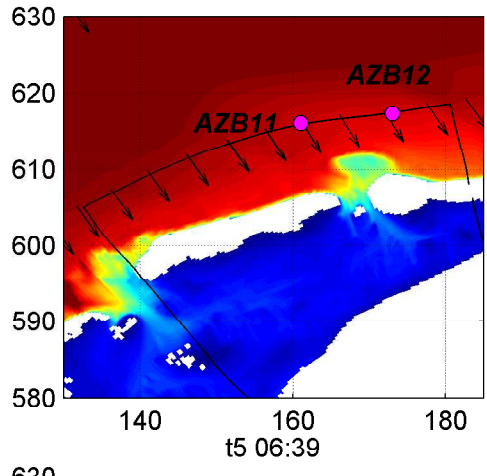
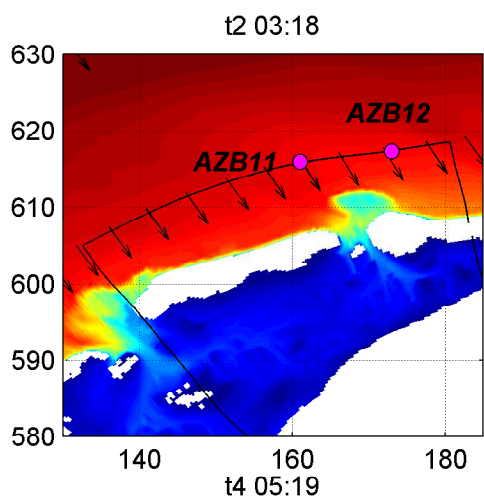
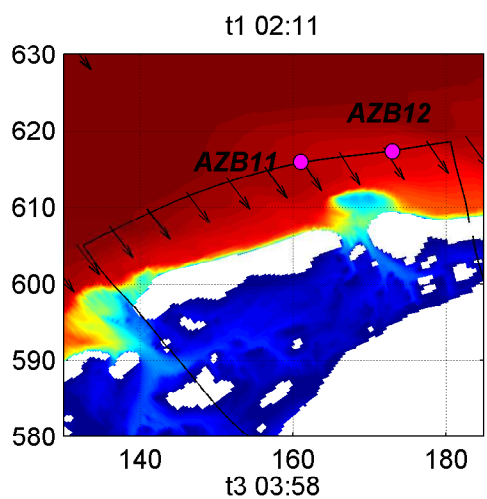
$$W2 = (138618.049; 597658.294) \quad E22 = (182900.00; 608910.000)$$

$$W3 = (141066.000; 594787.564) \quad E3 = (183667.926; 605360.905)$$

$$W4 = (145542.769; 589433.963) \quad E4 = (184490.219; 601989.921)$$

$$W5 = (155602.247; 579002.129) \quad E5 = (185080.354; 599929.380)$$

Grids G1 (green) and G2(red) (every 3rd grid line) and locations for wave boundary conditions	Amelander Zeegat	
		Wave-current interaction
DELTARES	1202119.003	Fig 4.4.a



SWAN Results H_{m0} [m] and wave direction on grid G1

Amelander
Zeegat

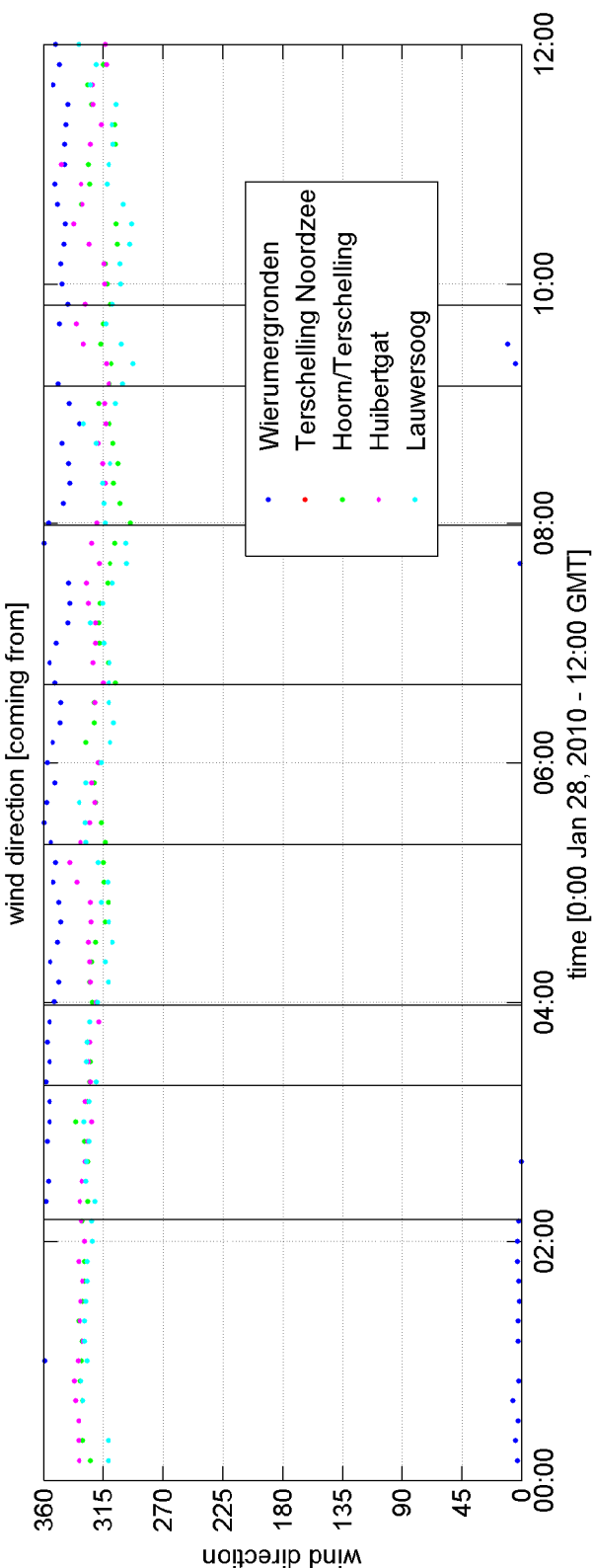
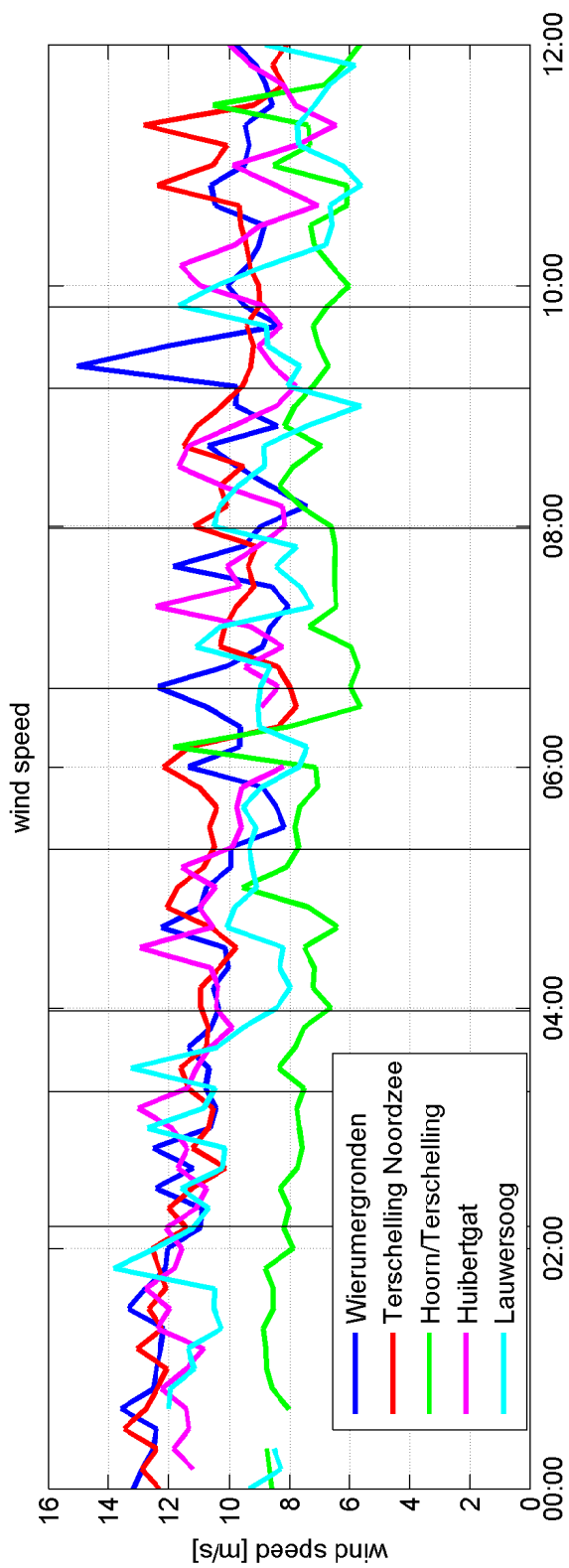
t1 - t8
28-Jan-2010

Wave-current interaction

DELTARES

1202119.003

Fig. 4.4.b



Timeseries wind velocity and direction

Amelander
Zeegat

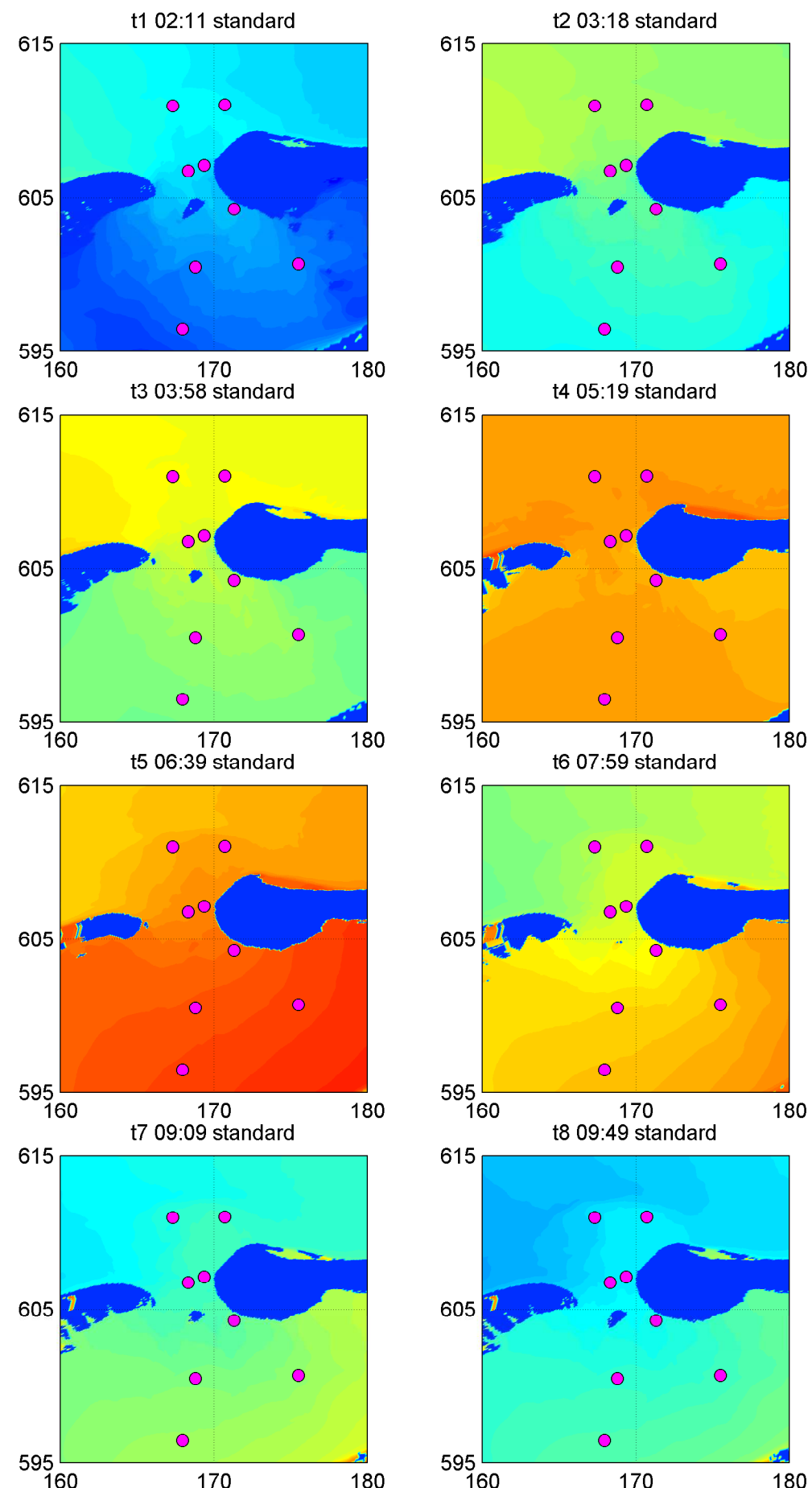
28-Jan-2010

Wave-current interaction

DELTARES

1202119.003

Fig 4.5



SWAN Input: waterlevel [m + NAP]
standard
(pink dots indicate buoy locations)

Amelander
Zeegat

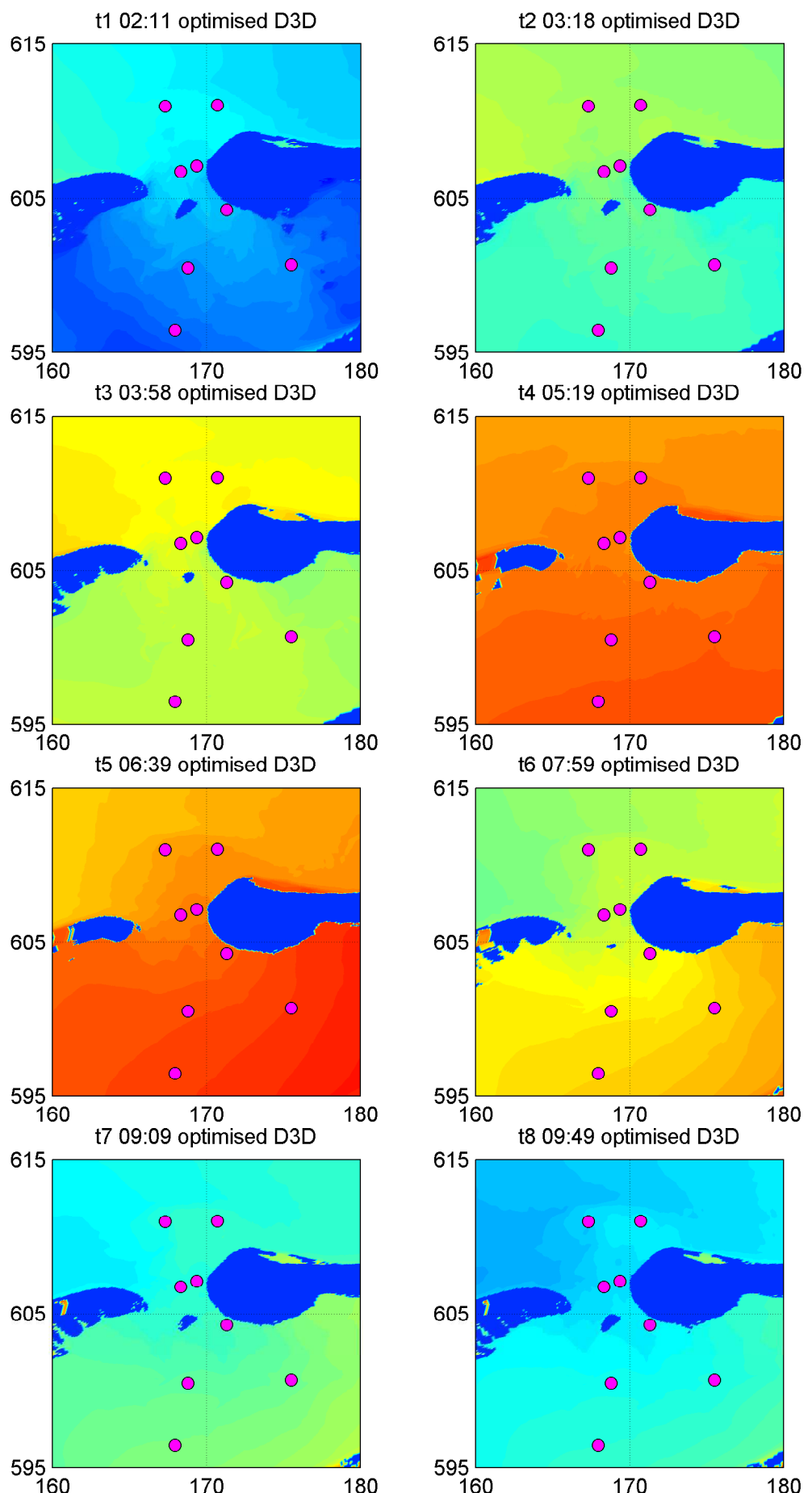
t1 - t8
28-Jan-2010

Wave-current interaction

DELTARES

1202119.003

Fig. 4.6.a



SWAN Input: waterlevel [m + NAP]
optimised D3D
(pink dots indicate buoy locations)

Amelander
Zeegat

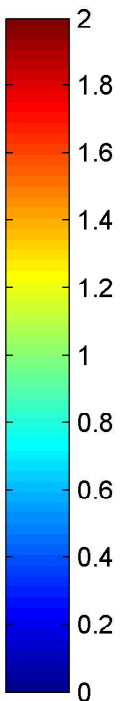
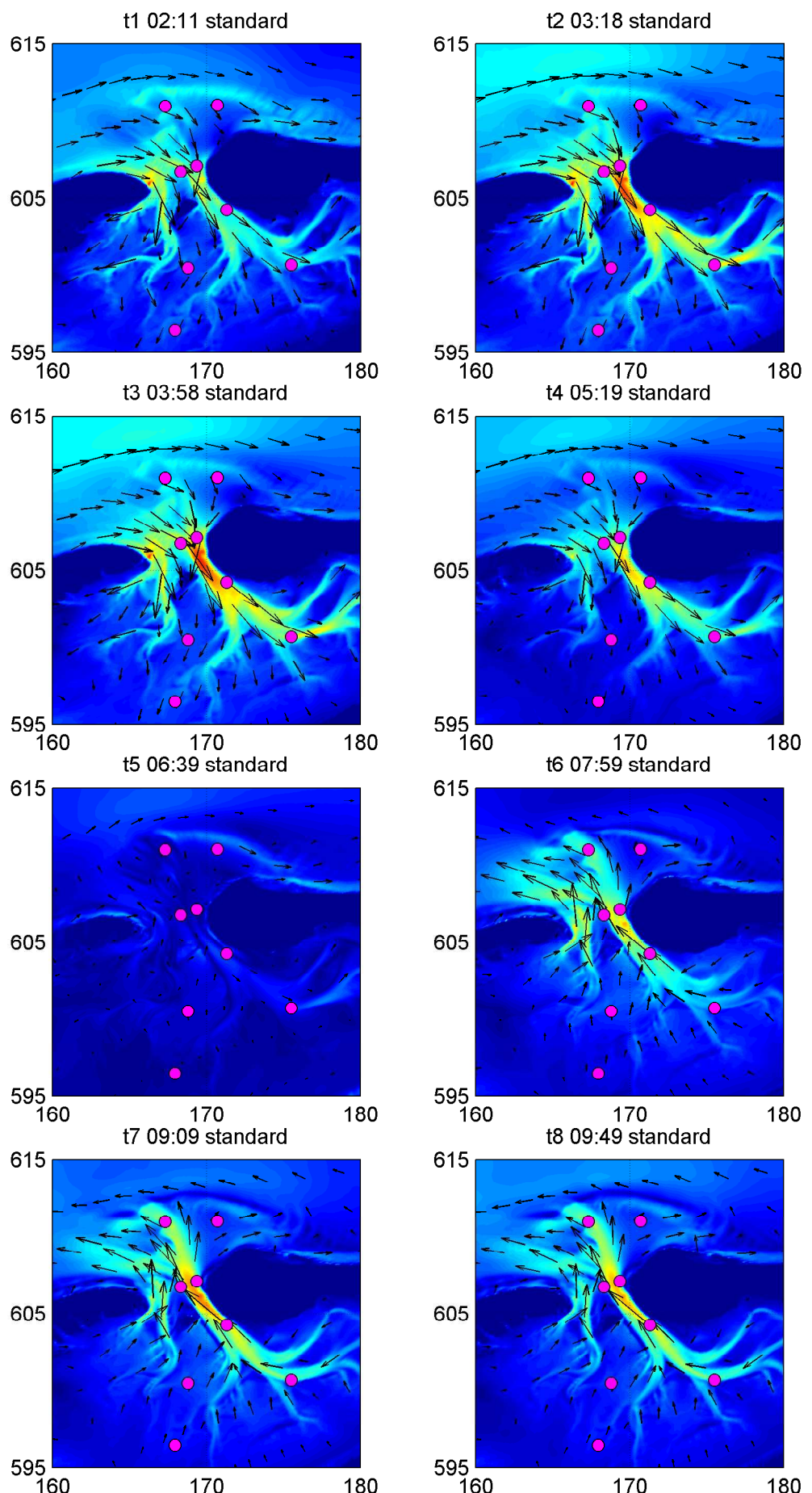
t1 - t8
28-Jan-2010

Wave-current interaction

DELTARES

1202119.003

Fig. 4.6.b



SWAN Input: Current velocity [m/s]
standard

Amelander
Zeegat

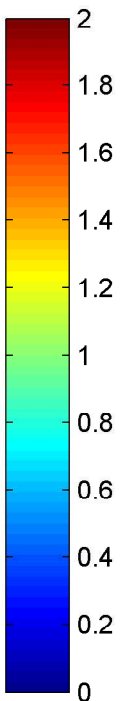
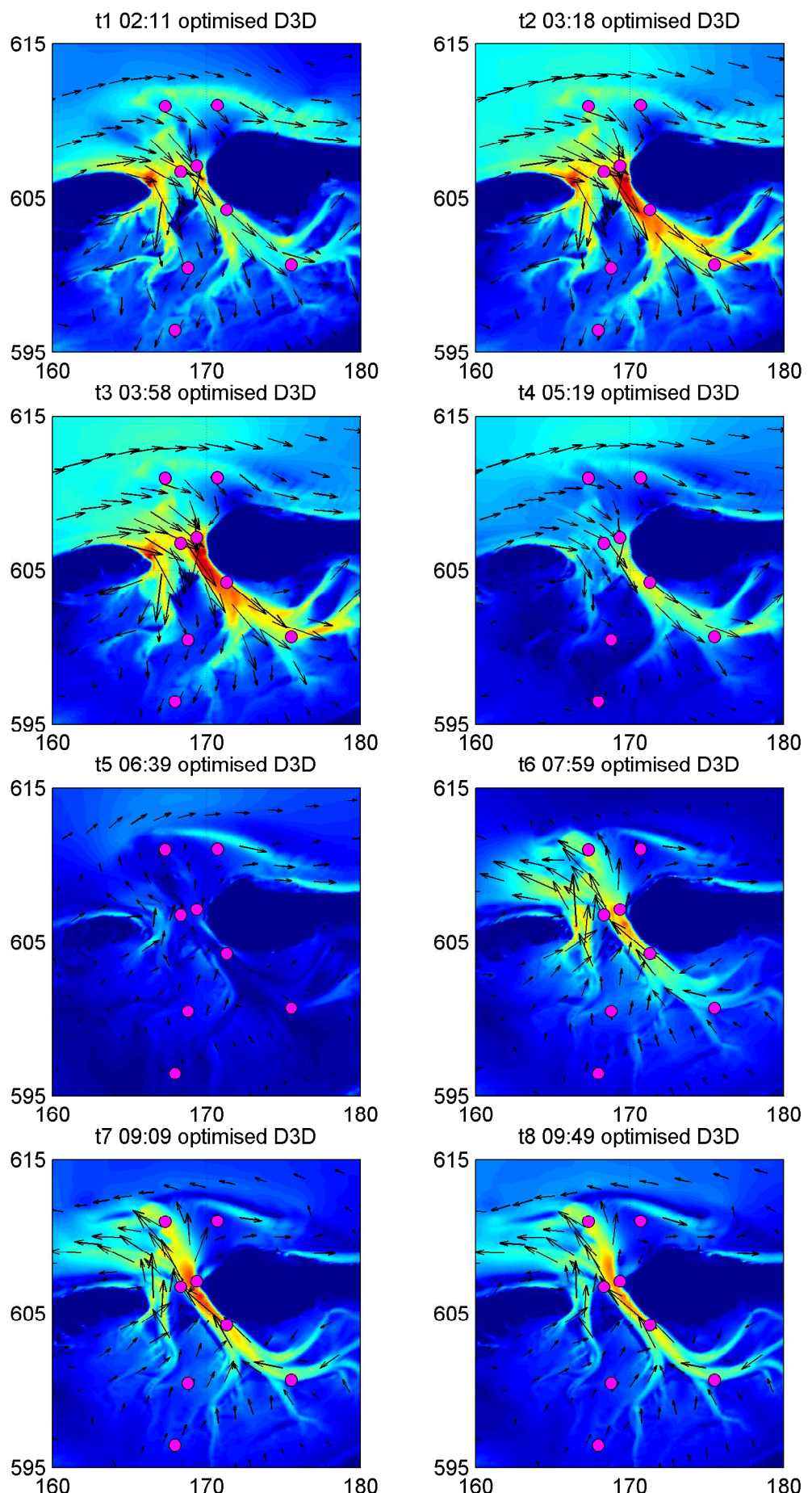
t1 - t8
28-Jan-2010

Wave-current interaction

DELTARES

1202119.003

Fig. 4.7.a



SWAN Input: Current velocity [m/s]
optimised D3D

Amelander
Zeegat

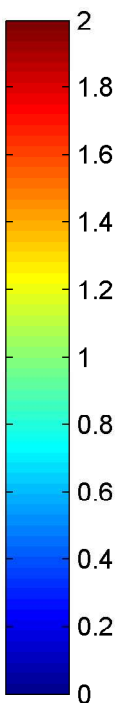
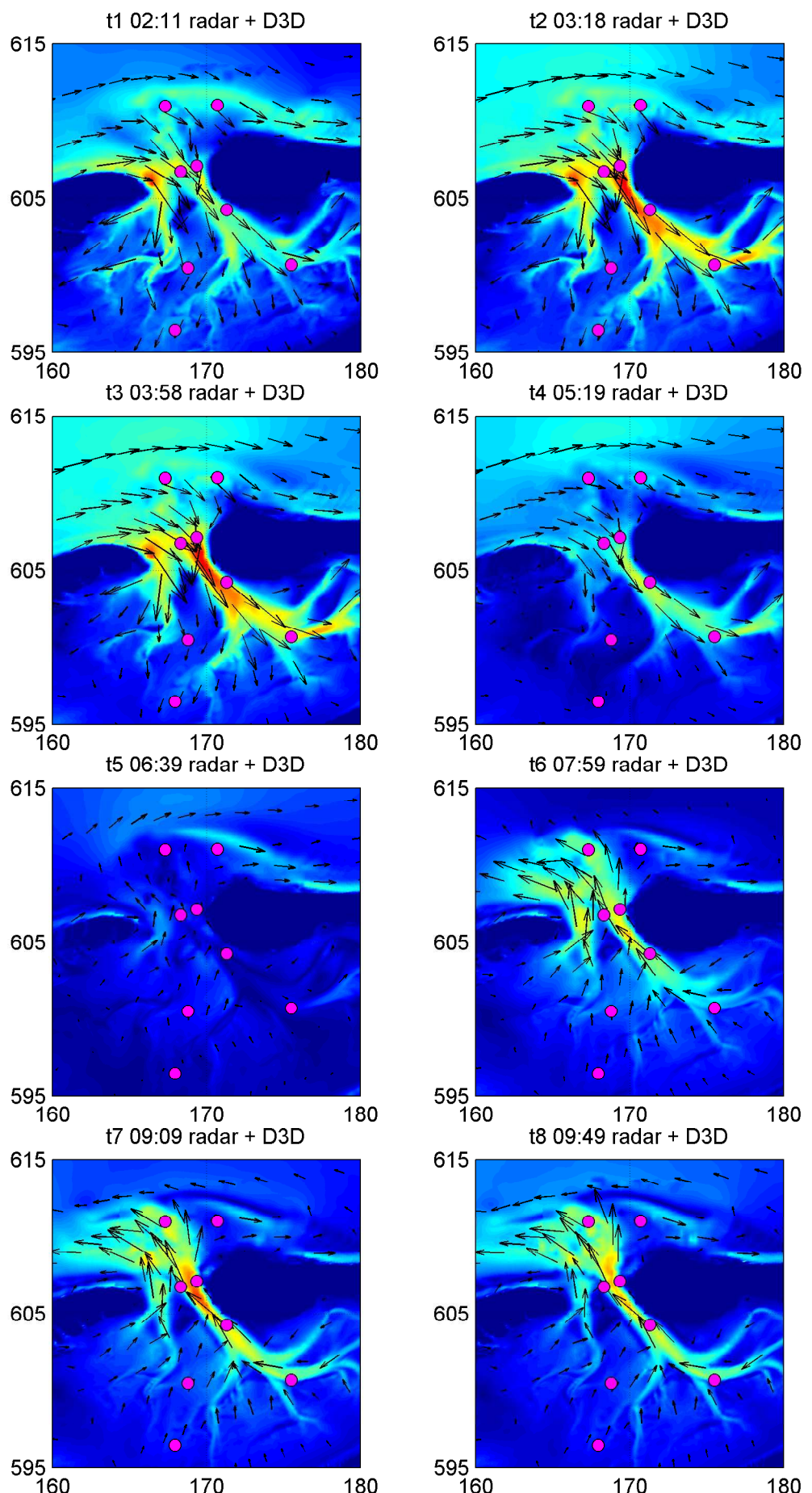
t1 - t8
28-Jan-2010

Wave-current interaction

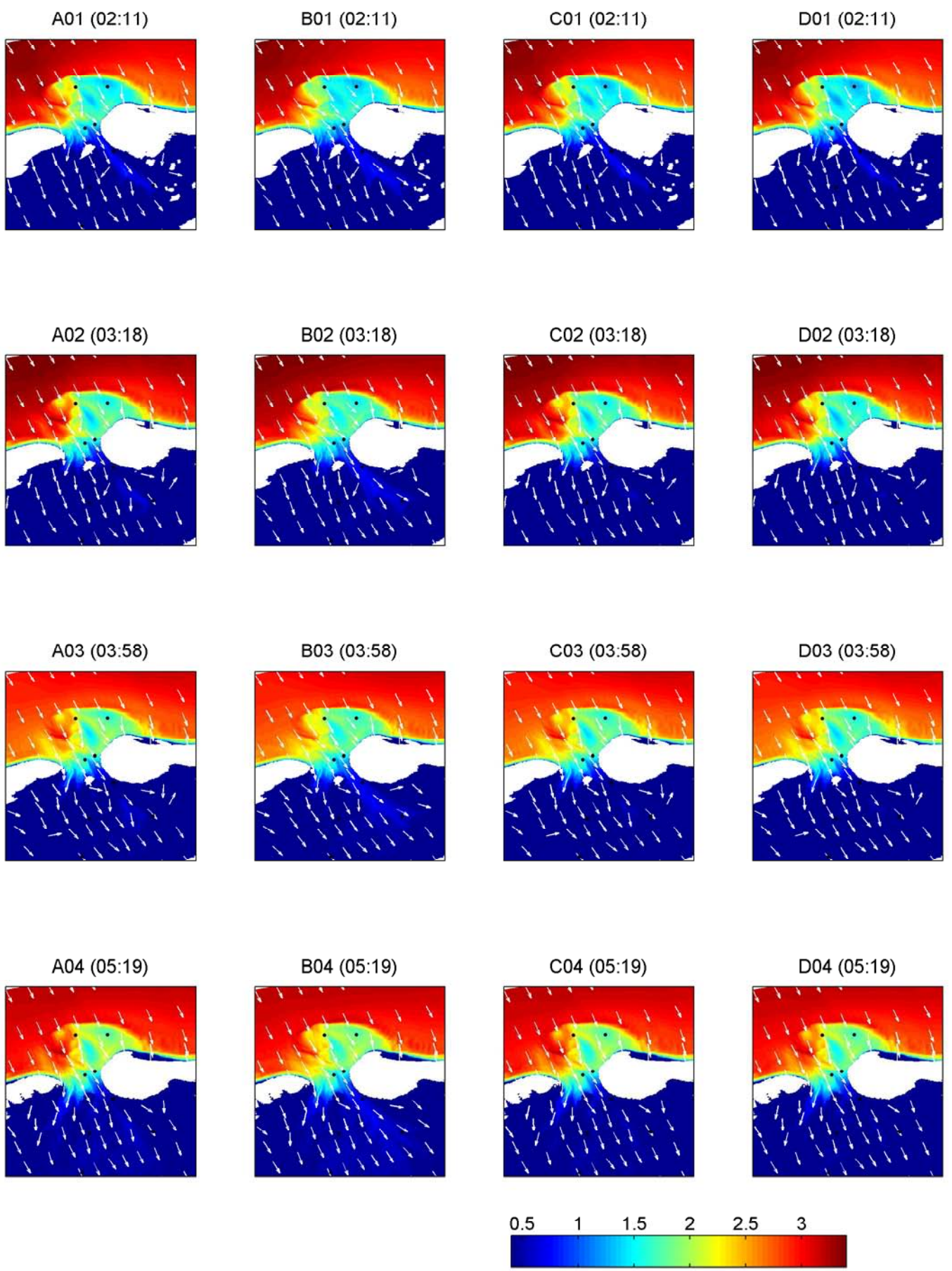
DELTARES

1202119.003

Fig. 4.7.b



SWAN Input: Current velocity [m/s] radar + D3D	Amelander Zeegat	t1 - t8 28-Jan-2010
	Wave-current interaction	
DELTARES	1202119.003	Fig. 4.7.c



SWAN Results: H_{m0} [m]
Series A, B, C, D; instants 1 - 4

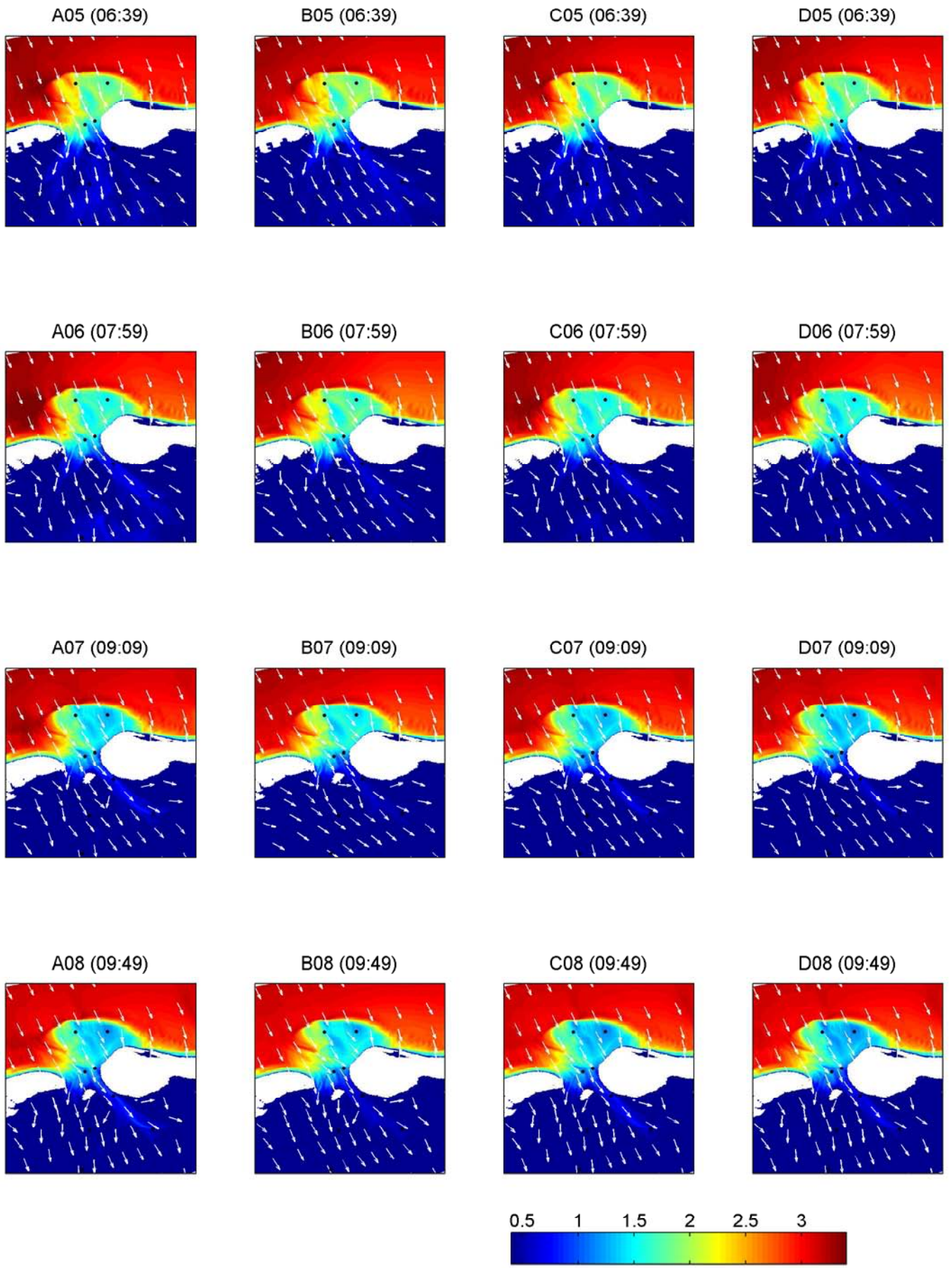
Amelander
Zeegat 28-Jan-2010

Wave-current interaction

DELTARES

1202119.003

Fig. 4.8.a



SWAN Results: H_{m0} [m]
Series A, B, C, D; instants 5 - 8

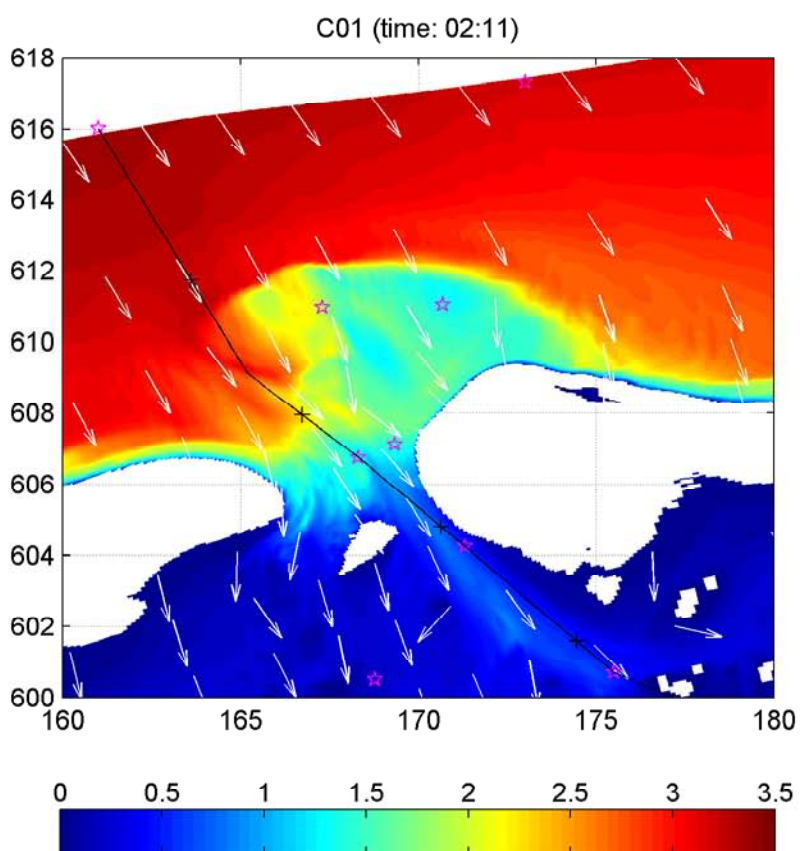
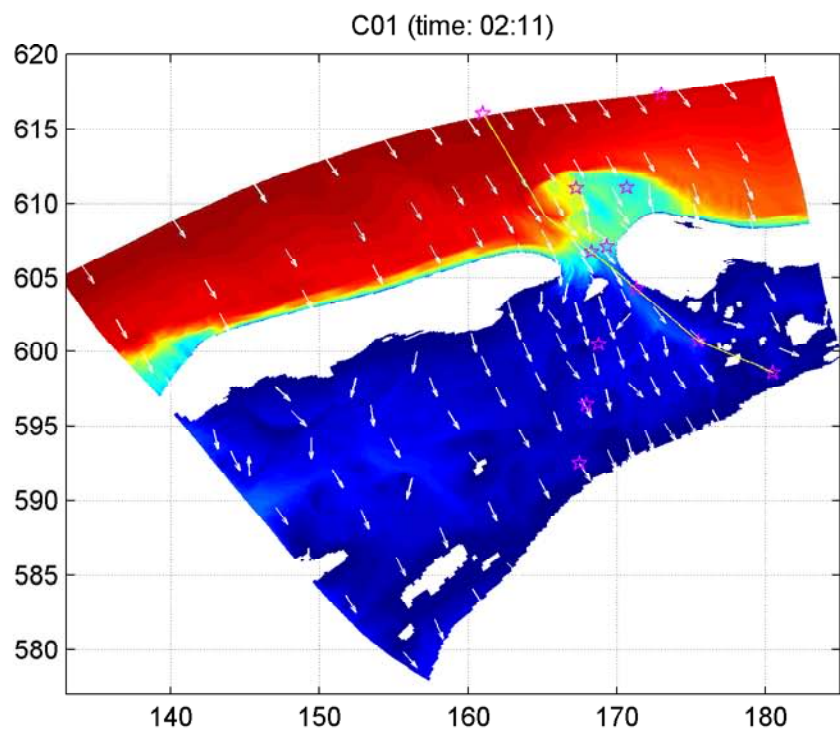
Amelander
Zeegat 28-Jan-2010

Wave-current interaction

DELTARES

1202119.003

Fig. 4.8.b



Overview SWAN results H_{m0} [m] and position transect
(plusses indicate 5000 m distance; pink pentagons the buoys)

Amelander
Zeegat

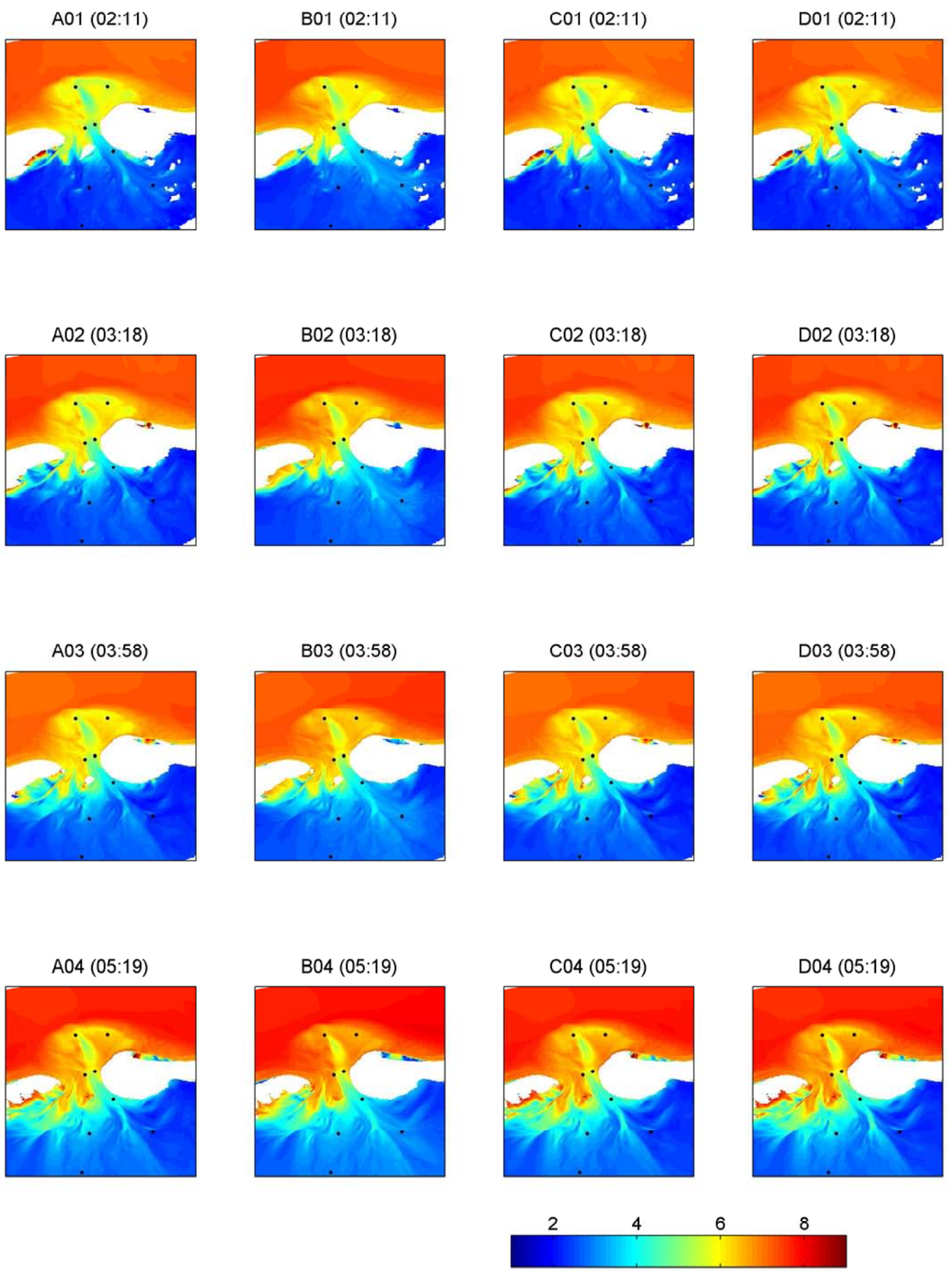
28-Jan-2010

Wave-current interaction

DELTARES

1202119.003

Fig. 4.8.c



SWAN Results: $T_{m-1,0}$ [s]
Series A, B, C, D; instants 1 - 4

Amelander
Zeegat

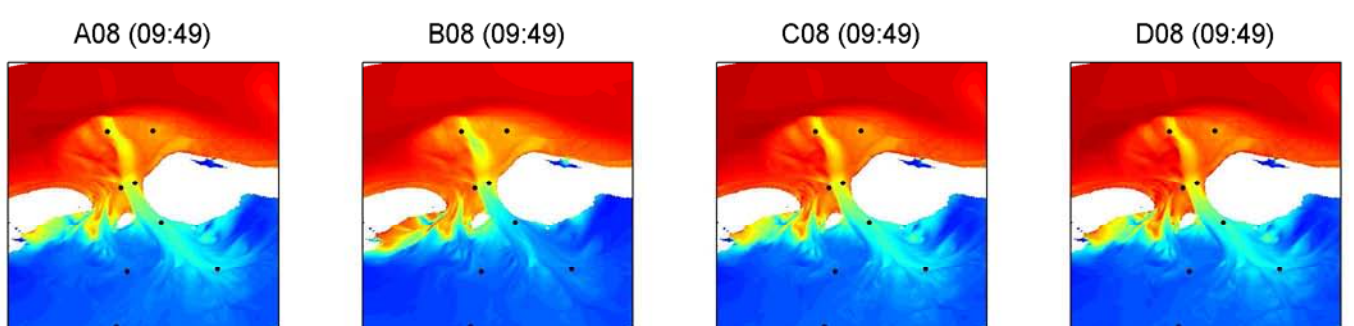
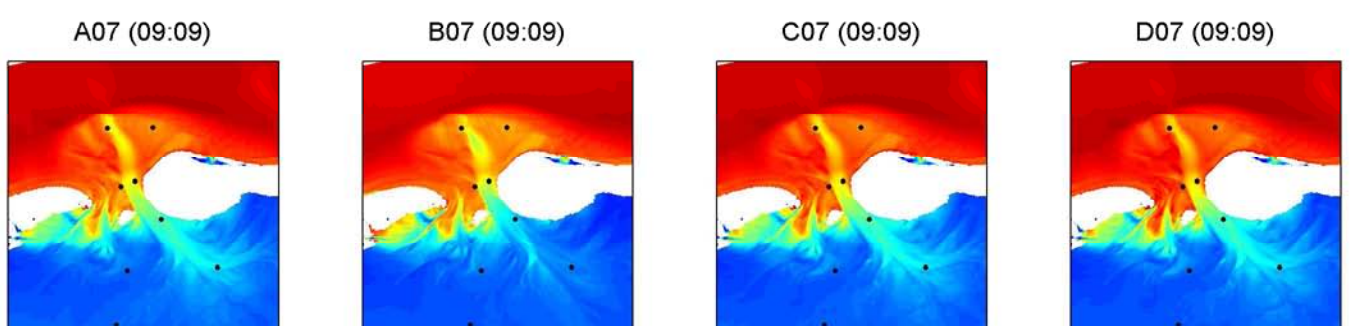
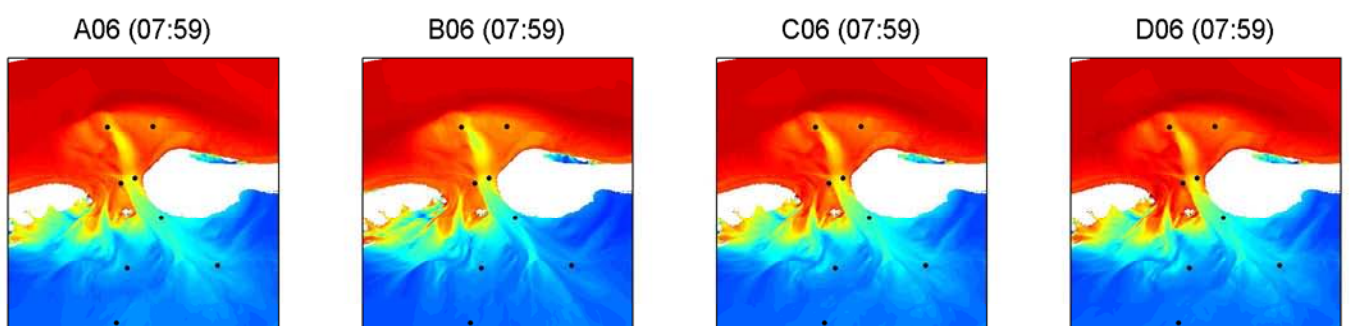
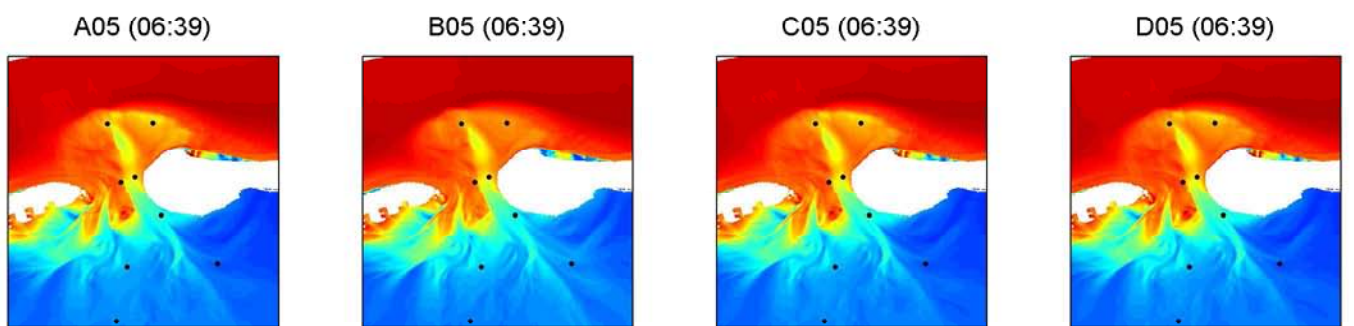
28-Jan-2010

Wave-current interaction

DELTARES

1202119.003

Fig. 4.9.a



SWAN Results: $T_{m-1,0}$ [s]
Series A, B, C, D; instants 5 - 8

Amelander
Zeegat

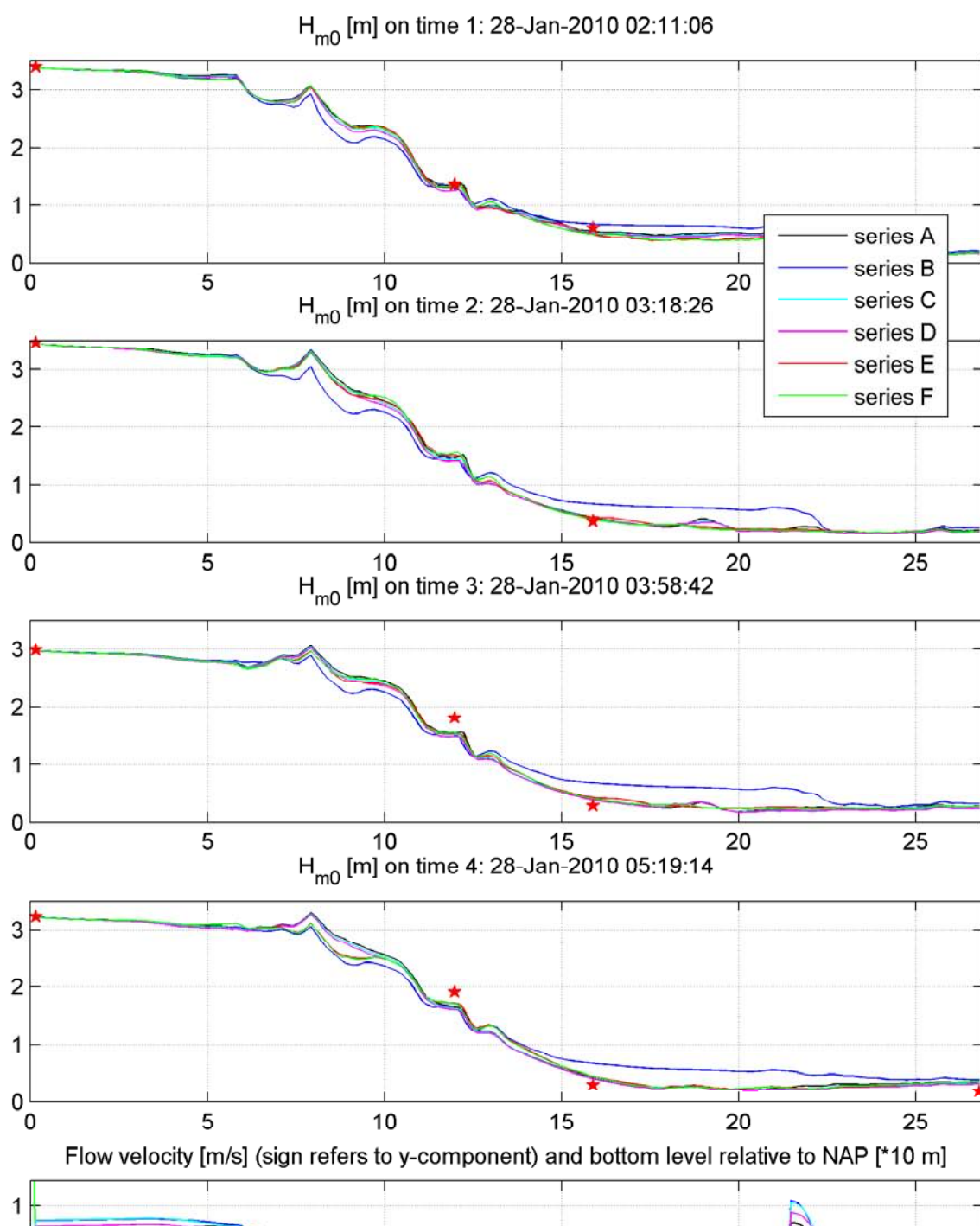
28-Jan-2010

Wave-current interaction

DELTARES

1202119.003

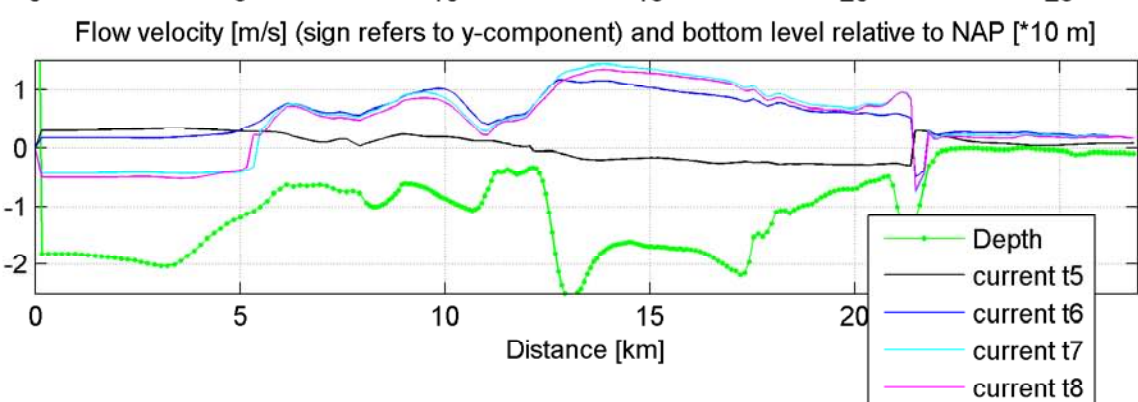
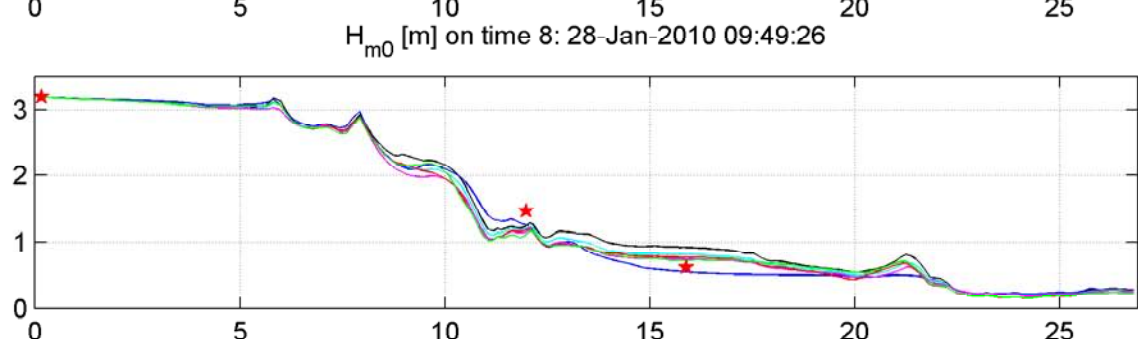
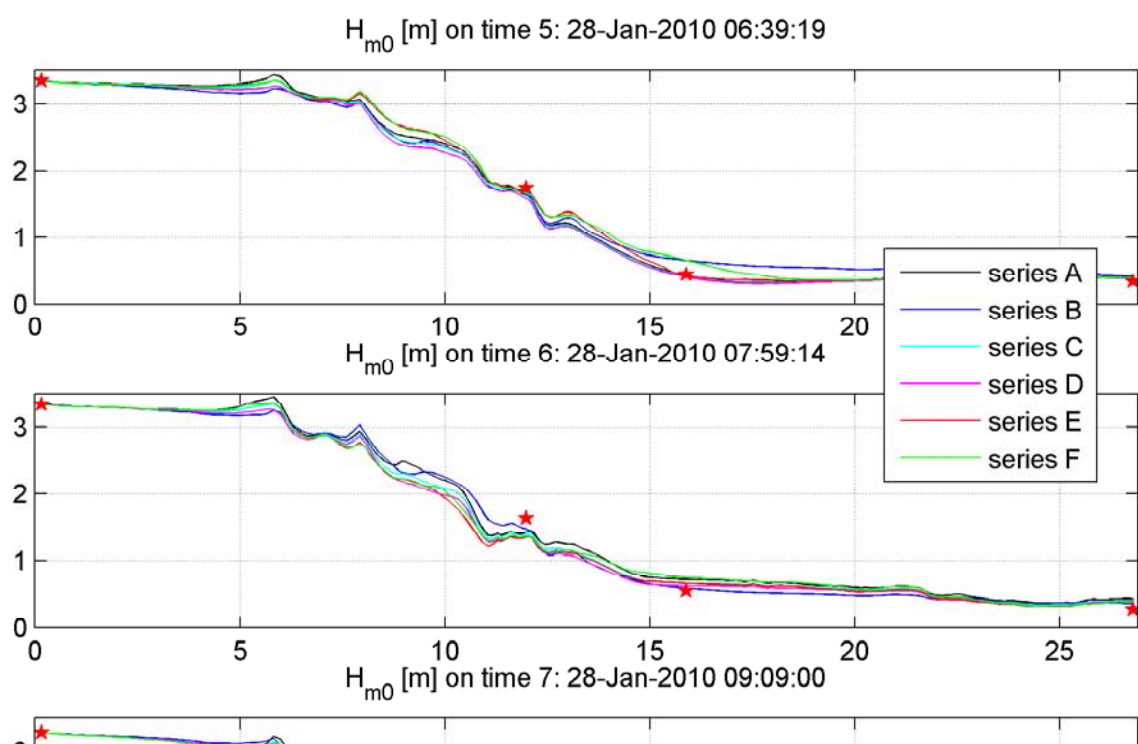
Fig. 4.9.b



Model results of H_{m0} for series A, B, C, D, E, F
stars indicate observations at AZB11, AZB31, AZB42, AZB62

Amelander
Zeegat instants t1 - t4

Wave-current interaction

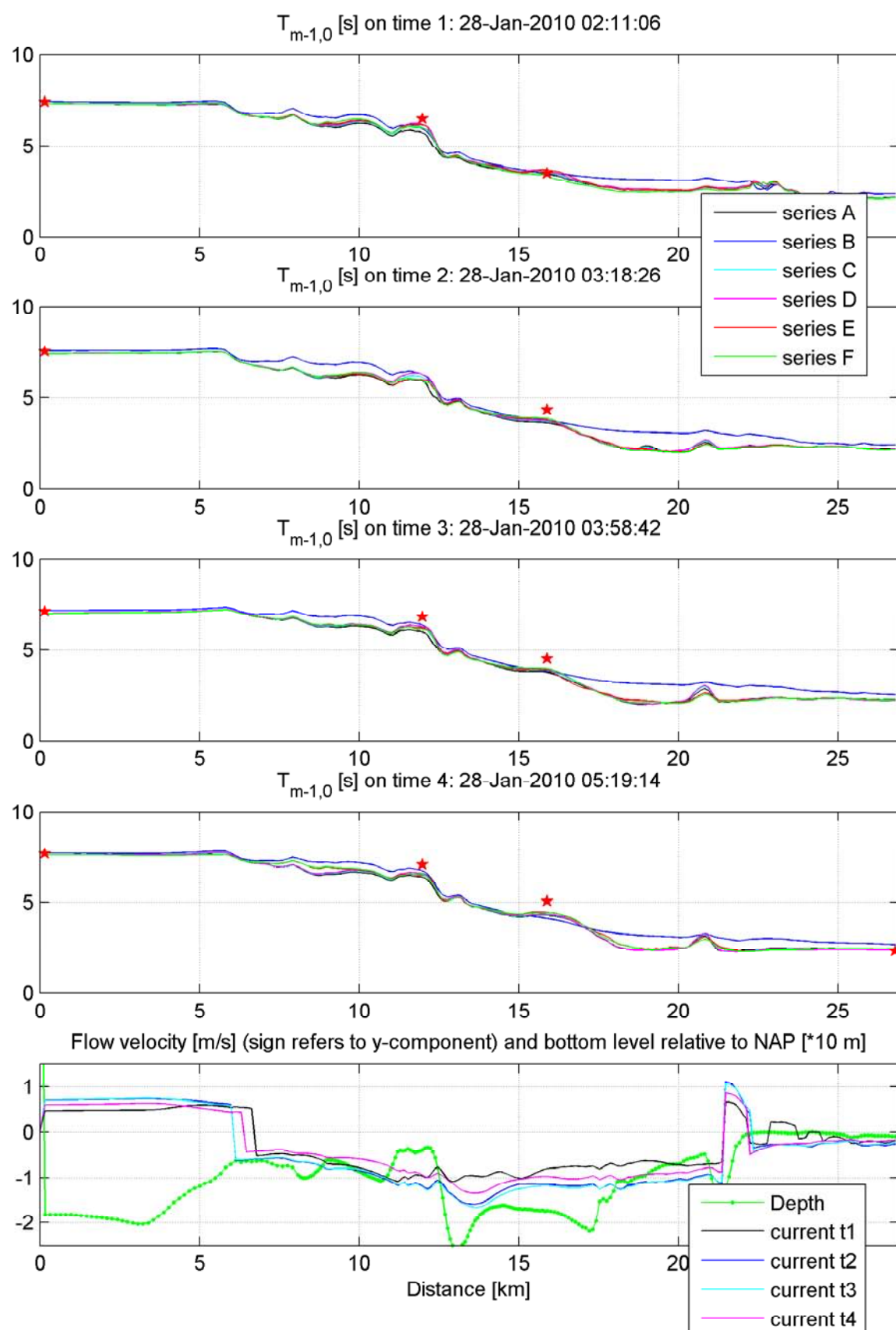


Model results of H_{m0} for series A, B, C, D, E, F
stars indicate observations at AZB11, AZB31, AZB42, AZB62

Amelander
Zeegat

instants t5 - t8

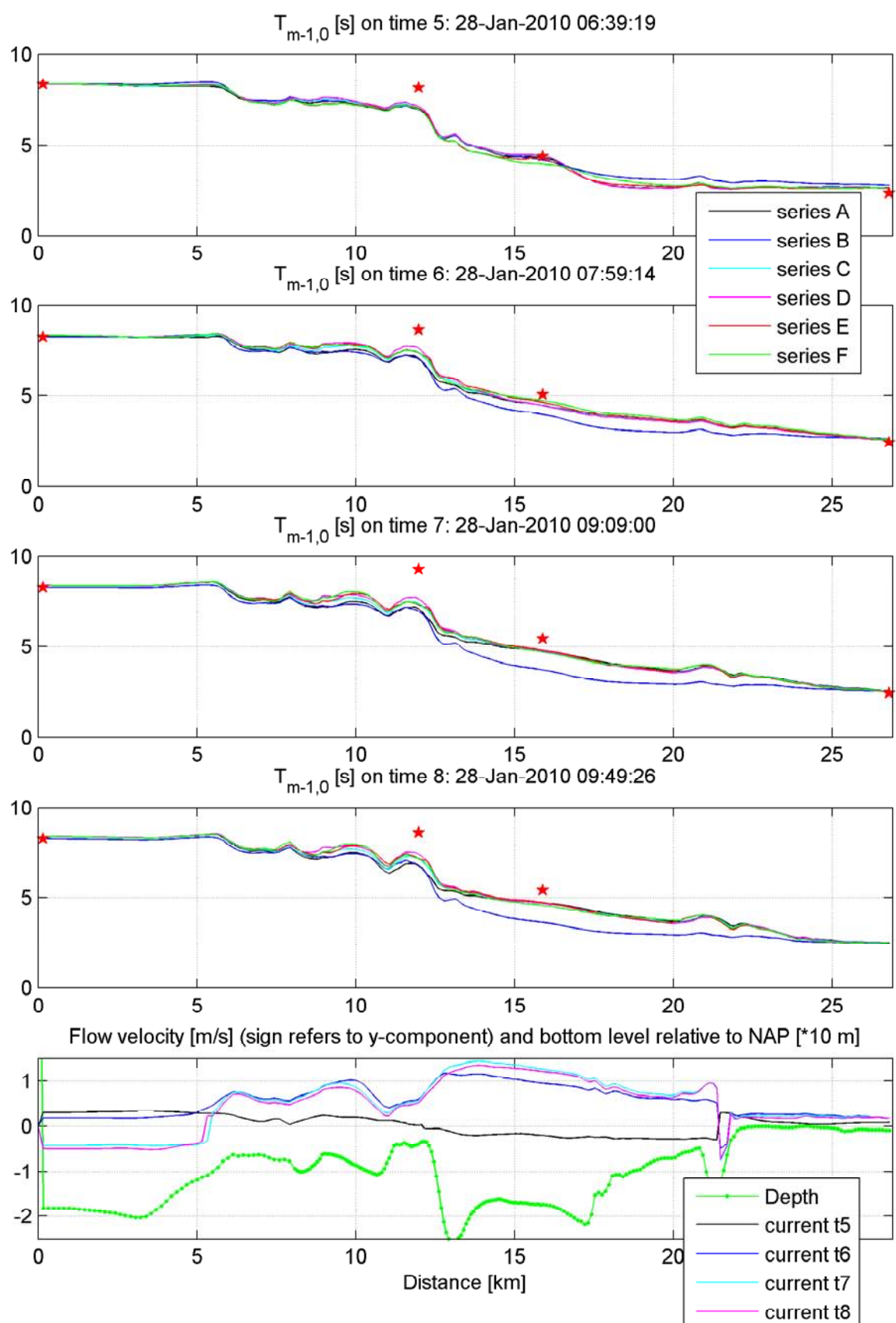
Wave-current interaction



Model results of $T_{m-1,0}$ for series A, B, C, D, E, F
 stars indicate observations at AZB11, AZB31, AZB42, AZB62

Amelander
 Zeegat instants t1 - t4

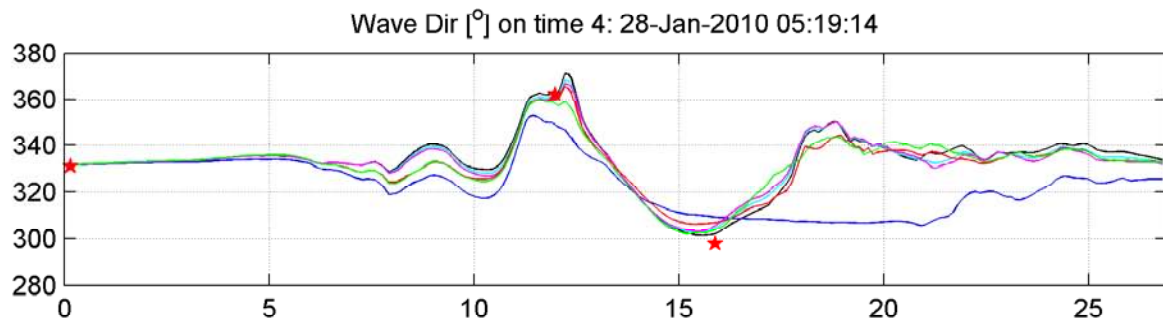
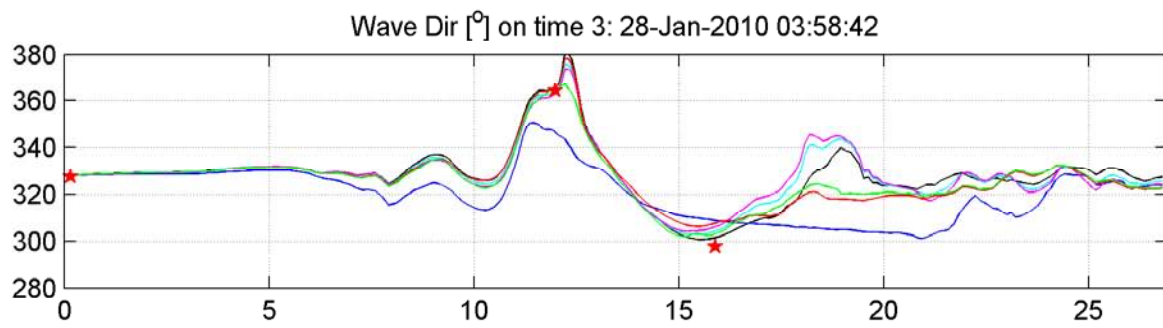
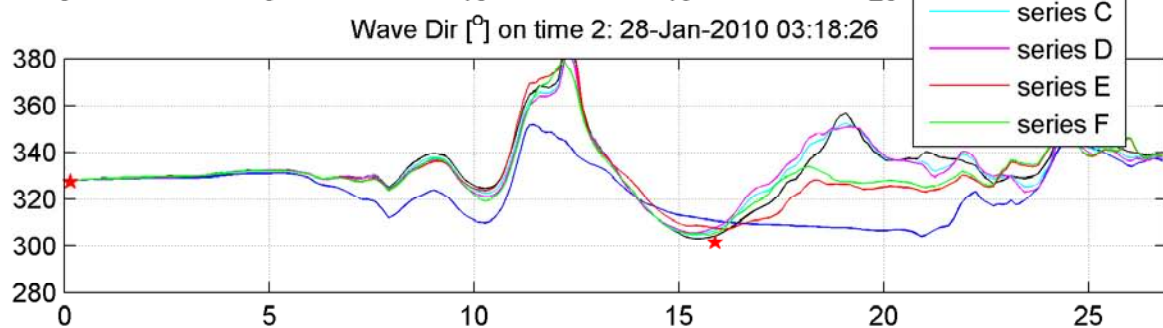
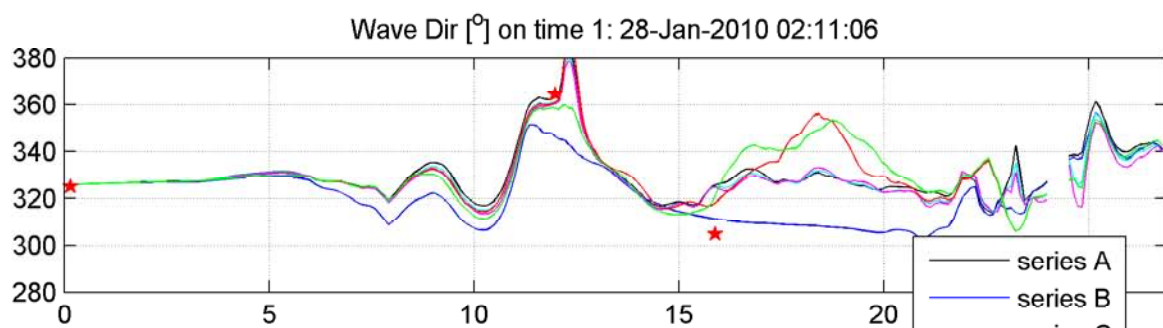
Wave-current interaction



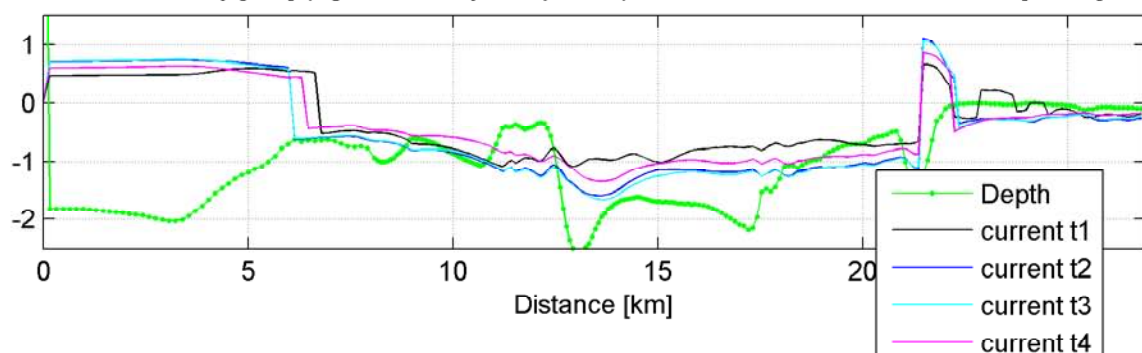
Model results of $T_{m-1,0}$ for series A, B, C, D, E, F
 stars indicate observations at AZB11, AZB31, AZB42, AZB62

Amelander
 Zeegat instants t5 - t8

Wave-current interaction



Flow velocity [m/s] (sign refers to y-component) and bottom level relative to NAP [*10 m]



Model results of Wave Dir for series A, B, C, D, E, F
stars indicate observations at AZB11, AZB31, AZB42, AZB62

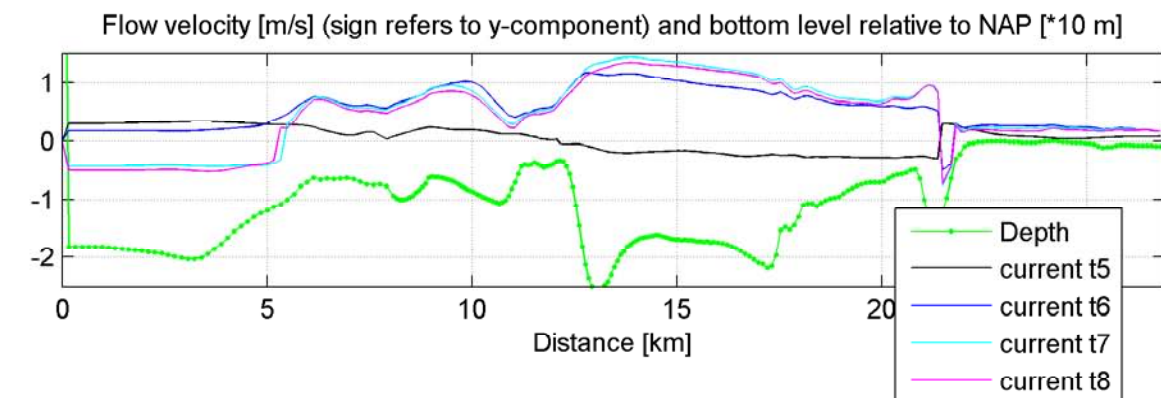
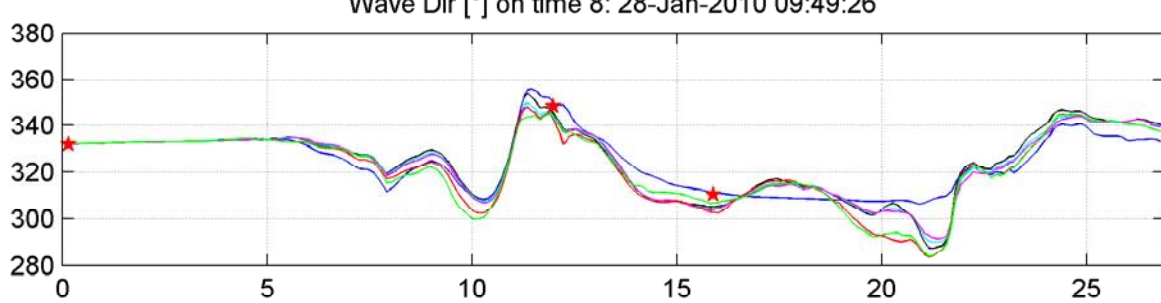
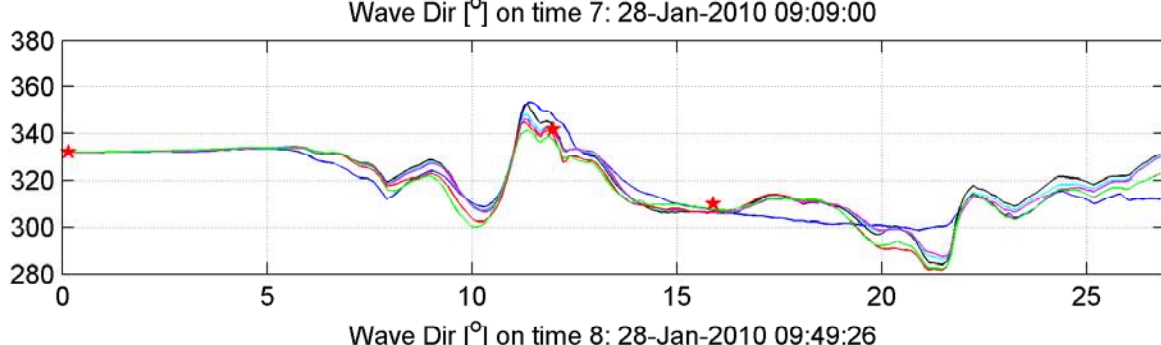
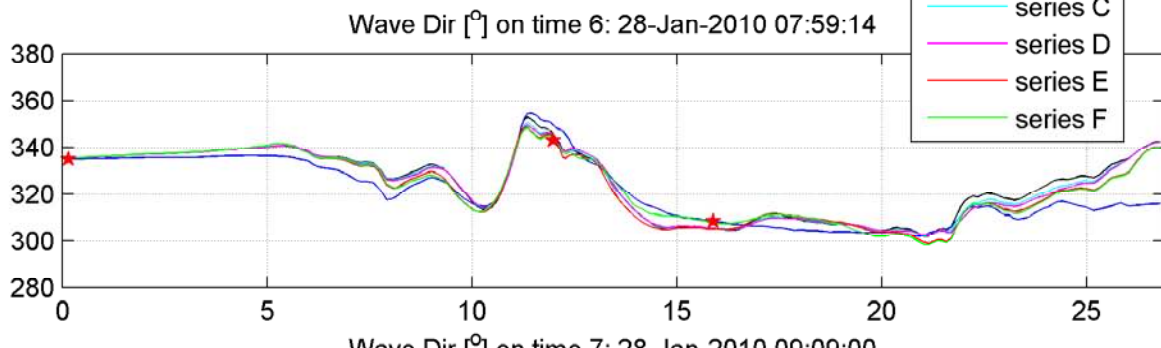
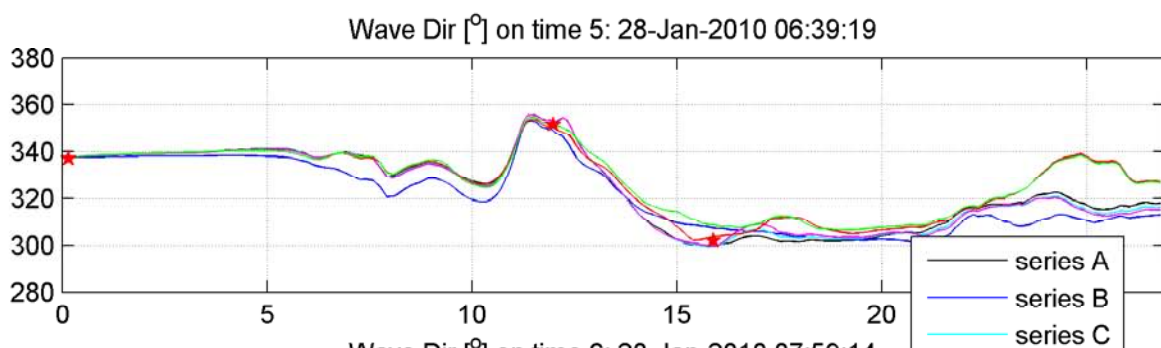
Amelander
Zeegat
instants t1 - t4

Wave-current interaction

DELTARES

1202119.003

Fig. 4.12.a



Model results of Wave Dir for series A, B, C, D, E, F
stars indicate observations at AZB11, AZB31, AZB42, AZB62

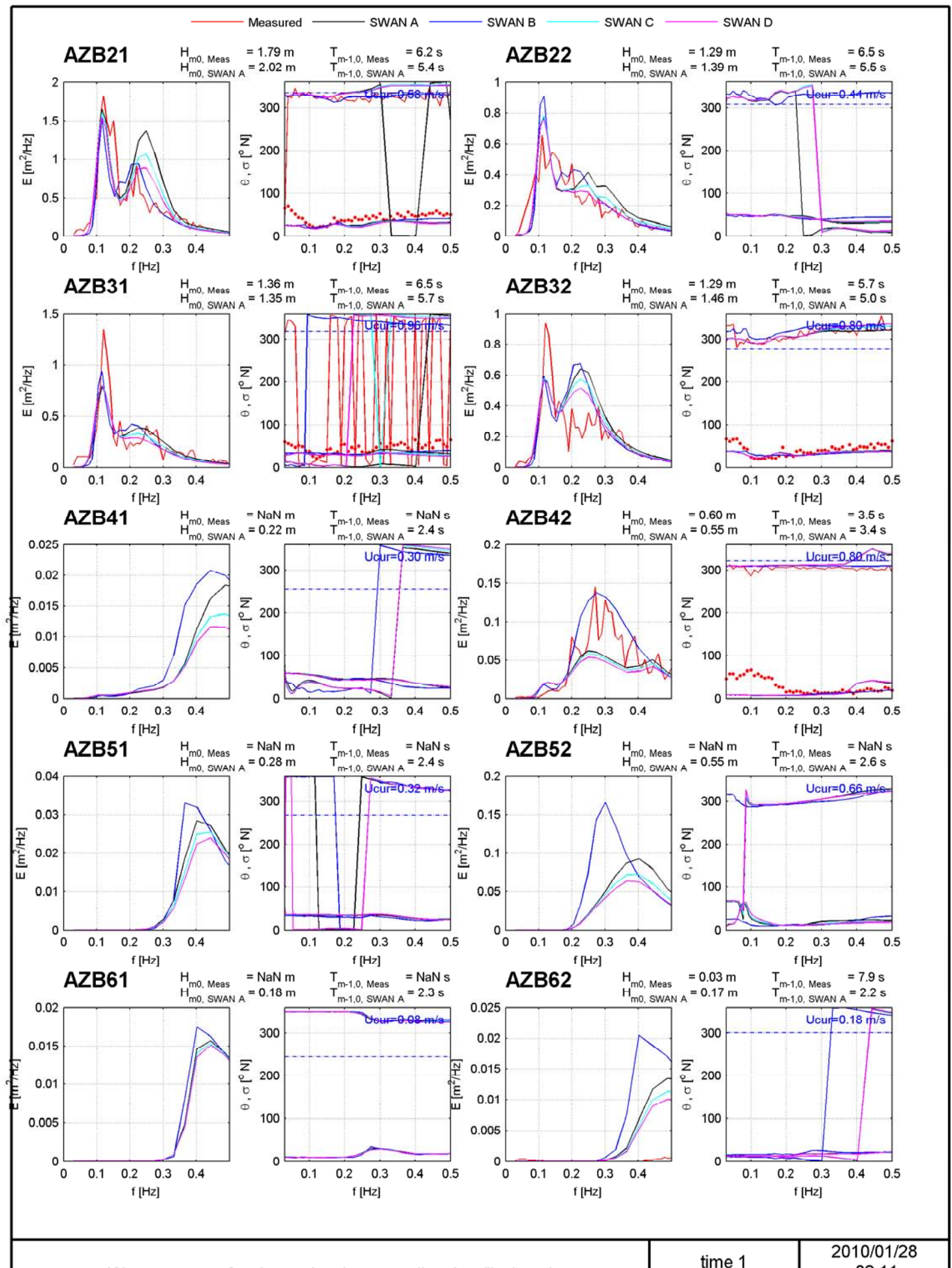
Amelander
Zeegat
instants t5 - t8

Wave-current interaction

DELTARES

1202119.003

Fig. 4.12.b



Wave spectra of variance density, wave direction (line) and wave spreading (dots), series A, B, C, D

time 1

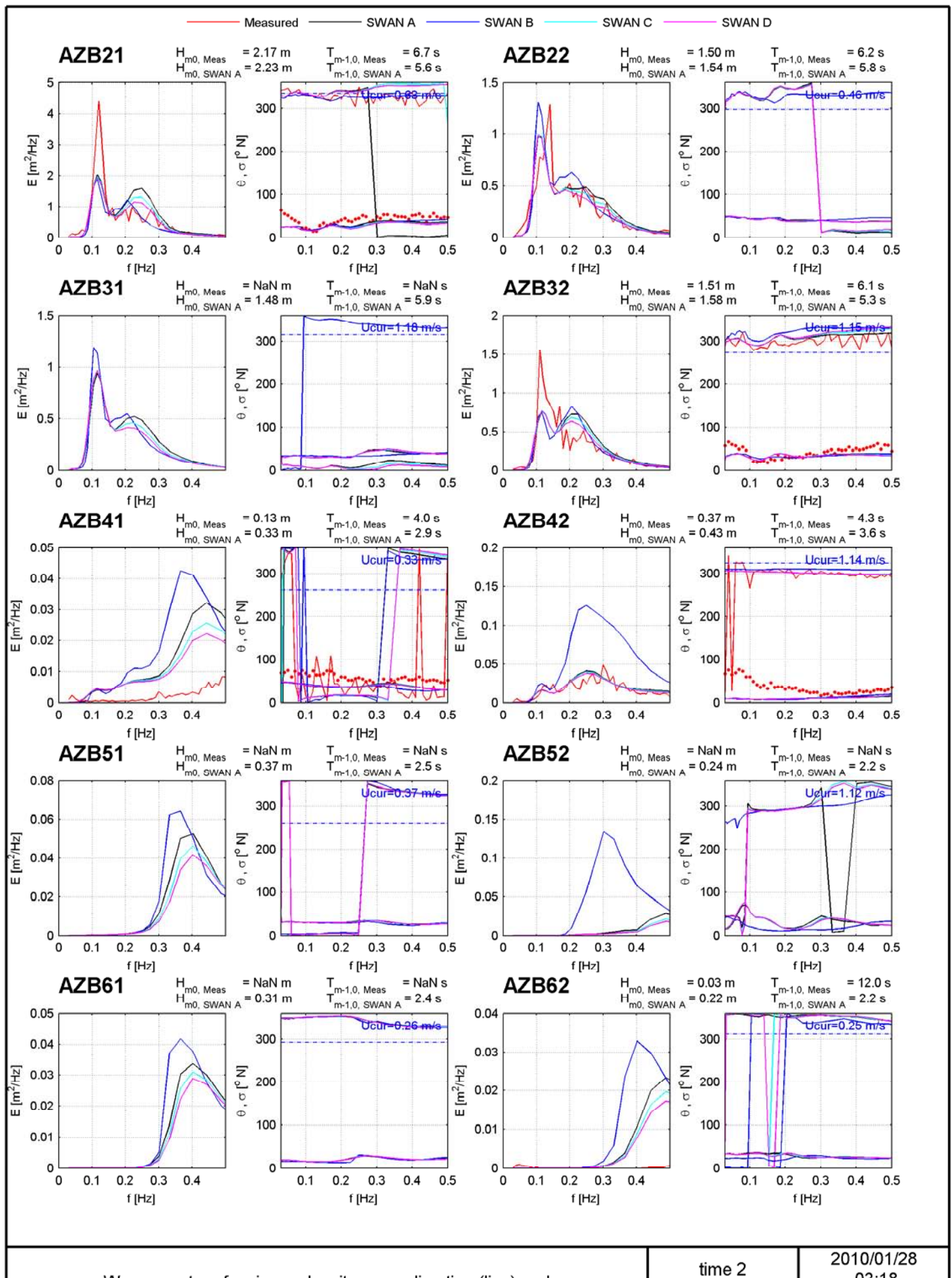
2010/01/28
02:11

Wave-current interaction

DELTARES

1202119.003

Fig 4.13.a



Wave spectra of variance density, wave direction (line) and wave spreading (dots), series A, B, C, D

time 2

2010/01/28

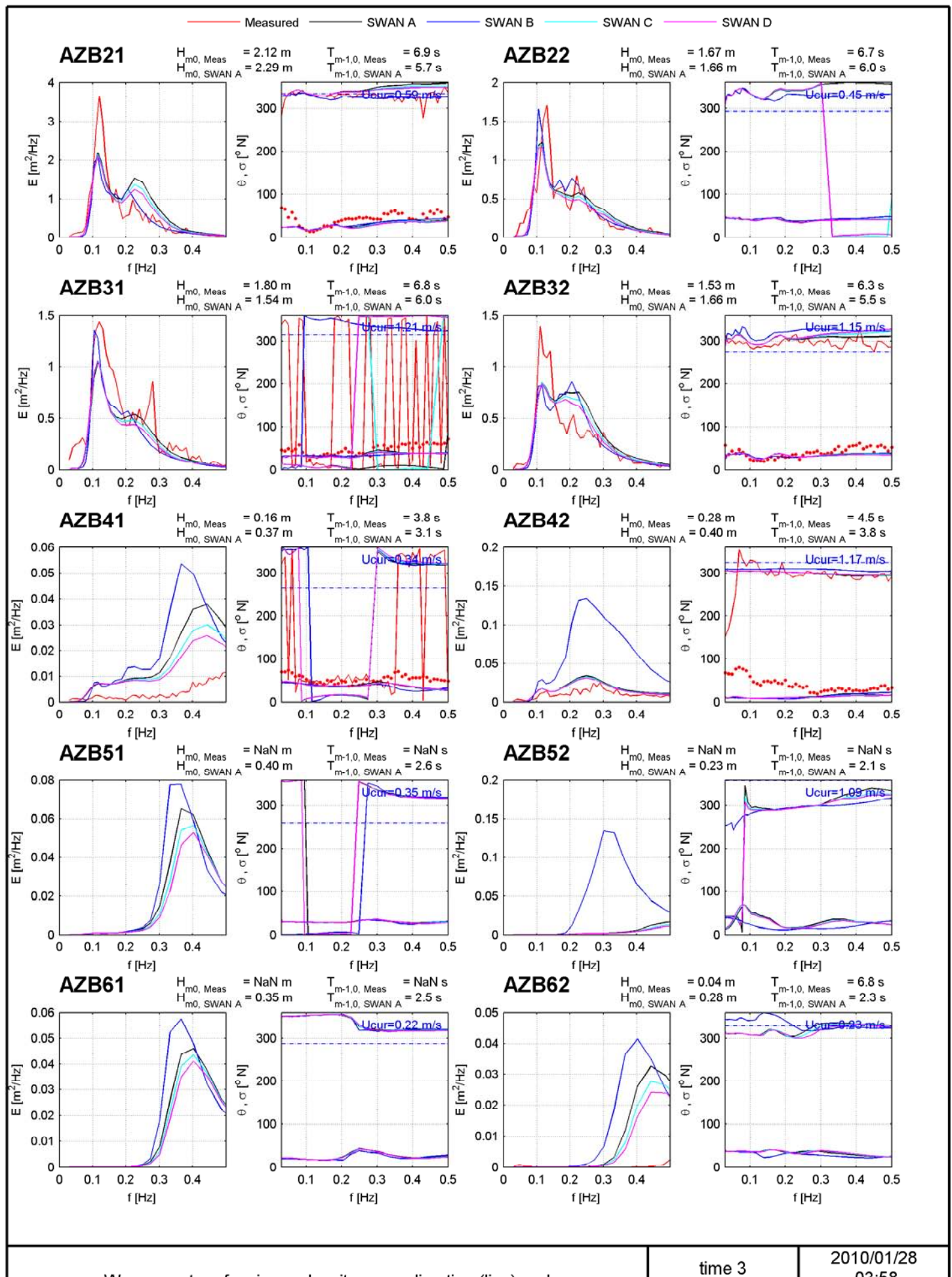
03:18

Wave-current interaction

DELTARES

1202119.003

Fig 4.13.b



Wave spectra of variance density, wave direction (line) and wave spreading (dots), series A, B, C, D

time 3

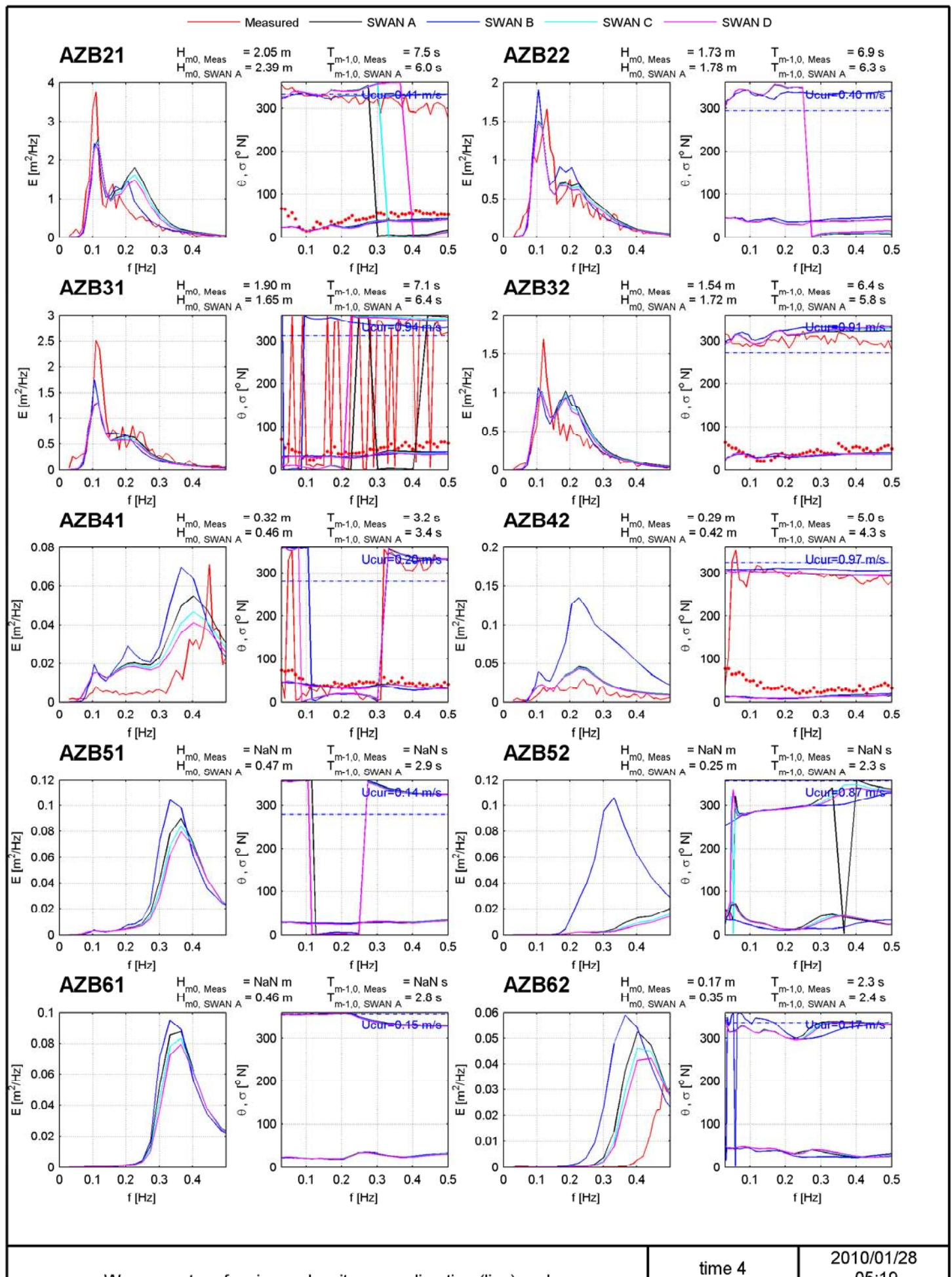
2010/01/28
03:58

Wave-current interaction

DELTARES

1202119.003

Fig 4.13.c



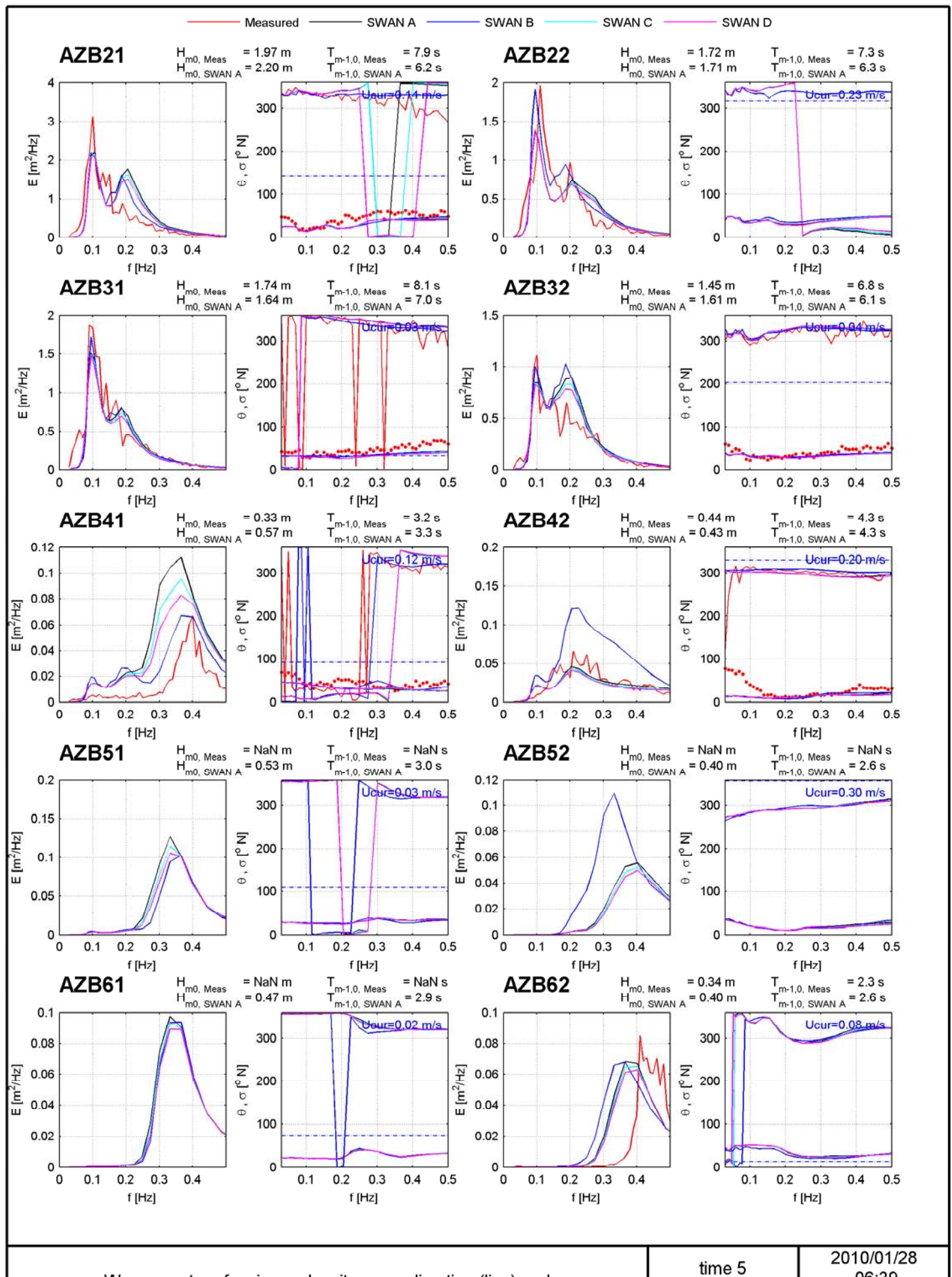
Wave spectra of variance density, wave direction (line) and wave spreading (dots), series A, B, C, D

time 4

2010/01/28

05:19

Wave-current interaction



Wave spectra of variance density, wave direction (line) and wave spreading (dots), series A, B, C, D

time 5

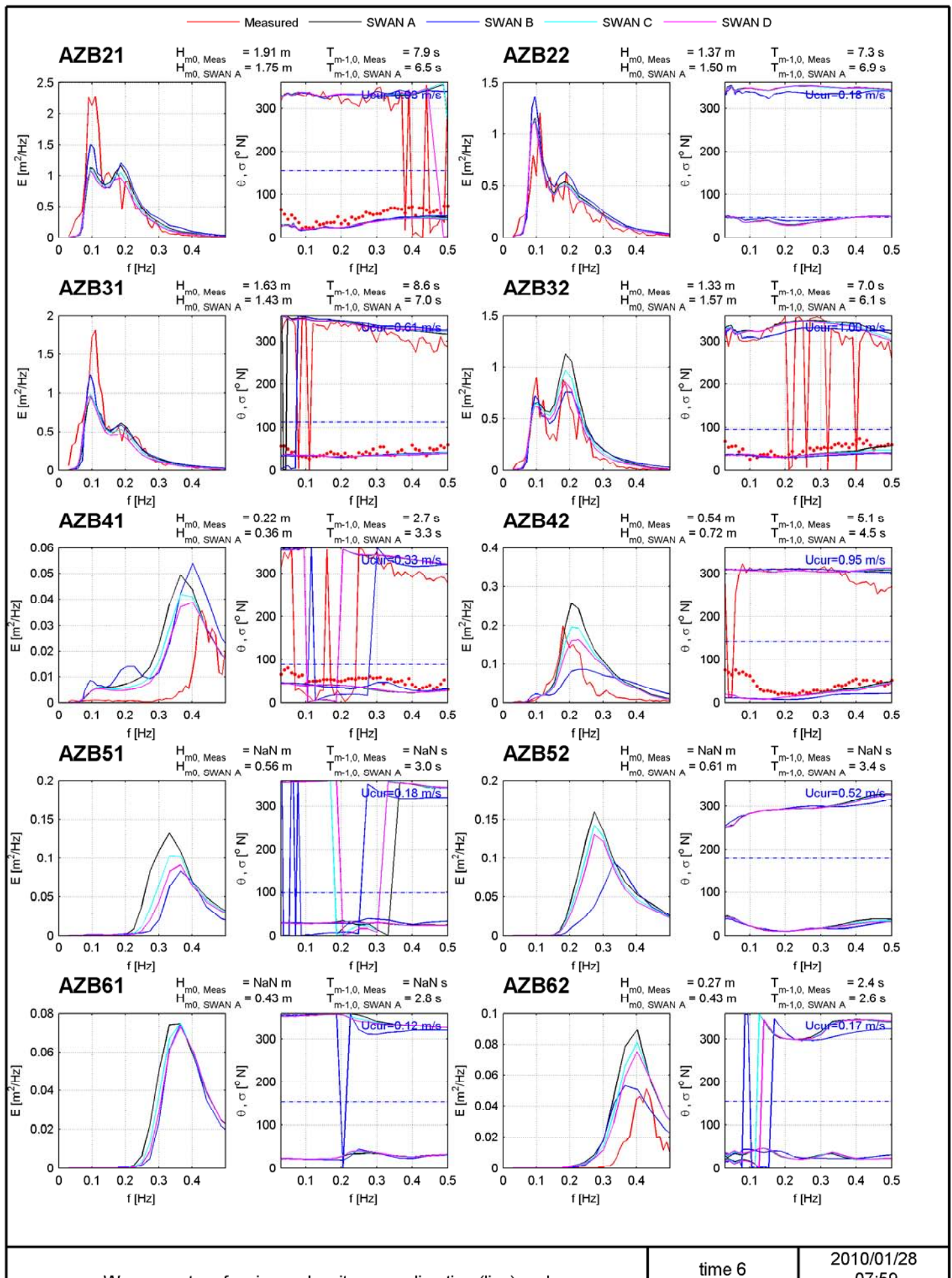
2010/01/28
06:39

Wave-current interaction

DELTARES

1202119.003

Fig 4.13.e



Wave spectra of variance density, wave direction (line) and wave spreading (dots), series A, B, C, D

time 6

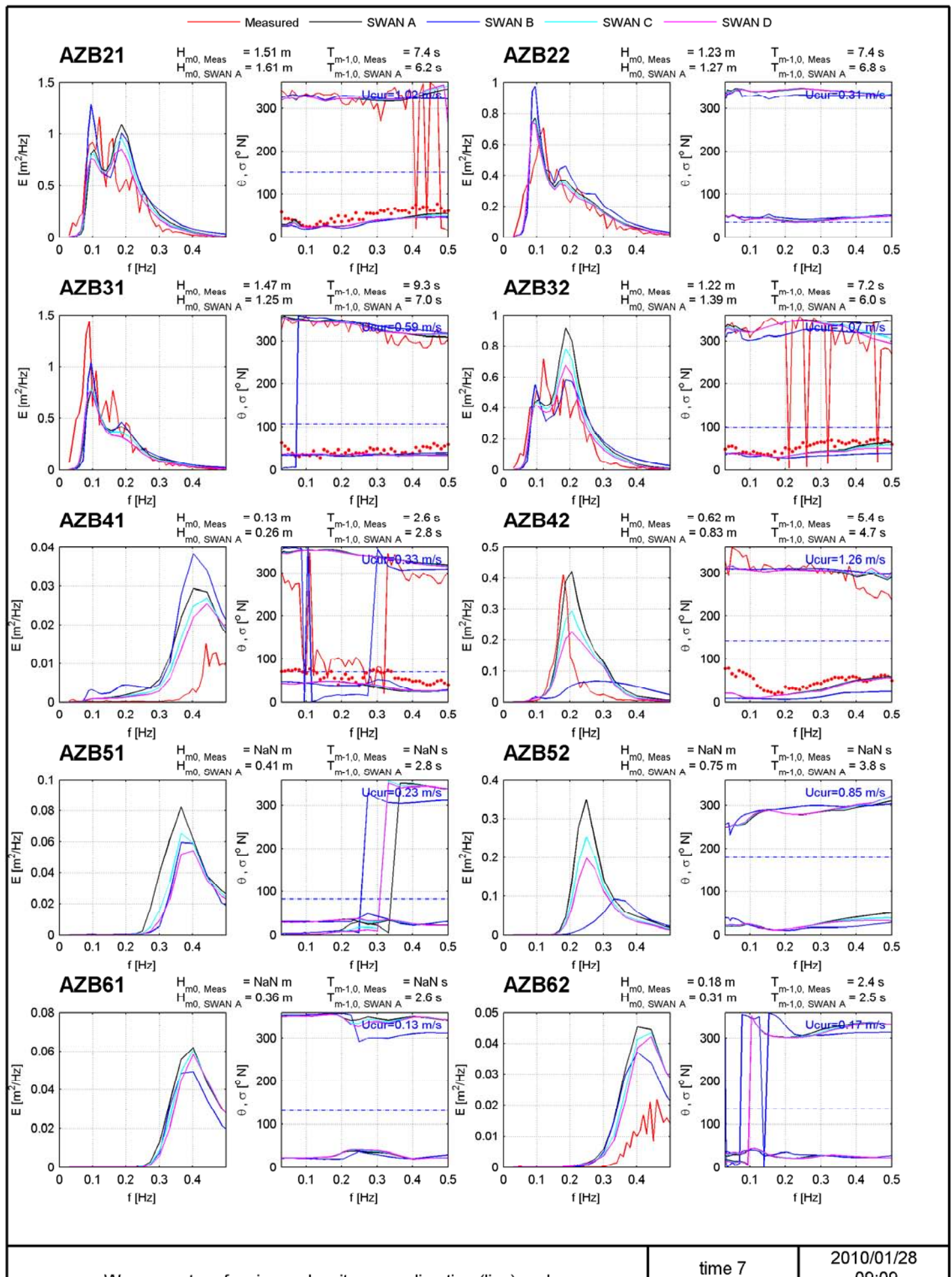
2010/01/28
07:59

Wave-current interaction

DELTARES

1202119.003

Fig 4.13.f



Wave spectra of variance density, wave direction (line) and wave spreading (dots), series A, B, C, D

time 7

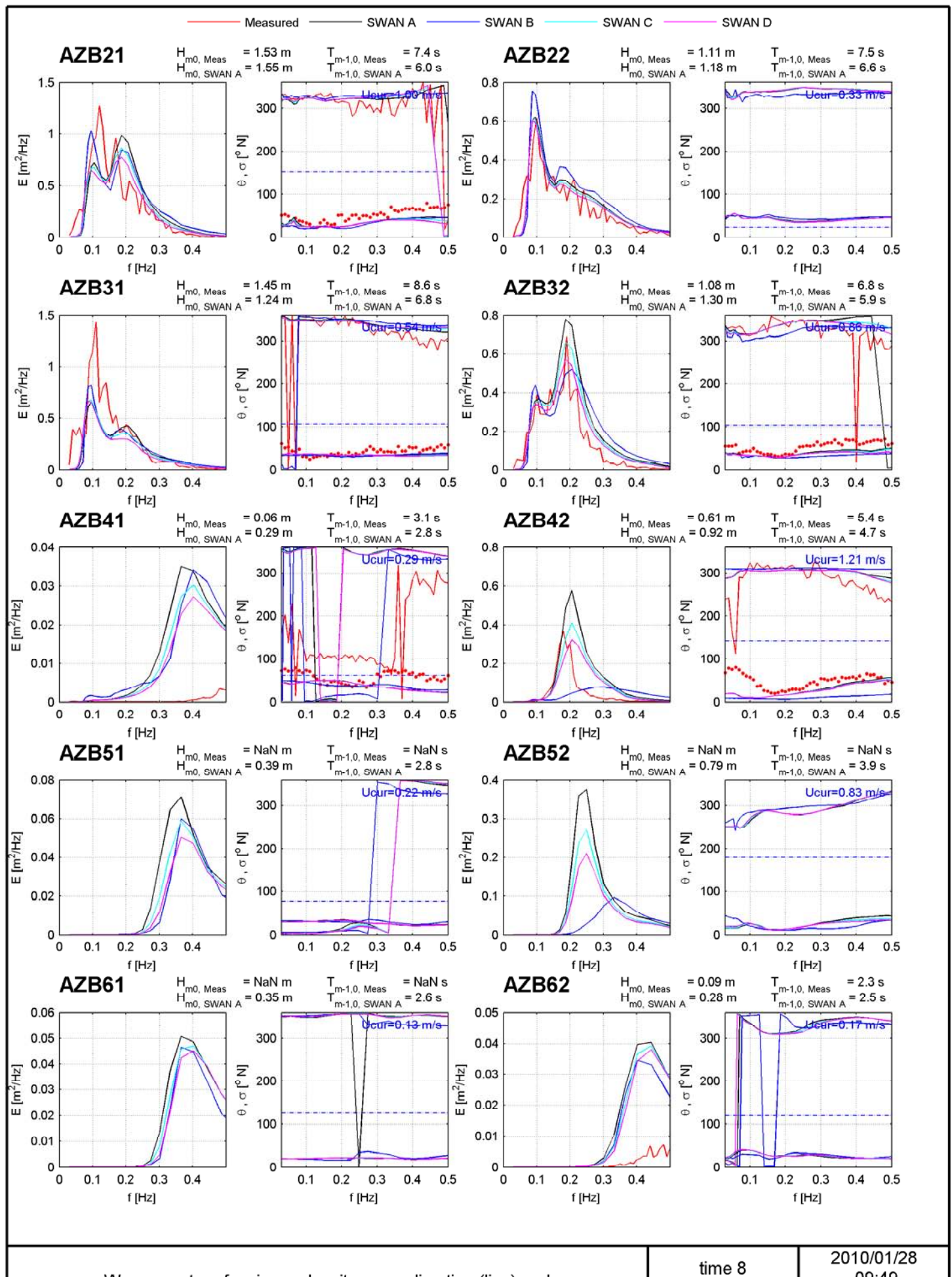
2010/01/28
09:09

Wave-current interaction

DELTARES

1202119.003

Fig 4.13.g



Wave spectra of variance density, wave direction (line) and wave spreading (dots), series A, B, C, D

time 8

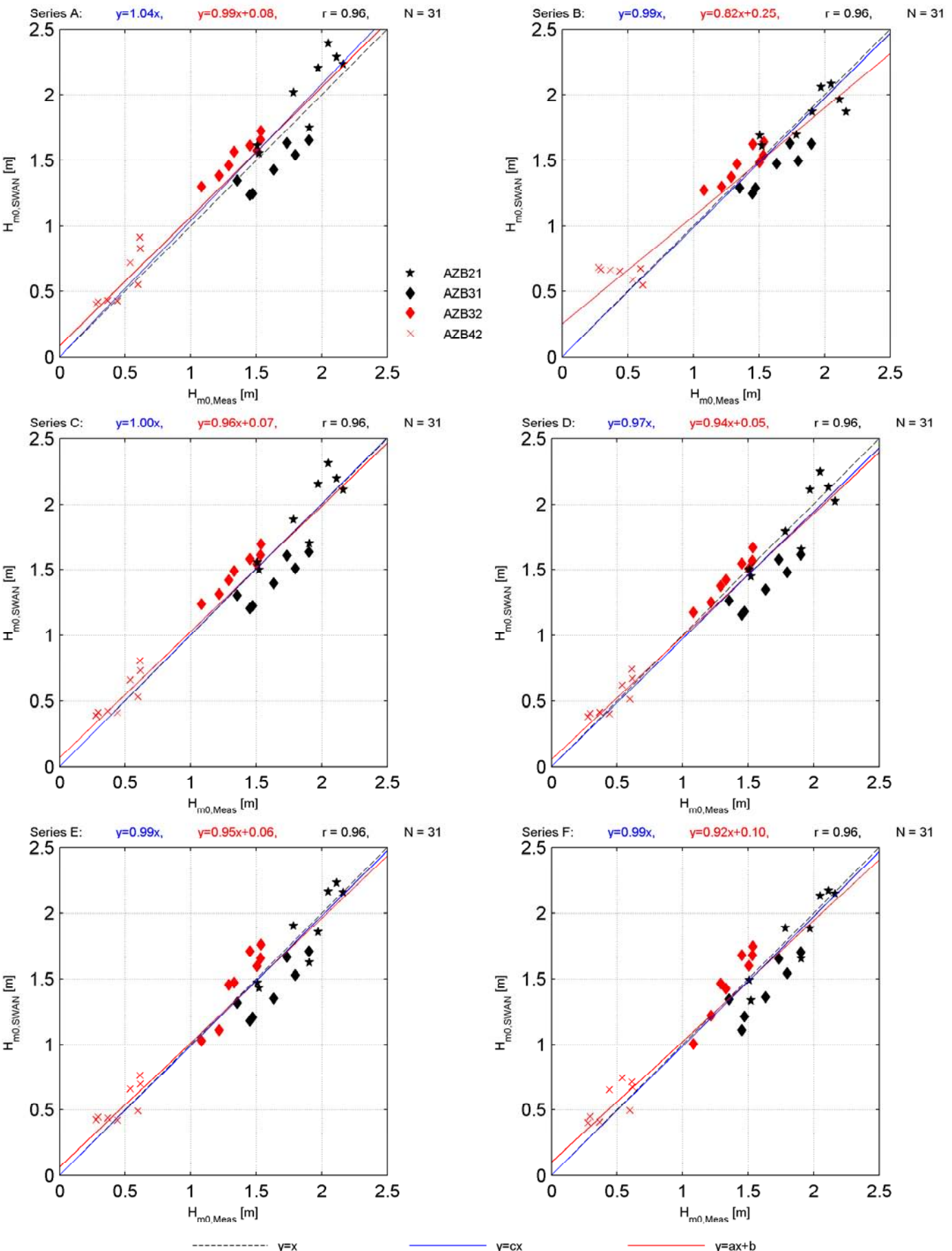
2010/01/28
09:49

Wave-current interaction

DELTARES

1202119.003

Fig 4.13.h



Scatter diagram and statistical parameters Amelander Zeegat series A, B, C, D, E, F

8 instants
28 Jan 2010

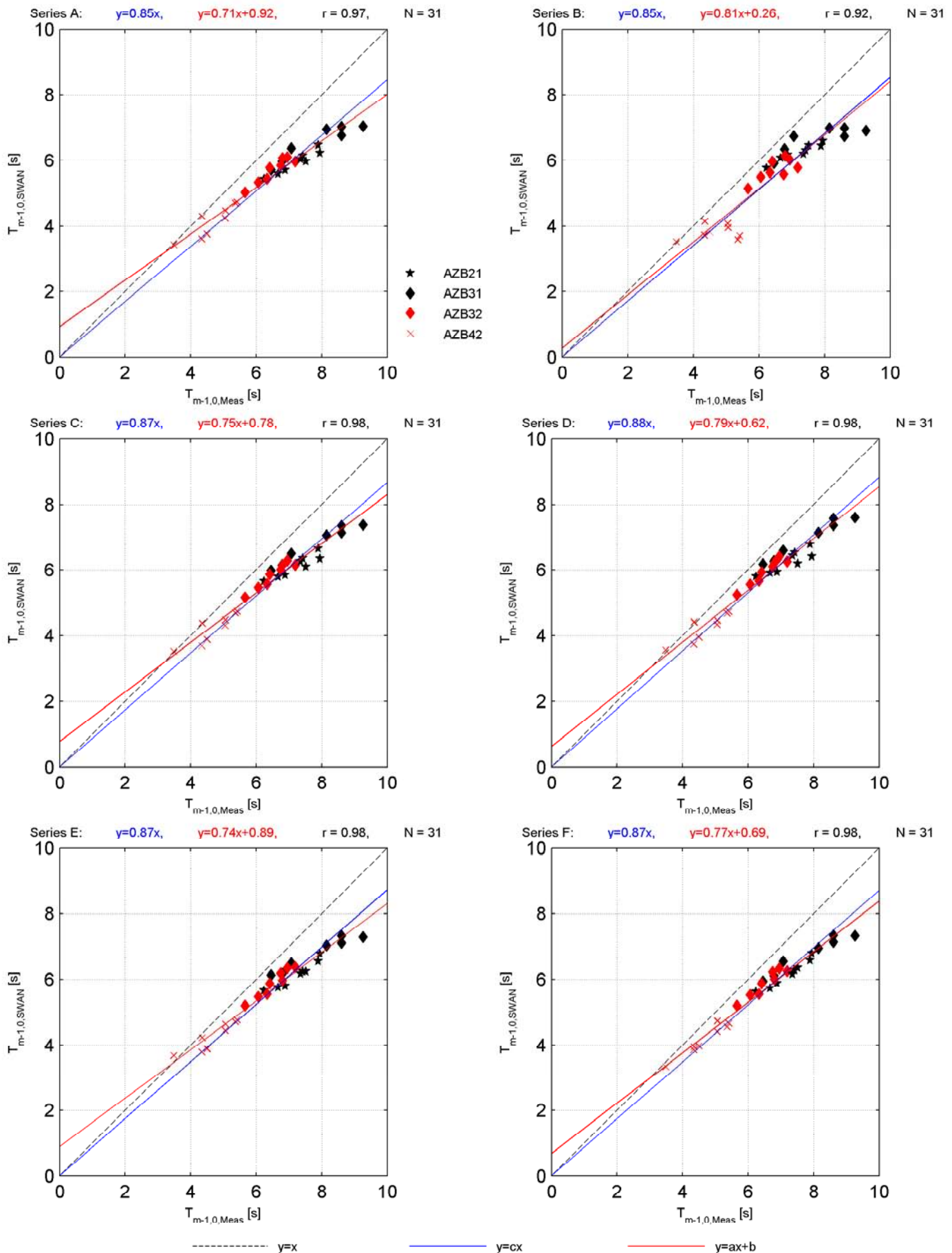
H_{m0}

Wave-current interaction

DELTARES

1202119.003

Fig 4.14



Scatter diagram and statistical parameters Amelander Zeegat series A, B, C, D, E, F

8 instants
28 Jan 2010

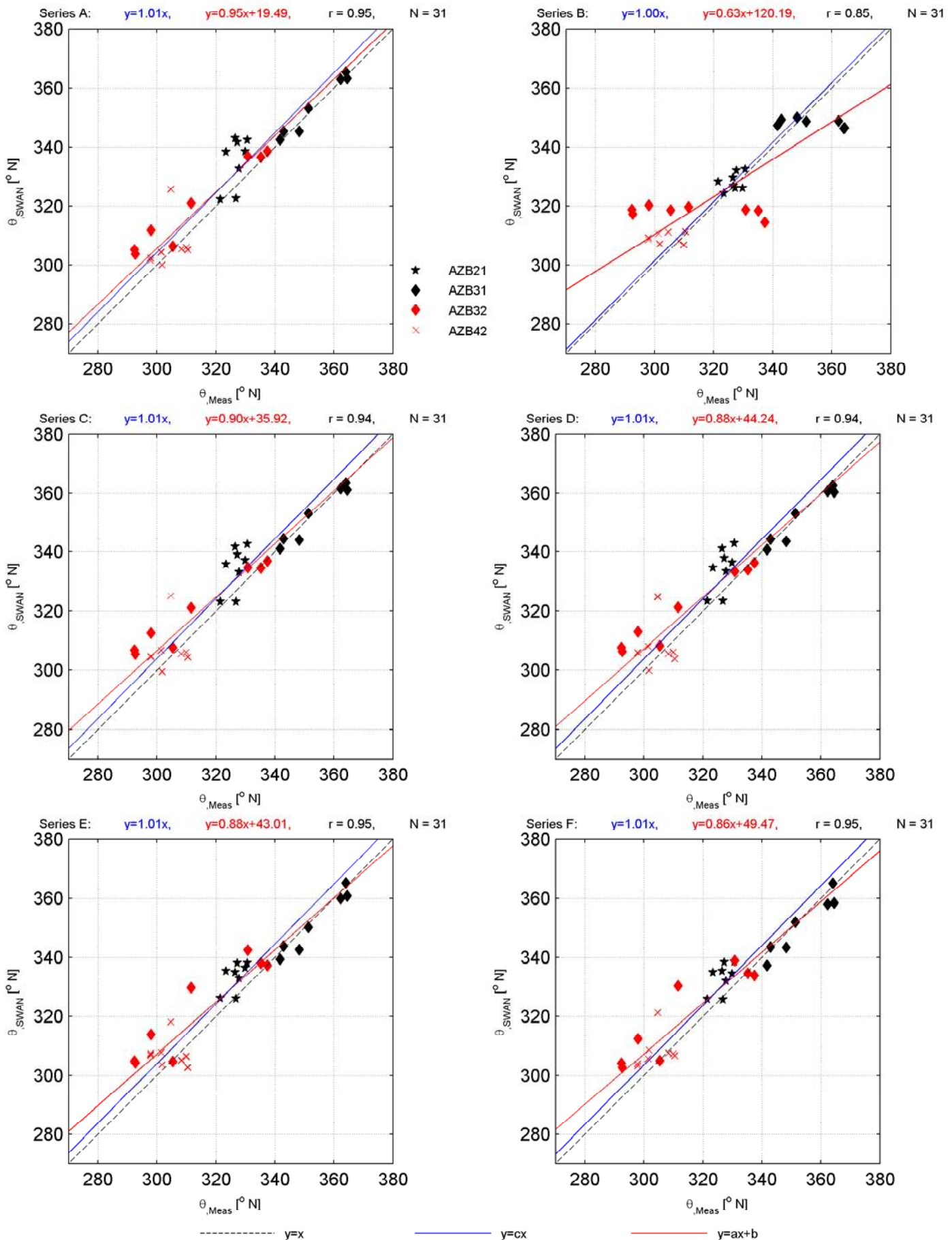
$T_{m-1,0}$

Wave-current interaction

DELTARES

1202119.003

Fig 4.15



Scatter diagram and statistical parameters Amelander Zeegat series A, B, C, D, E, F

8 instants
28 Jan 2010

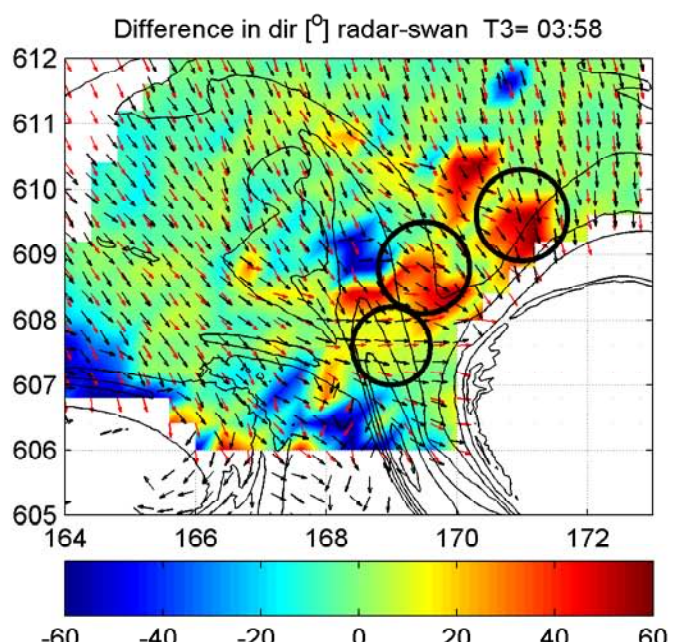
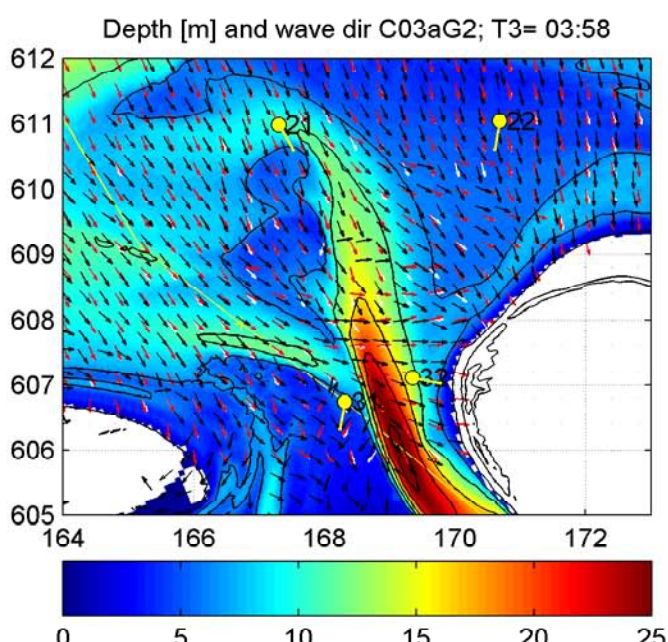
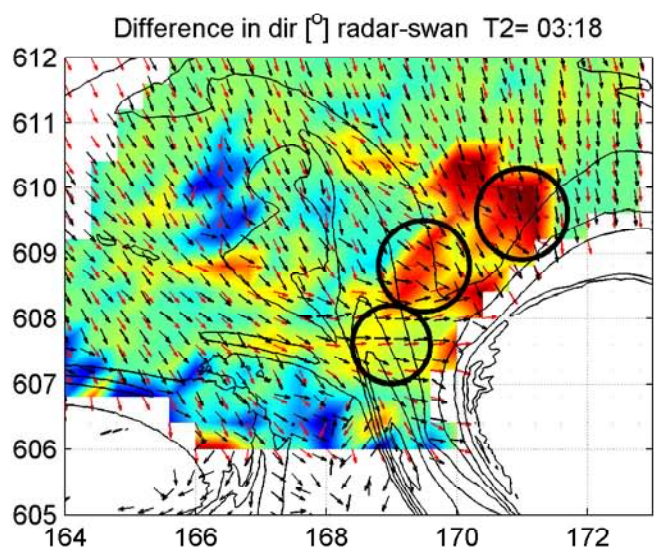
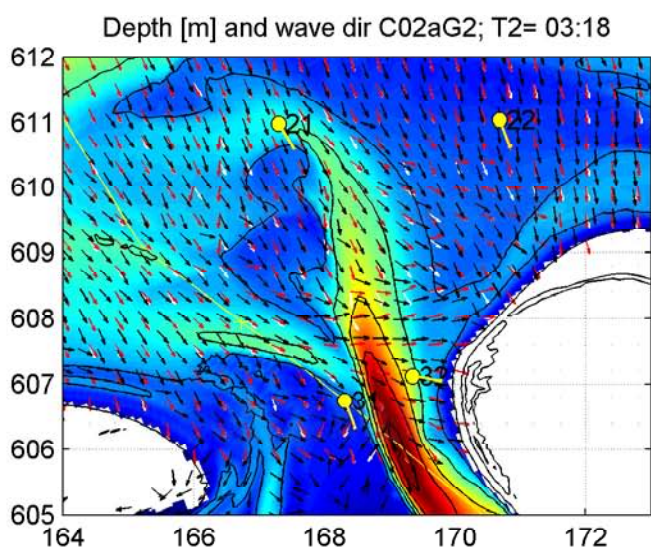
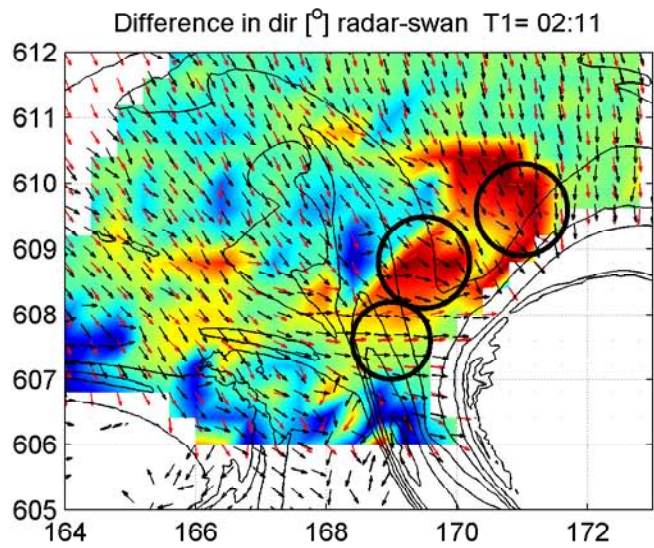
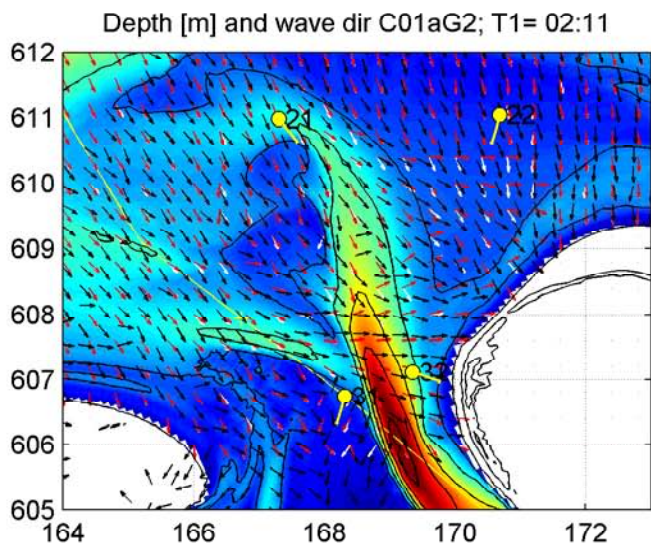
θ

Wave-current interaction

DELTARES

1202119.003

Fig 4.16



Comparison dominant wave direction SWAN and radar
left: depth; right: difference in dominant direction
vectors: black=radar dominant dir; white=SWAN peak dir; red=SWAN dominant dir

28 Jan 2010

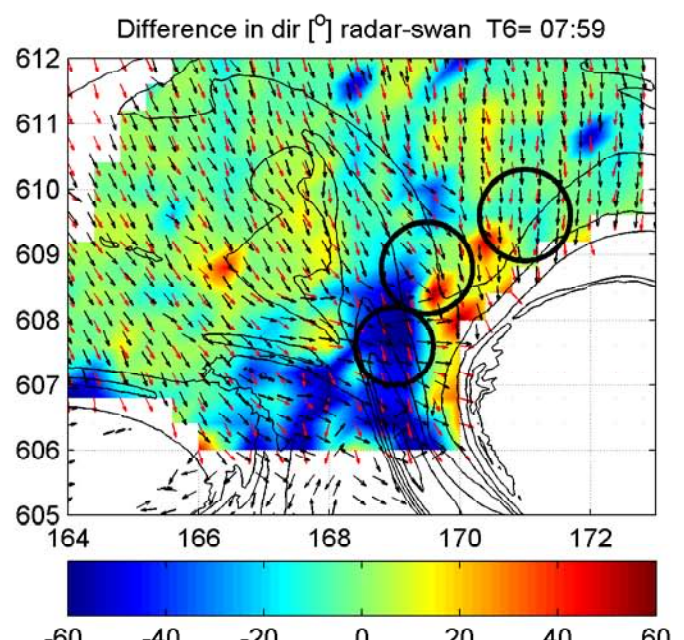
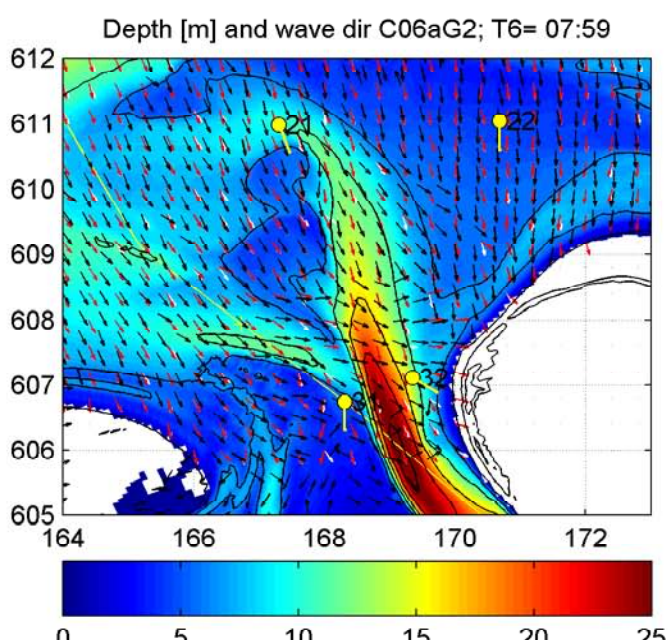
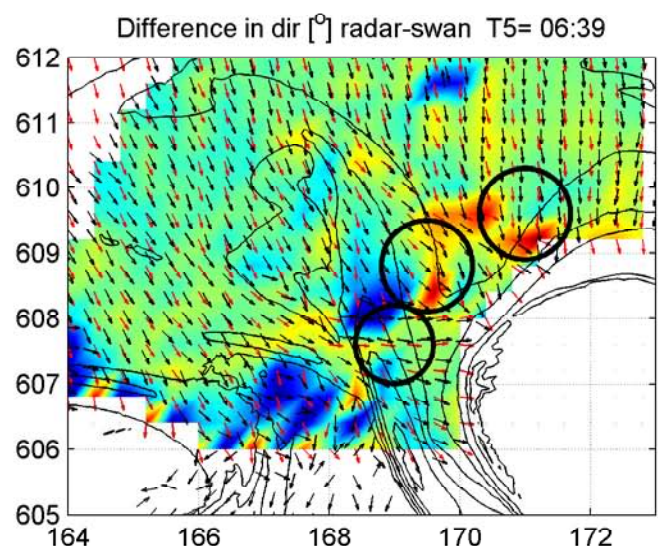
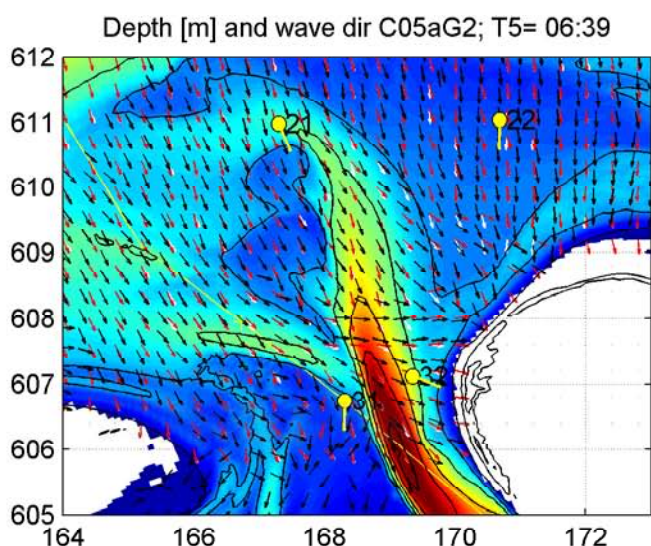
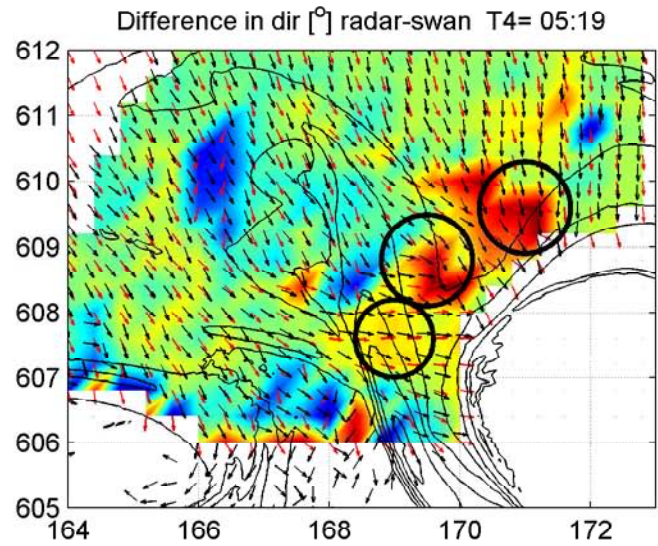
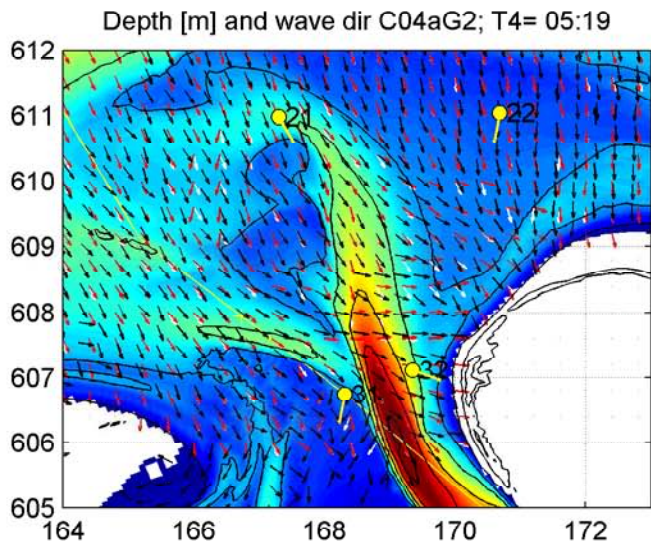
wavedir
SWAN & radar

Wave-current interaction

DELTARES

1202119.003

Fig 4.17.a



Comparison dominant wave direction SWAN and radar
left: depth; right: difference in dominant direction
vectors: black=radar dominant dir; white=SWAN peak dir; red=SWAN dominant dir

28 Jan 2010

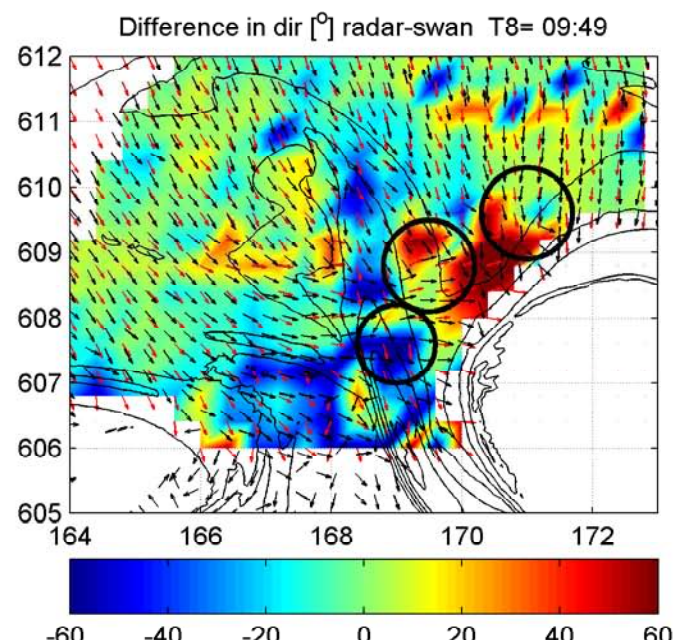
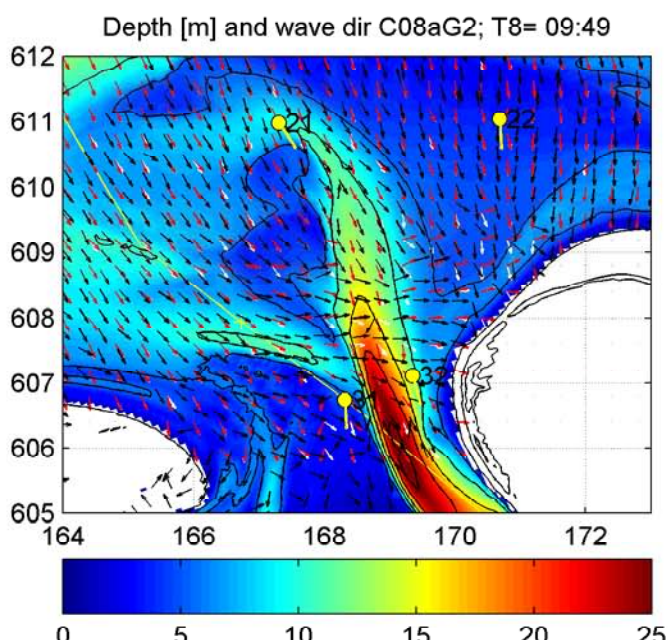
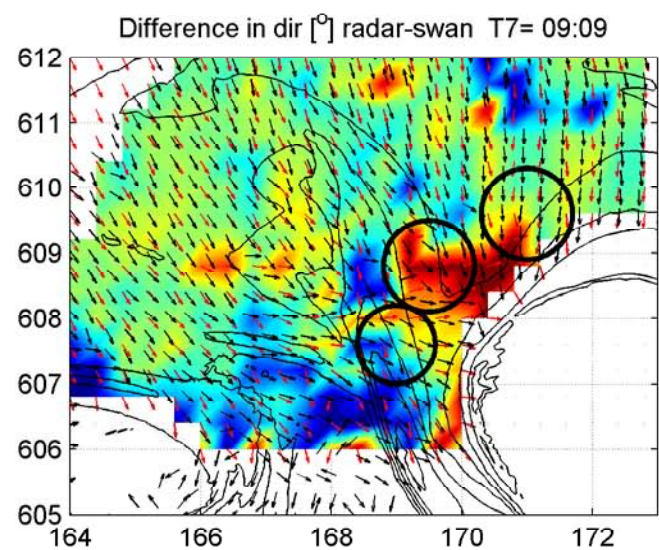
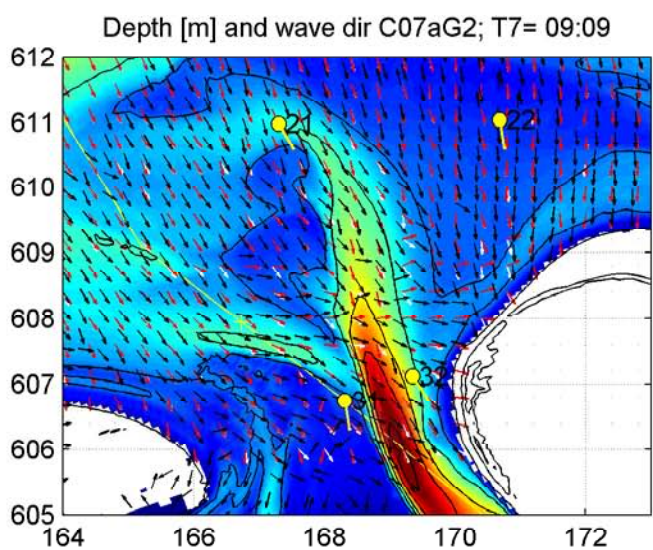
wavedir
SWAN & radar

Wave-current interaction

DELTARES

1202119.003

Fig 4.17.b



Comparison dominant wave direction SWAN and radar
left: depth; right: difference in dominant direction
vectors: black=radar dominant dir; white=SWAN peak dir; red=SWAN dominant dir

28 Jan 2010

wavedir
SWAN & radar

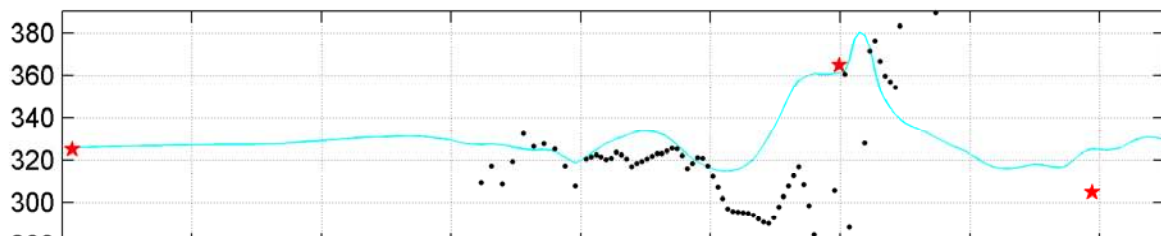
Wave-current interaction

DELTARES

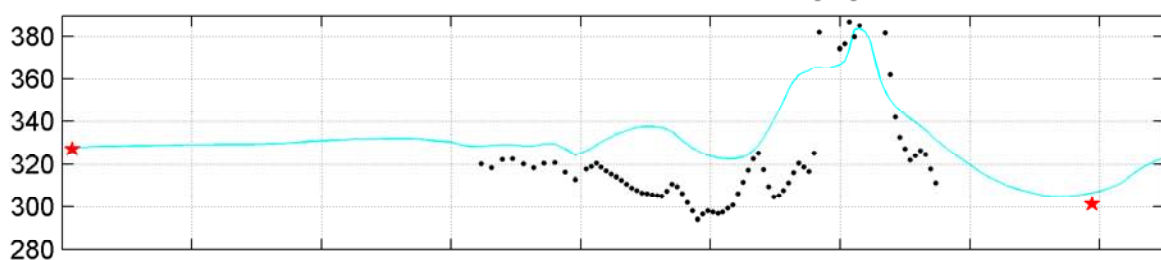
1202119.003

Fig 4.17.c

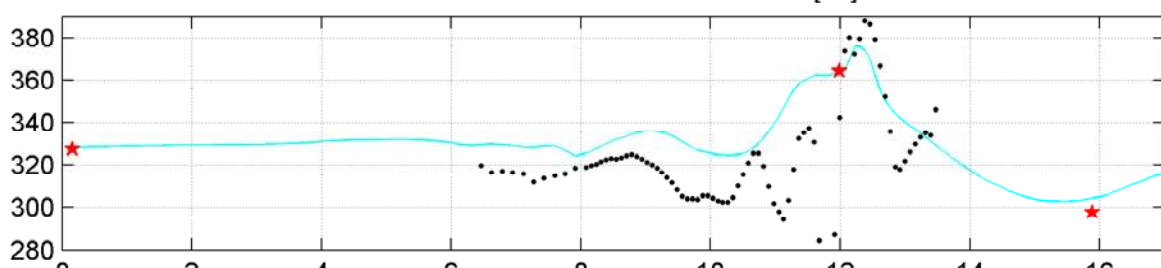
SWAN Wave Peak Dir and Radar Dominant Wave Dir [$^{\circ}$ N] on time 1: 02:11



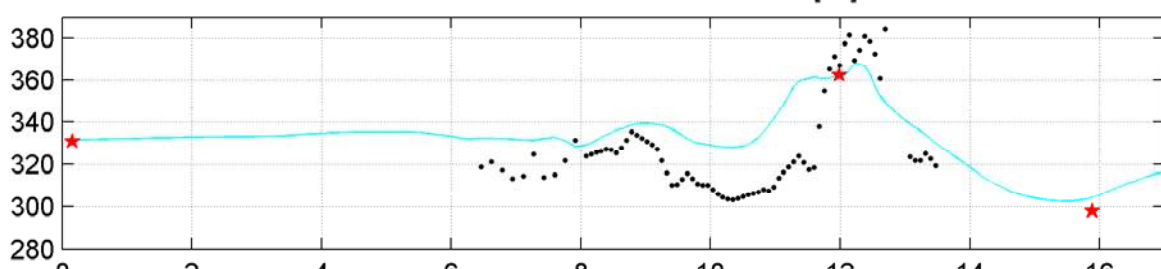
SWAN Wave Peak Dir and Radar Dominant Wave Dir [$^{\circ}$ N] on time 2: 03:18



SWAN Wave Peak Dir and Radar Dominant Wave Dir [$^{\circ}$ N] on time 3: 03:58



SWAN Wave Peak Dir and Radar Dominant Wave Dir [$^{\circ}$ N] on time 4: 05:19



Model results of peak dir for series C
stars indicate observations at resp AZB11, AZB31, AZB42
black dots (.) indicate radar dominant wave direction

Amelander
Zeegat

times t1 - t4

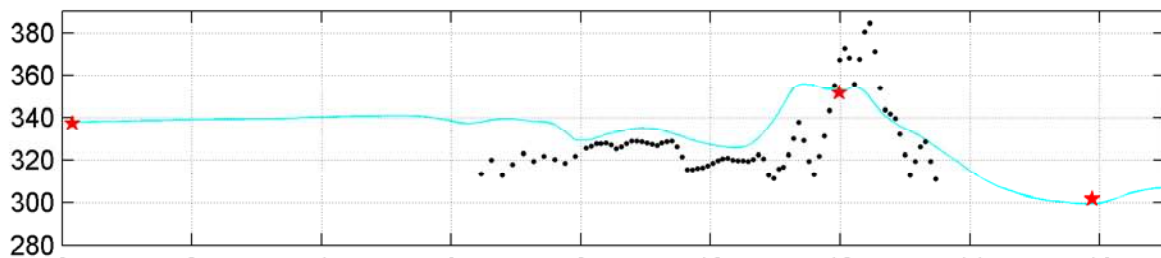
Wave-current interaction

DELTARES

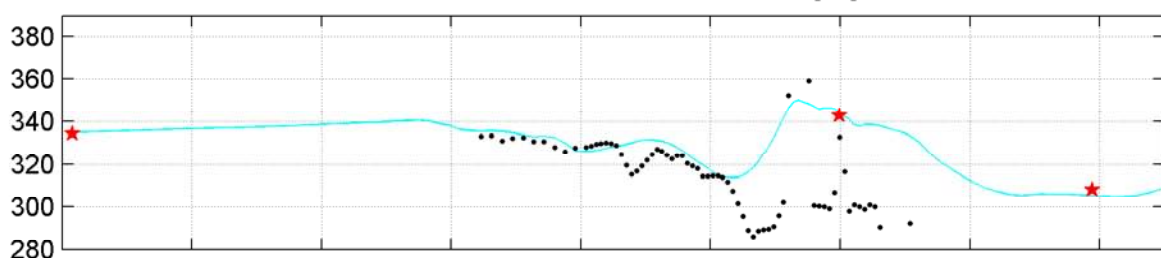
1202119.003

Fig. 4.18.a

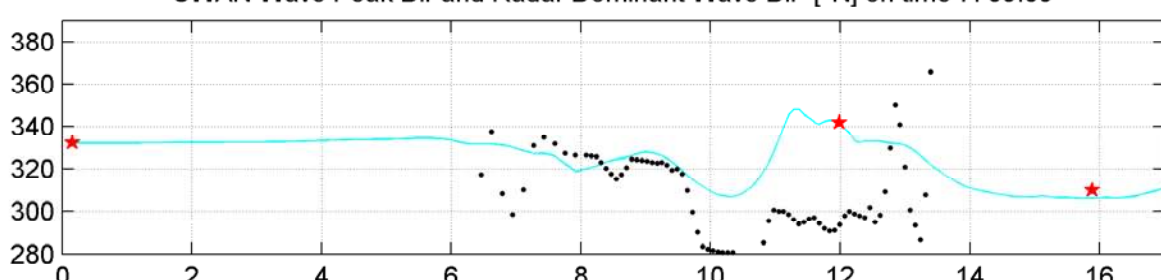
SWAN Wave Peak Dir and Radar Dominant Wave Dir [$^{\circ}$ N] on time 5: 06:39



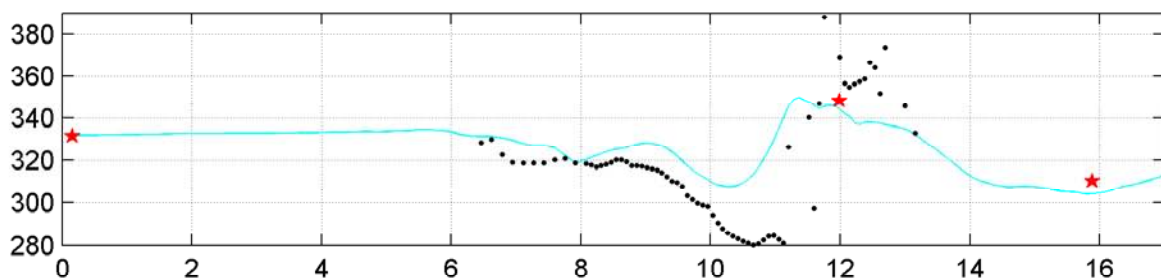
SWAN Wave Peak Dir and Radar Dominant Wave Dir [$^{\circ}$ N] on time 6: 07:59



SWAN Wave Peak Dir and Radar Dominant Wave Dir [$^{\circ}$ N] on time 7: 09:09



SWAN Wave Peak Dir and Radar Dominant Wave Dir [$^{\circ}$ N] on time 8: 09:49



Model results of peak dir for series C
stars indicate observations at resp AZB11, AZB31, AZB42
black dots (.) indicate radar dominant wave direction

Amelander
Zeegat

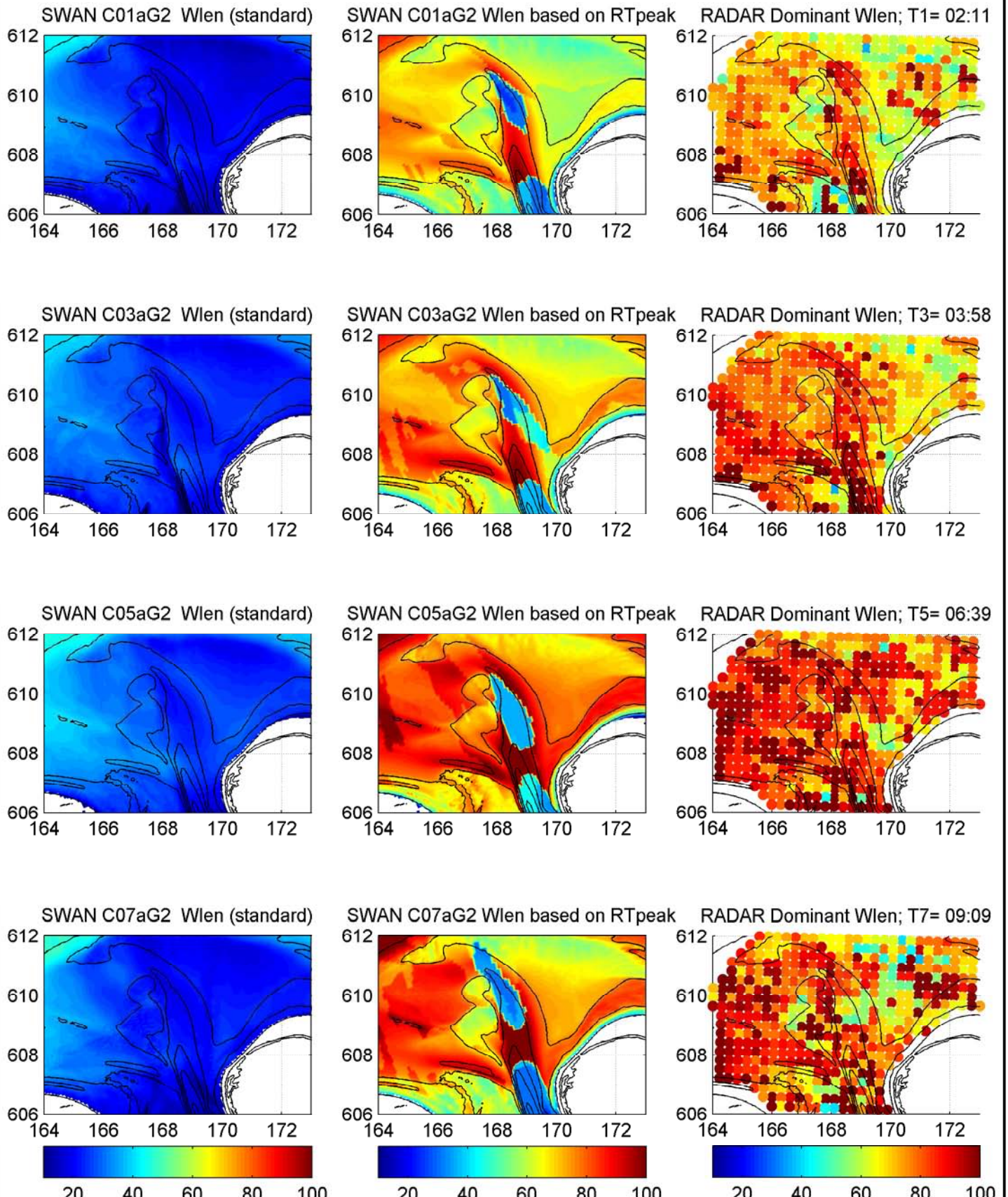
times t5 - t8

Wave-current interaction

DELTARES

1202119.003

Fig. 4.18.b

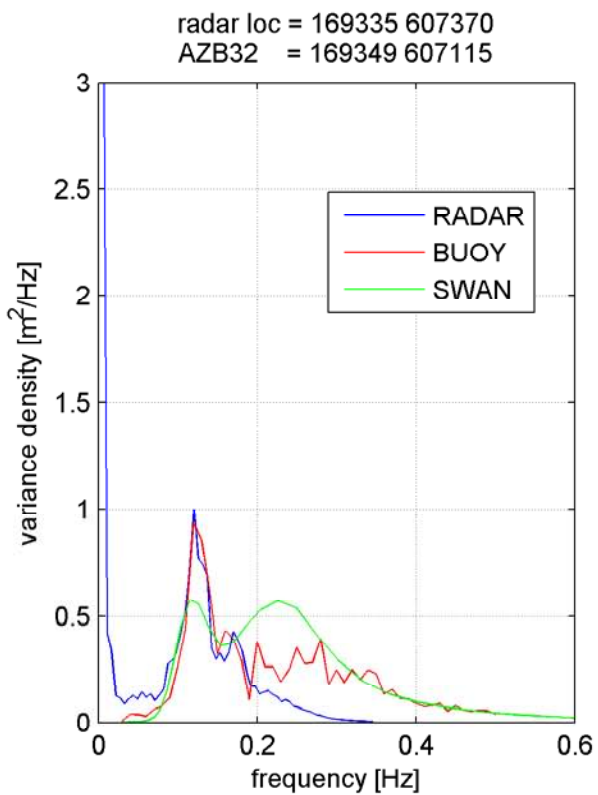
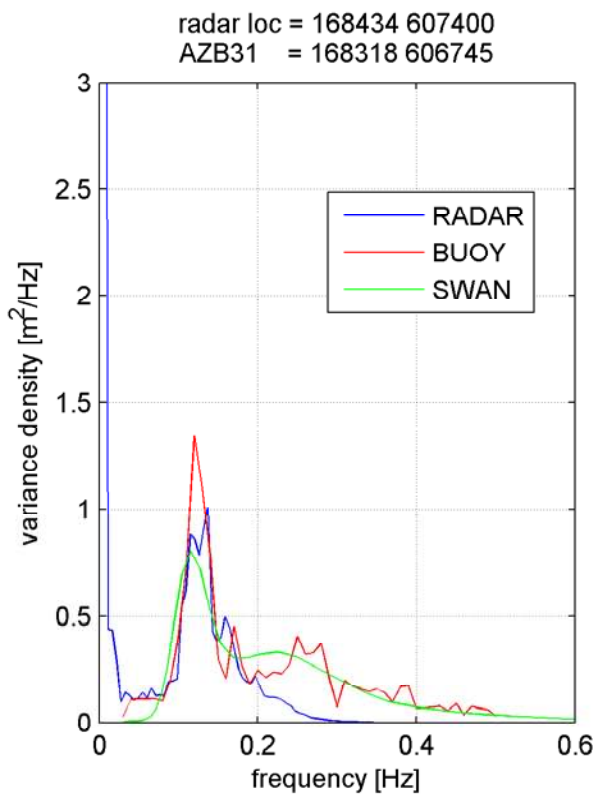
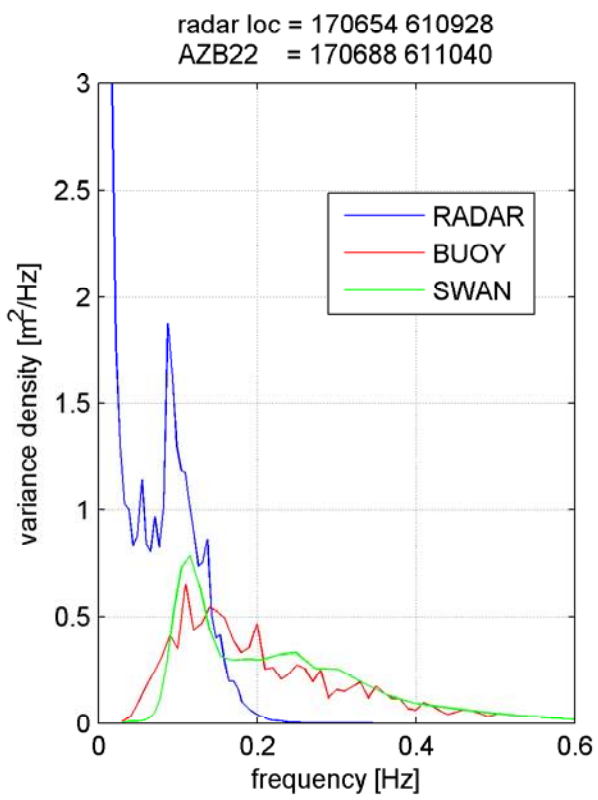
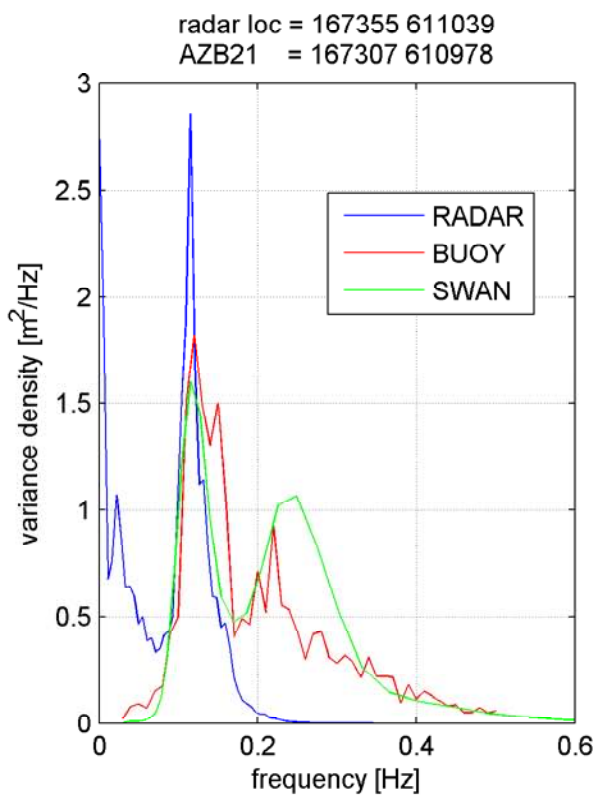


Comparison wave length [m] SWAN and radar
 left: SWAN (average wlen); mid: indication of SWAN wlen based on RTpeak
 right: radar dominant wave length

t 1/3/5/7
28 Jan 2010

wavelength
SWAN & radar

Wave-current interaction



Comparison wave spectra
RADAR, BUOY, SWAN

02:11
28 Jan 2010

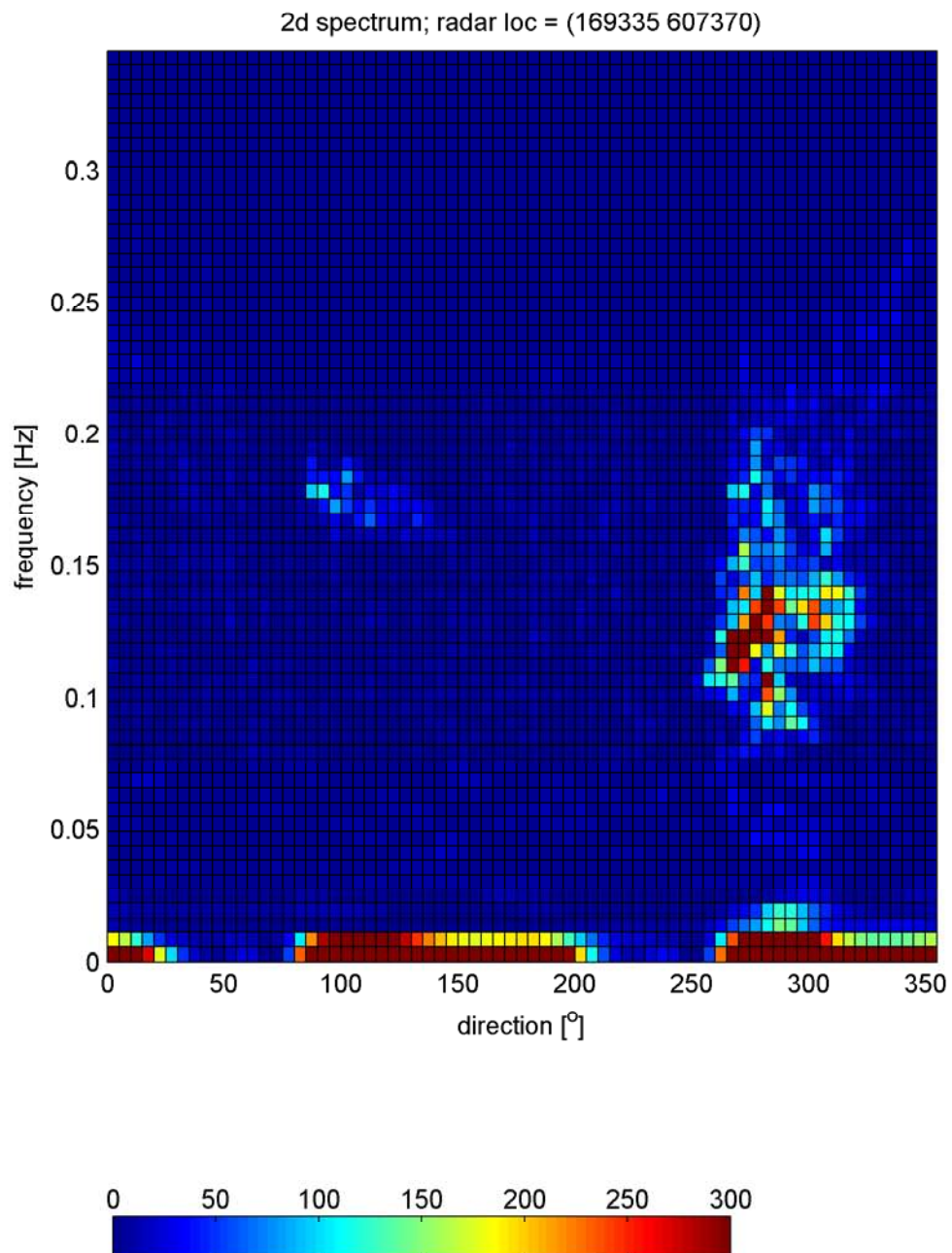
wave spectra

Wave-current interaction SWAN

DELTARES

1202119.003

Fig 4.20



2d Radar intensity spectrum
location AZB31

02:11
28 Jan 2010

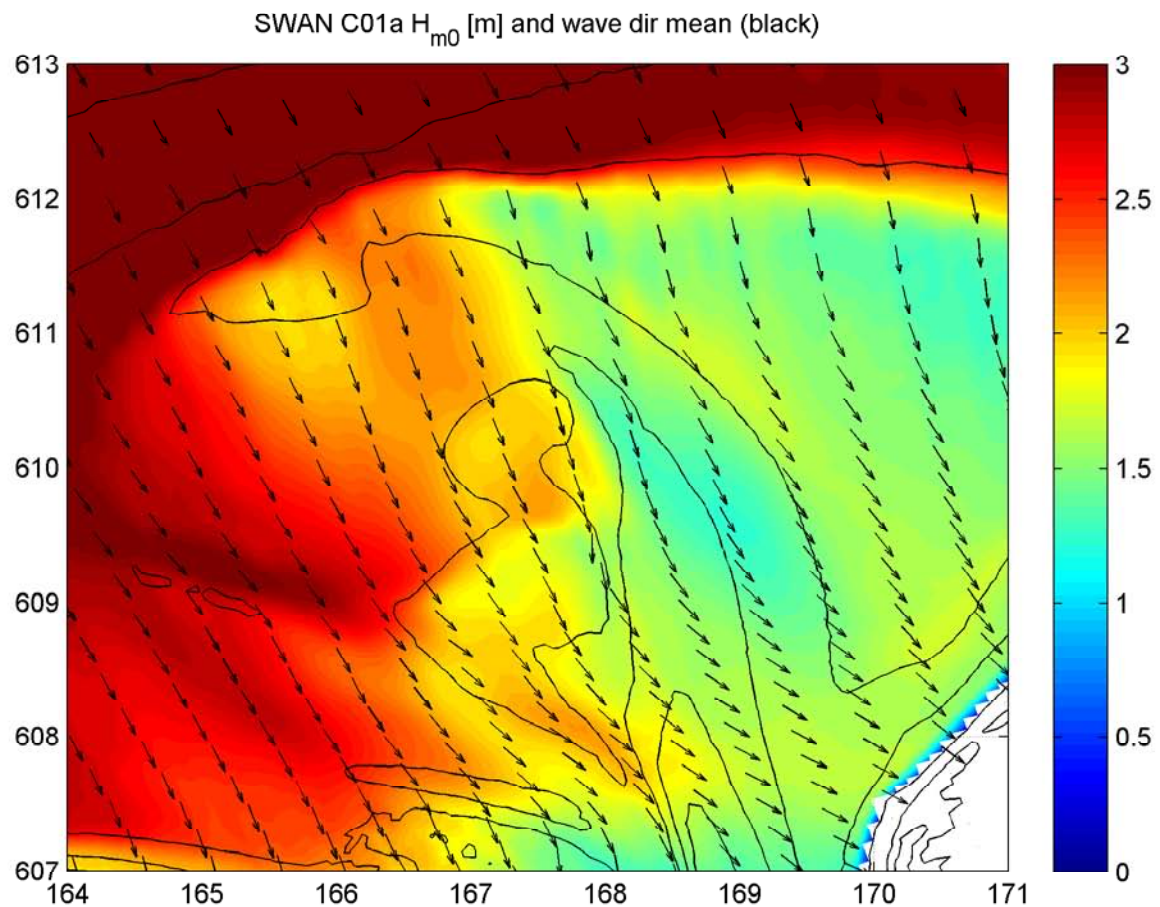
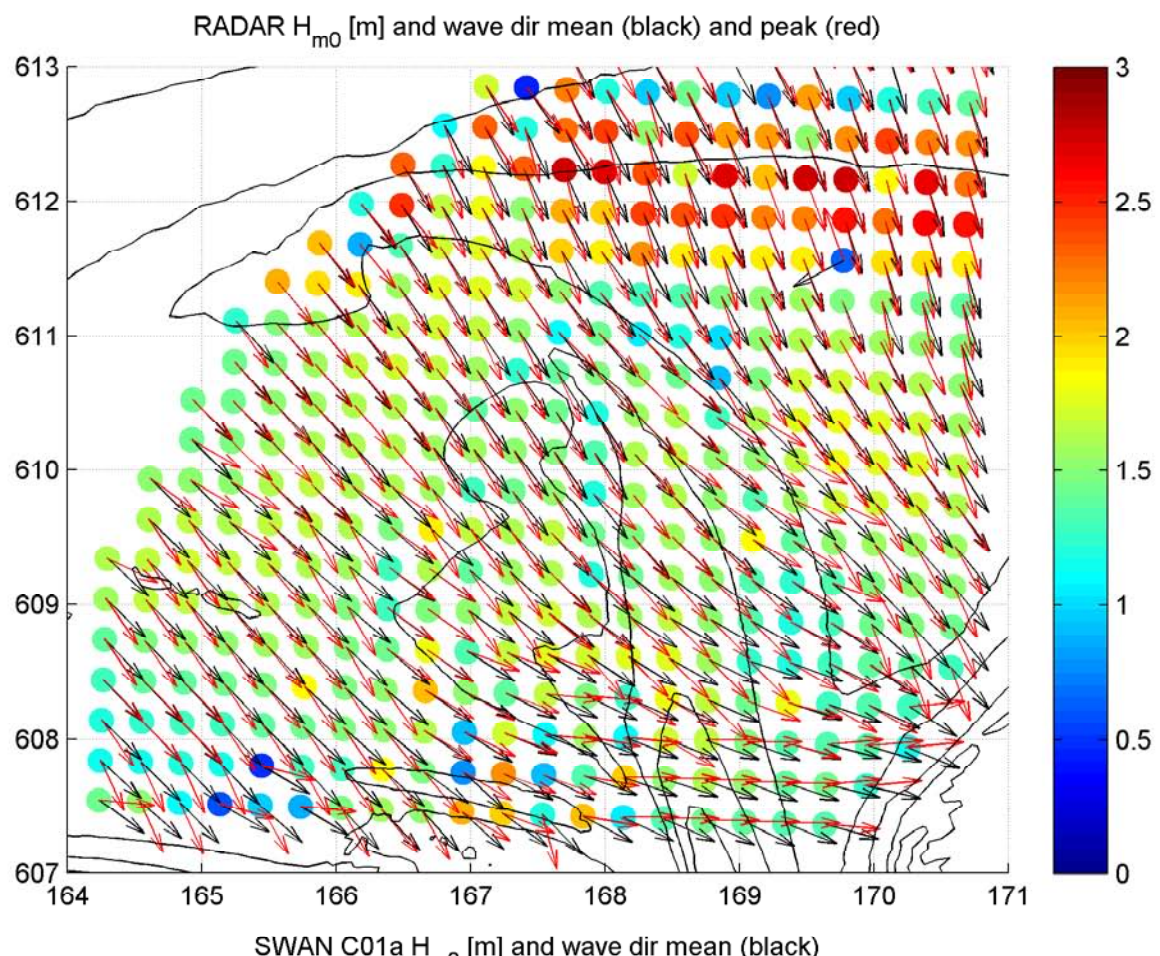
wave spectra

Wave current interaction

DELTARES

1202119.003

Fig 4.21



Comparison wave height [m] SWAN and radar
upper: RADAR; lower: SWAN

t1
28 Jan 2010

waveheight
SWAN & radar

Wave-current interaction

DELTARES

1202119.003

Fig 4.22